Entrained Flow Gasification - Conversion of Liquid and Suspension Fuels in the Burner Near Field

Zur Erlangung des akademischen Grades eines

DOKTORS DER INGENIEURWISSENSCHAFTEN

von der KIT-Fakultät für Chemieingenieurwesen und Verfahrenstechnik des Karlsruher Instituts für Technologie (KIT)
genehmigte

DISSERTATION

von

Manuel Haas

Tag der mündlichen Prüfung: 18.06.26

Erstgutachter/-in: Prof. Dr.-Ing. Thomas Kolb

Zweitgutachter/-in: Prof. Dr.-Ing. Hartmut Spliethoff

Dissertation, KIT, Department of Chemical and Process Engineering

Date of the oral exam:	June 18, 2026
Examination chair:	Prof. Dr. Harald Horn
First supervisor:	Prof. Dr.-Ing. Thomas Kolb
Second supervisor:	Prof. Dr.-Ing. Hartmut Spliethoff
Examiner:	Prof. Dr.-Ing. Gregor Wehinger

© Manuel Haas, ORCID: 0000-0003-4489-7430, Germany, 2026

This is an open access document distributed under the terms of the CC-BY-NC-ND license (http://creativecommons.org/licenses/by-nc-nd/4.0/).

Registered names, trademarks, etc. used in this document, even when not specifically marked as such, are not to be considered as unprotected by law.

DOI: 10.5445/IR/1000197864

Printed in Germany, 2026

Danksagung

Die vorliegende Dissertation entstand während meiner Tätigkeit als wissenschaftlicher Mitarbeiter am Institut für Technische Chemie (ITC) des Karlsruher Instituts für Technologie (KIT) mit finanzieller Unterstützung durch die Helmholtz-Gemeinschaft Deutscher Forschungszentren (HGF) im Rahmen des Forschungsprogramms Materials and Technologies for the Energy Transition (MTET).
Ich möchte mich bei meinem Betreuer Prof. Dr.-Ing. Thomas Kolb für das entgegengebrachte Vertrauen und die große wissenschaftliche Freiheit bei der Konzeptionierung und Beantwortung der Forschungsfragen in meiner Promotionsarbeit bedanken. Die zahlreichen Diskussionen, gespeist aus einem großen Erfahrungsschatz, halfen mir dabei, meine eigenen Arbeitsergebnisse kritisch zu hinterfragen, Probleme aus einem neuen Blickwinkel zu betrachten und damit zu einem selbstständigen Forscher zu werden. Prof. Dr.-Ing. Hartmut Spliethoff möchte ich für sein Interesse an meiner Promotionsarbeit und die freundliche Übernahme des Korreferats danken.
Ein besonderer Dank gilt allen meinen aktuellen und ehemaligen Kolleginnen und Kollegen sowie Studierenden für die Unterstützung und die vielen hilfreichen Diskussionen. Besonders zu erwähnen sind an dieser Stelle Dr.-Ing. Sabine Fleck, Dr.-Ing. Tobias Jakobs, Ulrike Santo, Dr.-Ing. Christian Hotz, Dr.-Ing. Simon Wachter, Juliana Richter, Stella Walker, Helmut Reis, Timo Körber, Pia Bengert und Melina Peters.
Prof. Dr.-Ing. Frederik Scheiff danke ich für die Möglichkeit, meine wissenschaftliche Laufbahn am Engler-Bunte-Institut des Karlsruher Instituts für Technologie weiterführen zu dürfen.
Ein letzter, besonderer, Dank gilt meinen Freunden und meiner Familie für die Unterstützung in der teilweise sehr intensiven Zeit meiner Promotion.

Abstract

The present work attempts a comprehensive assessment of the interaction of sub-processes in the flame zone of an Entrained Flow Gasifier (EFG) for liquid and suspension fuels based on detailed experimental data and validated model calculations.
EFG convert liquid, solid or suspension feedstocks into syngas (CO and H_2) by partial oxidation. In the EFG process, a fuel rich spray flame is stabilized within a hot syngas environment, featuring a reaction zone structure different from typical combustion conditions. The burner controls reactand mixing and temperature field and determines spray properties, providing the boundary conditions for conversion of the fuel. Despite the relevance for process efficiency, the relation between burner related parameters, flame structure and fuel conversion in EFG is not well explored. This is especially true for suspension fuels. Major gaps in literature concerning experimental data and suitable models of the EFG flame zone were identified.
One EFG burner concept (central liquid jet surrounded by an annular oxidizer stream) is selected as reference configuration for this work. A system for measurement of OH-LIF and Fuel-Tracer-LIF was installed at an atmospheric pressure EFG plant, complemented by PDA and invasive temperature measurements. Different liquid and suspension surrogate fuels were applied. A previously developed 2-Phase Free Jet Model (2-Ph-FJM) was extended and validated with respect to an improved reaction model, the description of a variable spray angle and suspension droplets. This simplified model allows to independently analyze the impact of selected process parameters on the flame and enables the simple exchange of sub-process models in order to evaluate their applicability to the EFG flame. The model was used to interpret experimental results and to conduct sensitivity studies on process parameters and droplet conversion models.
In the EFG flame, a core zone, an oxidation zone and a gasification zone were identified. The liquid fuel EFG flame can be regarded as a turbulent inverse diffusion flame of an oxidizer jet reacting with syngas from the surrounding atmosphere, which is superimposed by a fuel spray. Syngas entrainment and fuel evaporation are the dominant sub-processes. The impact of gas momentum flow, droplet size and spray angle on flame length, flame shape and fuel conversion within the flame were described quantitatively. Two different flame shapes (closed and hollow cone) were identified. A significant portion of liquid fuel evaporates outside the flame, depending on process conditions. This may cause the formation of unwanted by-products like soot or cenospheres in a technical process. When

suspension fuels are applied, the reaction zone structure does not fundamentally differ from liquid fuels. Under the investigated conditions, most solid fuel was released from droplets after the flame. The choice of the droplet conversion sub-model shows critical influence on the prediction of the flame.
The 2-Ph-FJM shows the capability to reproduce the experimentally observed trends for liquid and suspension fuels in the investigated range of operating conditions and input parameters, improving process understanding of the EFG flame zone. The model provides a framework to evaluate sub-process models and conduct parameter sensitivity studies, making it suitable to assist the further development of more complex CFD models and EFG burners.

Kurzfassung

Die vorliegende Arbeit hat zum Ziel, die Interaktion der Teilprozesse in der Flammenzone eines Flugstromvergasers für flüssige und suspensionsförmige Einsatzstoffe auf Grundlage detaillierter experimenteller Daten und validierter Modellrechnungen umfassend zu beschreiben.

In Flugstromvergasern werden feste, flüssige oder suspensionsförmige Einsatzstoffe durch partielle Oxidation zu Synthesegas (CO und H_2) umgesetzt. Dabei bildet sich eine unterstöchiometrische Sprayflamme in einer Umgebung aus heißem Synthesegas. Die ausgebildete Flammenstruktur unterscheidet sich dabei grundlegend von einer Sprayflamme unter Verbrennungsbedingungen. Der Brenner bestimmt die Mischung der Reaktanden, das Temperaturfeld und die Eigenschaften des Brennstoffsprays und definiert somit die Randbedingungen für die Umsetzung des Brennstoffs im Reaktor. Trotz der Relevanz dieser Vorgänge für die Effizienz des Gesamtprozesses ist die Wechselwirkung zwischen den brennerspezifischen Parametern, der Flammenstruktur und der Brennstoffumsetzung im Flugstromvergaser nur unzureichend untersucht. Dies gilt insbesondere für Suspensionsbrennstoffe. Forschungslücken bezüglich experimenteller Daten und geeigneter Modelle zur Beschreibung der Flammenzone im Flugstromvergaser wurden im Rahmen dieser Arbeit identifiziert.

Eine Brennerkonfiguration (zentraler Flüssigkeitsstrahl mit Gaszugabe über einen umgebenden Ringspalt) wurde als Referenzkonzept für diese Arbeit ausgewählt. Ein System zur Messung der laserinduzierten Fluoreszenz von OH-Radikalen und Brennstofftracern wurde an einem bei Atmosphärendruck betriebenen Flugstromvergaser installiert. Die damit gewonnenen Messdaten wurden durch Spraymessungen mittels PDA und invasiven Temperaturmessungen ergänzt. Verschiedene flüssige und suspensionsförmige Modellbrennstoffe wurden in den Experimenten eingesetzt. Ein in Vorarbeiten entwickeltes 2-Phasen Freistrahlmodell wurde im Rahmen dieser Arbeit im Hinblick auf ein verbessertes Reaktionsmodell, die Beschreibung eines variablen Spraywinkels und die Beschreibung von Suspensionstropfen erweitert und validiert. Das vereinfachte Modellkonzept ermöglicht die unabhängige Variation verschiedener Prozessparameter zur Charakterisierung ihrer Auswirkung auf die Flamme sowie den einfachen Austausch von Teilprozessmodellen zur Bewertung ihrer Anwendbarkeit auf die Flammenzone. Das Modell wurde zur Interpretation experimenteller Ergebnisse und für Sensitivitätsstudien bezüglich Prozessparametern und Tropfenmodellen eingesetzt.

Im Flammenbereich wurden eine Kernzone, eine Oxidationszone und eine Vergasungszone identifiziert. Die Flamme in Flugstromvergaser kann aufgefasst werden als eine von einem Brennstoffspray überlagerte turbulente inverse Diffusionsflamme eines oxidierenden Gasstrahls in einer heißen Synthesegasumgebung. Die Einmischung von Synthesegas in den Strahl sowie die Brennstoffverdampfung stellen die dominierenden Teilprozesse dar. Der Einfluss von Gasimpulsstrom, Tropfengröße und Spraywinkel auf die Flammenlänge- und Form sowie die Brennstoffumsetzung innerhalb der Flamme wurde im Rahmen der Arbeit quantitativ beschrieben. Zwei unterschiedliche Flammenformen (geschlossene Flamme und Hohlkegelflamme) wurden identifiziert. In Abhängigkeit der Prozessbedingungen verdampft ein signifikanter Teil des flüssigen Brennstoffs außerhalb der Flamme in der Vergasungszone. Dies kann im technischen Prozess zur Bildung unerwünschter Nebenprodukte wie Ruß und Cenosphären beitragen. Die Flammenstruktur beim Einsatz von Suspensionsbrennstoffen unterscheidet sich nicht prinzipiell von der Flammenstruktur bei Flüssigbrennstoffen. Unter den untersuchten Bedingungen wird der größte Teil des festen Brennstoffs nach der Flamme in der Vergasungszone aus den Tropfen freigesetzt. Die Wahl des zur Simulation verwendeten Tropfenumsetzungsmodells zeigt einen entscheidenden Einfluss auf die Vorhersage der Flamme.
Das 2-Phasen Freistrahlmodell ist in der Lage, die im Experiment beobachteten Abhängigkeiten für flüssige und suspensionsförmige Brennstoffe im untersuchten Parameterbereich korrekt vorherzusagen. Das Modell trägt somit zu einem tieferen Verständnis der Prozesse in der Flammenzone von Flugstromvergasern bei. Das Modell ermöglicht die einfache Durchführung von Sensitivitätsstudien und den Vergleich von Teilprozessmodellen und ist daher geeignet, die weitere Entwicklung von CFD-Modellen und Brennerdüsen für die Flugstromvergasung zu unterstützen.

Contents

Abstract ii

Kurzfassung iv

List of figures xvi

List of tables xviii

List of symbols xix

Latin symbols . . . xx

Greek symbols . . . xxii

Indices . . . xxiii

List of acronyms xxvi

1 Introduction 1

1.1 Motivation and Background . . . 1

1.2 Scope and Objectives of this Work . . . 3

2 Fundamentals 7

2.1 Entrained Flow Gasification . . . 7

2.1.1 Gasification Definitions and Fundamentals . . . 7

2.1.2 Situation in EFG Burner-Near Field . . . 9

2.2 Physical and Thermochemical Sub-Processes in EFG . . . 14

2.2.1 Atomization . . . 14

2.2.2 Mixing in Turbulent Free Jets . . . 16

2.2.3 Liquid Droplet Evaporation . . . 23

2.2.4 Suspension Droplet Conversion . . . 25

2.2.5 Solid Fuel Conversion . . . 28

2.2.6 Gas Phase Reactions . . . 30

2.2.7 Flame Stabilization . . . 31

3 Experimental Facilities and Methods 35

3.1 Research Entrained Flow Gasifier REGA . . . 35

3.2 Atmospheric Spray Test Rig ATMO . . . 36

3.3 Diagnostics . . . 37
3.3.1 OH Laser Induced Fluorescence . . . 37
3.3.2 Fuel Tracer Laser Induced Fluorescence . . . 39
3.3.3 Phase-Doppler Anemometry . . . 41
3.3.4 High Speed Imaging and Shadowgraphy . . . 42
3.3.5 Mechanical Patternator . . . 42
3.3.6 Gas Temperature Measurement . . . 44
3.4 Burner Nozzles and Operating Conditions . . . 44
3.4.1 Dataset MEG . . . 45
3.4.2 Dataset GLYCEROL . . . 45
3.4.3 Dataset SLURRY . . . 46

4 2-Phase Free Jet Model 49
4.1 Model Concept . . . 49
4.2 Original 2-Ph-FJM by Hotz . . . 51
4.3 Extended 2-Ph-FJM . . . 54
4.3.1 Radial Distribution of Liquid Mass Flux and Droplet Size . . . 54
4.3.2 Reaction Model . . . 55
4.3.3 Suspension Fuels . . . 56
4.3.4 Suspension Droplet- and Solid Particle Conversion Models . . . 59
4.3.5 Characteristic Parameters for Reaction Zone Analysis . . . 63

5 Results and Discussion 65
5.1 Flame Structure . . . 65
5.1.1 Reaction Zone Structure in EFG Flame . . . 65
5.1.2 Influence of Gas Momentum Flow on EFG Flame . . . 70
5.1.3 Influence of Fuel Droplet Size on EFG Flame . . . 72
5.1.4 Influence of Spray Angle on EFG Flame . . . 74
5.1.5 Comparison of Parameter Sensitivities . . . 76
5.2 Fuel Evaporation . . . 80
5.2.1 Droplet Evaporation in the EFG Flame . . . 80
5.2.2 Influence of Droplet Residence Time on Evaporation Progress in Flame . . . 84
5.2.3 Influence of Spray Parameters on Evaporation Progress in Flame 87
5.3 Suspension Fuels . . . 90
5.3.1 Comparison of Liquid and Suspension Fuel EFG Flame . . . 90
5.3.2 Conversion of Suspension Droplets in EFG Flame . . . 93
5.3.3 Influence of Suspension Droplet Model on Flame . . . 96
5.3.4 Impact of Suspension Fuel Specifications on Flame . . . 98

6 Conclusions 103

References **108**

A Appendix - Methods **131**
A.1 Experimental Facilities 131
A.2 Burner Nozzles 133
A.3 Diagnostics 134
A.4 Evaluation of Flame Parameters 137

B Appendix - Fuel Data **141**
B.1 Liquid Fuels 141
B.2 Solid and Suspension Fuels 141
B.3 Adaptation of Process Parameters for Changing Fuels 144

C Appendix - Model **147**
C.1 Model Details 147
C.1.1 Implementation of Droplet Size Distributions 147
C.1.2 Correlation for Droplet Diameter 148
C.1.3 Reaction Model 149
C.2 Model Validation 153
C.2.1 Prediction of Characteristic Flame Parameters 153
C.2.2 Impact of Gas Momentum Flow, Spray Angle and Droplet Size 154
C.2.3 Deviations between Measured and Calculated OH-Data in the Nozzle-Near Region 156
C.2.4 Prediction of Spray Behavior 159
C.2.5 Prediction of Gas Temperature 165
C.2.6 Turbulent Droplet Dispersion 165
C.3 Additional Modeling Studies 166
C.3.1 Comparison of Liquid Evaporation Models 166
C.3.2 Conversion of Suspension Droplets 167
C.3.3 Influence of Recirculation Gas on Flame 170

D Appendix - Experimental Datasets **173**
D.1 Dataset MEG 173
D.2 Dataset GLYCEROL 179
D.3 Dataset SLURRY 187

List of Publications **197**

List of figures

1.1 Selected relevant thermochemical sub-processes in the burner near field in an Entrained Flow Gasifier. Adapted from [8]. 2

2.1 Schematic of the CCLab EFG reactor at KIT depicting different stages of suspension droplet conversion, temperature field and flow field. Adapted from [9, 27] 9

2.2 Different EFG flame structures reported in literature, visualized for gasification of a liquid fuel. 11

2.3 Primary breakup regimes for central liquid jet nozzles according to [109]. High speed images were obtained in this work (see section 3.4.2) 15

2.4 Axial velocity, mixture fraction and entrainment rate in a non-swirled, round homogeneous free jet according to [117, 118] 18

2.5 Morphology development of a suspension droplet during evaporation when liquid phase pyrolysis is not relevant. Adapted and modified from [140]. The original graphic by Handscomb was developed with focus on low temperatures, the processes depicted are however also found at high temperature (see text) 26

2.6 Example Flame Front in a laminar CH4 - Air 32

3.1 Sketch of REGA reactor (upper part) and OH-/Fuel-Tracer-LIF setup applied and this work. Modified from [15]. 36

3.2 Example dataset of measured radial mass flux distribution and logistic fit (left) and determination of spray angle (right). Case MEG-A, z = 100 mm 43

3.3 Sketch and characteristic parameters of the burner nozzles applied in this work. Gas (green) and liquid (blue) channels are marked. 44

4.1 Modeling geometry (left) and calculation procedure (right) of the original 2-Ph-FJM, adapted from [11, 13]. 51

5.1 Normalized OH-LIF- (left) and Fuel-Tracer-LIF-signals (right) for case MEG-A. Smoothed radial profiles of both quantities are shown at different nozzle distances with respect to the nozzle equivalent diameter d_{eq}. The dotted red line in the Fuel-Tracer-LIF-image indicates the 10%-OH contour. Process conditions: J_{gas}=0.20 N, ID_{32} = 160 µm, $\theta_{0.9}$ = 40.4 °, Fuel: MEG. Data published in [15]. For better display, the scale of the Fuel-Tracer-LIF profile at $z/d_{\mathrm{eq}} = 5$ differs from the scale in the other diagrams. 67

5.2 Normalized OH-LIF- and Fuel-Tracer-LIF-signals for case MEG-B. Radial profiles of both quantities are shown at different nozzle distances respective to the nozzle equivalent diameter d_{eq} to enable a comparison with case MEG-A above. Process conditions: J_{gas}=0.45 N, ID_{32} = 73 µm, $\theta_{0.9}$ = 23.5 °, Fuel: MEG. Data published in [15]. 68

5.3 Radial profiles of gas temperature measured using a double-bead-thermocouple for cases MEG-A (J_{gas}=0.20 N, ID_{32} = 160 µm, $\theta_{0.9}$ = 40.4 °) and MEG-B (J_{gas}=0.45 N, ID_{32} = 73 µm, $\theta_{0.9}$ = 23.5 °) at $z/d_{\mathrm{eq}} = 47$. Fuel: MEG. Data published in [15]. 69

5.4 Normalized OH-LIF-signals for cases A50 (J_{gas}=0.20 N, $\mathrm{ID}_{32,jet}$ = 88 µm, $\theta_{0.9}$ = 40 °) and B200 (J_{gas}=0.45 N, $\mathrm{ID}_{32,jet}$ = 68 µm, $\theta_{0.9}$ = 39 °) from the GLYCEROL data set. Radial profiles of both quantities are shown at different normalized nozzle distances z/d_{eq}. Fuel: Glycerol. 71

5.5 Calculated λ_{abs}, T_{gas}, x_{SG} and y_{OH} on jet axis for different d_{eq}, using input mass flows conditions analogous to the GLYCEROL data set. Constant parameters: d_{32} = 100 µm, $\theta_{0.9}$ = 40 °, evaporation model: d^2-law, Fuel: Glycerol. 72

5.6 Calculated OH-concentration fields and L_{OH} derived from the OH-data for droplet sizes from d_{32} = 50 µm to d_{32} = 400 µm. Constant parameters: J_{gas}=0.45 N, $\theta_{0.9}$ = 25 °, evaporation model: d^2-law. Fuel: Glycerol, input mass flows analogous to the GLYCEROL-experiments. 73

5.7 Impact of droplet size on axial profiles of λ_{abs}, T_{gas}, x_{FV}, y_{OH} calculated using the 2-Ph-FJM. Droplet size was varied from d_{32} = 50 µm to d_{32} = 400 µm. Constant parameters: J_{gas}=0.45 N, $\theta_{0.9}$ = 25 °, evaporation model: d^2-law. Fuel: Glycerol, input mass flows analogous to the experiment. . 74

5.8 OH-concentration fields and L_{OH} for spray angles from $\theta_{0.9}$ = 15 ° to $\theta_{0.9}$ = 40 ° calculated using the 2-Ph-FJM. Constant parameters: J_{gas}=0.45 N, d_{32} = 50 µm, evaporation model: d^2-law. Fuel: Glycerol, input mass flows analogous to the GLYCEROL-experiments. 75

5.9 Radial profiles of λ_{abs}, T_{gas}, x_{FV}, y_{OH} at z = 150 mm for spray angles from $\theta_{0.9}$ = 15 ° to $\theta_{0.9}$ = 40 °. Constant parameters: J_{gas}=0.45 N, d_{32} = 50 µm, evaporation model: d^2-law. Fuel: Glycerol, input mass flows analogous to the GLYCEROL-experiments. 76

5.10 Calculated L_{OH} for spray angles from $\theta_{0.9} = 15\,^\circ$ to $\theta_{0.9} = 40\,^\circ$ and droplet sizes from $d_{32} = 25$ µm to $d_{32} = 400$ µm using the d^2-law as evaporation model. Measured values of L_{OH} from cases B50, B100 and B200 are displayed for reference. Constant parameters: J_{gas}=0.45 N, Fuel: Glycerol. 77

5.11 Calculated fields of λ_{abs} and AR_{OH} for spray angles from $\theta_{0.9} = 15\,^\circ$ to $\theta_{0.9} = 50\,^\circ$ and droplet sizes from $d_{32} = 25$ µm to $d_{32} = 400$ µm using the d^2-law as evaporation model. J_{gas}=0.45 N, Fuel: Glycerol, input mass flows analogous to the GLYCEROL-experiments. 78

5.12 Sensitivity of L_{OH} towards changes in $\theta_{0.9}$, d_{32} and d_{eq} calculated using the 2-Ph-FJM. Fuel: Glycerol, evaporation model: d^2-law, input mass flows analogous to the GLYCEROL-experiments. 79

5.13 High-speed camera images of the nozzle near area for case MEG-A under ambient and reacting conditions. Spray angle (dashed blue lines) and gas free jet angle starting from the virtual jet origin (dotted red lines) are marked. Process conditions: J_{gas}=0.20 N, $ID_{32} = 160$ µm, $\theta_{0.9} = 40.4\,^\circ$, T_{ad} = 1700 °C, Fuel: MEG. Data published in [15]. 81

5.14 Radial half-profile of droplet velocity and radial half-profile of droplet size for case MEG-A measured by PDA under reactive conditions. Process conditions: J_{gas}=0.20 N, $ID_{32} = 160$ µm, $\theta_{0.9} = 40.4\,^\circ$, Fuel: MEG. Data published in [16]. 82

5.15 Droplet size distribution at the jet centerline for different nozzle distances, measured under reaction conditions using PDA (upper). Calculated diameter of different droplet size classes along the jet centerline using the d^2-law as evaporation model (lower) using the 2-Ph-FJM. Process conditions: MEG-A, J_{gas}=0.20 N, $ID_{32} = 160$ µm, $\theta_{0.9} = 40.4\,^\circ$, Fuel: MEG. Data published in [16]. 83

5.16 Calculated fields of OH concentration c_{OH}, liquid fuel concentration χ_{liq} and local liquid evaporation progress X_{liq} applying the d^2-law as evaporation model. Process conditions: MEG-A, J_{gas}=0.20 N, $ID_{32} = 160$ µm, $\theta_{0.9} =$ 40,4 °, Fuel: MEG. Data published in [16]. 84

5.17 Calculated and experimentally determined droplet residence times along the jet axis for cases MEG-A (J_{gas}=0.20 N, $ID_{32} = 160$ µm, $\theta_{0.9} = 40{,}4\,^\circ$) and MEG-B ($J_{gas}$=0.45 N, $ID_{32} = 73$ µm, $\theta_{0.9} = 23{,}5\,^\circ$). Fuel: MEG. Data published in [16]. 85

5.18 Influence of J_{gas} on droplet residence time $\tau_{OH,axis}$ and evaporation progress $X_{liq,OH,axis}$ within the OH zone along the jet centerline calculated using the 2-Ph-FJM. Constant parameters: $\theta_{0.9} = 20\,^\circ$, $d_{32} = 100$ µm, evaporation model: d^2-law. Fuel: MEG, input mass flows analogous to the MEG-experiments. 86

5.19 Calculated $X_{\mathrm{liq,OH}}$ for spray angles from $\theta_{0.9} = 15\,^\circ$ to $\theta_{0.9} = 40\,^\circ$ and droplet sizes from $d_{32} = 50$ µm to $d_{32} = 250$ µm using the d^2-law as evaporation model. J_{gas}=0.21 N, Fuel: MEG, input mass flows analogous to the MEG-experiments. Data published in [16]. 88

5.20 Fuel evaporation within the OH zone $X_{\mathrm{liq,OH}}$ calculated for different J_{gas} and droplet sizes from $d_{32} = 50$ µm to $d_{32} = 400$ µm. The red dots indicate values where d_{32} is calculated from J_{gas} using a correlation developed by Sänger [110]. Evaporation model: d^2-law, $\theta_{0.9} = 20\,^\circ$, Fuel: MEG, input mass flows analogous to the MEG-experiments. Data partially published in [16]. 89

5.21 Normalized measured OH-LIF intensities and normalized calculated OH concentration fields for cases S0 (J_{gas}=0.34 N, $\mathrm{ID}_{32} = 114$ µm, $\theta_{0.9} = 27\,^\circ$, Fuel: MEG) and S30-A ($J_{\mathrm{gas}}$=0.34 N, $\mathrm{ID}_{32} = 189$ µm, $\theta_{0.9} = 29\,^\circ$, $d_{\mathrm{p,sol}} = 9$ µm, Fuel: MEG with 30 wt-% BWC-A). Evaporation model: Fragmenting Particle model. 91

5.22 Radial profiles of calculated mixture fractions of gasification agent (GA), syngas (SG), fuel vapor (FV) and gasified solid fuel (FG) for cases S0 (J_{gas}=0.34 N, $\mathrm{ID}_{32} = 114$ µm, $\theta_{0.9} = 27\,^\circ$, Fuel: MEG) and S30-A ($J_{\mathrm{gas}}$=0.34 N, $\mathrm{ID}_{32} = 189$ µm, $\theta_{0.9} = 29\,^\circ$, $d_{\mathrm{p,sol}} = 9$ µm, Fuel: MEG with 30 wt-% BWC-A). Evaporation model: Fragmenting Particle model. 92

5.23 Calculated OH concentration fields and particle conversion steps of a 75 µm droplet along selected trajectories for two different suspension droplet conversion models. Input conditions of case S30-A were applied (J_{gas}=0.34 N, $d_{32} = 189$ µm, $\theta_{0.9} = 29\,^\circ$, $d_{\mathrm{p,sol}} = 9$ µm, Fuel: MEG with 30 wt-% BWC-A). The trajectories displayed are in an angle of 0°, 7° and 15° to the jet centerline. 94

5.24 Calculated evaporation progress variables of a 75 µm droplet along the jet centerline for the suspension droplet conversion models investigated in this work. Input conditions of case S30-A were applied (J_{gas}=0.34 N, $d_{32} = 189$ µm, $\theta_{0.9} = 29\,^\circ$, $d_{\mathrm{p,sol}} = 9$ µm, Fuel: MEG with 30 wt-% BWC-A). . . . 95

5.25 Calculated integral conversion variables of the flame zone for the suspension droplet conversion models investigated in this work. Input conditions of case S30-A were applied (J_{gas}=0.34 N, $d_{32} = 189$ µm, $\theta_{0.9} = 29\,^\circ$, $d_{\mathrm{p,sol}} = 9$ µm, Fuel: MEG with 30 wt-% BWC-A). 97

5.26 Calculated integral conversion variables of the flame zone for the Fragmenting Particle model applying different evaporation and char conversion conditions. Input conditions of case S30-A were applied (J_{gas}=0.34 N, $d_{32} = 189$ µm, $\theta_{0.9} = 29\,^\circ$, $d_{\mathrm{p,sol}} = 9$ µm, Fuel: MEG with 30 wt-% BWC-A). 98

5.27 Experimental and calculated L_{OH} for different initial suspension solid content under input conditions of case S0 - S30-A. Calculated values for the liquid mass flow evaporated within the OH zone are added for comparison. Evaporation model: Fragmenting Particle. 100
5.28 Experimental and calculated L_{OH} for different initial particle size in the suspensions at $x_{sol,0} = 30$ % under input conditions of case S30-A - S30-C. Calculated values for the liquid mass flow evaporated within the OH zone are added for comparison. Evaporation model: Fragmenting Particle. . 101

A.1 Flow sheet of REGA plant, adapted from [8, 9]. 131
A.2 Flow sheet of ATMO plant, adapted from [242]. 132
A.3 Wavelength dependent transmission of the quartz glass windows applied at REGA [255]. 132
A.4 Detailed sketches of the applied burner nozzles. 133
A.5 Normalized absorption and emission of OH and Rhodamine 6G. 134
A.6 Normalized calculated LIF signals considering quenching compared to normalized calculated OH concentration for case S30-A. 135
A.7 Integral droplet size distributions for case S0 measured at z = 100 mm using PDA and Shadowgraphy. 137
A.8 Values of L_{OH} and V_{OH} determined using 2 different normalization methods for all experimental datapoints in this work. 138
A.9 Axial profiles of normalized (left) and absolute (right) OH concentrations for cases S0 and S30-A calculated using the 2-Ph-FJM. Different calculation methods for L_{OH} are visualized. 139

B.1 Viscosity of glycerol at different temperatures. Values measured in this work were fitted by a bi-exponential fit function and compared with literature values [257]. 142
B.2 Particle size distribution of the chars applied in this work, measured by laser diffraction. 144
B.3 REM images of the applied char fractions. 145
B.4 Viscosities of all applied suspension fuels at $\gamma = 1000 \cdot 1/s$ and $T_{liq} = 20°C$. 146
B.5 Flow curves of the non-Newtonian suspensions at $x_{sol,0} = 30$ % and $T_{liq} = 20°C$. 146

C.1 Measured droplet size distributions under ambient conditions for case MEG-A at z = 100 mm and different radial positions. Measured data was fit using Weibull-distributions. 148
C.2 Calculated maximum molar fractions $y_{i,max}$ of the 53 species contained in GRI 3.0 for mixtures of example syngas and gasification agent. 150
C.3 Calculated gas temperature T for mixtures of example syngas and gasification agent compared for different model approaches. 151

C.4 Calculated molar fractions y_i of main species and radicals for example mixtures of syngas and gasification agent compared for different model approaches. 152
C.5 Comparison of measured and calculated L_{OH} and V_{OH} for all experimental cases. 154
C.6 Axial profiles of normalized OH-LIF intensity and normalized calculated OH concentrations for cases A50, A200, B50 and B200. Profiles are shown for absolute (left) and normalized (right) axial coordinates. 156
C.7 Spray image under ambient conditions and single OH-LIF raw images in the vicinity of the nozzle exit (Case MEG-A). 158
C.8 Mixture fraction of gasification agent for case MEG-A calculated using the 2-Ph-FJM. Radial profiles are shown at different nozzle distances (left). An axial profile featuring a hypothetical improvement is also displayed (right) 158
C.9 Comparison of measured and calculated mass averaged droplet velocities (PDA, ambient conditions) for cases MEG-A and MEG-B. 159
C.10 Comparison of measured and calculated gas velocities (PDA, ambient conditions) for cases MEG-A and MEG-B. 160
C.11 Comparison of measured and calculated liquid mass flux (Patternator, ambient conditions) for cases MEG-A and MEG-B. 161
C.12 Comparison of measured and calculated Sauter mean diameter (PDA, ambient conditions) for cases MEG-A and MEG-B. 162
C.13 Comparison of measured and calculated mass averaged droplet velocities (PDA, reacting conditions) for cases MEG-A and MEG-B. 163
C.14 Comparison of measured and calculated Sauter mean diameter (PDA, reacting conditions) for cases MEG-A and MEG-B. 164
C.15 Comparison of measured and calculated gas temperatures (double-bead thermocouple) for cases MEG-A and MEG-B. Profiles are diesplayed for z = 300 mm (MEG-A) and z = 150 mm and z = 200 mm (MEG-B). . 165
C.16 Measured raw data of droplet velocity and droplet size, together with calculated droplet velocities and size in the 2-Ph-FJM (Case MEG-A, ambient conditions, z = 150 mm, r = 0 mm). 166
C.17 Calculated $X_{liq,OH}$ for spray angles from $\theta_{0.9} = 15\,^\circ$ to $\theta_{0.9} = 40\,^\circ$ and droplet sizes from $d_{32} = 50$ µm to $d_{32} = 250$ µm. The d^2-law (left) and the evaporation rate controlled by convective heat transfer (right) are compared. (J_{gas}=0.21 N, Fuel: MEG, input mass flows analogous to the MEG-experiments.) Adapted from [16]. 167
C.18 Calculated gas temperature T_{gas}, particle temperature T_p and mole fractions y_i of O_2, OH, CO_2 of case S30-A are shown for different droplet sizes and trajectories using the Fragmenting Particle model. The profiles are plotted as function of particle / droplet residence time τ. 169

C.19 Composition of recirculated syngas for different degrees of char conversion in the recirculation zone and its impact on longitudinal extension of the OH zone. Input conditions for case S30-A were applied. Adapted from [17] 171

D.1 Spray images for case MEG-A and MEG-B under ambient and reacting conditions (adapted from [15]). 174
D.2 Radial profiles of droplet size and droplet velocity measured under ambient and reactive conditions by PDA for cases MEG-A and MEG-B. 175
D.3 Radial profiles of liquid mass flux measured under ambient and reactive conditions by Patternator for cases MEG-A and MEG-B. 176
D.4 Fields of normalized measured OH-LIF intensity and normalized caclulated OH concentration for cases MEG-A and MEG-B. Model results displayed were obtained using the evaporation rate determined by convective heat transfer. 177
D.5 Axial and radial profiles of normalized measured OH-LIF intensity and normalized caclulated OH concentration for cases MEG-A and MEG-B. Model results displayed were obtained using the evaporation rate determined by convective heat transfer. 178
D.6 Spray images for the **GLYCEROL**-dataset under ambient conditions. 180
D.7 Radial profiles of droplet size for the **GLYCEROL**-dataset at z = 100 mm measured by PDA under ambient conditions. 181
D.8 Radial profiles of liquid mass flux for the **GLYCEROL**-dataset at z = 100 mm measured by Patternator under ambient conditions. 182
D.9 Fields of normalized measured OH-LIF intensity and normalized caclulated OH concentration for the **GLYCEROL**-dataset. Model results were obtained using the d^2-law. 183
D.10 Fields of normalized measured OH-LIF intensity and normalized caclulated OH concentration for the **GLYCEROL**-dataset (continued). Experimental data around z = 250 mm (Case A200) and z = 20 mm (Case B200) are not available. Model results were obtained using the d^2-law. 184
D.11 Radial and axial profiles of normalized measured OH-LIF intensity and normalized caclulated OH concentration for the **GLYCEROL**-dataset. Experimental data around z = 250 mm (Case A200) are missing. Model results were obtained using the d^2-law. 185
D.12 Radial and axial profiles of normalized measured OH-LIF intensity and normalized caclulated OH concentration for the **GLYCEROL**-dataset (continued). Experimental data around z = 20 mm (Case B200) are missing. Model results were obtained using the d^2-law. 186
D.13 Integral Sauter Diameter for the **SLURRY**-dataset measured at z = 100 mm under ambient conditions using shadowgraphy. 188

D.14 Liquid mass flux for the **SLURRY**-dataset measured at z = 100 mm under ambient conditions using shadowgraphy. 188
D.15 Fields of normalized measured OH-LIF intensity and normalized caclulated OH concentration for the **SLURRY**-dataset. Model results were obtained using the Fragmenting Particle Model. 189
D.16 Fields of normalized measured OH-LIF intensity and normalized caclulated OH concentration for the **SLURRY**-dataset (continued). Model results were obtained using the Fragmenting Particle Model. 190
D.17 Radial and axial profiles of normalized measured OH-LIF intensity and normalized caclulated OH concentration for the **SLURRY**-dataset. Model results were obtained using the Fragmenting Particle Model. 191
D.18 Radial and axial profiles of normalized measured OH-LIF intensity and normalized caclulated OH concentration for the **SLURRY**-dataset (continued). Model results were obtained using the Fragmenting Particle Model. . . 192
D.19 Normalized calculated OH concentration fields for different suspension droplet conversion models compared against the normalized measured OH-LIF intensity for case S30-A. 193
D.20 Setup for particle extraction experiments [17] 195
D.21 Particle sample for case S30-A extracted at the end of the reactor. [17] 195

List of tables

2.1 Overview of model concepts for suspension fuels applied in literature on CFD simulation of EFG. 27

3.1 Case names, applied nozzles and operating conditions of experimental cases in the **MEG**-dataset. Input gas volume flow is $\dot{V}_{\mathrm{GA,STP}} = 7.5\ \mathrm{m^3/h}$ for all cases. 47

3.2 Case names, applied nozzles and operating conditions of experimental cases in the **GLYCEROL**-dataset. Input gas volume flow is $\dot{V}_{\mathrm{GA,STP}} = 7.5\ \mathrm{m^3/h}$ for all cases. 47

3.3 Case names, fuel parameters, operating conditions and nozzle parameters for the **SLURRY**-dataset. Input gas volume flow is $\dot{V}_{\mathrm{GA,STP}} = 7.5\ \mathrm{m^3/h}$ for all cases. 48

A.1 System parameters and instrument settings of the PDA system. 136

B.1 Fuel data of MEG and glycerol. 141

B.2 Fuel data of the chars applied in this work. Measured by *Eurofins Umwelt Ost GmbH*, DIN EN ISO/IEC 17025:2018. 143

B.3 Kinetic data for BWC-A. 143

C.1 Example gas compositions for the verification of the implemented Gibbs-minimization approach. 149

D.1 Integral Sauter mean diameter ID_{32}, spray angle $\theta_{0.9}$ and Patternator mass balance error Δm_{liq} at z = 100 mm for the **MEG**-dataset. Longitudinal extensions of the OH zone from experiment $L_{\mathrm{OH,exp}}$ and model $L_{\mathrm{OH,mod}}$ are also provided. Model results were obtained for both evaporation models 174

D.2 Integral Sauter mean diameter ID_{32}, Sauter mean diameter integrated within the gas jet boundaries $\mathrm{ID}_{32,\mathrm{jet}}$, spray angle $\theta_{0.9}$ and Patternator mass balance error Δm_{liq} at z = 100 mm for the **GLYCEROL**-dataset. Longitudinal extensions of the OH zone from experiment $L_{\mathrm{OH,exp}}$ and model $L_{\mathrm{OH,mod}}$ are also provided. Model results were obtained using the d^2-law. 179

D.3 Spray data at z = 100 mm for the **SLURRY**-dataset with longitudinal extensions of the OH zone from experiment $L_{\mathrm{OH,exp}}$ and model $L_{\mathrm{OH,mod}}$. Model results were obtained using the Fragmenting Particle Model. . . 187

D.4 Total and solid phase carbon conversion for the experiments in dataset **SLURRY** determined by gas phase balancing. 194

List of symbols

Latin symbols

Symbol	Unit	Description
A	m^2	Area
A	$kg/m^2/s$	Amplitude in Logistic function
A	$1/s$	Spontaneous Emission Rate coefficient
AR	-	Aspect ratio
B	$1/s$	Einstein coefficient for absorption
bin	-	Binarized OH distribution
c	m/s^2	Speed of light
c	mol/m^3	Molecule number density
c	J/kg/K	Specific heat capacity
d	m	Distance
d	m	Diameter
E	J	Energy
F	W/m^2	Laser fluence
GLR	-	Gas to liquid mass flow ratio
G	J	Gibbs Free Energy
h	J/kg	Mass specific enthalpy
h	m	Liquid height
H	J	Enthalpy
h	$J \cdot s$	Planck constant
I	counts	Detector intensity
J	$kg/m/s^2$	Momentum flow
K	m^2/s	Evaporation factor
k	variable	Arrhenius pre-exponential factor
L	m	Longitudinal extension

Symbol	Unit	Description
m	kg	Mass
$\dot{m}$	kg/s	Mass flow
M	kg/mol	Molar mass
N	-	Population density
N	-	Total number
n	-	Mole number
n	-	Reaction order
N	-	Total number
p	bar	Pressure
q	J/s/kg	Mass specific heat
Q	J/s	Heat
Q	1/s	Quenching rate coefficient
Q	-	Cumulative size distribution
r	m	Radial distance from jet centerline
r	mol/s/kg	Reaction rate
R	J/mol/K	Universal gas constant
s	m	Wall thickness
SMD	m	Sauter Mean Diameter
T	K	Temperature
t	s	Time
u	m/s	Velocity
V	m^3	Volume
$\dot{V}$	m^3/s	Volume flow
w	m	Width parameter in Logistic function
x	-	Mass fraction
X	-	Conversion progress
y	-	Molar fraction
z	m	Axial distance from nozzle

Greek symbols

Symbol	Unit	Description
α	$^\circ$	Nozzle gas exit angle
α	$W/m^2/K$	Heat transfer coefficient
β	m/s	Mass transfer coefficient
δ	-	Thickness
Δ	-	Difference
ϵ	-	Volume fraction
ϵ	-	Emissivity
ϕ	$kg/m^2/s$	Mass flow density per area
ϕ	-	Thiele modulus
η	-	Effectiveness factor
η	$kg/m/s^2$	Viscosity
η	-	Nondimensional radial coordinate
λ	-	Stoichiometry
λ	W/m/K	Heat conductivity
ν	1/m	Wave number
ν	$-$	Number of atoms in molecule
ρ	kg/m^3	Mass density
σ	1/m	Weibull distribution scale parameter
θ	$^\circ$	Spray angle
ξ	-	Exponent in Lorentz function
ζ	-	Nondimensional axial coordinate
Ω	-	Collection solid angle

Indices

Subscripts

Symbol	Description
0	Initial
0.9	90 % of spray mass contained within angle
12	Transition of state 1 to state 2
21	Transition of state 2 to state 1
3	Volume weighted
32	Sauter Mean Diameter
∞	Bulk phase
A	Activation energy
abs	Absolute
ad	Reaction under adiabatic conditions
CO	CO molecule
CO2	CO_2 molecule
crit	Critical
con	Convective and conductive heat transfer
cubic	Cubical packing of spheres
drop	Droplet specific
dry	Dry solid phase released from suspension droplet
eq	Equivalent
f	Formation from elements
fix	Fixed carbon
fuel	Total fuel to reactor
FG	Solid fuel transfered to gas phase
FV	Liquid fuel transfered to gas phase
gas	Gas phase
GA	Gasification agent

Symbol	**Description**
H2	H_2 molecule
H2O	H_2O molecule
i	Species index
in	Input
j	Stream Index
k	Element index
local	Specific for droplet trajectory
LIF	LIF signal
liq	Liquid phase
max	Maximum
n	Droplet class index
N2	N_2 molecule
O2	O_2 molecule
OH	OH molecule
OH	Within 10 % OH contour
p	Isobaric
por	Pore volume
R	Reaction
rad	Radiative heat transfer
reac	Enthalpy change through reaction
sol	Solid phase
surf	Particle surface
STP	Standard pressure and temperature
SG	Syngas
tec	Technical
total	Total inital fuel mass flow
vap	Evaporation
vol	Volatile mass

Superscripts

Symbol	Description
0	Initial
$\ominus$	Standard conditions
$+$	Reference

List of acronyms

Acronym	Description
2-Ph-FJM	2-Phase Free Jet Model
ATMO	Atmospheric Spray Test Rig
AWS	Asphalt water slurry
BWC	Beech wood char
CFD	Computational Fluid Dynamics
CWS	Coal water slurry
DNS	Direct numerical simulation
EFG	Entrained Flow Gasification
FT	Fuel Tracer
HFO	Heavy fuel oil
LES	Large Eddy Simulation
LIF	Laser Induced Fluorescence
MEG	Monoethylene glycol
PCWS	Pet-coke water slurry
PDA	Phase Doppler Anemometry
RANS	Reynolds averaged Navier Stokes
REGA	Research Entrained Flow Gasifier
S	Slurry

1 Introduction

1.1 Motivation and Background

Motivation

Society is becoming increasingly aware that with the current linear economic model, humanity is exceeding the planetary boundaries [1]. It is thus imperative to transform established linear production chains into a circular system where waste streams and biomass can be integrated in order to reduce CO_2-emissions and save fossile resources. Processes featuring the ability to make such feedstocks accessible for industrial use are therefore required.

Entrained Flow Gasification

Thermochemical processes are expected to play an important role for providing base chemicals in a future system featuring closed material cycles [2–5]. Entrained Flow Gasification (EFG) provides the capability to convert liquid and solid feedstocks originating from biomass and waste, e.g. pyrolysis products, into syngas (CO and H_2) by partial oxidation, making these feedstocks accessible for the C_1 chemical value chain [6]. EFG allows pressurized operation at high throughput and produces a high quality, tar-free syngas that can be directly integrated into chemical synthesis with minimal aftertreatment. EFG plants operating on fossil based feedstocks already exist in chemical industry. Most of these plants currently operate on coal and heavy refinery residues [7]. The switch to new waste based feedstocks poses challenges, as these materials are often characterized by low fuel quality, i.e. high heterogeneity, low heating value and high content of inorganics. In the context of circular economy, suspension fuels gain importance. Efficient and fuel flexible operation of EFG plants applying these alternative feedstocks requires detailed understanding of the complex interaction of physical and thermochemical sub-processes in the reactor (see Fig. 1.1).

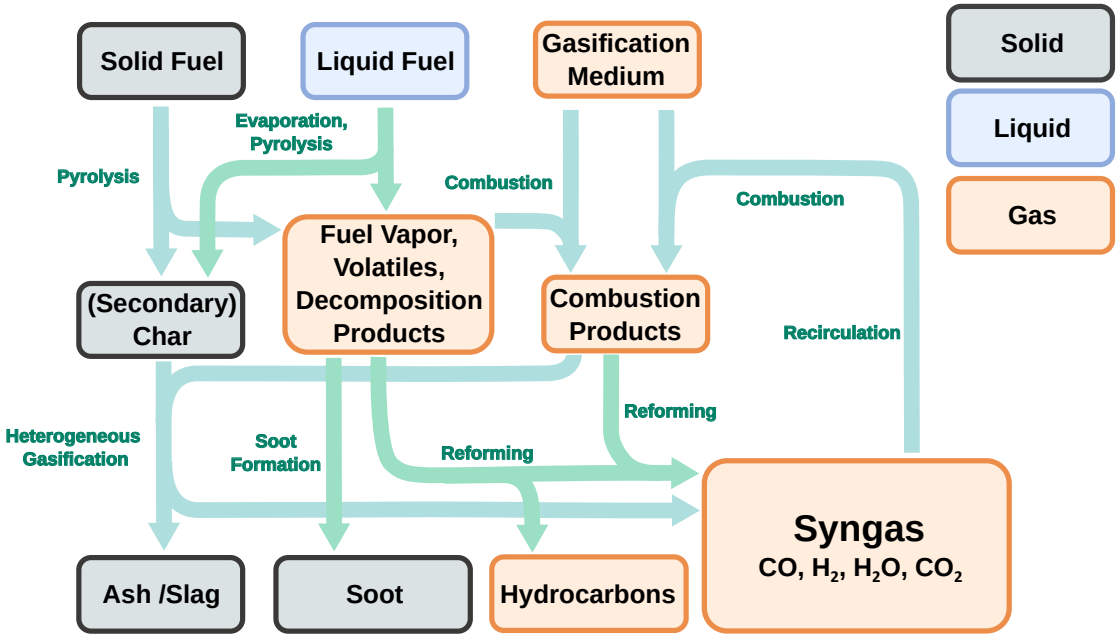


Figure 1.1: Selected relevant thermochemical sub-processes in the burner near field in an Entrained Flow Gasifier. Adapted from [8].

Processes in the Burner Near Field

In the EFG process, the solid, liquid or suspension feedstock is fed to the reactor through a burner nozzle together with the gasification agents, typically oxygen and steam, that also act as atomization medium for the liquid / suspension feedstock. This leads to the stabilization of a fuel rich spray flame within a hot syngas environment. The resulting reaction zone structure of the flame depends on the specific burner. The flame initiates the gasification process and provides thermal thermal energy required for the endothermic gasification reactions. Flame geometry and thermal radiation define the temperature field in the reactor and therefore directly influence the fuel conversion processes. As the burner also dominates reactand mixing and spray pattern, it provides the boundary conditions for the initial conversion of the fuel within the flame and the further conversion in the downstream reactor volume. The burner near processes are thus highly relevant for global fuel conversion, syngas yield and composition as well as the formation of unwanted by products like soot, hydrocarbons and cenospheres (see section 2.1.2).

Current State of Research

Despite the importance for process performance, the relation between burner related parameters, flame structure and fuel conversion in EFG is not well explored. This is especially true for suspension fuels. As the EFG flame is stabilized in a fuel rich environment, it features a different reaction zone structure and parameter dependencies than flames under combustion conditions, hence typical design rules for such burners are not transferable. The conversion steps of suspension fuel droplets and the impact of atomization on the EFG flame zone receive little attention in EFG literature. Diagnostic limitations in EFG systems make it difficult to provide meaningful experimental data, which also induces a lack of validated models for the EFG flame zone. Existing literature often investigates single cases without systematic parameter variations. Studies feature different burner concepts, reactor types, fuels, and operating conditions, which makes it difficult to derive a systematic process understanding (see section 2.1.2).

1.2 Scope and Objectives of this Work

Preceding Works and Scope

This thesis has been written at the Institute for Technical Chemistry (ITC) at Karlsruhe Institute of Technology (KIT) and is embedded in the frameworks of Carbon Cycle Lab (CCLab, formerly bioliq®), and the prior Helmholtz Virtual Institute for Gasification Technology (HVIGasTech). Within this framework, research on EFG has been conducted from laboratory to pilot scale under cooperation with various institutions, including TUC, DLR, RWTH, FZJ, LTU, TNO, TUW and STEMS-CNR. Research topics involve solid fuel kinetics, liquid fuel atomization, reaction mechanisms, slagging, thermal radiation and modeling.

RANS and LES models for high-pressure EFG were developed within this research framework before [9, 10]. The models are based on sub-process models developed under pressurized conditions, while their interaction in a technical system has been studied under atmospheric pressure conditions to increase experimental accessibility. A lack of understanding of the EFG flame zone was identified in this context. The need for a more detailed assessment of the interaction of sub-processes in the EFG flame and the necessity to evaluate suitable sub-process models have both motivated the development of a 2-Phase Free Jet Model (2-Ph-FJM) based on the theory of turbulent jets in prior works [11–13]. The model allows to independently analyze the impact of selected process parameters (e.g. droplet size, gas momentum flow) on the flame. The modular architecture of the 2-Ph-FJM further allows the simple exchange of sub-process models (e.g. for droplet evaporation) in order to evaluate their applicability to the EFG flame. This simplified and flexible model can be used as a tool to (i) to interpret experimental observations in

order to provide a more profound understanding of the sub-processes in the EFG flame and (ii) to improve CFD simulations by enabling identification of relevant parameters and evaluation of sub-process models.

Thesis Objectives

One task of this work was to extended and validate the existing 2-Ph-FJM developed by Hotz [13] with respect to (i) the radial distribution of liquid mass flux in the fuel spray in order to describe the effect of spray angle on the flame, (ii) the gas phase reaction model including the description of flame radicals like OH to enable an experimental validation of the flame structure and (iii) the addition of a solid fuel phase together with the implementation of droplet conversion models for suspension fuels (see chapter 4).
A further task of this work was to provide detailed experimental data of the EFG flame for assessment of the flame structure and model validation. The atmospheric pressure REGA plant at ITC was used as a well defined model system for the complementary gasification experiments in the present work. For detailed spray and flame diagnostics, a Laser Induced Fluorescence (LIF) system was implemented at the plant over the course of this work. The OH radical detected by LIF was used as flame front marker which was complemented by invasive temperature measurements. Fuel-Tracer-LIF and PDA were applied to characterize the reacting sprays, accompanied by spray characterization under ambient conditions using the atomization facilities at ITC (see chapter 3).
Building on this foundation, the present thesis attempts a comprehensive assessment and description of the interaction of sub-processes in the EFG flame zone for liquid and suspension fuels based on detailed experimental data and validated model calculations. For this purpose, one burner concept (central liquid jet surrounded by an annular oxidizer stream) is selected as reference configuration in this work. Burners of this principle are widely established in combustion applications and have in more complex configurations been successfully applied for gasification for example at the 5 MW High Pressure Entrained Flow Gasifier (HP-EFG) pilot plant operated at the Carbon Cycle Lab at KIT [14]. The present work aims to achieve the following research objectives:

Objective 1: *Quantitative description of the impact of the burner related parameters gas momentum flow, droplet size and spray angle on the reaction zone structure of a liquid fuel EFG flame.* (addressed in chapter 5.1).

Objective 2: *Quantification of the influence of gas momentum flow, droplet size and spray angle on liquid fuel conversion within a liquid fuel EFG flame.* (addressed in chapter 5.2).

Objective 3: *Assessment of the conversion of suspension fuels in an EFG flame, including (i) the impact of suspension fuel parameters (solid content, solid particle size) on flame structure and (ii) the impact of different suspension droplet models on the predictions of the flame.* (addressed in chapter 5.3)

These objectives are dealt with in chapter 5. First, the individual objectives are assessed using experimental observations, which are then further studied using the 2-Ph-FJM. During these investigations, the model is validated at selected examples. Full experimental datasets and detailed validation of the model are provided in the Appendix. The results of this thesis have partly been published in [15–17].

2 Fundamentals

2.1 Entrained Flow Gasification

2.1.1 Gasification Definitions and Fundamentals

In gasification, an organic feedstock is partially oxidized to form a product gas consisting of the value products hydrogen and carbon monoxide and the fully oxidized components water and carbon dioxide. Soot and hydrocarbons may be formed as by-products in the process:

$$\begin{aligned} \mathrm{C}_{\alpha\mathrm{C}}\mathrm{H}_{\alpha\mathrm{H}}\mathrm{O}_{\alpha\mathrm{O}} + \left(\alpha_{\mathrm{C}} + \frac{1}{4}\alpha_{\mathrm{H}} - \frac{1}{2}\alpha_{\mathrm{O}}\right) \cdot \lambda_{\mathrm{tec}} \cdot \mathrm{O}_2 \rightarrow \quad & \alpha_{\mathrm{CO}} \cdot \mathrm{CO} && + && \alpha_{\mathrm{CO2}} \cdot \mathrm{CO}_2 \\ & \alpha_{\mathrm{H2}} \cdot \mathrm{H}_2 && + && \alpha_{\mathrm{H2O}} \cdot \mathrm{H}_2\mathrm{O} \\ & \text{Hydrocarbons} && + && \text{Soot} \end{aligned} \tag{2.1}$$

The terms synthesis gas (= *syngas*) and product gas are used as synonyms in this work. The technical air-to-fuel ratio λ_{tec} is defined as the ratio of the oxygen amount present in the system $\dot{n}_{\mathrm{O2}}$ and the oxygen amount required for complete oxidation $\dot{n}_{\mathrm{O2,stoic}}$ of the feedstock:

$$\lambda_{\mathrm{tec}} = \frac{\dot{n}_{\mathrm{O2}}}{\dot{n}_{\mathrm{O2,stoic}}}. \tag{2.2}$$

In the broadest sense, processes featuring technical air-to-fuel ratios of $0 < \lambda_{\mathrm{tec}} < 1$ can be referred to as gasification. This distinguishes gasification from other thermochemical conversion processes like pyrolysis ($\lambda_{\mathrm{tec}} = 0$) and combustion ($\lambda_{\mathrm{tec}} \geq 1$). In gasification, a part of the chemical enthalpy in the fuel $H^{\ominus}_{\mathrm{fuel}}$ is converted to thermal energy, whereas the remaining chemical enthalpy is contained in the syngas $H^{\ominus}_{\mathrm{SG}}$. The ratio of chemical enthalpy transferred to the product gas to the chemical enthalpy of the feedstock at standard conditions is denoted as cold gas efficiency CGE

$$\mathrm{CGE} = \frac{H^{\ominus}_{\mathrm{SG}}}{H^{\ominus}_{\mathrm{Fuel}}}. \tag{2.3}$$

The carbon conversion CC is defined as the amount of fuel carbon transferred to permanent gases [7]

$$\mathrm{CC} = \frac{\dot{n}_{\mathrm{CO}} + \dot{n}_{\mathrm{CO2}} + \dot{n}_{\mathrm{C,GaseousHydrocarbons}}}{\dot{n}_{\mathrm{C,Fuel}}} = 1 - \frac{\dot{n}_{\mathrm{C,residue}}}{\dot{n}_{\mathrm{C,Fuel}}}. \tag{2.4}$$

A comprehensive description of the fundamentals of gasification, reactor configurations and technical aspects is provided in [7, 18].
Typically, gasifiers are distinguished in fixed bed, fluidized bed and entrained flow gasifiers (EFG), the latter being the subject of this work. In EFG, fuel droplets and solid particles are dispersed in the reacting gases [7]. This requires a small size of fuel droplets / particles, typically $d_{\mathrm{p}} < 100$ µm and high temperature, typically $T > 1200$°C, to ensure their reaction within adequate residence time. EFG feature the highest degree of oxidation and the highest operating temperature of the 3 gasifier types and thus allow for high throughput and low amounts of hydrocarbons and soot in the product gas. Together with their capability of pressurized operation, this makes EFG especially relevant for syngas production in the context of chemical synthesis.
Liquid, solid and suspension fuels can be used as EFG feedstocks. The fuel is fed to the reactor through a burner nozzle together with the gasification agents, typically oxygen and steam, which also act as atomizaton medium in case of a liquid or suspension feed (see section 2.2.1). This makes the mass flow ratio of gasification agent $\dot{m}_{\mathrm{GA}}$ and fuel $\dot{m}_{\mathrm{Fuel}}$ a relevant parameter for operation of EFG:

$$\mathrm{GLR} = \frac{\dot{m}_{\mathrm{GA}}}{\dot{m}_{\mathrm{Fuel}}} \tag{2.5}$$

Today, EFG are mainly applied for gasification of dry coal, coal-water-slurry (CWS) and heavy refinery residues. Applications for pulverized biomass, biomass pyrolysis oils, suspensions of biomass pyrolysis oils with biogenic char and more recently also plastic pyrolysis oils are reported in pilot projects and research literature, e.g. [3, 14, 19–25].
The typical operating window of EFG in terms of λ_{tec} depends strongly on the feedstock and the intended usage of the syngas. The advantages of higher λ_{tec}, i.e. higher process temperature, lie in higher CC and less hydrocarbons and soot, with the disadvantages of lower CGE, more production of waste heat and CO_2 and a higher demand in oxygen and steam.
The most widely used reactor designs for EFG are the GE Energy (formerly Chevron-Texaco), ConocoPhillips E-Gas, Shell, PRENFLO (thyssenkrupp-Uhde), Siemens (formerly GSP-Noell) and Lurgi MPG designs [7, 18, 26]. The CCLab EFG at KIT [14] is an EFG reactor of the Lurgi MPG type equipped with a cooling screen for slagging operation and is selected as an example configuration for this work shown in Fig. 2.1, where a schematic of the reaction chamber during operation on a suspension fuel is depicted. The fuel is fed together with the oxidizer through a burner at the top of the reactor. At the

burner outlet, the suspension fuel is atomized into a spray (section 2.2.1) and a flame zone is formed (see section 2.1.2). The liquid phase evaporates (section 2.2.3), which is accompanied by droplet conversion phenomena leading to solid residues featuring highly variable morphologies (section 2.2.4). The remaining solid organic matter then reacts further downstream (section 2.2.5). The flow field in the reactor can be divided into a region in the vicinity of the burner which is dominated by the gas jet emerging from the burner, whereas the surrounding atmosphere is characterized by a recirculation eddy that is driven by the jet momentum (section 2.2.2). The temperature field in the recirculation zone is comparatively uniform, whereas the burner near jet zone is characterized by both high temperatures and strong temperature gradients induced by the interaction of gas phase mixing and oxidation reactions (sections 2.2.6, 2.2.7).

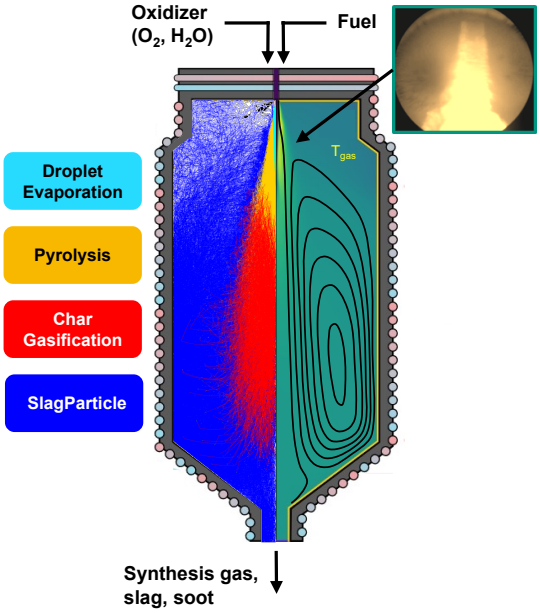


Figure 2.1: Schematic of the CCLab EFG reactor at KIT depicting different stages of suspension droplet conversion, temperature field and flow field. Adapted from [9, 27]

2.1.2 Situation in EFG Burner-Near Field

Overview of EFG Burner Concepts

EFG systems commonly use external mixing burner nozzles with coaxial configuration of the input streams [18, 28]. Most industrially applied burner designs are confidential. Research and patent literature provides a large variety of concepts differing in number of input streams and arrangement of the streams, in which two principal concepts dominate. The first group features a central fuel jet surrounded by oxidizer streams and is for example described for solid [29–31], liquid [10, 32–34] and suspension feedstocks [35–37]. The second,

inverse, configuration featuring central streams of oxidizer surrounded by an annular fuel stream is also reported for solid [38–40], liquid [41] and suspension [42] feedstock.
Configurations featuring alternating orders of fuel and oxidizer also exist [43–48]. Arrangements of multiple burners are sometimes applied in order to intensify mixing and eliminate dead zones in the reactor that do contribute litte to carbon conversion [39, 49–52].
Application of swirl is also an often investigated concept for EFG burners [38, 39, 53–57], because it can have beneficial impact on CC but as a downside also increases thermal stress on reactor walls and burner. Several experimental, non-coaxial burner concepts are also reported in research literature [53, 58, 59].
The burner design in EFG systems dominates flow field, reactand mixing, droplet size, droplet dispersion and temperature field and therefore directly influences reaction zone structure and fuel conversion processes [28, 60–64]. It has been shown in various numerical [39, 53, 65] and experimental studies [28, 29, 59, 66] that the EFG burner impacts syngas yield, carbon conversion and the formation of undesired by-products like soot or methane, underlining its relevance for process efficiency.

Flame Structure under EFG Conditions

For the 2 main burner concepts discussed above, a direct comparison is conducted by Bader et al. [65], Li et al. [67] and Ulber [68]. They showed significant differences in reaction zone structure and temperature field between the two configurations. For the first concept featuring a central fuel jet and an annular gas stream, the authors describe a hollow cone flame (Fig. 2.2 left). For the inverse configuration, a lifted, closed flame is reported (Fig. 2.2 right) [65, 67, 68]. In contrast, there have also been descriptions of a closed, non-lifted flame for the first concept (Fig. 2.2 center) [10, 69]. These flame structures are however only addressed in modeling literature and have not been described in sufficent detail in the limited experimental literature on EFG flames [33, 64, 67, 70–72]. The effects determining temperature field, species concentrations, reaction zone geometry and fuel conversion within these flames are currently not well understood.
In this thesis, the configuration featuring a central fuel jet and an annular gas stream is selected as a reference for further investigation. The flame structure in this configuration can be described as a turbulent inverse diffusion flame of oxidizer and surrounding hot syngas that is superimposed by a fuel spray (see section 2.2.7).
The gasification medium forms a turbulent jet, leading to entrainment of hot syngas into the jet. The entrainment rate can be described by the theory of turbulent jets and is dependent on the gas momentum flow (see section 2.2.2). The high relative velocity between gas and liquid phase at the burner outlet disintegrates the liquid jet into droplets. The resulting spray properties such as droplet diameter and radial distribution of liquid mass flux are influenced by fuel specifications and are likewise dependent on gas momentum flow (see section 2.2.1).

At the burner outlet, a core zone exists at the jet axis where no mixing between jet

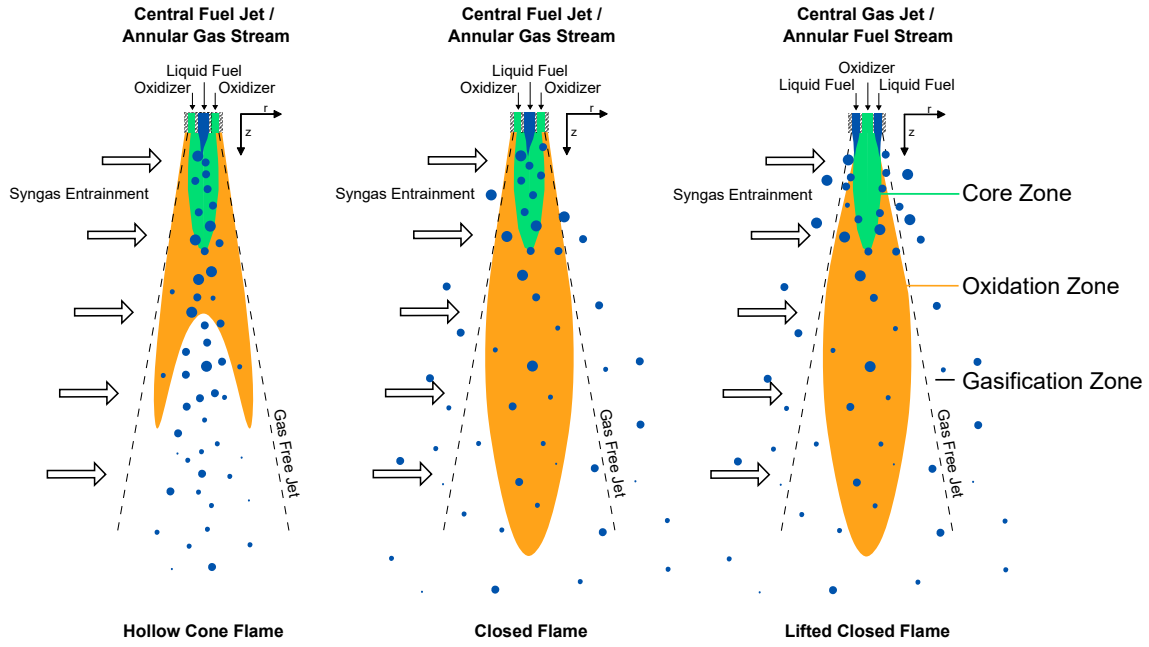


Figure 2.2: Different EFG flame structures reported in literature, visualized for gasification of a liquid fuel.

medium and the surrounding syngas has occured. This zone is characterized by low temperatures and the absence of chemical reactions. At the outer jet boundary, the oxygen rich gasification medium mixes with syngas at high temperatures, leading to immediate oxidation reaction. This serves as a stabilization mechanism of an high temperature oxidation zone that envelopes the core zone [10, 15, 69]. Along the oxidation zone, oxygen is consumed through reaction with syngas entrained into the gas jet and through the reaction with fuel vapor released from the droplets. After complete oxygen consumption, endothermic gasification reactions together with fuel evaporation and further entrainment of syngas into the jet lead to a decrease in temperature. The oxidation zone is embedded in a gasification zone, which is characterized by moderate temperatures and fuel rich conditions. The remaining fuel droplets in the gasification zone are converted in a fuel rich syngas atmosphere, which may result in the formation of soot and hydrocarbons [59]. As stated above, hollow cone and closed oxidation zone shapes have both been reported in literature for the reference burner configuration, while the determining factors are not clear. In this work, both flame shapes could be experimentally observed and explained using modeling results. More detail is given in section 5.1.1.

State of Research on EFG Flame Zone

This section attempts to list major research gaps concerning the EFG flame zone.
In general, high quality experimental data of flames under EFG conditions is scarce. Limited optical access at pressurized systems, high temperatures and a particle laden turbulent

gas flow causes difficulties for diagnostic equipment. Local heat flux measurements at the reactor wall [73] and non-spatially resolved spectroscopy [74, 75] have been applied for flame studies in EFG systems, but the insight provided by such techniques is limited. Information on temperature and species concentration fields in the post flame region has been provided by invasive probe measurements [8, 29, 76, 77] and line-of-sight absorption spectroscopy [78–81]. Spray behavior and flame dynamics have been investigated in EFG reactors using camera systems [33, 35, 53, 64, 82]. For reaction zone mapping, chemiluminescence imaging of OH and CH radicals has been applied [11, 70, 71, 83]. However, these studies mostly focus on single effects like flame lift-off distance, temperature field or particle dispersion, which makes it difficult to derive an overall process understanding [15]. A number of numerical studies explicitly addresses the EFG flame, e.g. [9, 10, 65, 69] but the lack of comprehensive experimental datasets makes validation difficult. The majority of simulation studies focuses on global reactor performance without detailed assessment of the flame zone. Most simulation studies on EFG systems apply RANS-models (see section 2.2.2). While RANS models provide a good tool for reactor simulations, they have shown difficulties in predicting droplet and solid particle dispersion, gas temperature and species concentrations in the burner near field [9, 15]. Mancini et al. [84] and Eckel et al. [10] conducted RANS and LES simulations for the same boundary case described in [8] but predicted different flame structures (see above). Abani et al. [85] also compared RANS and LES simulations for coal gasification. They found that the RANS model predicted an accumulation of coal particles at the jet axis, whereas the LES model showed stronger dispersion of particles in radial direction. This again lead to significant differences in flame structure between both models. Similar observations were made by Kumar et al. [86]. As EFG is characterized by the interaction of multiple sub-processes on different time and length scales, such approaches cause high computational cost. The suitability of LES for sensitivity studies for EFG systems is therefore currently limited. The further development of validated models for the flame zone is necessary.

Although it is known that the size and dispersion of fuel droplets and solid particles affect EFG flame geometry [10, 61, 65, 87], the consequences have not been comprehensively investigated to the author's knowledge. The process of atomization - linking arrangement and momentum of the inlet streams with size and dispersion of fuel droplets - is dealt with in a few experimental studies in-situ, e.g. [35, 37, 64, 88] but the implications on flame structure or fuel conversion were not sufficiently discussed. The preceding work by Hotz [13] provides a sensitivity study on the impact of droplet size and gas momentum flow on an EFG flame using the model that is expanded in this work, but the trends predicted by the model were not experimentally verified. For combustion conditions, the relation between spray parameters, flame geometry and fuel conversion has been extensively researched for coaxial jet burners. Droplet size [89–93] and the radial dispersion of the liquid phase [91–96] were shown to exhibit an influence on flame geometry and on the formation of soot. The influence of gas momentum flow on flame length has been well researched and

scaling laws based on entrainment of ambient air have been developed [91–93, 97–100]. Studies of EFG burners investigated under combustion conditions are found in literature [32, 44], but the transferability of information on flames under gasification conditions is limited due to the different flame structure in a syngas environment (see above).
Furthermore, the influence of fuel specifications on the EFG flame zone is not well investigated, which is especially the case for suspension fuels. Experimental work provides little insight. Model sensitivity studies on the impact of suspension fuel specifications like solid mass fraction [42, 101, 102] and solid particle size [42] for Asphalt-Water-Slurry (AWS) and CWS focus on global process performance and elaborate little on the fuel conversion processes in the flame zone. The impact of solid mass fraction on the flame zone was explicitly investigated for Pet-Coke-Water-Slurry (PCWS) by [103]. More insight on the flame zone of suspension fuel EFG is given by [9, 36, 104], but only for single cases without variation of fuel parameters.
For suspension droplets, different droplet conversion pathways are possible during EFG depending on fuel specifications and process conditions (see section 2.2.4). This impacts the release rates of fuel vapor to the gas phase and the morphology of the remaining solid particles, which is critical for their further conversion in the post-flame region. Solid agglomerates from oils and suspensions formed under EFG conditions have been described by [77, 105–107]. Due to high computational costs, modeling studies usually neglect these phenomena and apply simplified droplet models (see section 2.2.4).
It can be summarized that on the topic of the EFG flame zone, existing literature often investigates single cases without systematic parameter variations. Studies feature different burner concepts, reactor types, fuels, and operating conditions, which makes it difficult to derive a systematic understanding of the processes in the flame zone and their impact on fuel conversion. As the EFG flame is stabilized in a fuel rich environment, it features a different reaction zone structure and parameter dependencies than flames under combustion conditions, hence typical design rules for such burners are not transferable. The process of atomization, despite its high relevance, is often neglected in literature on EFG flames. The conversion steps of suspension fuel droplets in the EFG flame zone are also mostly ignored in literature. Diagnostic limitations at EFG systems make it difficult to provide high-quality experimental data, which also induces a lack of validated models for the EFG flame zone.
The intention of this thesis is to contribute to closing these research gaps by a comprehensive assessment of the interaction of sub-processes in the EFG flame zone for liquid and suspension fuels based on detailed experimental data and validated model calculations (see research objectives in section 1.2).

2.2 Physical and Thermochemical Sub-Processes in EFG

2.2.1 Atomization

In EFG, gas assisted atomization is used. The liquid phase is exposed to a gas stream featuring a high relative velocity, leading to the transfer of kinetic energy from the gas to the liquid phase. A part of the kinetic energy is converted to surface energy of the liquid phase, resulting in the formation of a spray, whereas the major part of the kinetic energy is used for acceleration of the resulting droplets and entrainment of ambient gas [108]. A decisive parameter for gas assisted atomization is the mass flow ratio of atomization medium and liquid phase expressed by the gas to liquid ratio GLR (eq. 2.5).
During gas assisted atomization, surface tension poses a stabilizing force on the liquid phase. Liquid viscosity also poses a resistance against changes in geometry of the liquid phase. Aerodynamic forces induced by the gas phase counteract the stabilizing forces and promote deformation and disintegration of the liquid phase [108]. The aerodynamic Weber number We_{aero} is a commonly applied dimensionless number describing the ratio of destabilizing aerodynamic forces to stabilizing surface forces:

$$We_{\mathrm{aero}} = \frac{\left(u_{\mathrm{gas}} - u_{\mathrm{liq}}\right)^2 \cdot \rho_{\mathrm{gas}} \cdot L_{\mathrm{c}}}{\sigma}. \tag{2.6}$$

The velocities of gas and liquid phase are denoted as u_{gas} and u_{liq} respectively, ρ_{gas} is the gas phase density, L_{c} is the characteristic length and σ is the surface tension. The liquid Reynolds number Re_{liq} is an often applied dimensionless quantity that takes the ratio between inertia and viscous forces in the liquid phase into account:

$$Re_{\mathrm{liq}} = \frac{u_{\mathrm{liq}} \cdot \rho_{\mathrm{liq}} \cdot L_{\mathrm{c}}}{\eta_{\mathrm{liq}}} \tag{2.7}$$

It contains the density ρ_{liq} and dynamic viscosity η_{liq} of the liquid phase.
When a liquid jet emerges from a twin-fluid atomizer nozzle, the relative velocity between liquid and gas phase causes shear forces at the gas-liquid interface. Dependent on liquid properties and gas flow, this leads to the formation of Kelvin-Helmholtz instabilities or Rayleigh-plateau-instabilities. These give rise to the formation of large droplets and ligaments, which is referred to as primary breakup. The aerodynamic forces then cause a further disintegration of droplets and ligaments into smaller fragments, which is denoted as secondary breakup [91, 108]. For the central liquid jet nozzle configuration applied in this work, different primary breakup regimes are distinguished in literature. The most widely applied classification is the one based on We_{aero} and Re_{liq} proposed by Chigier and Farago [109] shown in Fig. 2.3.
The *fiber* and *membrane* breakup regimes are the most relevant regimes in this work. In both fiber and membrane breakup regime, a periodic oscillation of the liquid primary jet

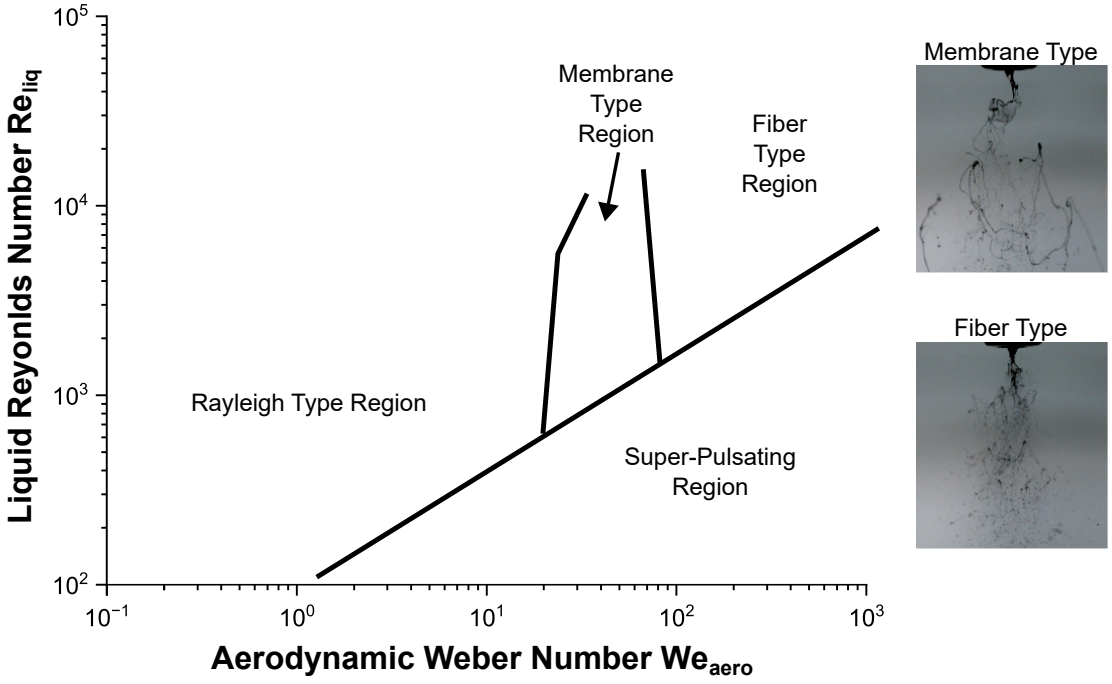


Figure 2.3: Primary breakup regimes for central liquid jet nozzles according to [109]. High speed images were obtained in this work (see section 3.4.2)

can take place. This oscillation can either occur radially symmetric (pulsating) or radially asymmetric (flapping) and is described for example in [110, 111].
The resulting sprays are polydisperse and can be described using distributions of the droplet diameter d. In this work, droplet size distributions $Q_0(d)$ based on droplet number n and droplet size distribution $Q_3(d)$ based on droplet volume V are applied [92]

$$Q_0(d) = \sum_{n=1}^{n(d)} n_n \Big/ \sum_{n=1}^{N} n_n \,, \tag{2.8}$$

$$Q_3(d) = \sum_{n=1}^{n(d)} V_n \Big/ \sum_{n=1}^{N} V_n \tag{2.9}$$

where droplets are categorized into N droplet classes. The Sauter mean diameter d_{32} is evaluated as a characteristic parameter of the droplet collective [108].

$$d_{32} = \sum_{n=1}^{N} d_n^3 \Big/ \sum_{n=1}^{N} d_n^2 \tag{2.10}$$

The Sauter diameter describes the diameter of an hypothetical monodisperse spray featuring the same volume to surface ratio as the polydisperse spray [108]. It is a commonly applied quantity to describe two-phase flows which feature heat and mass transport as well as chemical reactions. Besides droplet size, spray dispersion is of high relevance for conversion

of droplets in reacting sprays. This can be described using the local liquid mass flux ϕ_{liq}, which is defined as the liquid mass flow $\dot{m}_{\mathrm{liq}}(A)$ passing through a unit area A perpendicular to the flow:

$$\phi_{\mathrm{liq}} = \frac{\dot{m}_{\mathrm{liq}}(A)}{A}, \text{ for } A \to 0. \tag{2.11}$$

2.2.2 Mixing in Turbulent Free Jets

Physics and Modeling of Turbulent Flows

Most flows in technical systems are of turbulent nature. Turbulence occurs when viscous forces in the flowing medium are not sufficient to damp instabilities in the flow, which is the case at high Reynolds numbers. Turbulence is a chaotic phenomenon characterized by random fluctuations of velocity around a temporal average value and the occurence of 3-dimensional vortex-like structures called eddies at every length scale. This allows momentum, species and energy to be transported perpendicular to the stream lines at much higher rates than in laminar flows, where molecular diffusion of these quantities is the governing mechanism [92, 112, 113] The temporal average of this exchange can be described using effective transport coefficients depending on the state of the flow, e.g. turbulent viscosity η_{t}, turbulent diffusion coefficient D_{t} and turbulent heat conductivity λ_{t} [92].

A turbulent flow features a size spectrum of eddies, where large eddies at the scale of the system gradually decay towards smaller scales in a cascade-like process. The largest scale eddies are typically generated by external forces or hydrodynamic instabilities and provide the dominant contribution to the kinetic energy spectrum of the turbulent flow. Kinetic energy is then gradually transferred to increasingly smaller eddy length scales. Spatial velocity gradients within and between the eddies become steeper with decreasing eddy size, increasing the influence of viscosity, until at the smallest scale at which eddies can exist *(Kolmogorov Scale)*, viscous friction eventually leads to dissipation of kinetic energy into thermal energy of the fluid [92, 113, 114].

Like laminar flows, turbulent flows can be described using the Navier-Stokes equation, which can be solved numerically by discretization in time and space. To completely describe a turbulent flow by this means, all length and time scales occuring in the flow need to be resolved by the model. This approach called *Direct Numerical Simulation (DNS)* requires an immense amount of computational capacity that makes it unsuitable to solve practical problems with the currently available methods [92, 113]. A compromise is the application of *Large Eddy Simulation (LES)* where the flow is spatially and temporally resolved up to a certain scale, while smaller features of the flow down to the Kolmogorov scale are modeled. By this approach, the large-scale unsteady features of the flow that are relevant for macroscopic transport of momentum, energy and mass remain intact, which is

of special relevance for the description of reacting and multiphase systems [92, 113]. As the computational effort of LES is still considerable, the *Reynolds-Averaged-Navier-Stokes (RANS)* approach is by far the most commonly used concept in engineering applications. In this approach, the Navier-Stokes equations are temporally averaged and the impact of turbulence on scalar transport is no longer resolved but is entirely modeled. In comparison to LES, the accuracy of RANS for prediction of turbulent free jets is reduced, especially for two phase flows [85, 86, 115, 116].
A special role is taken by semi empirical and analytical models, where exact or approximate solutions to the temporally averaged equations are given for a certain application under additional assumptions. While these approaches are typically less accurate than the numerical models described above, they feature the advantage of an explicit formulation of the equations, enabling an evaluation with minimum computational effort and a direct insight into parameter dependencies. This idea is also the basis of the 2-Phase Free Jet Model (2-Ph-FJM) applied in this work.

Single Phase Turbulent Free Jet

A stream that expands into a quiescent gas ambience that is not influenced by other flows or walls is referred to as free jet. A characteristic of free jets is the entrainment and subsequent mixing of ambient medium from the surrounding atmosphere into the jet.
A non-swirled turbulent free jet exiting a circular orifice with diameter d_0 first shows a *Potential Core* in which the flow keeps its initial state (see Fig. 2.4). At the jet boundaries, shear forces caused by the velocity gradient between ambient medium and jet medium lead to exchange of momentum. This also causes transfer of mass and energy. The potential core narrows towards the jet centerline in consequence. With increasing nozzle distance, the potential core ends when the velocity at the jet centerline falls below its initial value, which is the case at approximately $z \approx 4 \cdot d_0$ for a circular homogeneous gas free jet [117, 118].
In the following *Transition Region*, exchange of momentum with the surrounding medium continues and the profiles of velocity, mixture fraction and temperature lose their initial shape and gradually approach the profiles in the self similar region. The transition region ends at approximately $z \approx 8 \cdot d_0$ for a circular homogeneous gas free jet [117, 118].
While in the potential core and transition region, the profiles of velocity, mixture fraction and temperature are highly dependent on input conditions [117, 119–121], the *Self Similar Region* is characterized by the fact that these quantities can be described using the same self similar function for all nozzle distances (see below).
During the process of entrainment, momentum is exchanged between jet and environment, while the total momentum flow remains constant and equal to the momentum flow of the

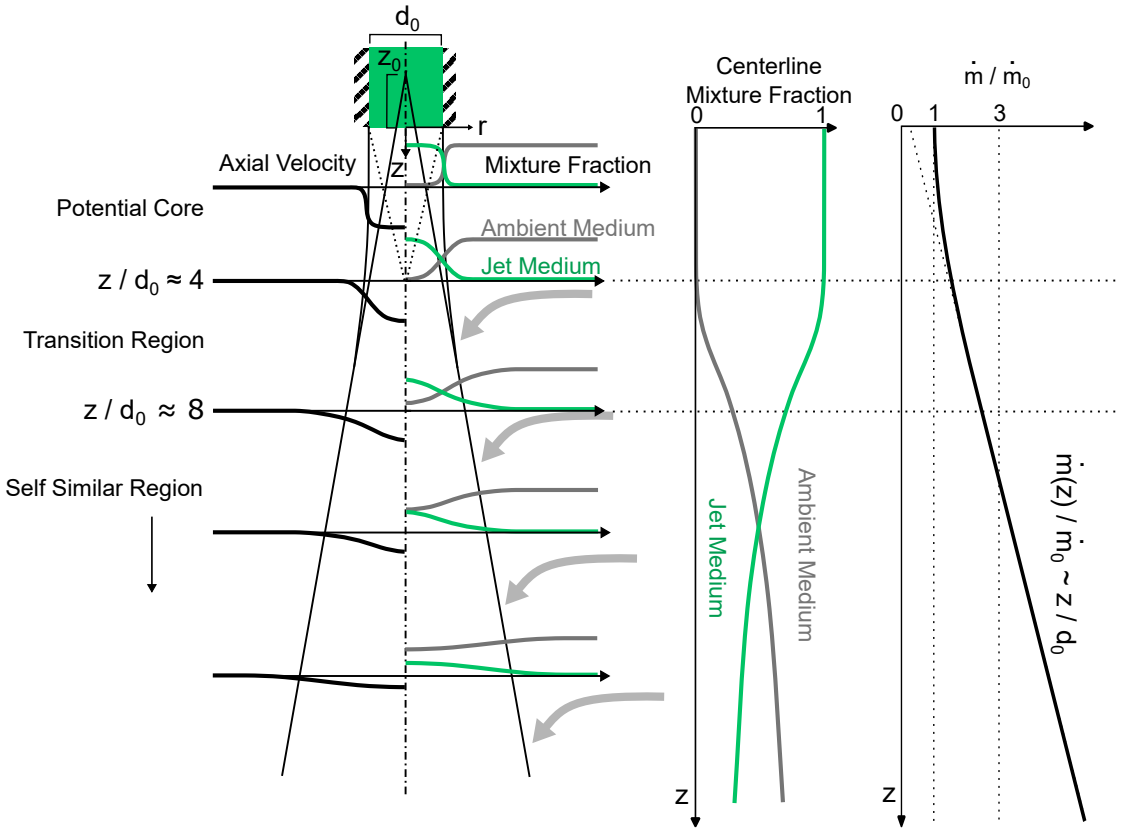


Figure 2.4: Axial velocity, mixture fraction and entrainment rate in a non-swirled, round homogeneous free jet according to [117, 118]

initial input stream:

$$J_0 = \dot{m}_0 \cdot u_0 \tag{2.12}$$

This exchange of momentum is the driving force for entrainment in turbulent free jets [117]. According to Thring and Newby [98], each turbulent free jet with initial momentum and mass flows J_0 and $\dot{m}_0$ emerging from an arbitrary nozzle geometry into a medium with density ρ_1 can be described by a hypothetical homogeneous free jet emerging from a round nozzle with a generalized equivalent diameter $d_{\mathrm{eq,gen}}$:

$$d_{\mathrm{eq,gen}} = \frac{2 \cdot \dot{m}_0}{\sqrt{J_0 \cdot \pi \cdot \rho_1}}. \tag{2.13}$$

Jets consisting of multiple streams emerging from different coaxial outlets can be described using eq. 2.13 when their individual mass and momentum flows are summed [117]. For a single homogeneous free jet emerging from a non-circular outlet like an annulus, the

equation simplifies to the geometric equivalent diameter

$$d_{\mathrm{eq}} = \sqrt{\frac{4 \cdot A_{\mathrm{gas}}}{\pi}}. \tag{2.14}$$

with the nozzle exit area A_{gas}. If the jet's initial density ρ_0 differs from the density of the surrounding medium, eq. 2.13 can be written as

$$d_{\mathrm{eq,gen}} = d_{\mathrm{eq}} \cdot \sqrt{\frac{\rho_0}{\rho_1}}. \tag{2.15}$$

The mass flow entrained by the free jet $\dot{m}\,(z)$ increases linearly with nozzle distance in the self similar region (see Fig. 2.4), which can be described using the well known correlation by Ricou and Spalding [122]

$$\frac{\dot{m}\,(z)}{\dot{m}_0} = 0.32 \cdot \frac{z - z_0}{d_{\mathrm{eq}}} \cdot \sqrt{\frac{\rho_1}{\rho_0}}. \tag{2.16}$$

The virtual jet origin z_0 is the axial distance at which the extrapolated linear relationship becomes zero (see Fig. 2.4) [117, 118]. Recent publications have shown that while LES simulations perform excellently at predicting entrainment rates of turbulent jets, the simple eq. 2.16 still shows better agreement with experimental data than most modern RANS approaches for circular jets [115, 116].
To describe fields of velocity, mixture fraction and temperature in the self similar region of a free jet, nondimensional radial and axial coordinates η and ζ can be used:

$$\eta = \frac{r}{z - z_0}, \tag{2.17}$$

$$\zeta = \frac{z - z_0}{d_{\mathrm{eq}}}. \tag{2.18}$$

If this coordinate system is applied, radial profiles of velocity normalized to the axial maximum can each be described using the same function at all nozzle distances past the transition region, giving the self-similar region its name. This is also true for mixture fraction and temperature and has been extensively investigated in literature [117, 120, 121].
It has been shown that universal self-similarity between all free jets independent of the input conditions (Reynolds number, nozzle geometry, and properties of jet and ambient medium) does not exist. As detailed in the literature reviews by Hotz [13] and Ball [120], this fact is mainly relevant for turbulent moments of higher order and the implications for the temporal averages of velocity, mixture fraction and temperature are minor. The assumption of universal self-similarity provides the advantage of a simplified description of the processes in the free jet, which has lead to the development of several models [13, 112, 118]. The approach developed by Günther [118] is the basis of the 2-Phase Free Jet Model

(2-Ph-FJM) applied in this work and will thus be discussed in the following.
Günther proposes the description of the field of axial velocity u_{gas} in the self similar region by the semi-empirical relationship

$$\frac{u_{\mathrm{gas}}\left(\zeta,\eta\right)}{u_{\mathrm{gas},0}} = \frac{1}{2\cdot\omega_i}\cdot\frac{1}{\zeta}\cdot\sqrt{\frac{\rho_0}{\rho_1}}\cdot\exp\left[-\left(\frac{1}{{\omega_i}^2}-\frac{1}{2\cdot{\omega_i}^2}\right)\cdot\eta^2\right]. \tag{2.19}$$

The derivation of this equation is detailed in [13, 118]. The experimentally determined coefficient ω_i contains the information on turbulent exchange of momentum. For gas free jets, a value of around $\omega_i \approx 0.07$ provides a good approximation [118]. Eq. 2.19 shows that in axial direction, the axial velocity decreases proportional to $1/\zeta$, while in radial direction, a Gaussian profile occurs. Due to the self similar properties of the Gaussian function, a constant free jet angle can be defined, which is typically given as 19°[118]. The radial component of velocity is neglected in this description, as the axial component is typically of much larger magnitude [117, 121]. It has been shown that the radial integration of the Gaussian profiles yields the correlation by Ricou and Spalding (eq. 2.16) [13, 115].
For the mixture fraction of jet medium m_{jet} and ambient medium m_{amb}

$$x_{\mathrm{jet}}\left(\zeta,\eta\right) = \frac{m_{\mathrm{jet}}\left(\zeta,\eta\right)}{m_{\mathrm{jet}}\left(\zeta,\eta\right)+m_{\mathrm{amb}}\left(\zeta,\eta\right)} \tag{2.20}$$

an analogous description has been proposed [12, 117, 118]:

$$\frac{x_{\mathrm{jet}}\left(\zeta,\eta\right)}{x_{\mathrm{jet},0}} = \frac{\omega_i}{2\cdot{\omega_x}^2}\cdot\frac{1}{\zeta}\cdot\sqrt{\frac{\rho_0}{\rho_1}}\cdot\exp\left[-\left(\frac{1}{{\omega_x}^2}-\frac{1}{2\cdot{\omega_i}^2}\right)\cdot\eta^2\right] \tag{2.21}$$

The coefficient for turbulent exchange of mass is denoted as ω_x, which can be derived from the turbulent Schmidt number

$$Sc_{\mathrm{t}} = \frac{\eta_{\mathrm{t}}}{D_{\mathrm{t}}\cdot\rho} = \frac{{\omega_i}^2}{{\omega_x}^2} \tag{2.22}$$

where η_{t} is the turbulent viscosity and D_{t} the turbulent diffusion coefficient (see above). Günther gives a typical value of $Sc_{\mathrm{t}} \approx 0.75$ [118].
If a jet is enclosed by walls, the fluid entrained by the jet cannot flow in freely from the environment. A recirculation eddy in the form of a closed loop as depicted in Fig. 2.1 is established due to conservation of mass. Theories for enclosed jets have been developed for example by Thring and Newby [98], and Curtet [123]. An enclosed jet emerging into a cylindrical space can be divided into three regions. In the first region, the jet entrains mass from the recirculation eddy. If the nozzle diameter d_0 is small compared to the diameter of the surrounding space d_{R} (typically $d_0 < 0.1\cdot d_{\mathrm{R}}$), the flow field in this region does not considerably differ from the one in an open free jet. For nozzle distances larger than the center of the recirculation eddy z_{rec}, the jet gives off mass to the recirculating flow and the flow field can no longer be described by free jet theory. Thring and Newby propose

the following relationship to calculate z_{rec}:

$$z_{\mathrm{rec}} = \frac{d_{\mathrm{r}}}{2} \cdot \left(2.925 + \frac{\Theta}{0.32}\right), \text{ using } \Theta = \frac{d_0}{d_{\mathrm{R}}} \cdot \sqrt{\frac{\rho_0}{\rho_1}} \tag{2.23}$$

After the point where the extrapolated jet angle meets the wall, the flow transitions into a plug flow [117, 118].

Two Phase Turbulent Free Jet

While single phase turbulent free jets have been thoroughly investigated over the last decades, the knowledge on two phase turbulent free jets is comparatively scarce and there is no comprehensive description available in literature. Notable work on two-phase jets relevant for the scope of this work is provided for the aspects of velocity field and turbulence [124–126], particle dispersion [13, 125, 127, 128] and entrainment [12, 13, 127, 129]. These studies however mostly focus on single effects and no general theory for two phase turbulent free jets has been developed.

The two phase jets considered in this work feature a continuous gas phase and a dispersed liquid phase, where the gas phase carries the major portion of the initial momentum. Such a two phase jet can be considered as a gas free jet that is superimposed by a liquid spray [12]. The mass of the gas phase within the jet increases through entrainment while the liquid mass remains constant. The liquid phase is gradually diluted and its influence on the flow field decreases with increasing ζ [12].

The most essential difference of the above described situation to pure gas free jets is that the dispersed phase exchanges momentum with the gas phase. Initially, droplets feature a lower velocity than the gas phase and are thus accelerated while the gas phase is decelerated due to the conservation of momentum. If buoyancy and gravity are neglected, the acceleration of a droplet featuring velocity $\vec{u}_{\mathrm{drop}}$ can be described by [92]

$$\frac{\pi \cdot d^3 \cdot \rho_{\mathrm{liq}}}{6} \cdot \frac{\mathrm{d}\vec{u}_{\mathrm{drop}}}{\mathrm{d}t} = \frac{\pi}{8} \cdot c_{\mathrm{w}} \cdot d^2 \cdot \rho_{\mathrm{gas}} \cdot (\vec{u}_{\mathrm{gas}} - \vec{u}_{\mathrm{drop}}) \cdot |\vec{u}_{\mathrm{gas}} - \vec{u}_{\mathrm{drop}}|. \tag{2.24}$$

The drag coefficient c_{w} depends on droplet Reynolds number, droplet shape and, for the case of high temperature systems, droplet evaporation. It can be calculated using empirical correlations [13]. The residence time of a droplet, which is relevant for assessing droplet conversion later in this work, can be obtained by integration of droplet velocity over the path $\vec{s}$ along the droplet trajectory T:

$$\tau = \int_T \frac{1}{|\vec{u}_{\mathrm{drop}}|} \mathrm{d}|\vec{s}| \tag{2.25}$$

A second major difference between pure gas free jets and two phase free jets is the influence of the disperse phase on the turbulence properties of the flow. Small droplets can damp

turbulence by absorption of kinetic energy, while large droplets can induce additional turbulence by generation of eddies [12, 91, 130, 131]. Of special relevance to this work is the atomization process (see section 2.2.1). Through the large differences of density and velocity of gas and liquid phase, the breakup process of a liquid jet emerging from a coaxial jet nozzle causes additional flow instabilities that can influence mixing processes in the nozzle near region and provide a source of turbulence [97, 111, 131–135]. The impact of the atomization process on jet mixing under conditions similar to this work has been studied in [12].

The radial distribution of mass flux and velocity of the dispersed phase in two phase free jets does not necessarily follow the mass flux distribution of the gas phase. Especially in the nozzle near region, mass flux of the disperse phase is predominantly defined by atomization. For fine particles and larger nozzle distances, mass flux distribution and velocity field of the disperse phase are typically bell shaped and approach the distribution of gas phase. For large particles with high momentum, de-mixing of gas and liquid phase can occur [12, 127, 136]. By relating local gas and liquid mass flux (eq. 2.11), a local gas-to-liquid-ratio $\mathrm{GLR}_{\mathrm{local}}$ can be defined:

$$\mathrm{GLR}_{\mathrm{local}} = \frac{\phi_{\mathrm{gas}}}{\phi_{\mathrm{liq}}}. \tag{2.26}$$

Among the studies investigating the concept of self similarity in two-phase jets [125, 127, 136, 137], the studies by Hotz [12, 13] are the most relevant for this work because the investigated nozzles and operating conditions match those applied in this work most closely. Hotz investigates local mixture fraction $x_{\mathrm{jet}}(\zeta, \eta)$ and local liquid mass flux ϕ_{liq} for central liquid jet nozzles applying 2-phase flows at GLR = 0.5 - 1.5 using air and water under ambient conditions including a single phase air jet for comparison. It is shown that the radial profiles of mixture fraction in the investigated range of $\zeta = 10 - 50$ are self similar and can be described using the same Gaussian function as in the original model for single phase free jets developed by Günther (eq. 2.21). The coefficients of turbulent exchange of mass ω_x and momentum ω_i differed from the pure gas jet case, but were found to be dependent solely on the atomization regime and independent of GLR in the investigated range. For a fiber-type breakup (see section 2.2.1), enhanced mixing between jet medium and ambient medium was observed while for a super-pulsating-type breakup, no significant difference to a gas free jet was found.

Free jet theory and the concept of self similarity was also shown to be applicable to evaporating and reacting sprays [92, 97].

2.2.3 Liquid Droplet Evaporation

Evaporation of droplets transfers liquid fuel to the gas phase, where reaction of the fuel with other gaseous species can take place. Heat can be transferred to a liquid droplet from the surrounding by convection, conduction and radiation. This causes liquid temperature to rise, increasing liquid vapor pressure. Liquid fuel molecules at the droplet surface are transferred to the gas phase and are transported away from the droplet by diffusion and convection. Mass and diameter of the droplet decrease as a consequence. To mathematically describe the process of droplet evaporation, the conservation laws for mass, energy and species must be solved together with the respective kinetics of heat and mass transfer for both phases. This subject has been extensively researched over the last decades, leading to comprehensive descriptions in literature [138, 139].
Numerous droplet evaporation models with varying degrees of complexity have been proposed in literature, with the d^2-law as one of the simplest and most widely applied approaches in engineering applications. The d^2-law, which is also applied in this work (see section 4.2) relies on the following assumptions. The evaporation process is assumed to be quasi-steady and spherically symmetric in a quiescent medium. The liquid consists of one single component with infinite thermal conductivity, eliminating temperature gradients in the droplet. The droplet temperature during evaporation is assumed to be equal to the boiling point. The thermophysical properties of the species involved in the evaporation process are constant. The Lewis number is assumed to be $Le = 1$, leading to equal heat and mass transfer rates. The heat capacities of fuel vapor and gas phase are assumed to be equal [113].
Heat transfer to droplets is typically described in literature using the Ranz-Marshal correlation for the Nusselt number Nu:

$$Nu = 2 + 0.6 \cdot Re^{1/2} \cdot Pr^{1/3} \tag{2.27}$$

applying a Reynolds number Re based on the relative velocity of gas phase and droplets and the Prandtl number Pr containing the gas phase properties. The heat transfer coefficient α is calculated from Nu by

$$\alpha = \frac{Nu \cdot \lambda_{\text{gas}}}{d} \tag{2.28}$$

using the gas phase heat conductivity λ_{gas} and the droplet diameter d. Under high ambient temperatures, the heat-up period is typically quick in comparison to the evaporation period and is neglected in the d^2-law. The temporal change of droplet temperature T_{drop} is then modeled by

$$m_{\text{drop}} \cdot c_{\text{p,liq}} \cdot \frac{\mathrm{d}T_{\text{drop}}}{\mathrm{d}t} = \alpha \cdot \pi d^2 \cdot (T_{\text{gas},\infty} - T_{\text{drop}}). \tag{2.29}$$

with the droplet mass m_{drop}, mass specific heat capacity of the liquid phase $c_{\mathrm{p,liq}}$ and bulk gas temperature $T_{\mathrm{gas},\infty}$. Once the droplet reaches its boiling point, evaporation is assumed to start. Under the above given assumptions, the decrease of droplet diameter over time t can then be written as

$$d^2(t) = d_0^2 - K \cdot t \text{ ; using } K = \frac{8 \cdot \lambda_{\mathrm{gas}}}{\rho_{\mathrm{liq}} \cdot c_{\mathrm{p,gas}}} \cdot \ln\left(1 + B_T\right) \tag{2.30}$$

containing the initial diameter d_0, the liquid density ρ_{liq}, the gas phase heat conductivity λ_{gas} and the mass specific heat capacity of the gas phase $c_{\mathrm{p,gas}}$. The term B_T is referred to as the Spalding number and is given by

$$B_T = c_{\mathrm{p,gas}} \cdot \frac{(T_{gas,\infty} - T_{\mathrm{drop}})}{\Delta h_{\mathrm{vap,liq}}} \tag{2.31}$$

featuring the liquid heat of evaporation $\Delta h_{\mathrm{vap,liq}}$ [113, 138].
The d^2-law relies on many simplifying assumptions, and models considering more effects are available. One approach applied in this work additionally considers liquid evaporation during the heat-up period and also abandons the assumption of a quiescent surrounding atmosphere, taking additional heat and mass transfer through convection into account. During the heat up period, the evaporation process is governed by mass transport of fuel vapor from the droplet surface

$$\frac{\mathrm{d}m_{\mathrm{liq,drop}}}{\mathrm{d}t} = -\pi d^2 \cdot \beta \cdot (c_{\mathrm{vap,s}} - c_{\mathrm{vap},\infty}). \tag{2.32}$$

The mass transfer coefficient β is provided by a Sherwood correlation analogous to eq. 2.27, the concentration of fuel vapor at the droplet surface $c_{\mathrm{vap,s}}$ is calculated from the vapor pressure at the droplet temperature. The bulk concentration of fuel vapor is denoted as $c_{\mathrm{vap},\infty}$. When droplet heating and evaporation occur in parallel, the droplet energy balance to determine droplet temperature is given by

$$m_{\mathrm{drop}} \cdot c_{\mathrm{p,liq}} \cdot \frac{\mathrm{d}T_{\mathrm{drop}}}{\mathrm{d}t} = \alpha \cdot \pi d^2 \cdot (T_{\mathrm{gas},\infty} - T_{\mathrm{drop}}) - \frac{\mathrm{d}m_{\mathrm{drop}}}{\mathrm{d}t} \cdot \Delta h_{\mathrm{vap,liq}} \tag{2.33}$$

with α being calculated using eqs. 2.27 and 2.28. When the droplet temperature reaches the boiling point, the evaporation rate can be assumed to be solely controlled by heat transfer [113]. The rate of liquid evaporation is then given by

$$\frac{\mathrm{d}m_{\mathrm{drop}}}{\mathrm{d}t} = -\pi d^2 \cdot \alpha \cdot \frac{\ln\left(1 + B_T\right)}{c_{\mathrm{p,gas}}}. \tag{2.34}$$

2.2.4 Suspension Droplet Conversion

The presence of a solid phase in suspension fuels strongly increases the complexity of droplet conversion. In technical fuels, pyrolysis of solid and liquid phase can occur. Thus, a large number of droplet conversion pathways are possible for suspension droplets, affecting the temporal development of droplet mass, composition and morphology. These depend on initial thermochemical properties of liquid and solid phase, solid mass fraction and particle size, heating rate, surrounding atmosphere as well as possible chemical reactions of the components in the droplet. Liquid evaporation times for suspension droplets can be significantly longer than for pure liquid droplets.
For low solid mass fractions $x_{\mathrm{sol}} < 1$ wt-% and low pyrolysis tendency of the liquid component, the droplet typically evaporates without formation of a solid agglomerate [140, 141]. Otherwise, after an initial period of regressing diameter, agglomerate formation starts with the development of a shell at the droplet surface [141–145]. This can be caused by accumulation and caking of solid particles at the droplet surface [146, 147] or enrichment and pyrolysis of less volatile liquid fuel components, which is especially relevant for biogenic pyrolysis oils [148–152] or heavy fuel fractions like HFO [153–157]. For a better overview, these two main mechanisms are regarded separately in the further description.

Non-Pyrolyzing Liquid Phase
For suspension fuels where solid formation by liquid phase pyrolysis is not relevant, i.e. for conversion of CWS or the suspensions of MEG and beech wood char (MEG-BWC) applied in this work (see section 3.4.3), droplet conversion is comparatively well characterized. It has been shown that for a non-pyrolyzing liquid phase, the caking behavior of the solid fuel phase plays a decisive role for agglomerate formation [158]. Two main pathways are reported in literature after initial shell formation, which are visualized in Fig. 2.5. According to the review by Handscomb [140], it is at present not possible to reliably predict the development of suspension droplet morphology during conversion with currently available suspension droplet models.
In a bubble forming pathway, local boiling inside the droplet leads to the emergence of gas bubbles and possible pressure increase. This can result in droplet inflation, formation of blowholes or fragmentation of the droplet, leaving different possible hollow solid agglomerate morphologies at the end of the process. These are especially relevant at high temperatures and heating rates [142, 145, 159, 160]. Droplet models including bubble formation leading to hollow agglomerates (cenospheres) have been developed for low and high temperature conditions [140, 141]. The model proposed by Lee and Law [141] has been validated for combustion of CWS and is chosen as an example of a simple cenosphere formation model in this work (see Shell Formation Model, section 4.3.4).
In the wet kernel pathway, an evaporation front recedes into the droplet while a wet kernel

remains inside [142]. Vapors diffuse outwards through the porous shell, which poses a resistance to mass transport. At lower temperatures and heating rates, the agglomerate completely dries to a porous solid particle [140]. At higher heating rates and temperatures, local superheating inside the agglomerate can again lead to fragmentation into sub-particles. Droplet models dealing with the wet kernel pathway relevant for this work are for example presented by [142, 146]. One approach of this type is also implemented in this work (see Fragmenting Particle Model, section 4.3.4).

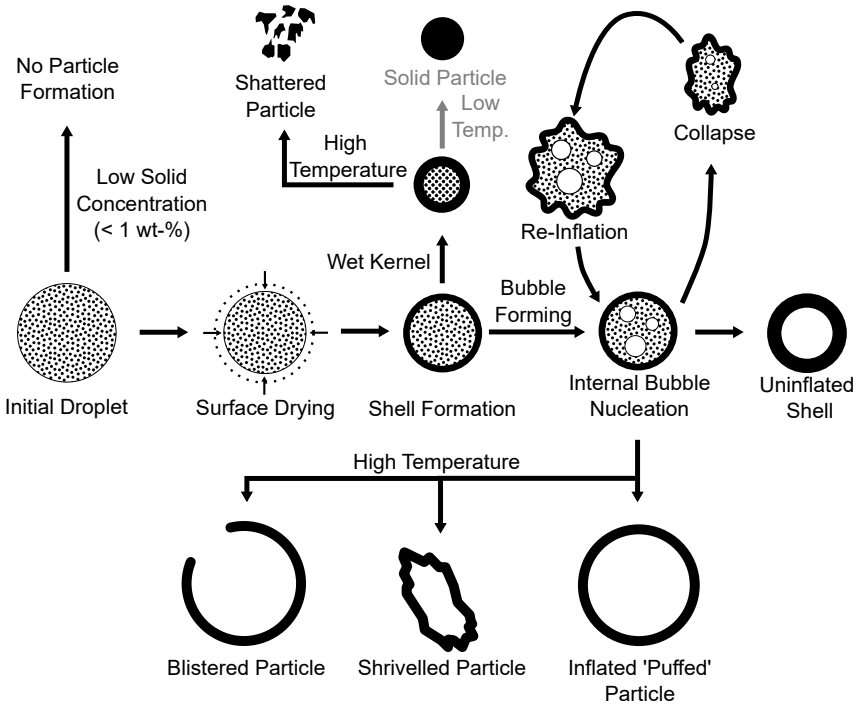


Figure 2.5: Morphology development of a suspension droplet during evaporation when liquid phase pyrolysis is not relevant. Adapted and modified from [140]. The original graphic by Handscomb was developed with focus on low temperatures, the processes depicted are however also found at high temperature (see text)

Pyrolyzing Liquid Phase

Pyrolysis of the liquid phase complicates the above mentioned processes, as additional solid can be formed. A number of phenomenological studies investigated the effects of liquid phase pyrolysis in droplets under high temperature conditions for biogenic pyrolysis oils and HFO [148–157]. For HFO and suspensions of biogenic pyrolysis oils with biogenic chars, solid agglomerates formed under EFG conditions have been experimentally characterized [77, 105, 107]. Only a few droplet models explicitly take into account pyrolysis of the liquid phase, as this requires a discretized calculation of heat and mass transport in the particle together with a model of the pyrolysis reactions specific to the fuel and process

conditions [143, 151, 156, 161].

Models for Suspension Droplets applied in EFG Literature

Table 2.1 summarizes different model concepts for suspension fuels applied in literature on CFD simulations of EFG systems. To the author's best knowledge, none of the above mentioned models dedicated to suspension droplets have been applied to simulate EFG systems in literature. The most common approach applied in EFG literature is the simple Wet Particle model, where single solid particles are assumed to be covered by a liquid film. The film thickness is defined by the liquid mass fraction in the suspension and the solid particle diameter. This model is also applied in this work as a comparison to the more detailed models outlined above (see Wet Particle Model, section 4.3.4). Some studies also inject liquid droplets and solid particles as two separate phases. The description of suspension droplets is entirely avoided by this approach. Another treatment of suspension droplets found in EFG literature is based on the assumption that suspension droplets are injected and the solid mass is released from the droplets proportionally to the evaporating liquid mass.

Table 2.1: Overview of model concepts for suspension fuels applied in literature on CFD simulation of EFG.

Concept	**Description**	**Droplet Size**	**Used by**
Wet Particle	Single solid particles are each surrounded by a liquid film, applying a standard liquid evaporation model.	Droplet size and solid particle size coupled by liquid mass fraction	[36, 101, 102, 162–166] (CWS), [42] (AWS), [167] (MEG-BWC), [65] (HFO)
Separate Injection	Pure liquid droplets and solid particles are injected as separate phases.	Droplet size and solid particle size are defined independently	[9, 168] (MEG-BWC), [103] (PCWS)
Simultaneous Release	Solid phase suspended in liquid phase. Liquid phase evaporates acording to standard evaporation model, solid is released proportional to liquid phase.	Droplet size and solid particle size are defined independently	[69, 104] (MEG-BWC)

2.2.5 Solid Fuel Conversion

The conversion of solid fuel particles in an EFG reactor is characterized by high temperatures and high heating rates that can act upon the particle under both oxidizing and reducing conditions [169]. During heat up of a carbonaceous solid fuel particle, moisture is first released from the particle which is succeeded by thermal decomposition of the fuel at higher temperatures (*Devolatilization / Pyrolysis*). This process typically yields gaseous species (*Volatile Species*) and a solid phase (*Char*), consisting primarily of the remaining carbon matrix (*Fixed Carbon*) and ash. Conversion of the char takes place in heterogeneous gas-solid reactions that mostly occur after complete devolatilization at higher temperatures, but can also temporally overlap with late phases of devolatilization [169]. Devolatilization and char conversion processes strongly dependent on the morphology, chemical composition and minerals content of the solid fuel particle, as well as temperature and species concentrations of the surrounding gas phase. A detailed review of these complex dependencies and their modeling is provided in the literature reviews by Hasse [169] and Mularski [170].
During the devolatilization process, pyrolysis reactions within the particle lead to the breakup of chemical bonds, producing light gases that are released from the particle to the surrounding atmosphere. This process can be modeled using empirical models like single-step, multi-step or distributed activation energy models [169, 170]. More comprehensive approaches approximate the fuel structure using lattice statistics or pseudo-components and apply detailed reaction mechanisms as for example the network pyrolysis models CPD or FLASHCHAIN. These models provide higher flexibility in terms of process conditions and an enhanced level of detail but are rarely used in global reactor simulations [169]. In this work, a single-step first order Arrhenius type approach is applied that is elaborated in section 4.3.4.
For the heterogeneous char conversion, the most important reactions under gasification conditions are the Boudouard reaction (eq 2.35) and the heterogeneous water gas reaction (2.36):

$$\mathrm{C} + \mathrm{CO_2} \longrightarrow 2\mathrm{CO} \tag{2.35}$$

$$\mathrm{C} + \mathrm{H_2O} \longrightarrow \mathrm{CO} + \mathrm{H_2} \tag{2.36}$$

The microkinetic rate r_i of these reactions is often described using a Langmuir-Hinshelwood model or a power law approach, which is also applied in this work (section 4.3.4). As these reactions occur at the gas-solid-interface, they require transport of gaseous reactands from the bulk phase to the solid surface, their adsorption at the solid surface, followed by desorption and mass transport of products to the bulk phase after reaction. Due to the fact that the inner surface of char particles is typically much larger than the outer surface due to the high porosity of chars induced by pyrolysis, the mass transport processes within

the particle require special attention. The morphology and reaction properties of the char are strongly influenced by the devolatilization process [171–173]. Typically, three regimes are distinguished in literature [169, 170]. In the chemically controlled regime (I), transport processes are considerably faster than chemical reactions, leading to a uniform profile of reactand concentrations over the particle. In this regime, the effective rate $r_{\mathrm{eff,i}}$ of reaction i is equal to the microkinetic or intrinsic rate r_{i}. In the pore diffusion controlled regime (II), the microkinetic rate exceeds the rate of mass transport of reactands within the pores, which is typically the case at higher temperatures. This gives rise to a concentration gradient over the particle cross section, causing $r_{\mathrm{eff,i}}$ to be determined by pore diffusion processes. In the external mass transfer controlled regime (III) present at the highest temperatures, the microkinetic rate is faster than the transport processes from the bulk phase to the particle. In this regime, reactand concentration within the particle is nearly zero and the reaction predominantly occurs at the outer particle surface. $r_{\mathrm{eff,i}}$ is determined by reactand transport from the bulk phase to the particle surface. EFG conditions feature all three regimes, with regime II as the most relevant one [170].
The most common approach to account for mass transport limitations within the particle is to use an effectiveness factor η_{i}:

$$r_{\mathrm{eff,i}} = \eta_{\mathrm{i}} \cdot r_{\mathrm{i}} \tag{2.37}$$

that is calculated from a Thiele modulus ϕ_{i} [170]

$$\eta_{\mathrm{i}} = \frac{1}{\phi_{\mathrm{i}}} \cdot \left(\frac{1}{\tanh(3 \cdot \phi_{\mathrm{i}})} - \frac{1}{3 \cdot \tanh(\phi_{\mathrm{i}})} \right) \qquad \text{(Compact Sphere)} \tag{2.38}$$

$$\eta_{\mathrm{i}} = \frac{\tanh(\phi_{\mathrm{i}})}{\phi_{\mathrm{i}}} \qquad \text{(Hollow Sphere)} \tag{2.39}$$

For a power law kinetic equation, the Thiele modulus is defined as

$$\phi_{\mathrm{i}} = L_{\mathrm{c}} \cdot \sqrt{\frac{n_{\mathrm{i}} + 1}{2} \cdot \frac{k_{\mathrm{i}} \cdot c_{\mathrm{i},\infty}^{n_{\mathrm{i}}-1}}{D_{\mathrm{eff}}}} \tag{2.40}$$

using the reaction order n_{i}, the pre-exponential factor k_{i} from the power law kinetic equation (eq. 4.37). The characteristic length is defined as $L_{\mathrm{c}} = d_{\mathrm{p,sol}}/6$ (compact sphere with diameter $d_{\mathrm{p,sol}}$) or $L_{\mathrm{c}} = \delta_{\mathrm{s}}/2$ (hollow sphere with shell thickness δ_{s}). The effective diffusion coefficient D_{eff} depends on the particle porosity and the radius of the porous structures, taking into account molecular and Knudsen diffusion [170].
More advanced models also consider the evolution of the morphological structure of the char during the heterogeneous gasification process or account for thermal annealing [169].

2.2.6 Gas Phase Reactions

Relevant Gas Phase Reactions under EFG Conditions

In the EFG flame zone, oxygen from the gasification agent reacts exothermally with CO and H_2 from the surrounding syngas (eq. 2.41 and 2.42). In the product gas, the water gas shift reaction is dominant (eq. 2.43):

$$H_2 + \frac{1}{2}O_2 \longrightarrow H_2O \tag{2.41}$$

$$CO + \frac{1}{2}O_2 \longrightarrow CO_2 \tag{2.42}$$

$$H_2O + CO \rightleftharpoons CO_2 + H_2 \tag{2.43}$$

Gas phase reactions of vaporized fuel components are more complex and depend on the fuel composition. Typically, large hydrocarbon molecules are cracked towards smaller hydrocarbons that can be directly oxidized or converted to syngas via reforming reactions with H_2O and CO_2. Depending on the reaction conditions and molecule structure, soot may form during this process. Reaction mechanisms for hydrocarbons under fuel rich conditions are for example discussed by Bockhorn [174]. Kathrotia et al. [175] and Hafner et al. [176] discuss the reactions of monoethylene glycol under fuel rich conditions, which is used as a surrogate fuel in this work.

At the high temperatures present in an EFG, oxidation reactions feature the highest reaction rates, followed by the water gas shift reaction. Decomposition and reforming reactions are typically slower. An overview about time scales of in-flame and post-flame reactions for autothermal methane reforming, which is comparable to EFG concerning reaction conditions, is given by Hunger et al. [177, 178].

Thermodynamics of Gas Phase Reactions

The thermodynamic state of a system can be described by the Gibbs Free Energy

$$G = H - T \cdot S \tag{2.44}$$

using the enthalpy H and entropy S of the system. For a multicomponent mixture of N species n_i, G can be expressed by

$$G(n_i,T) = \sum_{i=1}^{N} n_i \cdot \left(\Delta G_{f,i}^{\ominus} + RT\ln(p_i/p^+)\right) \tag{2.45}$$

featuring the Gibbs energy of formation $\Delta G_{f,i}^{\ominus}$, the reference pressure $p^+ = 1$ bar and the partial pressure p_i of component i [179, 180]. In chemical equilibrium, the differential of G for constant temperature, system mass and pressure is zero, which can be used to

calculate the equilibrium composition of the reaction mixture:

$$(\mathrm{d}G)_{T,p,m} = 0 \tag{2.46}$$

This procedure is also implemented in the model applied in this work (see section 4.3.2 for further details). When a mixture reacts to equilibrium under adiabatic and isobaric conditions, the resulting temperature is referred to as adiabatic equilibrium temperature T_{ad}.

Intermediate Species

The reactions discussed above involve numerous intermediate species that are formed and consumed along the process. While these species are typically not stable at ambient conditions, some (e.g. OH, H, and O) can exist in significant concentrations in chemical equilibrium at high temperatures in a flame.

The OH radical is produced during oxidation processes and is among the most well investigated flame intermediates. Reactions of OH formation during the oxidation of hydrocarbons and syngas are for example discussed by [181, 182]. A strong increase of equilibrium OH concentration with temperature is usually reported [183]. OH has been widely used in flame structure analysis and is typically measured by laser induced fluorescence (LIF, see section 3.3.1) [184–187]. Under non-premixed conditions, OH is mostly found at the interface between oxidizer and fuel gas and marks the transition from unburned to burned gases in the flame (see section 2.2.7 and Fig. 2.6). Examples and additional details on the interpretation of OH-LIF signals as flame front marker are provided by [187–192]. The suitability of OH as a marker for heat release has been discussed but was found to be limited without further information on other intermediate concentrations [193, 194]. Several studies also applied OH as a spatial marker for the oxidation zone in rich inverse diffusion flames [178, 195–197], which is of special relevance for this work.

2.2.7 Flame Stabilization

Flame Fronts

Flames can be distinguished in premixed flames, where combustible gas and oxidizer have been homogeneously mixed before reaction, and non-premixed flames, where both gases are separate and the reaction occurs at the interface of both streams. In premixed flames, the propagation of the flame front is determined by the interaction of chemical kinetics and diffusive processes within the reaction mixture, which is characterized by the laminar flame velocity Λ_{f}. In non-premixed flames, mass transport of oxidizer and combustible

gas towards the flame front is the defining mechanism for the flame structure [92, 113, 179, 198]. The flame in an EFG reactor can as a first approximation be regarded as non-premixed.

Fig. 2.6 shows schematic profiles of relevant species concentrations, mixture fraction

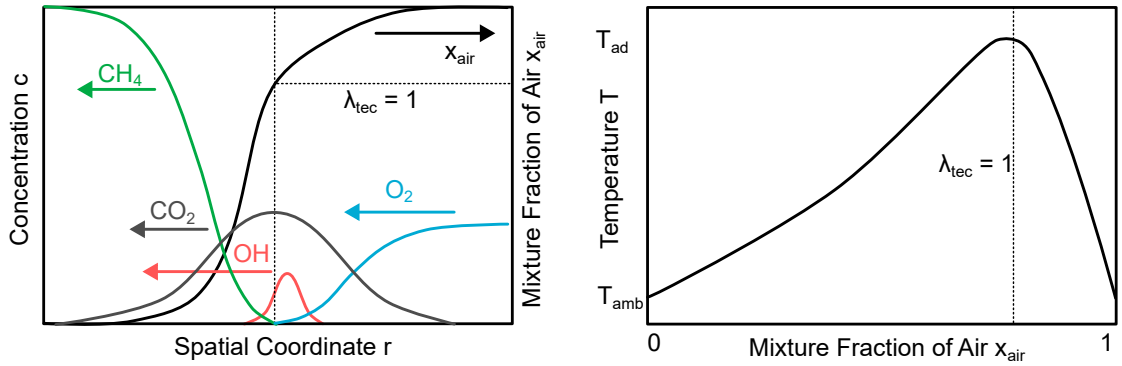


Figure 2.6: Example Flame Front in a laminar CH4 - Air

and temperature around the flame front of an exemplary laminar non-premixed CH_4 - air flame. The reaction takes place in a narrow zone where the mixture of both streams is stoichiometric ($\lambda_{tec} = 1$). Oxidizer and combustible gas are transported by molecular diffusion towards this flame front where they are consumed, whereas product gases formed in the flame front diffuse away in both directions. The gradients of the species induced by the chemical reactions are the driving force for species transport, which in turn determines reaction rate. The heat released by the reaction leads to a temperature maximum near the flame front. Due to the high temperatures and ongoing chemical reaction, intermediate species like OH exist in a limited space around the flame front. These can then be used as diagnostic markers (see sections 2.2.6 and 3.3.1). For the description of non-premixed flames, the assumption that chemical reactions are fast compared to mixing (*»mixed = burned«*) can often be applied as a good approximation, allowing the use of equilibrium chemistry. For further information, the reader is referred to the respective literature literature [92, 113, 179, 198]

Turbulent Jet Flames

Due to the relevance of mixing of oxidizer and combustible medium, the description of turbulent non-premixed jet flames is closely linked to the theory of turbulent jets (section 2.2.2). With the assumptions that (i) the transport of thermal energy proceeds with the same rate as the transport of species ($Le = 1$) and (ii) no heat loss through radiation

occurs, the enthalpy field in a turbulent jet is directly related to mixture fraction [179]:

$$x_{\mathrm{jet}}\left(\zeta,\eta\right)=\frac{h\left(\zeta,\eta\right)-h_{\mathrm{amb}}}{h_{\mathrm{jet}}-h_{\mathrm{amb}}}. \tag{2.47}$$

Together with the equilibrium chemistry assumption, species concentrations and temperature in a non-premixed jet flame are an exclusive function of mixture fraction. Based on this approach, different simple models and scaling laws for turbulent non-premixed jet flames based on gas momentum have been developed [113, 117, 118]. From thee models it can be derived that the length of an ideal turbulent jet flame scales linearly with the nozzle equivalent diameter (eq. 2.13, [118]).
However, flame phenomena like local extinction and flame liftoff cannot be modeled using the equilibrium chemistry assumption. Especially at higher turbulent mixing rates, the times scales of mixing and reaction become comparable and the assumption of equilibrium chemistry must be relaxed. More advanced approaches and concepts for these issues are reviewed in [92, 179].

Inverse Diffusion Flames

An *Inverse Diffusion Flame* (IDF) is a special configuration of a non-premixed flame where an oxidizer jet emerges into a combustible environment, in contrast to a *Normal Diffusion Flame* (NDF). This configuration has gained interest over the last years. The current state of research is summarized in the literature reviews by Hariharan et al. [199] and Zhen et al. [200]. However, most of the literature on IDF is of minor relevance for EFG conditions. The flame situation in an EFG reactor (see section 2.1.2) is characterized by (i) globally fuel rich conditions, (ii) high oxygen concentrations in the gas jet, (iii) high temperature of the combustible ambient atmosphere, (iv) turbulent flow, (v) superposition of the oxidizer jet with a fuel spray. There are no known studies conducted at well defined laboratory systems that take effects (i)-(iv) into account simultaneously. Further, there are no known publications on laboratory systems for IDF combined with aspect (v).
Studies within the scope of this work are provided by [201–205] where the effect of oxygen enrichment on the structure of IDFs is investigated within the context of autothermal methane reforming. Li et al. [67, 204] and Richardson et al. [206] investigate the structure of fuel rich IDFs in a high temperature surrounding atmosphere. It is shown that under the conditions relevant for autothermal methane reforming, which are comparable to EFG, the high temperature surrounding gas leads to a flame stabilization by autoignition [204]. Hunger et al. [178] compare a fuel rich, turbulent, oxygen enriched IDF and an analogous NDF in detail using LES. It was shown that although the stoichiometric mixture fraction of jet medium changes through inversion of the streams, the same flame structure emerges as long as the flow remains in the turbulent regime. Stelzner et al. [195, 207] investigate a fuel rich, oxygen enriched, laminar IDF using OH-LIF, focusing on

temperature measurements and the relationship between temperature and OH concentration. It is shown that due to the oxygen enrichment, temperatures up to 3000 K can be reached. Rabee et al. [208] shows that for fuel rich turbulent IDFs, a linear relationship of flame length and nozzle diameter is observed analogously to normal jet flames (see above).

Spray Flames

The main difference between spray flames and gas flames is that in a gas flame, the fuel is directly available for reaction, whereas in a spray flame, fuel droplets first need to evaporate to enable a reaction (see section 2.2.3). This leads to different flame structures and stabilization mechanisms than for gas flames. Spray flames can typically be considered to be of predominantly non-premixed character but can also feature local zones of premixed combustion [91].

The presence of a second phase makes spray flames considerably more complex than gas flames. Effects of droplet inertia on the gas velocity field and volume expansion by evaporation need to be considered when modeling spray flames. Turbulence properties of the gas phase that impact mixing of reactands are also affected by droplets (see section 2.2.2). Local stoichiometry is strongly influenced by the unsteady local dispersion of droplets [91, 93, 209]. A detailed overview of the effects occuring in spray flames and corresponding modeling approaches is provided in the reviews by Kuo [92], Jenny et al. [91] and Brito Lopes et al. [210]. Modeling spray combustion is still an active area of research.

3 Experimental Facilities and Methods

This chapter describes the experimental facilities for the gasification and atomization experiments (sections 3.1 - 3.2), as well as the diagnostics and data evaluation methods applied in this work (section 3.3). The description and operating conditions of the individual experimental datasets are given in section 3.4.

3.1 Research Entrained Flow Gasifier REGA

The gasification experiments were carried out at the Research Entrained Flow Gasifier REGA. The plant has been detailed in various publications [8, 13, 15], thus only a brief description will be given here.

The gasifier consists of a ceramic tube featuring an inner diameter of $d = 280$ mm and a length of $L = 3.1$ m. The plant is typically operated at fuel mass flows around $\dot{m}_{\text{fuel}} \approx 10$ kg/h, resulting in an input thermal power of $P_{\text{fuel}} \approx 50 - 100$ kW, depending on the fuel. The ceramic refractory lining is electrically heated to a temperature of $T = 1200$ °C and surrounded by a thermal insulation and a steel containment. A schematic of the upper reactor section is shown in Fig. 3.1, a detailed sketch of the entire reactor is provided in A.1.

The gasifier can be operated on liquid and suspension fuels that are fed to the reactor via an external mixing twin fluid nozzle. The burner nozzle is embedded in a burner plate made of the same ceramic material as the refractory lining. Fuel flow is controlled using a progressing cavity pump and a Coriolis mass flow meter. Oxygen enriched air is applied as gasification medium, which is fed to the burner nozzle along the liquid fuel stream in a twin fluid lance (see section 3.4). Fuel and gasification agent enter the reaction chamber and form a product gas, which is cooled down at the reactor outlet by a heat exchanger and a water quench, after which it is burned in a flare. Gas samples are continuously taken at the reactor outlet and analyzed in standard gas analytics provided by ABB in order to measure concentrations of permanent gases (H_2, CO, CO_2, CH_4, O_2). The elemental balancing is described in [8].

Due to safety reasons, the plant is operated at $\Delta p = 1$ to 2 mbar below atmospheric pressure in order to avoid leakage of syngas into the ambience. The operation near atmospheric

pressure facilitates detailed diagnostic access to the reactor volume by access ports at different levels along the reactor axis (E0 - E3, see 3.1). The access ports can be equipped with nitrogen purged Quartz glass windows (Appendix A.1) for optical measurements or probes for invasive measurements. The layout of the ports allows optical measurements in angles of 180°, 110°, 90°and 70°. The burner plate is movable in axial direction, which enables measurements over the entire main reaction zone.

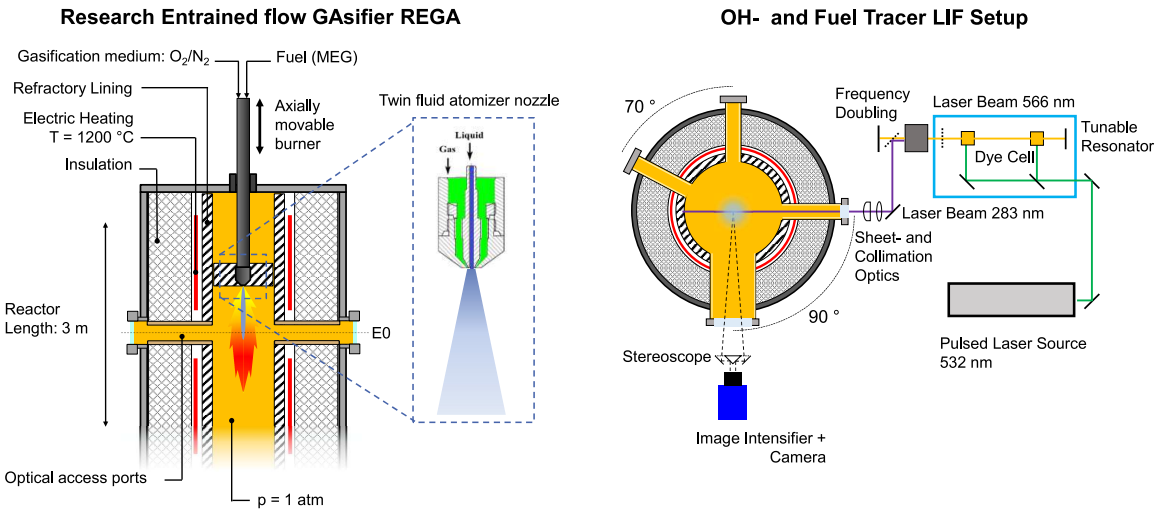


Figure 3.1: Sketch of REGA reactor (upper part) and OH-/Fuel-Tracer-LIF setup applied and this work. Modified from [15].

3.2 Atmospheric Spray Test Rig ATMO

Atomization experiments under ambient conditions were performed at the Atmospheric Spray Test Rig ATMO, which has been described in prior publications [110, 167]. A twin fluid atomizer nozzle is mounted to an axially movable feeding lance. The liquid or suspension fuel is fed by a progressing cavity pump and controlled by a Coriolis mass flow meter. The atomization experiments are conducted using air. The spray emerges into the ambient atmosphere and is then analyzed using the diagnostic techniques described in the sections below. In order to avoid recirculation of droplets and gas, the two-phase flow is collected in an honeycomb structure below the measurement plane. A sketch of the plant is included in Appendix A.1.

3.3 Diagnostics

3.3.1 OH Laser Induced Fluorescence

A system for measuring laser induced fluorescence (LIF) of the OH radical was installed at the REGA plant over the course of this work. LIF allows the spatially resolved, non-invasive detection of reaction intermediates in low concentrations in-situ and is thus ideal for studying flames [211, 212]. This section first describes the physical principle of the OH-LIF measurement, followed by a description of the applied devices and an outline of the procedure for measurement and data evaluation. The relation of OH to the processes in the flame has been elaborated in the respective Fundamentals section 2.2.6.

Measurement Principle

The measurement principle of OH-LIF is the electronic excitation of OH molecules by absorption of photons from a laser pulse, which is followed by the detection of the resulting photon emission through fluorescence by a camera system. In a diatomic molecule like OH, rotational, vibrational and electronic states can be excited by incoming photons. During a LIF measurement, the wavelength of a laser source is tuned to match the energy of a selected transition of states in the target molecule. As OH-LIF is a well established and widely applied method in combustion diagnostics, the reader is referred to literature for details [186, 211, 212]

According to fluorescence theory, at excitation laser fluences F_0 sufficiently below saturation, the intensity of the fluorescence signal measured by the detection optics I_{LIF} originating from an illuminated volume V_{det} is given by

$$I_{\mathrm{LIF}} = V_{\mathrm{det}}\ F_0\ N_1^0\ B_{12}\ c_i \cdot \frac{A_{21}}{A_{21}+Q_{21}} \cdot \frac{h\ \nu}{c} \cdot \frac{\Omega}{4\ \pi} \cdot \eta_{\mathrm{opt}}. \tag{3.1}$$

The first term of this expression describes laser absorption by the molecules, with the Einstein coefficient for absorption B_{12}, the population density of the ground state N_1^0 and the number density of the absorbing molecule c_i. The middle term is referred to as fluorescence quantum efficiency and contains the spontaneous emission rate constant A_{21} and the collisional quenching rate constant Q_{21}. The last term represents the signal detection, where $h\nu/c$ is the emitted photon energy, Ω is the collection solid angle and η_{opt} is the efficiency of the detection optics [185, 186, 211].

Measurement Uncertainties

According to eq. 3.1, the measured signal intensity I_{LIF} is linearly proportional to the number density c_i of the target species i. Thus, a quantitative measurement of OH

concentration is possible if the other parameters are known. B_{12}, A_{21} and ν are quantum properties that only depend on the energy levels of the respective transition and are tabulated [186].
The ground state population density N_1^0 is temperature dependent and can be described by a Boltzmann distribution [186]. This temperature dependency can be minimized for a given temperature range by selecting an appropriate ground state, which is described in [177] for oxygen-rich inverse diffusion flames in a similar temperature range. In accordance with this investigation, the rotational $Q_1(8)$-line of the vibrational (1-0)-band of the electronic $A^2\Sigma X^2\Pi$ transition at a wavelength of $\lambda_{\text{laser}} \approx 283.55$ nm was selected, which exhibits a temperature variation of 7 % in the temperature range of 2000-2800 K.
The parameters η_{opt}, Ω and V_{det} can be obtained in different ways, most simply by a calibration experiment featuring a known OH concentration using the measurement setup [192].
The most difficult effect to quantify is the process of collisional quenching described by Q_{21}, which is dependent on the collision rate of the OH molecules with the other gas phase species depending on pressure, temperature and their mole fractions [186, 211, 213, 214]. Quantifying this effect in-situ would either require steady state conditions like in a laminar flame [182, 185, 186] or require a simultaneous measurement of temperature and species concentration in a turbulent flame [215–217]. Methods requiring additional data input from simulations [218] have also been reported. In this work, the influence of collisional quenching on the measured signal has been quantified in Appendix A.3 using data from 2-Ph-FJM calculations.
Another source of uncertainty is the absorption of laser light, which affects F_0, and fluorescence light, which additionally decreases η_{opt} [192]. This may be caused by spray droplets, solid fuel particles, soot and fouling of the optical access windows.
As detailed by [192], most relevant information for flame analysis can already be obtained using qualitative OH-LIF measurement without determining absolute concentrations. As a consequence of the reported limitations, a quantitative calibration of the OH measurement was thus not attempted in this work.

Optical Setup

The measurements were carried out using an optical setup provided by *LaVision*. A schematic of the setup at the REGA plant is shown in Fig. 3.1. A pulsed, frequency doubled Nd-YAG laser (*Quantel Q-smart 850*) was coupled into a frequency doubled tunable dye laser (*Sirah Cobra-Stretch*) using Rhodamine 6G as laser medium to create a laser wavelength of $\lambda_{\text{laser}} \approx 283.55$ nm. The output energy of the dye laser was determined to be $E_{\text{laser}} \approx 20$ mJ per pulse at a pulse frequency of $f_{\text{laser}} = 10$ Hz. The beam was steered through a cylindrical lens optics and a collimator optics, resulting in a laser sheet with a height of 50 mm and a width of 0.5 mm. The laser sheet was steered into the

reactor at measurement plane E0 (see Fig. 3.1) and adjusted to the centerline of the gas jet emerging the burner nozzle. Fluorescence was measured in a 90°angle to the measurement plane using an image intensifier (*LaVison IRO)* and a CMOS camera (*Lavision Imager M-lite 2M*) applying a gate time of 50 ns. The image intensifier was equipped with an UV objective and a bandpass filter featuring a transmission of 320 nm/40 nm FWHM. The spatial resolution of the detection optics was determined to be 132 x 132 µm.

Measurement and Data Evaluation Procedures

Before each flame measurement, the position of the laser sheet relative to the gas jet in the reactor and the laser pulse energy E_{laser} were checked. Since the wavelength calibration of the tunable dye laser is highly sensitive towards changes in internal beam steering and temperature, the tunable optics were recalibrated before each flame measurement using a peakfinding scan. During a flame measurement, the burner was axially moved in 20 mm steps, while taking one set of images at each position. An image set consists of 500 images of each (i) fluorescence images at the $Q_1(8)$-line at a wavelength of $\lambda_{\text{laser}} \approx 283.55$ nm, (ii) offline images with laser excitation at $\lambda_{\text{laser}} \approx 283.51$ nm and (iii) background images without laser illumination.

For data evaluation, the single images in each set were averaged. In order to remove the background signal and possible fluorescence of trace components other than OH from the measurement signal, the averaged offline and background images were subtracted from the averaged OH fluorescence images. The OH-images were then smoothed and corrected for spatial inhomogeneities in laser sheet and camera sensitivity using standard procedures [219]. The OH-images of each burner position were combined to yield an image of the entire reaction zone. The OH-LIF intensity I_{LIF} was used to determine longitudinal extension L_{OH} and volume V_{OH} of the OH zone using a procedure described in section 4.3.5.

3.3.2 Fuel Tracer Laser Induced Fluorescence

Measurement Principle

Fuel-Tracer LIF (FT-LIF) is a diagnostic technique that has been widely applied for investigation of mixing and reaction processes in single- and two-phase systems. The theory and applications of the method are reviewed in detail by Fansler et al. [220] and Schulz and Sick [219]. In FT-LIF, the fuel stream (gaseous or liquid) is doped with a molecule featuring known fluorescence characteristics at a predefined concentration (*tracer*). The spatial distribution of fuel in the investigated system can then be derived from the spatial distribution of the tracer molecule, which is detected by laser induced fluorescence. In this work, FT-LIF of the liquid fuel phase was conducted. The physical fundamentals of liq-

uid phase fluorescence are similar to fluorescence in the gas phase described in section 3.3.1.

Measurement Uncertainties

Ideally, the FT-LIF signal is proportional to the number of tracer molecules in the excitation volume and thus also proportional to the local concentration of fuel. Quantitative measurements are possible, as for example shown by [221–227]. Several additional factors must be considered in measurements of liquid phase FT-LIF in comparison to measurements in the gas phase. (i) The curved gas-liquid interface of droplets can lead to non-linear effects like scattering of light, droplet lensing or morphology dependent resonances, causing measurement errors. This affects dense sprays featuring fine droplets as for example present in internal combustion engine systems, but becomes less relevant in dilute sprays [220, 228–231]. (ii) Due to the higher rate of molecule collisions in the liquid phase in comparison to the gas phase, fluorescence quenching plays a major role in liquid phase LIF. A consequence is that the fluorescence spectrum and fluorescence quantum yield of the tracer strongly depends on the chemical composition of the liquid phase it is dissolved in [232]. Quenching typically also causes a strong temperature sensitivity of fluorescence quantum yield in liquid systems that must be accounted for [220, 233, 234]. (iii) For quantitative measurements in evaporating systems, it must be ensured that tracer and fuel have similar vapor pressures and that the fluorescence signal of gas and liquid phase can be spectrally separated [220, 235–237]. Sophisticated detection techniques applying so-called exciplex-substances have been developed for this purpose, but are currently limited to gasoline and diesel surrogates [220]. A different strategy is to use a tracer with negligible vapor pressure that remains in the liquid phase. This eliminates signal interference from the gas phase but prohibits quantitative concentration measurements in evaporating system due to enrichment of fuel tracer in the droplets [238].

Measurement Approach and Optical Setup

In this work, Rhodamine 6G was applied as a fuel tracer because its fluorescence properties are well characterized and spectral data for solutions in MEG is available [232, 239, 240]. The substance class of Rhodamines has been successfully applied as fuel tracer for non-reactive as well as reactive conditions [234, 238, 241]. Rhodamine 6G features a negligible vapor pressure and is reported to thermally decompose at temperatures above 219 °C [240].

A tracer concentration of $c_{\mathrm{Rh6G}} = 10^{-6}$ mol/l was applied in all experiments. Under reactive conditions, simultaneous measurements of OH and fuel tracer fluorescence were conducted applying the LIF setup described in section 3.3.1 using the same experimental procedure and measurement parameters. The emission spectra of OH and Rhodamine 6G are shown in Appendix A.3. To measure both fluorescence signals in separate spectral channels, a stereoscope (LaVision Image Doubler) was used, which was equipped with the

bandpass filter for the OH fluorescence and a bandpass filter (572 nm/33 nm FWHM) for the fuel tracer fluorescence. Spatial overlap of both signals was ensured by applying a calibration plate before the measurement. For the reasons described above, the measurements conducted under reactive conditions are of qualitative nature.

3.3.3 Phase-Doppler Anemometry

Droplet size and axial velocity were measured using a *DANTEC Dynamics SprayExplorer* system described in [242]. For the fundamentals of the Phase-Doppler Anemometry (PDA) technique, the reader is referred to the respective literature [243].
Measurements were conducted in forward scattering mode over an off-axis angle of 70°. Lenses featuring a focal length of 1000 mm for laser and receiver were applied. The receiver was equipped with a slit featuring a length of 200 µm and an asymmetric mask for high data rates in dense spray conditions and to reduce measurement errors due to the Gaussian beam effect [243]. This configuration was able to detect droplet sizes ranging from $d = 1$ µm up to $d = 1357$ µm for MEG. PDA measurement parameters were determined in a sensitivity study. Further system specifications and instrument settings are given in Appendix A.3.
To enable the measurement of radial profiles of droplet size and axial velocity in the spray, the system was mounted on a traverse system with a spatial accuracy of < 0.1 mm. Radial profiles were recorded from r = -40 mm to 40 mm in steps of 4 mm. In order to provide a statistically relevant sample, a measurement time of 60 seconds was applied at each position to ensure the detection of 50000 droplets when possible. As the data rate diminishes in the outer spray region, only measurements with at least 5000 droplets were taken into account in the data evaluation.
For each axial position in a dataset, one full radial profile and two half profiles were recorded. Under reactive conditions, only one full profile was measured. At each measurement point of a radial profile, a number based droplet size distribution Q_0, a volume based droplet size distribution Q_3 and the Sauter mean diameter d_{32} were evaluated. For each radial profile, the integral Sauter mean diameter ID_{32} was calculated (see eqs. 2.8-2.10). A modified version of the *SprayCAT* routine described in [110] was applied in the evaluation. Mean axial droplet velocities weighted by droplet number and droplet mass were calculated at each measurement point. Velocity profiles along the jet axis were used to calculate droplet residence times using eq. 2.25 assuming a linear trajectory and a linear interpolation of droplet velocity between measurement points using $u_{liq,0}$ at the nozzle outlet as starting value.

3.3.4 High Speed Imaging and Shadowgraphy

In order to qualitatively characterize the sprays, images of the nozzle near region were recorded using a high speed camera (*Vision Research, Phantom v1840*). The camera was mounted at the Atmospheric Spray Test Rig ATMO. A section of 74 x 74 mm below the nozzle exit was recorded with a resolution of 1007 x 1007 pixels at a frame rate of 8000 fps and an exposure time of 2 µs. Backlight illumination was provided using an LED array with a light intensity of 100 000 Lumen.
For the quantitative droplet size measurement using shadowgraphy reported in section 3.4.3, the intensified relay optics (IRO) was equipped with a far field microscope (*DANTEC Dynamics*) while keeping the backlight illumination. This was done because the opaque suspension fuels could not be investigated using the PDA system. The resulting measurement area accessible by the shadowgraphy setup spanned a range of 3.2 x 3.2 mm with a spatial resolution of 3.1 µm / pixel. 300 images were recorded with a frame rate of 50 fps at an axial nozzle distance of z = 100 mm. An image evaluation routine described by Sänger [110] was applied to calculate droplet size distributions from the image sets. The system was calibrated using a calibration plate and tested using a monodisperse droplet generator. The minimum detectable droplet size using this method was determined to be 30 µm. Further validation was conducted at a MEG spray, where the droplet size distribution measured by Shadowgraphy was compared to a droplet size distribution determined using the PDA system under the same conditions (see Appendix A.3).

3.3.5 Mechanical Patternator

Radial distribution of liquid mass flux ϕ_{liq} in sprays was measured under ambient conditions applying a mechanical patternator initially presented by Hotz [13]. The mechanical patternator is a linear array of 62 chambers featuring a width of 4.9 mm, a length of 6.2 mm and a height of 150 mm. The chambers are separated by walls of 0.25 mm thickness. At the beginning of a measurement, the patternator is positioned below the nozzle with the chambers closed by a cover panel. When liquid and gas mass flows reach steady state, the patternator is uncovered until at least one chamber is filled with liquid by 90 %. The patternator is then covered again. 3 Measurements are conducted and averaged for each experimental case. The measurement time t and the liquid height h in each chamber are used to determine the local mass flux [13]:

$$\phi_{\mathrm{liq}}(r) = \frac{h(r) \cdot \rho_{\mathrm{liq}}}{t} \tag{3.2}$$

As the system measures mass flow per area, the area of the chamber does not occur in the equation. The measured radial profiles are fitted by a logistic distribution:

$$\phi_{\mathrm{liq}}(r) = A \cdot \frac{e^{-\xi}}{\left(e^{-\xi}+1\right)^2}, \text{ using } \xi = \frac{r-\Delta r}{w}. \tag{3.3}$$

The parameters A and w are the amplitude and the width of the distribution. The fit function is corrected for the center offset from zero, Δr, and then used to determine the integral mass flow:

$$\dot{m}_{\mathrm{liq}}(r) = \int_0^r \phi_{\mathrm{liq}}(r) \cdot r \, dr. \tag{3.4}$$

The total mass flow $\dot{m}_{\mathrm{liq}}(r \to \infty)$ is used to quantify the measurement error by a mass balance. The normalized mass flow $\dot{m}_{\mathrm{liq}}(r)/\dot{m}_{\mathrm{liq}}(r \to \infty)$ is used to determine the angle $\theta_{0.9}$ that contains 90 % of the spray mass:

$$\theta_{0.9} = 2 \cdot \arctan\left(\frac{r_0}{z}\right), \text{ where } \frac{\dot{m}_{\mathrm{liq}}(r_0)}{\dot{m}_{\mathrm{liq}}(r \to \infty)} = 0.9. \tag{3.5}$$

The evaluation procedure is shown for an example dataset in Fig. 3.2.

In order to derive input data for the extended 2-Ph-FJM, the logistic distributions derived

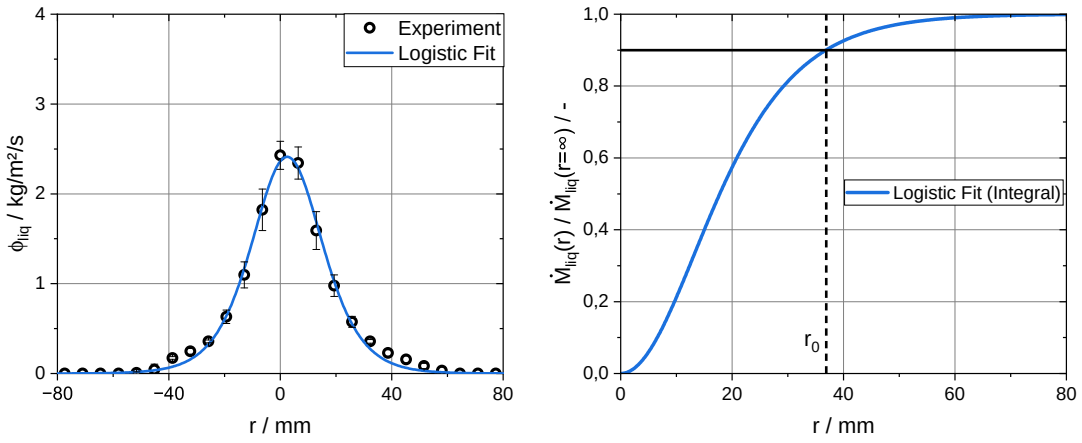


Figure 3.2: Example dataset of measured radial mass flux distribution and logistic fit (left) and determination of spray angle (right). Case MEG-A, z = 100 mm

from the experiments were corrected for the mass balance error by modifying the amplitude A, which keeps the shape of the distribution including spray angle $\theta_{0.9}$ intact. Validation data for this approach under ambient conditions is presented in Appendix C.2.4.

3.3.6 Gas Temperature Measurement

Radial profiles of gas temperature T_{gas} were measured using type B thermocouples. The thermocouples were inserted into the reactor using a ceramic rod. At each radial position, temperature data were averaged over a time of 30 s. Due to the high temperatures in the gasifier, radiation effects are relevant for invasive temperature measurement. To take this into account, a method developed by Fischer was used [244, 245], applying a double bead thermocouple with bead diameters of 300 and 1500 µm. In the calculation, a wall temperature of 1473 K was assumed to correct the measured values for radiation.

3.4 Burner Nozzles and Operating Conditions

For fuel feeding, external mixing twin-fluid atomizer nozzles were applied. The liquid fuel is fed as a central jet while the gasification medium enters the reactor through a surrounding annulus (see Fig. 3.3). Three nozzles were applied. The liquid jet width d_{liq}, gas exit angle α and the wall thickness between gas and liquid s were constant for all nozzles. The three nozzles are distinguished by their width of the gas annulus d_{gas}, which leads to different gas exit areas and results in different nozzle equivalent diameteres (**Nozzle A**: $d_{eq,geo} = 6.5$ mm, **Nozzle B**: $d_{eq,geo} = 4.3$ mm, **Nozzle C**: $d_{eq,geo} = 5.0$ mm, see eq. 2.14). Detailed technical drawings of the nozzles are presented in Appendix A.2. Three experimental datasets were produced in this work. The operating conditions are presented in the following.

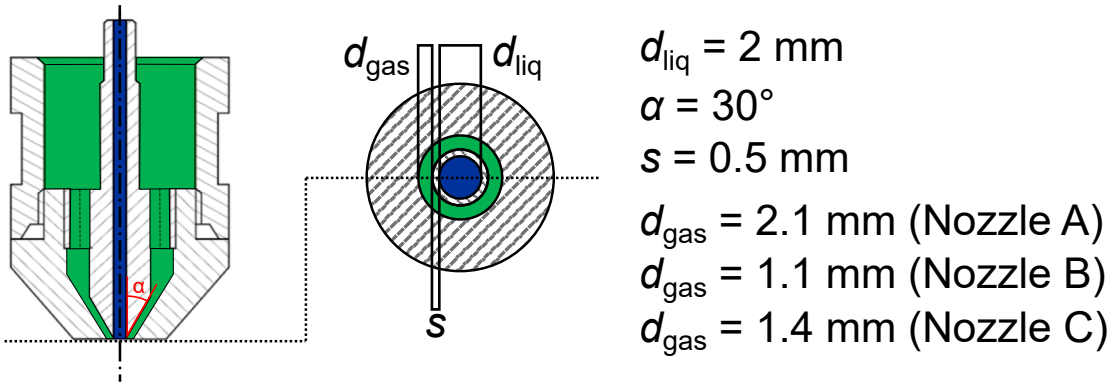


Figure 3.3: Sketch and characteristic parameters of the burner nozzles applied in this work. Gas (green) and liquid (blue) channels are marked.

3.4.1 Dataset MEG

The **MEG**-dataset was generated for detailed assessment of reaction zones and fuel evaporation in the EFG flame and is used in chapters 5.1 and 5.2. The complete experimental data is given in Appendix D.1. The **MEG**-dataset consists of two experimental cases featuring nozzles **A** and **B** (see Table 3.1). Monoethyle glycol (MEG) was applied as fuel with a liquid mass flow of $\dot{m}_{\mathrm{fuel}} = 12.4\,\mathrm{kg/h}$. MEG ($C_2H_6O_2$) is a monocomponent fuel featuring a boiling point of 196°C and a viscosity of 21 mPas at ambient conditions. MEG was chosen as a model fuel because of its optical transparency, low sooting tendency and a elemental composition which is similar to biogenic pyrolysis oils [8]. Additional fuel properties of MEG are given in Appendix B. The fuel was gasified applying a O_2/N_2-mixture at a volume flow of $\dot{V}_{\mathrm{GA,STP}} = 7.5\,\mathrm{m^3/h}$ and an oxygen content of $y_{\mathrm{O2,GA}} = 69\%$, resulting in an adiabatic equilibrium temperature of $T_{\mathrm{ad}} = 1700\,^{\circ}\mathrm{C}$ ($\lambda_{\mathrm{tec}} = 0.47$).
Under reactive conditions, spatial distributions of OH and liquid fuel were detected using OH- and Fuel-Tracer-LIF from the nozzle exit up to a nozzle distance of z ≈ 300 mm. Spray images were taken using the LIF-setup without bandpass filters and laser excitation. Gas temperatures were measured by double-bead thermocouples at z = 300 mm for **MEG-A** and z = 150, 200, 300 mm for **MEG-B**. For both cases, radial profiles of droplet size and droplet velocity were measured by PDA for z = 20 - 250 mm under gasification conditions. Syngas composition at the reactor outlet was measured using the standard analytics described above.
Under ambient conditions, a qualitative characterization of the primary jet breakup was conducted using the high speed camera. Radial profiles of droplet size and droplet velocitiy were measured by PDA for z = 50 - 250 mm for model input and comparison to the reactive data. Radial distributions of spray mass flux ϕ_{liq} for z = 50 - 250 mm were obtained in patterantor experiments.

3.4.2 Dataset GLYCEROL

The **GLYCEROL**-dataset was designed to vary spray parameters independently from gas momentum flow, in order to separately investigate their influence on the EFG flame. Based on the spray characterization experiments, experimental cases were selected to decouple the influence of the burner related parameters on the flame. This dataset also serves as the basis for the modeling study presented in chapter 5.1. The complete experimental data is given in Appendix D.2.
Glycerol ($C_3H_8O_3$) is a monocomponent fuel featuring a boiling point of 290 °C and a viscosity of 1412 mPas at ambient conditions. Glycerol was used as a model fuel due to its high temperature sensitivity of viscosity and an elemental composition similar to MEG

(see Appendix B). Liquid feed temperature T_{liq} was varied between 45 °C and 70 °C in order to modulate feed viscosity between 200 mPa · s and 50 mPa · s (see Appendix B). Feed temperature was controlled by a thermocouple placed in the liquid feeding channel 35 mm upstream of the nozzle exit. In order to minimize the impact of temperature deviations in the feeding system on viscosity, feed temperature was kept constant in a range of ±1.5 °C around the respective setpoint.
A liquid mass flow of $\dot{m}_{\mathrm{fuel}} = 13.2$ kg/h and gasification agent volume flow of $\dot{V}_{\mathrm{GA,STP}} = 7.5\,\mathrm{m^3/h}$ featuring an oxygen content of $y_{\mathrm{O2,GA}} = 71\%$ were applied ($\lambda_{\mathrm{tec}} = 0.47$). These conditions result in an adiabatic equilibrium temperature of $T_{\mathrm{ad}} = 1700\,°\mathrm{C}$. Based on these conditions, the set of experimental cases given in Table 3.2 is defined.
In the gasification experiments, flame structure was measured in an area of z = 0 - 330 mm using OH-LIF. Experiments under ambient conditions involved measurement of radial profiles of droplet velocity and droplet size in an axial nozzle distance of z = 100 mm, patternator measurements at z = 100 mm, and high speed camera imaging of the primary breakup.

3.4.3 Dataset SLURRY

The **SLURRY**-dateset provides a basis to study the flame structure of suspension fuels under gasification conditions. The dataset is discussed in section 5.3. The full data is provided in Appendix D.3.
In this series of experiments, reference suspensions consisting of MEG and 3 different beech-wood chars were used. These fuels are selected because MEG is a well defined monocomponent substance that does not exhibit formation of solids through pyrolysis reactions prior to evaporation, while the char does not show any caking behavior during conversion (see section 5.3). The chars BWC-A, BWC-B and BWC-C are different size fractions of a commercially available char originating from the pyrolysis of beech-wood (*Holzkohleverarbeitung Schütte*). The suspensions were stirred continuously during the experiments. Char BWC-A ($d_{32,\mathrm{sol}} = 9$ µm) was used to vary solid mass fraction in the suspensions, ranging from $x_{\mathrm{sol},0} = 0$ (pure MEG) up to $x_{\mathrm{sol},0} = 30\%$ (see Table 3.3). At $x_{\mathrm{sol},0} = 30\%$, the char particle size was varied by additionally using suspensions of BWC-B ($d_{32,\mathrm{sol}} = 4$ µm) and BWC-C ($d_{32,\mathrm{sol}} = 19$ µm). Data on chemical properties and particle size distribution of the chars are provided alongside rheological data of the suspensions in Appendix B.
The input conditions for the gasification of the suspension fuels were derived from case S0, which features the same input conditions as the cases in the **MEG**-dataset. As elemental composition and heating value of the suspension varies with char content, the suspension cases were adapted from case S0 in order to keep gas momentum flow, adiabatic equilibrium

temperature (T_{ad} = 1700°C) and reactor residence time (τ_R = 3.2 s) constant. The oxygen content in the gasification agent and to a lesser extent fuel mass flow were thus adjusted (see B.3).
For all cases, flame structure was measured in an area of z = 0 - 330 mm using OH-LIF. Under ambient conditions, liquid mass flux distributions were determined by Patternator. As PDA could not be applied in this dataset due to the opaqueness of the suspensions, droplet size was measured using Shadowgraphy.

Table 3.1: Case names, applied nozzles and operating conditions of experimental cases in the **MEG**-dataset. Input gas volume flow is $\dot{V}_{GA,STP}$ = 7.5 m³/h for all cases.

Case	Nozzle	d_{eq} / mm	J_{gas} / kg m/s²	$u_{GA,0}$ / m/s	$\dot{m}_{fuel}$ / kg / h	$y_{O2,GA}$ / %	λ_{tec} / –
MEG-A	A	6.5	0.20	69	12.4	69	0.465
MEG-B	B	4.3	0.45	156			

Table 3.2: Case names, applied nozzles and operating conditions of experimental cases in the **GLYCEROL**-dataset. Input gas volume flow is $\dot{V}_{GA,STP}$ = 7.5 m³/h for all cases.

Case	Nozzle	d_{eq} / mm	J_{gas} / kg m/s²	$u_{GA,0}$ / m/s	$\dot{m}_{fuel}$ / kg / h	$y_{O2,GA}$ / %	λ_{tec} / –	T_{liq} / °C	η_{liq} / mPa · s
A50								70	≈ 50
A100	A	6.5	0.20	69	13.2	71	0.471	57	≈ 100
A200								45	≈ 200
B50								70	≈ 50
B100	B	4.3	0.45	156	13.2	71	0.471	57	≈ 100
B200								45	≈ 200

Table 3.3: Case names, fuel parameters, operating conditions and nozzle parameters for the **SLURRY**-dataset. Input gas volume flow is $\dot{V}_{\mathrm{GA,STP}} = 7.5\ \mathrm{m^3/h}$ for all cases.

Case	Char	$\frac{d_{32,\mathrm{sol}}}{\mu\mathrm{m}}$	$\frac{x_{\mathrm{sol},0}}{-}$	Nozzle	$\frac{d_{\mathrm{eq}}}{\mathrm{mm}}$	$\frac{J_{\mathrm{gas}}}{\mathrm{kg\,m/s^2}}$	$\frac{u_{\mathrm{GA},0}}{\mathrm{m/s}}$	$\frac{\dot{m}_{\mathrm{fuel}}}{\mathrm{kg\ /h}}$	$\frac{y_{\mathrm{O2,GA}}}{\%}$	$\frac{\lambda_{\mathrm{tec}}}{-}$
S0	none	-	0	C	5.0	0.34	116	12.4	69	0.465
S10-A	BWC-A	9	10					12.5	72	0.447
S20-A	BWC-A	9	20					12.6	75	0.431
S30-A	BWC-A	9	30					12.7	77	0.417
S30-B	BWC-B	4	30					12.7	77	0.417
S30-C	BWC-C	19	30					12.7	77	0.417

4 2-Phase Free Jet Model

For theoretical investigations of the flame zone, a 2-Phase Free Jet Model (2-Ph-FJM) is used, which was originally developed by Hotz based on theoretical considerations and experimental work [11–13]. The modeling concept and the original calculation procedure developed by Hotz are explained in sections 4.1 and 4.2.
In this work, the model was expanded in order to investigate the conversion of liquid and suspension fuels in the EFG flame with respect to fuel composition and burner related process parameters. For this purpose, the model was improved regarding the following aspects:

- The description of the droplet injection was refined with respect to the radial distribution of liquid mass flux and droplet size, allowing the analysis of experimentally observed spray effects (section 4.3.1).
- The reaction model was expanded to a fuel flexible approach that also calculates intermediate species in chemical equilibrium (section 4.3.2). This enables a validation of the model using experimental OH-LIF data and provides the ability for a variable input fuel composition.
- An additional solid fuel phase was implemented in the model. Accompanied by the implementation of solid kinetics and appropriate droplet conversion models, this extension allows to study the conversion of suspension fuels in the EFG flame (sections 4.3.3 and 4.3.4).

4.1 Model Concept

The 2-Ph-FJM is a two-phase, steady state model based on the mathematical description of 2-phase free jets outlined in section 2.2.2. The model calculates fields of gas temperature, gas composition, gas velocity, and spray parameters in the jet dominated region based on input conditions given at the exit of the burner nozzle. In contrast to typical CFD models, the 2-Ph-FJM applies a simplified, semi-empirical description for the exchange of mass, momentum and energy and does not calculate these processes ab initio. The 2-Ph-FJM exclusively describes the flame zone and provides the advantage of substantially

reduced computing times in comparison to CFD models. The modular architecture of the 2-Ph-FJM allows to easily exchange and compare models for sub-processes within the model framework. This simplified and flexible approach enables sensitivity studies in order to analyze the response of the EFG flame towards changes in input conditions, identify relevant process parameters, evaluate sub-process models and generate a more profound understanding of the interaction of sub-process in the flame.

The model basis is provided by the description of two-phase free jets developed as an extension of the established single-phase free jet theory by Hotz (see section 2.2.2). In the 2-Ph-FJM, a jet of gasification agent originating at the nozzle exit expands into a surrounding atmosphere of syngas. The gas jet is mixed with the surrounding atmosphere and exchanges momentum, heat and mass with fuel droplets that are seeded into the gas jet using input conditions defined at the nozzle exit. The flow field in the recirculation zone is not resolved, instead, the surrounding atmosphere is assumed to be quiescent. This allows to describe the mixing processes using free jet equations. Sub-models for gas phase reaction and droplet conversion are added to this description (see section 4.2 below).
The simulation domain is divided into a grid of angular discretized radial segments using a nondimensional (ζ,η)-coordinate system from free jet theory (section 2.2.2). Geometry parameters are shown in Fig. 4.1. The inlet for gas and liquid phase is described as a circular orifice with an equivalent diameter d_{eq} (eq. 2.15). In this coordinate system, the free jet equations are applied to calculate the mixing of gaseous jet medium and ambient gas. Coefficients for turbulent exchange of momentum and mass for the gas phase were defined according to [12] based on the results of spray characterization experiments. In each radial segment, the liquid phase is introduced as droplet collective with a given droplet size distribution. Droplets are coupled to the gas phase via mass, momentum and energy balances. The droplets can move on fixed trajectories along their respective radial segment, where they heat up and evaporate (Fig. 4.1, left). Recirculation of droplets is not considered. Gas phase composition, temperature and velocity field as well as droplet temperature, velocity and mass are calculated in an iterative approach depicted in Fig. 4.1 (left). The procedure and the respective balance and transfer equations will be detailed in the following section.
The geometry of the surrounding environment determines the validity of the free jet assumption, which can, for the for the REGA plant, be applied up to a nozzle distance of around z = 0.4 m (see section 2.2.2). For larger nozzle distances, the flow field is influenced by the geometry of the reactor wall and the free jet description is no longer applicable. As global reactor variables like total fuel conversion, outlet syngas composition or reactor heat losses are highly influenced by processes outside the jet region, they cannot be predicted using the 2-Ph-FJM.

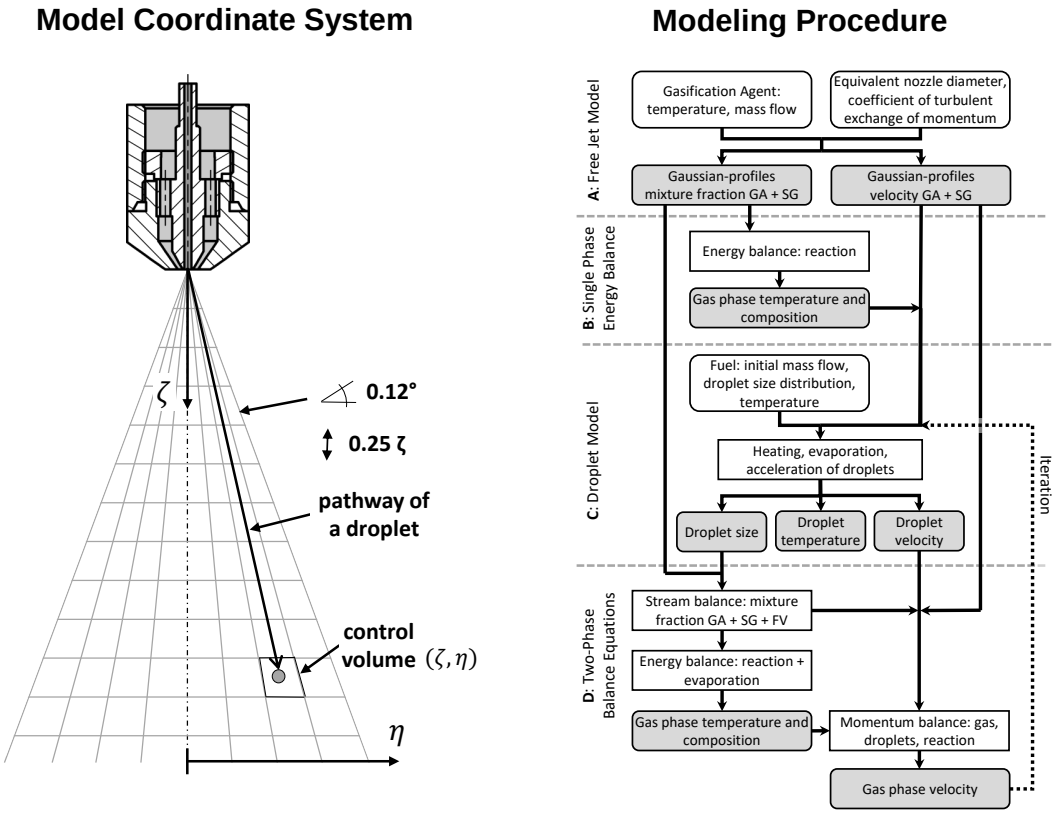


Figure 4.1: Modeling geometry (left) and calculation procedure (right) of the original 2-Ph-FJM, adapted from [11, 13].

4.2 Original 2-Ph-FJM by Hotz

The foundations and implementation of the original 2-Ph-FJM have been elaborated in great detail in [11–13], so the description in this work is reduced to the most relevant principles and equations. The theoretical fundamentals of two phase jets have been described in 2.2.2.

In a first step **A** in Fig. 4.1, mixing ratio and gas velocity are calculated for a non-reacting gas jet of gasification agent (GA) and a quiescent syngas atmosphere (SG) using the free jet equations (eqs. 2.19 and 2.21). In each control volume (ζ,η), a mixture fraction x_j is calculated for each stream $\dot{m}_j$:

$$x_j(\zeta,\eta) = \frac{\dot{m}_j(\zeta,\eta)}{\dot{m}_{\mathrm{GA}}(\zeta,\eta) + \dot{m}_{\mathrm{SG}}(\zeta,\eta)}. \tag{4.1}$$

In step **B**, the gas phase enthalpy h_{gas} in each control volume is calculated as

$$h_{\mathrm{gas}} = x_{\mathrm{GM}}(\zeta,\eta) \cdot h_{\mathrm{GM}} + x_{\mathrm{SG}}(\zeta,\eta) \cdot h_{\mathrm{SG}}. \tag{4.2}$$

with the enthalpy h_j of stream j given by

$$h_j = \sum_{i=1}^{N} y_{i,j} \left(\Delta h_{f,i}^{\ominus} + \int_{T_0}^{T} c_{p,i}\, dT \right) \tag{4.3}$$

For each of the N components i, the molar fraction in the stream j is given by $y_{i,j}$, standard heat of formation by $\Delta h_{f,i}^{\ominus}$ and isobaric heat capacity by $c_{p,i}$. In the original model, O_2, N_2, CO, CO_2, H_2 and H_2O are considered as gas phase species. The gasification agent consists of an O_2 / N_2 mixture at $T = 25\,°C$, the syngas entrained from the environment has the equilibrium composition of the input mass flows at reactor temperature $T = 1200\,°C$. In order to calculate the gas phase temperature and composition field in the first iteration, the oxidation of H_2 and CO and the WGS-reaction (eqs. 2.41 - 2.43 in section 2.2.6) are considered. Due to the high temperatures in the flame zone, the reaction rates are assumed to exceed the turbulent mixing rates. Thus, each control volume is modeled to be in chemical equilibrium (see section 2.2.7). The equilibrium reaction model assumes complete conversion of oxygen when reaction partners are available, followed by the water gas shift reaction being calculated from a temperature dependent equilibrium constant $K_p(T)$. Gas phase temperature and composition are calculated in an iterative approach under the constraint of the gas phase energy balance:

$$h_{\text{gas}} \stackrel{!}{=} \sum_{i=1}^{N} y_i h_i(T) \tag{4.4}$$

In the following step **C**, the liquid phase is taken into account. 50 discrete droplet size classes defined by a measured Q_3-distribution are fed to the individual trajectories (see Fig. 4.1). The original model assumes that the liquid phase in the jet is distributed proportionally to the gas phase. Before evaporation, the initial liquid mass flow in each control volume is thus given by

$$\dot{m}_{\text{liq}}(\zeta,\eta) = \frac{\dot{m}_{\text{GA}}(\zeta,\eta)}{\text{GLR}} \tag{4.5}$$

Starting at the nozzle exit $(0,\eta)$, droplets are accelerated along their respective trajectory through exchange of momentum with the gas phase. The initial momentum of the liquid phase is defined by the liquid velocity at the nozzle outlet $u_{\text{liq},0}$ given by liquid mass flow and nozzle geometry. Droplet velocities are calculated based on the gas phase mean velocity field from the prior step using a force balance regarding inertia and drag force (eqn. 2.24). The change of gas phase velocity via momentum transfer from the gas phase to the liqid phase is considered in the balance. Details on this aspect are given in [11, 13]. The effect of turbulence on droplet transport and interaction of closely spaced droplets is not accounted for by the model (see Appendix C.2.6).
Droplet heating and evaporation is described using the d^2-law outlined in section 2.2.3 using eqs. 2.29 and 2.30. During the evaporation process, the droplets transfer mass to

the gas phase. The liquid conversion X_{liq} is used to express the progress of evaporation along a trajectory η at a nozzle distance ζ:

$$X_{\mathrm{liq}}(\zeta,\eta) = \frac{\dot{m}_{\mathrm{liq}}(0,\eta) - \dot{m}_{\mathrm{liq}}(\zeta,\eta)}{\dot{m}_{\mathrm{liq}}(0,\eta)}. \tag{4.6}$$

In step **D**, fuel vapor is accounted for in the gas phase calculations. Considering eqs. 4.5 and 4.6, the mass flow of fuel vapor in the gas phase at a given position is expressed by

$$\dot{m}_{\mathrm{FV}}(\zeta,\eta) = \frac{\dot{m}_{\mathrm{GA}}(\zeta,\eta)}{\mathrm{GLR}} \cdot X_{\mathrm{liq}}(\zeta,\eta). \tag{4.7}$$

Since the gas phase now consists of gasification agent, syngas and fuel vapor, eqs. 4.1 and 4.2 are expanded to:

$$x_j(\zeta,\eta) = \frac{\dot{m}_j(\zeta,\eta)}{\dot{m}_{\mathrm{GA}}(\zeta,\eta) + \dot{m}_{\mathrm{SG}}(\zeta,\eta) + \dot{m}_{\mathrm{FV}}(\zeta,\eta)}, \tag{4.8}$$

$$h_{\mathrm{gas}}(\zeta,\eta) = x_{\mathrm{GM}}(\zeta,\eta) \cdot h_{\mathrm{GM}} + x_{\mathrm{SG}}(\zeta,\eta) \cdot h_{\mathrm{SG}} + x_{\mathrm{FV}}(\zeta,\eta) \cdot h_{\mathrm{FV}}, \tag{4.9}$$

$$h_{\mathrm{FV}} = \Delta h^{\ominus}_{f,liq} + \int_{T_0}^{T_{\mathrm{vap}}} c_{p,liq}\, dT + \Delta h_{vap,liq}. \tag{4.10}$$

The next step is to calculate gas phase composition and temperature for the reacting mixture containing fuel vapor. In the reaction model, fuel vapor is not considered as a gas phase species itself. Instead, a reaction equation for the decomposition of the fuel (MEG, in the present case) is applied, assuming instantaneous and complete conversion of MEG to the decomposition products:

$$\mathrm{C_2H_6O_2} \longrightarrow 2\mathrm{CO} + 3\mathrm{H_2} \tag{4.11}$$

The procedure to model the gas phase reactions described above is now repeated. Reaction induced changes in the gas phase molecule number and changes in temperature can lead to expansion of the gas phase volume, causing thrust. This affects the velocity field of the gas phase, which is considered in the original model by a thrust sub-model. Details on this are given in [11, 13].
As changes in gas phase velocity impact the movement of the droplets and their evaporation, steps **C** and **D** are iteratively repeated in the 2-Ph-FJM.

4.3 Extended 2-Ph-FJM

4.3.1 Radial Distribution of Liquid Mass Flux and Droplet Size

The first adaptation of the 2-Ph-FJM conducted in this work was the implementation of a variable radial distribution of liquid mass flux and droplet size. This modification has been published in [15]. In the original model, the initial droplet size distribution at $\zeta = 0$ was based on measured values and was the same for each trajectory. In the extended 2-Ph-FJM, each trajectory can be fed with an individual droplet size distribution and a variable fuel mass flux.
For this, in each trajectory the droplet size distribution is assumed as a Weibull-distribution using a scale parameter σ and a shape parameter of 2

$$Q_3(d) = 1 - \exp\left(-(\sigma \cdot d)^2\right). \tag{4.12}$$

The Weibull-distribution can be expressed as a function of Sauter mean diameter d_{32} with quantile diameters d_n representing the N = 50 droplet size classes:

$$Q_3(d) = 1 - \exp\left(-\left(\frac{d}{\sqrt{\pi} \cdot d_{32}}\right)^2\right) \tag{4.13}$$

$$d_\mathrm{n} = d_{32} \cdot \sqrt{-\pi \cdot \ln\left(1 - n/N\right)} \tag{4.14}$$

For modeling experimental datasets, the measured radial distribution of the d_{32} at z = 100 mm was used as input. The description of the experimental droplet size distributions by Weibull-distributions was verified. This definition also allows a simple variation of d_{32} in sensitivity studies. Further information is given in Appendix C.1.1
The original model distributes liquid mass flux over the trajectories based on the gas mass flow calculated from the free jet equations and the global GLR (eq. 4.5). The extended model uses a trajectory dependent liquid mass flux, resulting in a variable local GLR $\mathrm{GLR}_\mathrm{local}(\eta)$:

$$\mathrm{GLR}_\mathrm{local}(\eta) = \frac{\dot{m}_\mathrm{GA}(\eta)}{\dot{m}_\mathrm{liq}(\eta)}. \tag{4.15}$$

The logistic distributions obtained in the patternator experiments (eq. 3.3) are used as input for $\dot{m}_\mathrm{liq}(\eta)$ (see section 3.3.5). For sensitivity studies, the logistic function parameter w was modified in order to yield a mass flux distribution with the desired spray angle $\theta_{0.9}$ (eq. 3.3).

4.3.2 Reaction Model

The original model uses 4 distinct reactions to describe fuel decomposition (eq. 4.11), oxidation reactions (eqs. 2.41 and 2.42) and water gas shift equilibrium (eq. 2.43), which are coupled via an energy balance to calculate the gas temperature and concentrations of the main components. High temperature dissociation of main components is neglected by this approach, which leads to an overprediction of gas temperature and also limits the comparability of model results with experimental OH data [15]. The use of a fuel decomposition reaction also restricts the applicability of the model for complex fuels.
To overcome these restrictions, a new approach for the gas phase reactions applying adiabatic Gibbs Free Energy minimization was implemented. Instead of reaction equations, the method uses elemental and energy balances to calculate the equilibrium state of the reaction mixture [180, 198]. The fundamentals of this approach are described in 2.2.6. This reaction model was implemented in all modeling steps calculating gas phase reactions (steps **A**, **B** and **D**). As before, each control volume is assumed to be in chemical equilibrium. In each control volume, the Gibbs free energy

$$G(n_i,T) = \sum_{i=1}^{N} n_i \cdot \left(\Delta G_{f,i}^{\ominus} + RT\ln(p_i/p^{+})\right) \tag{4.16}$$

is minimized for all N species n_i using the Gibbs energy of formation $\Delta G_{f,i}^{\ominus}$ and the partial pressure p_i of component i at temperature T under isobaric conditions [198]. The elemental balance serves as a boundary condition for the minimization [198]. Since each control volume assumes adiabatic equilibrium, an iterative calculation with the additional constraint of constant enthalpy

$$h_{\text{gas}} \stackrel{!}{=} \sum_{i=1}^{N} y_i \cdot h_i(T) \tag{4.17}$$

is performed using thermodynamic data from NASA-polynoms [246], where h_{gas} is defined by the mixture fraction of the streams (eq. 4.9 in the original and 4.27 in the extended model). The calculation procedure is described [180], and its implementation in [247]. The main species O_2, N_2, CO_2, CO, H_2O and H_2 as well as the radicals OH, O, H and NO were considered. These were chosen based on a sensitivity study in which calculated temperatures and concentrations for typical mixtures in the 2-Ph-FJM were compared against validation data obtained using Aspen Plus and Cantera applying GRI 3.0 (see [247, 248] and Appendix C.1). Due to their absence in chemical equilibrium at high temperatures typical for EFG-conditions, hydrocarbons such as CH_4 were not considered as equlibrium species. To assess the local degree of oxidation of the gas phase mixture,

the absolute stoichiometry is defined as

$$\lambda_{\text{abs}} = \frac{\sum_{i=1}^{N} y_i \cdot \nu_{O,i}}{2 \cdot \sum_{i=1}^{N} y_i \cdot \nu_{C,i} + 0.5 \cdot \sum_{i=1}^{N} y_i \cdot \nu_{H,i}} \tag{4.18}$$

with the number of atoms $\nu_{k,i}$ in species i, (k = C, H, O).

4.3.3 Suspension Fuels

The original model describes single-component liquid fuels and uses the d^2-law as evaporation model (eq. 2.30). The model was expanded in the present work in order to account for more complex droplet evaporation models and the additional treatment of a solid fuel phase, including particle reaction sub-models. The model extensions necessary for the description of suspension fuels and the extended balance equations for mass and energy are presented in this section. The individual suspension droplet models as well as the treatment of the remaining solid particles after complete liquid evaporation are described in section 4.3.4. These model extensions have also been published in [17].
The extended model allows input of liquid and suspensions fuels, which are fed to the simulation domain as droplets containing a mixture of both phases. The following assumptions concerning solid particles and suspension droplets are universally applied within the 2-Ph-FJM:

- Suspension droplets and solid particles are spherical.
- Solid particles all have the same initial diameter corresponding to the measured d_{32} of the respective char.
- All suspension droplets contain the same initial solid mass fraction $x_{\text{sol},0}$.
- Ash and moisture content in the solid phase is neglected, the solid phase only consists of C, H and O.
- There is no change of solid phase composition during conversion. The composition of solid mass flow transferred to the gas phase $\dot{m}_{\text{FG}}$ (eq. 4.23) and the composition of the solid particle mass $m_{\text{sol,drop}}$ (eq. 4.35) are constant and correspond to the input elemental composition of the solid phase.

In the first modeling step **A**, the composition of the syngas in the recirculation zone is calculated (see section 4.2). For suspension fuels, the syngas was modeled to have the equlibrium gas phase composition of the input mass flows, assuming full liquid conversion and a variable solid conversion degree of $X_{\text{sol,rec}}$. Recirculation of solid particles into the free jet flame is not taken into account in the model. This is described in Appendix C.3.3,

where a sensitivity study on the influence of this parameter on the flame is also provided. Calculations of equilibrium compositions of the syngas from the recirculation zone (step **A**) and the local gas phase composition in the simulation domain (step **B**) were done using the Gibbs-approach presented in section 4.3.2.
The description of momentum exchange between the gas phase and the fuel droplets in step **C** is the same as in the original model (section 4.2). To calculate changes of droplet / particle temperature during liquid and solid conversion, an energy balance is solved for each single droplet in each control volume:

$$(m_{\mathrm{sol,drop}} \cdot c_{\mathrm{p,sol}} + m_{\mathrm{liq,drop}} \cdot c_{\mathrm{p,liq}}) \cdot \frac{\mathrm{d}T_{\mathrm{drop}}}{\mathrm{d}t} = \dot{Q}_{\mathrm{con,drop}} + \dot{Q}_{\mathrm{rad,drop}} + \dot{H}_{\mathrm{reac,drop}} \tag{4.19}$$

Convective and conductive heat transfer $\dot{Q}_{\mathrm{con,drop}}$, radiative heat transfer $\dot{Q}_{\mathrm{rad,drop}}$ and the change of thermal energy induced by chemical reaction and phase change $\dot{H}_{\mathrm{reac,drop}}$ are considered. These terms are relevant during heat up, evaporation and heterogeneous conversion steps and are calculated using the specific droplet model. The solid and liquid mass in the suspension droplet in eq. 4.19 are given by $m_{\mathrm{sol,drop}}$ and $m_{\mathrm{liq,drop}}$. As long as liquid and solid phase coexist in the suspension droplet, both phases have the same temperature which is limited by the liquid boiling temperature. If only solid is present, the particle temperature can increase further. During the droplet heat-up phase, the heat flows to the droplet are calculated by

$$\dot{Q}_{\mathrm{con,drop}} = \alpha \cdot \pi d^2 \cdot (T_{\mathrm{gas}} - T_{\mathrm{drop}}) \tag{4.20}$$

$$\dot{Q}_{\mathrm{rad,drop}} = \sigma \cdot \epsilon_{\mathrm{rad}} \cdot \pi d^2 \cdot (T_{\mathrm{rad}}^4 - T_{\mathrm{drop}}^4). \tag{4.21}$$

During the conversion phase, the heat flows are given by the respective droplet evaporation model (section 4.3.4). The calculation of the heat transfer coefficient α is analogous to the original model. For the calculation of radiation, suspension droplets and remaining solid particles are assumed as spherical ideal black bodies with emission factor $\epsilon_{\mathrm{rad}} = 1$ surrounded by a uniform temperature reactor wall. This results in the simplified description of the radiative heat flow given by eq. 4.21 with the Stefan-Boltzmann constant σ and the radiation temperature T_{rad} equal to the reactor wall temperature of 1200 °C [249]. After the heat-up phase is complete, heat transfer is described according to the selected droplet model. The term $\dot{H}_{\mathrm{reac,drop}}$ in eq. 4.19 expresses the change of thermal energy of a droplet by chemical reaction and phase changes. Depending on the stage of droplet conversion, the mass specific heat of evaporation $\Delta h_{\mathrm{vap,liq}}$ and the heat of the Boudouard and heterogeneous water gas reactions $\Delta h_{\mathrm{R,CO2}}$ and $\Delta h_{\mathrm{R,H2O}}$ are relevant:

$$\dot{H}_{\mathrm{reac,drop}} = -\frac{\mathrm{d}m_{\mathrm{liq,drop}}}{\mathrm{d}t} \cdot \Delta h_{\mathrm{vap,liq}} - \frac{\mathrm{d}m_{\mathrm{sol,drop}}}{\mathrm{d}t} \cdot \frac{r_{\mathrm{CO2}} \cdot \Delta h_{\mathrm{R,CO2}} + r_{\mathrm{H2O}} \cdot \Delta h_{\mathrm{R,H2O}}}{r_{\mathrm{CO2}} + r_{\mathrm{H2O}}} \tag{4.22}$$

The reaction enthalpy of devolatilization was neglected. The solid reaction rates r_i are defined in eq. 4.37.
For the description of the gas phase in modeling step **D**, a local mixing ratio of the mass flows of jet medium $\dot{m}_{\mathrm{GA}}$, surrounding syngas $\dot{m}_{\mathrm{SG}}$ and fuel vapor $\dot{m}_{\mathrm{FV}}$ is used in the original model (see eq. 4.8). This local mixing ratio is now extended to contain the fuel mass flow $\dot{m}_{\mathrm{FG}}$ that enters the gas phase through solid fuel gasification and devolatilization reactions. The local mixing ratio for stream i is defined in each control volume by

$$x_i(\zeta,\eta) = \frac{\dot{m}_i(\zeta,\eta)}{\dot{m}_{\mathrm{GA}}(\zeta,\eta) + \dot{m}_{\mathrm{SG}}(\zeta,\eta) + \dot{m}_{\mathrm{FV}}(\zeta,\eta) + \dot{m}_{\mathrm{FG}}(\zeta,\eta)}. \tag{4.23}$$

The relation between $\dot{m}_{\mathrm{FV}}$ and the local liquid conversion $X_{\mathrm{liq}}(\zeta,\eta)$ is now given by

$$m_{\mathrm{FV}}(\zeta,\eta) = \frac{m_{\mathrm{GA}}(\zeta,\eta)}{GLR_{\mathrm{local}}(\eta)} \cdot X_{\mathrm{liq}}(\zeta,\eta) \cdot (1 - x_{\mathrm{sol},0}). \tag{4.24}$$

where the original eq. 4.7 has been modified to consider the initial solid content $x_{\mathrm{sol},0}$ in the droplets in the last term. The mass flow transfered from the solid phase to the gas phase $\dot{m}_{\mathrm{FG}}$ is defined analogously as

$$\dot{m}_{\mathrm{FG}}(\zeta,\eta) = \frac{\dot{m}_{\mathrm{GA}}(\zeta,\eta)}{GLR_{\mathrm{local}}(\eta)} \cdot X_{\mathrm{sol}}(\zeta,\eta) \cdot x_{\mathrm{sol},0}. \tag{4.25}$$

with $X_{\mathrm{sol}}(\zeta,\eta)$ as the local degree of solid conversion:

$$X_{\mathrm{sol}}(\zeta,\eta) = \frac{\dot{m}_{\mathrm{sol}}(0,\eta) - \dot{m}_{\mathrm{sol}}(\zeta,\eta)}{\dot{m}_{\mathrm{sol}}(0,\eta)}. \tag{4.26}$$

Liquid and solid conversion in each control volume are determined by summing the individual droplet masses calculated by the selected droplet conversion model. The enthalpy of the conversion products of the solid fuel h_{FG} and the sum of the convective heat flows towards the droplets / particles $\dot{q}_{\mathrm{con}}$ have been added to the gas phase energy balance in each control volume:

$$h_{\mathrm{gas}} = x_{\mathrm{GA}}(\zeta,\eta)\cdot h_{\mathrm{GA}} + x_{\mathrm{SG}}(\zeta,\eta)\cdot h_{\mathrm{SG}} - \dot{q}_{\mathrm{con}}(\zeta,\eta) + x_{\mathrm{FV}}(\zeta,\eta)\cdot h_{\mathrm{FV}} + x_{\mathrm{FG}}(\zeta,\eta)\cdot h_{\mathrm{FG}}. \tag{4.27}$$

The enthalpy of the conversion products of the solid fuel h_{FG} is calculated analogously to eq. 4.10 with an enthalpy of formation $\Delta h^{\ominus}_{f,sol}$ derived from the char heating value and assuming a mean solid temperature equal to reactor temperature:

$$h_{\mathrm{FG}} = \Delta h^{\ominus}_{f,sol} + \int_{T_0}^{T_{\mathrm{R}}} c_{p,sol}\, dT + \Delta h_{R,sol}. \tag{4.28}$$

The reaction enthalpy of the char $\Delta h_{R,sol}$ accounts for conversion using heterogenous water gas and Boudouard reactions. Due to the small amount of solid typically converted within

the flame zone (see section 5.3), the contribution of h_{FG} to the gas phase energy balance in the model is insignificant.
The gas phase equilibrium composition in step **D** is calculated based on eqs. 4.27 and 4.23 using the adiabatic Gibbs reactor approach described in section 4.3.2.

4.3.4 Suspension Droplet- and Solid Particle Conversion Models

This sections deals with the models for conversion of suspension droplets and the following treatment of the solid particles which were implemented in this work. The models are taken as examples of the different approaches outlined in section 2.2.4. The implementation of these models has been published in [17].

Model 1: Wet Particle Model
The Wet Particle model is the most widely applied droplet model for simulation of gasification systems (see section 2.2.4). The model assumes each solid particle as a compact solid core that is surrounded by a liquid film. The resulting initial droplet diameter is thus determined by the size of the solid particle and the initial solid content in the suspension, posing a limitation of this approach.
In a first step, the droplet is heated according to eqs. 4.19 - 4.22 assuming a spatially uniform temperature in the suspension droplet. During the heat up phase, evaporation is calculated by

$$\frac{\mathrm{d}m_{\mathrm{liq,drop}}}{\mathrm{d}t} = -\pi d^2 \cdot \beta \cdot \rho_{\mathrm{gas}} \cdot (c_{\mathrm{FV,s}}(T) - c_{\mathrm{FV},\infty}(T)) \tag{4.29}$$

with β as the mass transfer coefficient calculated by a Sherwood correlation [162, 250]. The concentrations of fuel vapor at the droplet surface and in the bulk phase are given by $c_{\mathrm{FV,s}}$ and $c_{\mathrm{FV},\infty}$ respectively. After the droplet temperature reaches the liquid boiling point, evaporation rate is assumed to be governed by heat transfer and a quasi steady state model can be used [162, 250]. This is typically implemented using a Spalding-type evaporation rate:

$$\frac{\mathrm{d}m_{\mathrm{liq,drop}}}{\mathrm{d}t} = -\pi d^2 \cdot \alpha \cdot \frac{\ln(1 + c_{\mathrm{p,gas}} \cdot \frac{(T_\infty - T_{\mathrm{drop}})}{\Delta h_{\mathrm{vap,liq}}})}{c_{\mathrm{p,gas}}} \tag{4.30}$$

with T_∞ being the bulk gas temperature and $c_{\mathrm{p,gas}}$ the specific heat capacity of the surrounding gas atmosphere. The heat flow to the droplet $\dot{Q}_{\mathrm{con,drop}}$ is calculated using the droplet energy balance 4.19 assuming $T_{\mathrm{drop}} = T_{\mathrm{vap}} = \mathrm{const}$ (also see Fundamentals section 2.2.3). The droplet shrinks until the liquid phase is completely evaporated. Thereafter, the remaining solid core is regarded as one single particle that reacts according to the

description below in this section.

Model 2: Fragmenting Particle Model

This model is based on the wet-kernel models (section 2.2.4). The model uses a droplet size distribution and a single solid particle size as input, where $d_{\mathrm{drop}} > d_{\mathrm{p,sol}}$. Fast mixing within a suspension droplet is assumed, leading to uniformly distributed solid particles in the liquid phase. In the first evaporation phase, the droplet heating and liquid evaporation rate are described analogously to the prior model by eqs. 4.19, 4.29 and 4.30. The solid volume fraction in a droplet is defined as

$$\epsilon_{\mathrm{sol,drop}} = \frac{V_{\mathrm{sol,drop}}}{V_{\mathrm{sol,drop}} + V_{\mathrm{liq,drop}}} \tag{4.31}$$

with the solid and liquid volumes in the droplet $V_{\mathrm{sol,drop}}$ and $V_{\mathrm{liq,drop}}$. During the evaporation process, $\epsilon_{\mathrm{sol,drop}}$ increases until a critical particle density $\epsilon_{\mathrm{sol,drop,crit}}$ is reached where the particles cannot further contract. This value is assumed to correspond to the porosity of a cubical packing of spheres ($\epsilon_{\mathrm{por,cubic}} = 0.476$):

$$\epsilon_{\mathrm{sol,drop,crit}} = 1 - \epsilon_{\mathrm{por,cubic}} \tag{4.32}$$

If solid particles do not exhibit caking behavior under high temperatures and the liquid does not form any solid phase via pyrolysis reactions, agglomerate formation does not take place. After the droplet reaches $\epsilon_{\mathrm{sol,drop,crit}}$, a droplet disintegration is thus assumed where the suspension droplet disintegrates into its individual solid particles that are each surrounded by a liquid film corresponding to the remaining amount of liquid in the droplet. These wet solid particles are then converted according to the Wet Particle model using the corresponding equations (see above). The single solid particles are afterwards converted according to the description below.

Model 3: Shell Formation Model

The droplet model developed by Lee and Law [141] describes a shell formation process in two steps. Like the Fragmenting Particle model, the present model uses a droplet size distribution and a single solid particle size as input. The model requires small particles in comparison to the droplet size ($d_{\mathrm{drop}} \gg d_{\mathrm{p,sol}}$), posing a model limitation. In contrast to the Fragmenting Particle model, the transport of the solid particles in the liquid phase is assumed to be slow compared to the movement of the receding liquid phase boundary, leading to the formation of a porous shell at the droplet surface.

At the start of the evaporation process, the droplet is assumed to have a spatially homogeneous distribution of solid particles suspended in the liquid phase. Droplet heat up to the liquid boiling point is modeled using eq. 4.19 assuming a homogeneous temperature

distribution in the suspension droplet. Evaporation during the heat up is not accounted for.
After reaching the liquid boiling point, the droplet undergoes an initial regressing diameter period as outlined in section 2.2.4. In this phase, the evaporating liquid mass flux is given by

$$\frac{\mathrm{d}m_{\mathrm{liq,drop}}}{\mathrm{d}t} = -\frac{\pi}{4} \cdot d \cdot \rho_{\mathrm{liq}} \cdot K \tag{4.33}$$

with

$$K = \frac{8 \cdot \lambda_{\mathrm{gas}}}{\rho_{\mathrm{liq}} \cdot c_{\mathrm{p,gas}}} \cdot \ln\left(1 + c_{\mathrm{p,gas}} \cdot \frac{(T_\infty - T_{\mathrm{drop}})}{\Delta h_{\mathrm{vap,liq}}}\right). \tag{4.34}$$

These equations lead to the d^2-law that has also been applied in the 2-Ph-FJM for modeling the evaporation of pure liquid droplets (eq. 2.30) [141]. Convective heat transfer from the gas to the liquid phase $\dot{Q}_{\mathrm{con,drop}}$ in the 2-Ph-FJM is again calculated using the droplet energy balance 4.19 with $T_{\mathrm{drop}} = T_{\mathrm{vap}}$. During this period, solid particles accumulate at the droplet surface due to the receding evaporation front and the lack of particle transport in the liquid phase until a critical porosity $\epsilon_{\mathrm{sol,surf,crit}}$ is reached, where the particles at the surface reach their maximum packing density. This porous layer of solid particles thickens until a critical layer thickness δ_{crit} is reached, where a rigid porous shell is established. The diameter of the suspension droplet at this point is denoted as $d_{\mathrm{drop,crit}}$. The evaporation process now switches to a fixed diameter stage. The authors provide experimental values for suspensions of carbon particles with water and oil. On this basis, they propose to use the porosity of a cubical packing of spheres $\epsilon_c = 0.476$ for the shell and suggest $\delta_{\mathrm{crit}} = 3d_{\mathrm{p,sol}}$ as an estimate [141].
During the second stage, the droplet diameter is fixed by the rigid shell while the particle temperature is again assumed to be homogeneous and equal to the liquid boiling point. The particle surface is assumed to be continuously wetted by the liquid phase, which is supported by experimental data provided by the authors [141]. The mass flow of evaporating liquid is thus again given by eq. 4.33 using the diameter of the droplet at the transition $d_{\mathrm{drop,crit}}$. Since the droplet diameter is fixed and the liquid within the droplet is boiling, the continuous depletion of liquid through evaporation must create an expanding space of vapor within the droplet. For simplification, since the exact distribution of vapor inside the droplet is not known, it is assumed as a spherical bubble located at the droplet center. During further evaporation, continuous deposition of solid particles at the inside of the porous shell leads to its further thickening. Inhibition of vapor transport through transport limitations in the porous shell are neglected by the model. When the liquid is completely evaporated, a solid agglomerate in form of a hollow sphere with diameter $d_{\mathrm{drop,crit}}$ and a shell thickness calculated by a solid mass balance is left.

Solid Conversion Reactions

When the liquid evaporation processes described by the models above are complete, solid particle conversion through devolatilization reactions and heterogeneous gasification reactions is modeled. The fundamentals of these processes are provided in section 2.2.5. In the model implementation, the total solid mass $m_{\mathrm{sol,drop}}$ is separated in a volatile mass $m_{\mathrm{sol,vol,drop}}$ and a fixed carbon mass $m_{\mathrm{sol,fix,drop}}$ that has been determined in literature for the char applied in this work [251]:

$$m_{\mathrm{sol,drop}} = m_{\mathrm{sol,vol,drop}} + m_{\mathrm{sol,fix,drop}}. \tag{4.35}$$

Devolatilization and gasification reactions are assumed to occur sequentially. For simplification, the Uniform Conversion Model (UCM) was used to describe the particle conversion. In this approach, the depletion of mass due to devolatilization and heterogeneous reactions are assumed to only affect particle density, resulting in a constant solid particle diameter. The individual particles are modeled to have a spatially uniform temperature.
The devolatilization of the particles is modeled using a single first order Arrhenius law approach:

$$\frac{\mathrm{d}m_{\mathrm{sol,vol,drop}}}{\mathrm{d}t} = -m_{\mathrm{sol,vol,drop}} \cdot k_{0,\mathrm{vol}} \cdot \exp\left(-\frac{E_{\mathrm{A,vol}}}{RT}\right) \tag{4.36}$$

with the universal gas constant R and the pre-exponential factor $k_{0,\ \mathrm{vol}}$ and the activation energy $E_{\mathrm{A,vol}}$ for the devolatilization reaction. Kinetic data for devolatilization of the present char determined in a Drop-Tube-Reactor are given in [251]. The heterogeneous char reactions with CO_2 and H_2O were modeled using a power law approach:

$$r_{\mathrm{i}} = k_{0,\mathrm{i}} \cdot \exp\left(-\frac{E_{\mathrm{A,i}}}{RT}\right) \cdot p_{\mathrm{i}}^{n_{\mathrm{i}}} \tag{4.37}$$

with the intrinsic reaction rate r_{i}, the partial pressure p_{i} and the reaction order n_{i} for the component i (CO_2, H_2O). The heterogeneous gasification kinetics were determined for the applied char in a Pressurized Single Particle Reactor (pSPR) for both reactands [252]. Due to the high temperatures during char conversion under gasification conditions, the influence of pore diffusion on reaction rate must be considered [168, 170, 253]. The effective reaction rate for the gasification reactions is thus expressed by

$$\frac{\mathrm{d}m_{\mathrm{sol,fix,drop}}}{\mathrm{d}t} = -m_{\mathrm{sol,fix,drop}} \cdot \bar{M}_{\mathrm{C}} \cdot (r_{\mathrm{CO2}} \cdot \eta_{\mathrm{CO2}} + r_{\mathrm{H2O}} \cdot \eta_{\mathrm{H2O}}) \tag{4.38}$$

with the molar mass of carbon $\bar{M}_{\mathrm{C}}$ and the effectiveness factor η, which is calculated using a Thiele-modulus ϕ (eq. 2.40). The mean pore size required for calculation of ϕ was obtained using a pore size distribution measurement carried out for the char in [173].

4.3.5 Characteristic Parameters for Reaction Zone Analysis

The OH radical is used to define a series of characteristic parameters for flame evaluation, as it plays a significant role in high temperature oxidation reactions and is often applied as flame front marker (see section 2.2.6). Its spatial distribution is accessible by both experiment and model. These quantities are used to assess the impact of changes in input parameters on flame length and shape.
For this purpose, measured OH-LIF intensity fields $I_{\mathrm{LIF}}(z,r)$ and calculated OH concentration fields $c_{\mathrm{OH}}(z,r)$ are each normalized to their maximum value $I_{\mathrm{LIF,max}}$ or $c_{\mathrm{OH,max}}$ and binarized using a threshold value of 0.1:

$$\mathrm{bin}(z,r) = \left\{ \begin{array}{ll} 0, & \text{if } I_{\mathrm{LIF}}(z,r) < 0.1 \cdot I_{\mathrm{LIF,max}} \\ 1, & \text{if } I_{\mathrm{LIF}}(z,r) \geq 0.1 \cdot I_{\mathrm{LIF,max}} \end{array} \right\} \tag{4.39}$$

and correspondingly

$$\mathrm{bin}(z,r) = \left\{ \begin{array}{ll} 0, & \text{if } c_{\mathrm{OH}}(z,r) < 0.1 \cdot c_{\mathrm{OH,max}} \\ 1, & \text{if } c_{\mathrm{OH}}(z,r) \geq 0.1 \cdot c_{\mathrm{OH,max}} \end{array} \right\}. \tag{4.40}$$

The longitudinal extension of the OH zone L_{OH} is then defined as the axial nozzle distance at the jet centerline at which the OH profile falls below 10 % of the maximum value:

$$\mathrm{bin}(L_{\mathrm{OH}},0) < 1. \tag{4.41}$$

The volume of the OH zone is defined accordingly by integration of the volume within the 10 % OH contour over the measurement or simulation domain D and is derived assuming rotational symmetry of the flame:

$$V_{\mathrm{OH}} = \iint_D \mathrm{bin}(z,r) \cdot r \, dr \, dz \tag{4.42}$$

An uncertainty analysis of the procedure to derive these quantities is presented in Appendix A.4. In order to quantify the transition of the flame shape from a closed to a hollow cone structure as reported in section 2.1.2, the OH aspect ratio $\mathrm{AR_{OH}}$ is introduced as a shape parameter. It is defined as the ratio of the longitudinal extension of the OH zone at the jet centerline L_{OH} to the most distant point from the nozzle $z_{\mathrm{max,OH}}$ where $\mathrm{bin}(z,r) = 1$:

$$\mathrm{AR_{OH}} = \frac{L_{\mathrm{OH}}}{z_{\mathrm{max,OH}}} \tag{4.43}$$

In case of a closed flame shape, $z_{\mathrm{max,OH}}$ is found on the jet centerline, resulting in $\mathrm{AR_{OH}} = 1$. In case of a hollow cone flame shape, the most distant point within the OH zone is found

off the jet centerline, and $AR_{OH} < 1$ (compare Fig. 2.2).
The OH contour is also used to define fuel conversion progress variables within the flame. As these quantities are currently not experimentally accessible, they are only defined in the model. These definitions will later be applied to assess the impact of changes in process parameters and fuel properties on fuel conversion.
The liquid conversion progress within the OH volume $X_{liq,OH}$ is defined by the total mass of evaporated liquid integrated over the 10 % OH contour relative to the total input liquid mass. In each trajectory, a liquid mass flow $\dot{m}_{liq}(0,\eta)$ is initially applied. At the axial distance where a droplet trajectory reaches the boundary of the 10 % OH contour $\zeta_{max,OH}(\eta)$, the mass of evaporated liquid along the trajectory is evaluated. The evaporated liquid mass along all trajectories is summed and divided by the total input liquid fuel mass flow $\dot{m}_{liq,total} = \dot{m}_{fuel} \cdot (1 - x_{sol,0})$.

$$X_{liq,OH} = \frac{\int_{\eta=0}^{\eta_{max}} \left[\dot{m}_{liq}(0,\eta) - \dot{m}_{liq}\left(\zeta_{max,OH}(\eta),\eta\right)\right] d\eta}{\dot{m}_{liq,total}} \tag{4.44}$$

The solid conversion within the OH zone $X_{sol,OH}$ is defined analogously:

$$X_{sol,OH} = \frac{\int_{\eta=0}^{\eta_{max}} \left[\dot{m}_{sol}(0,\eta) - \dot{m}_{sol}\left(\zeta_{max,OH}(\eta),\eta\right)\right] d\eta}{\dot{m}_{sol,total}}. \tag{4.45}$$

In the evaporation models used in this work, solid reactions start when liquid evaporation of a droplet has finished and only solid phase is left. To quantify which amount of the solid phase is no longer contained in droplets and is available for reaction with the gas phase, the fraction of dried solid mass $X_{sol,dry,OH}$ is introduced analogously to the above definition:

$$X_{sol,dry,OH} = \frac{\int_{\eta=0}^{\eta_{max}} \left[\dot{m}_{sol,dry}\left(\zeta_{max,OH}(\eta),\eta\right)\right] d\eta}{\dot{m}_{sol,total}}. \tag{4.46}$$

5 Results and Discussion

5.1 Flame Structure

This section deals with the detailed analysis of the structure of the EFG flame, its governing sub-processes and their dependencies on process parameters. This section addresses **Objective 1** (Quantitative description of the impact of the burner related parameters gas momentum flow, droplet size and spray angle on the reaction zone structure of a liquid fuel EFG flame).
Section 5.1.1 first gives a detailed description of the structure of the EFG flame. The EFG flame is analyzed based on the comprehensive experimental **MEG**-dataset, featuring 2 cases with different input conditions, leading to different flame shapes. Both flame shapes described in numerical literature (see section 2.1.2) are verified and investigated.
Based on the experimental observations, the 2-Ph-FJM is used to conduct sensitivity studies on the influence of the burner related parameters gas momentum flow, droplet size and spray angle on length and shape of the EFG flame. The numerical studies are based on the input conditions of the **GLYCEROL**-dataset. The single-parameter variations are described in the following sections 5.1.2 - 5.1.4. Section 5.1.5 finally aims to quantify the interaction of the single process parameters and identifies the most relevant parameters for flame length and shape.
Throughout the sections, the model is validated at different examples. Full validation of the model is provided in Appendix section C.2 in order to improve readability. Validation of OH radical distribution, spray parameters and gas temperature is performed based on the **MEG**-dateset. The trends identified in the sensitivity studies are validated against data from the **GLYCEROL**-dataset. Both experimental datasets are fully provided in Appendix sections D.1 and D.2.

5.1.1 Reaction Zone Structure in EFG Flame

The typical features of the EFG flame are discussed in this section based on the experimental **MEG**-dataset. The dataset consists of spray data under ambient and reacting conditions,

OH-LIF data and temperature profiles. The data is fully provided in Appendix D.1 and partially published in [15, 16]. The discussion in this section is mostly based on [15].
As described in the Fundamentals section 2.1.2, the EFG flame can be considered as an inverse diffusion flame that is superimposed by a fuel spray. In this flame, the gasification agent and the fuel droplets form a two-phase jet that emerges into a hot syngas environment. Under these conditions, the oxygen in the gasification agent can react with both syngas entrained from the surrounding and fuel vapor from droplet evaporation. This oxidation reaction and the resulting high temperatures lead to the formation of OH, which is used as an indicator for the oxidation zone (see section 2.2.6).
Fig. 5.1 shows OH-LIF and Fuel-Tracer LIF data for case MEG-A, which is shown as an example case of a closed EFG flame structure. The presence of OH in close vicinity of the nozzle exit indicates an immediate ignition. The M-shaped OH radial profile at $z/d_{\mathrm{eq}} = 5$ indicates that most OH can be found at the outer region of the jet while at the jet centerline, the OH concentration is lower. This originates from the reaction of the surrounding hot syngas atmosphere and the oxygen rich gasification medium at the jet boundaries, which serves as a stabilization mechanism of the flame.
Further entrainment of syngas into the jet leads to an extension of the oxidation zone towards the centerline with increasing nozzle distance. This is indicated by the increase of OH-LIF intensity at the jet centerline and the transition of the M-shaped OH-LIF profile in the transition region at $z/d_{\mathrm{eq}} = 5$ into a bell shaped profile in the self similar region at $z/d_{\mathrm{eq}} = 15$.
Further downstream, the bell-shaped OH-LIF profiles broaden due to the radial expansion of the jet. The entrainment of syngas, which is cooler than the flame temperature, combined with ongoing evaporation lead to a decrease in temperature and local stoichiometry. These two factors cause the decrease of OH concentration, which is reflected by the lower OH-intensities at $z/d_{\mathrm{eq}} = 30$ and $z/d_{\mathrm{eq}} = 45$.
All Fuel-Tracer-LIF profiles show the highest liquid concentrations at the jet centerline and exhibit a bell-shape, which is consistent with the ambient spray characterization data (Appendix D.1) and the considerations on 2-Phase Free Jets by Hotz (see Fundamentals section 2.2.2). The profiles broaden with increasing nozzle distance, while the absolute intensity decreases. This is caused partly by the expansion of the gas jet, but also through fuel evaporation. The Fuel-Tracer-LIF-image and radial profiles show significant amounts of liquid fuel outside the flame volume, both in lateral and axial direction. This is indicated by the dotted red line in Fig. 5.1 and will be further discussed in section 5.2, which is dedicated to fuel evaporation.
Fig. 5.2 shows experimental OH-LIF and Fuel-Tracer-LIF data for case MEG-B. In this case, a different burner nozzle is used, featuring a smaller gas exit area ($d_{\mathrm{eq}} = 4.3$ mm) in comparison to case MEG-A. This leads to a higher gas momentum flow, causing enhanced jet mixing and a spray featuring smaller droplets ($\mathrm{ID}_{32} = 73$ µm) with narrower spray angle ($\theta_{0.9} = 23.5\,^{\circ}$). Detailed ambient and reactive spray data are given in Appendix D.1.

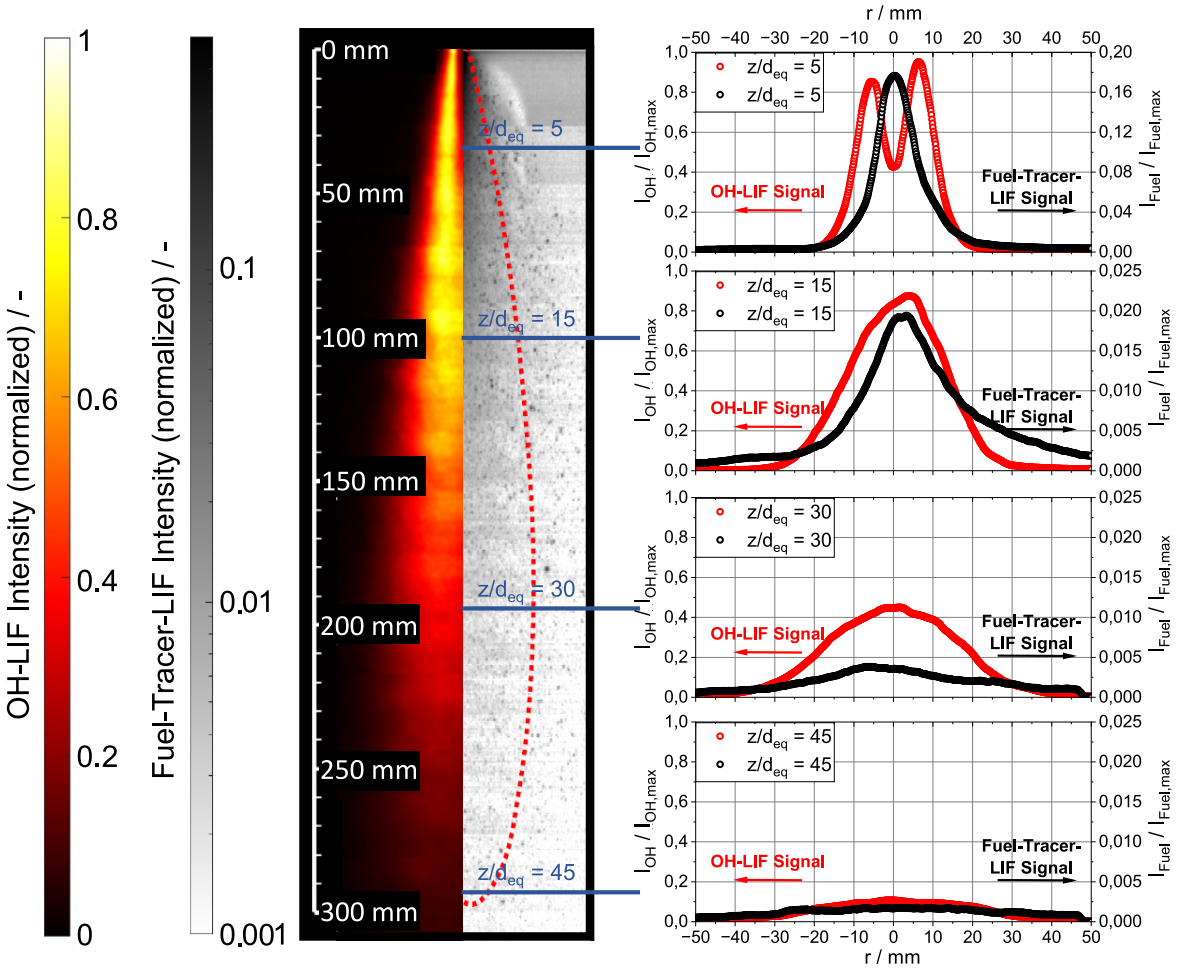


Figure 5.1: Normalized OH-LIF- (left) and Fuel-Tracer-LIF-signals (right) for case MEG-A. Smoothed radial profiles of both quantities are shown at different nozzle distances with respect to the nozzle equivalent diameter d_{eq}. The dotted red line in the Fuel-Tracer-LIF-image indicates the 10%-OH contour. Process conditions: J_{gas}=0.20 N, ID_{32} = 160 µm, $\theta_{0.9}$ = 40.4 °, Fuel: MEG. Data published in [15]. For better display, the scale of the Fuel-Tracer-LIF profile at $z/d_{eq} = 5$ differs from the scale in the other diagrams.

The higher entrainment rate caused by the higher gas momentum leads to a faster consumption of oxygen, which reduces the longitudinal extension of the OH zone. This is directly evident from the OH-LIF image. To compare the OH distributions of cases MEG-A and MEG-B despite the different gas entrainment rates, OH-LIF-intensity and Fuel-Tracer-LIF-intensity radial profiles in Fig. 5.2 are displayed at the same normalized nozzle distances as above (also see Fundamentals section 2.2.2).

In the vicinity of the nozzle exit at $z/d_{eq} = 5$, the radial distribution of OH is similar to case MEG-A, where OH is mostly found in a narrow region at the jet boundaries, as above. Further downstream at $z/d_{eq} = 15$ and 30, the bell shaped OH-LIF radial profiles from case A are not detected. Instead, M-shaped profiles are found. This effect

is a consequence of the high droplet concentration at the jet centerline, which creates a fuel rich low temperature zone. This will be investigated in detail in section 5.1.4. At $z/d_{eq} = 45$, where a considerable OH signal was still detected in case MEG-A, OH is almost absent in case MEG-B. This is again a consequence of the lower stoichiometry and lower temperature induced by the increased amount of fuel evaporation within the jet.
The Fuel-Tracer-LIF radial profiles in Fig. 5.2 do not show significant amounts of liquid fuel in the region lateral to the flame, which stands in contrast to case MEG-A and is a consequence of the narrow spray angle. At the jet centerline however, a considerable Fuel-Tracer-LIF singal is still detected after the end of the OH zone, again indicating incomplete fuel evaporation (see $z/d_{eq} = 45$).

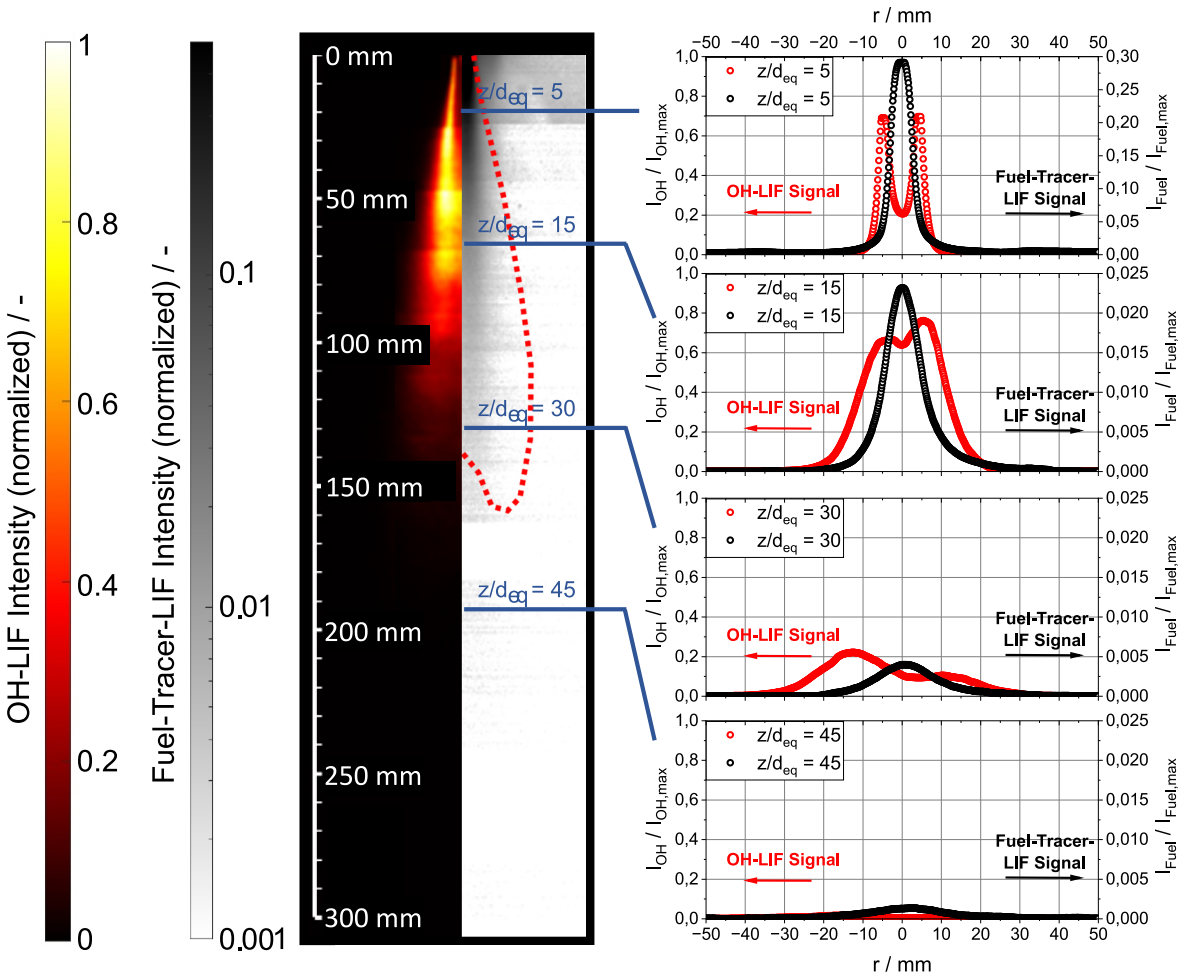


Figure 5.2: Normalized OH-LIF- and Fuel-Tracer-LIF-signals for case MEG-B. Radial profiles of both quantities are shown at different nozzle distances respective to the nozzle equivalent diameter d_{eq} to enable a comparison with case MEG-A above. Process conditions: J_{gas}=0.45 N, ID_{32} = 73 µm, $\theta_{0.9}$ = 23.5 °, Fuel: MEG. Data published in [15].

Fig. 5.3 displays gas temperature profiles measured by a double-bead-thermocouple for cases MEG-A and MEG-B at different normalized nozzle distances. In analogy to the OH-LIF-signal, the gas temperature profile for case MEG-A at $z/d_{eq} = 47$ shows a bell-shape. For case MEG-B, on the other hand, a flatter temperature profile without distinct temperature maximum at the jet axis is observed at this position. Temperatures for case MEG-B are also generally lower than for case MEG-A at $z/d_{eq} = 47$, which is consistent with the lower OH-intensities in the downstream flame region for case MEG-B described above. The temperature profile at $z/d_{eq} = 35$ for case MEG-B shows a clear M-shape, which is again in agreement with the OH-measurements. The observed asymmetry of the profiles is likely caused by a slight asymmetry of the burner nozzle that is also evident from the OH-LIF-profiles, and is further enhanced by infiltration air during the invasive temperature measurement.

The OH-LIF, gas temperature and Fuel-Tracer-LIF measurements in this section provide

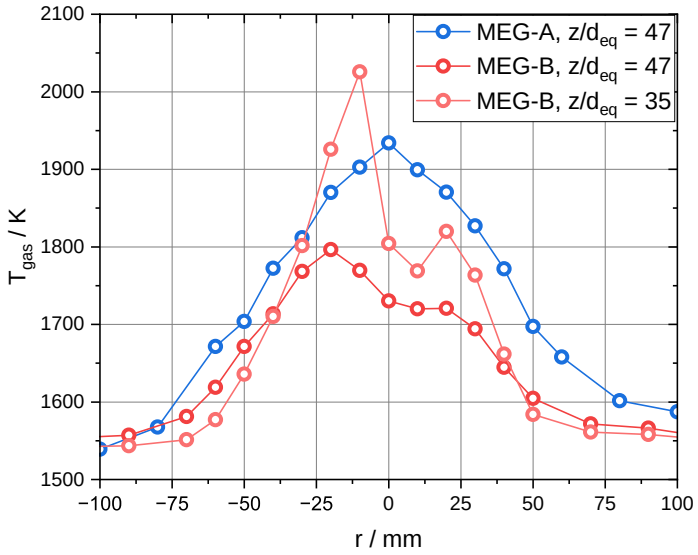


Figure 5.3: Radial profiles of gas temperature measured using a double-bead-thermocouple for cases MEG-A (J_{gas}=0.20 N, ID_{32} = 160 µm, $\theta_{0.9}$ = 40.4 °) and MEG-B (J_{gas}=0.45 N, ID_{32} = 73 µm, $\theta_{0.9}$ = 23.5 °) at $z/d_{eq} = 47$. Fuel: MEG. Data published in [15].

a comprehensive dataset and show a clear influence of syngas entrainment and fuel evaporation on length and shape of the EFG flame. These sub-processes are determined by gas momentum flow, spray angle and droplet size. Both flame shapes reported in modeling literature (see section 2.1.2) have been verified experimentally. This provides a starting point for further analysis, focusing on an independent assessment of the influence of the burner related process parameters on flame length and shape. This is discussed in the following sections 5.1.2 - 5.1.5.

5.1.2 Influence of Gas Momentum Flow on EFG Flame

This section investigates the influence of gas momentum flow on the EFG flame. First, as an example of the approach followed by the design of the underlying **GLYCEROL**-dataset, an experimental investigation of the influence of gas momentum flow on flame length and shape is presented. This is omitted in the following sections in order to improve readability. After that, a model based analysis of the influence of gas momentum flow on gas temperature, OH concentration, local fuel evaporation and local stoichiometry is discussed. Full data and spray characterization results are given in Appendix D.2. The trend prediction is validated in Appendix C.2.2.

In the **GLYCEROL**-dataset described in section 3.4.2, viscosity of the reference fuel glycerol was varied by temperature in order to modulate the spray parameters independently from the burner nozzle geometry. To study the role of syngas entrainment in the EFG flame, two cases featuring similar spray angle and droplet size at different gas momentum flow are compared (cases A50 and B200).

Fig. 5.4 a shows the measured normalized OH-LIF signals for cases A50 and B200. In both cases, the OH zones exhibit a similar shape. However, in case B200, the longitudinal extension is considerably reduced. As discussed in the previous section, the higher gas momentum flow J_{gas} in case B200 induces a higher entrainment rate of ambient syngas into the gas jet according to free jet theory. This results in a shorter OH zone for case B200 due to faster consumption of oxygen through combustion reactions with entrained syngas.

OH-LIF intensity radial profiles at different nondimensional distances z/d_{eq} are depicted in Fig. 5.4 b. In contrast to the previous section where spray parameters differed between the two cases, the profiles now show a good similarity as spray parameters are kept constant. This result suggests that under the given conditions, the flame is mainly governed by the entrainment rate of ambient syngas determined by J_{gas}.

To further study this effect, the 2-Ph-FJM is applied. Validation of the model is provided in detail in Appendix section C.2 and is thus not discussed here. A sensitivity study on the impact of gas momentum flow on the EFG flame was conducted where J_{gas} was changed by modulating d_{eq} from 3 to 9 mm applying input mass flows as in the **GLYCEROL**-experiments. A spatially homogeneous droplet size distribution featuring a Sauter mean diameter of $d_{32} = 100$ µm and a spray angle of $\theta_{0.9} = 40\,^{\circ}$ was postulated. Fig. 5.5 shows axial profiles along the jet axis of absolute stoichiometry λ_{abs}, mass fraction of entrained syngas in the jet mixture x_{SG} (eq. 4.8), gas temperature T_{gas} and OH mole fraction y_{OH}. For all investigated cases, the data shows a core region in the vicinity of the nozzle exit. In this core zone, syngas has not yet been mixed into the gas jet, which is indicated by $x_{\mathrm{SG}} = 0$. At nozzle distances of $z/d_{\mathrm{eq}} \approx 10$, the mass fraction of syngas at the jet axis increases. Higher gas momentum flows cause a higher entrainment rate, leading to an earlier increase of x_{SG} for smaller d_{eq}. The mixing of jet medium with syngas reduces

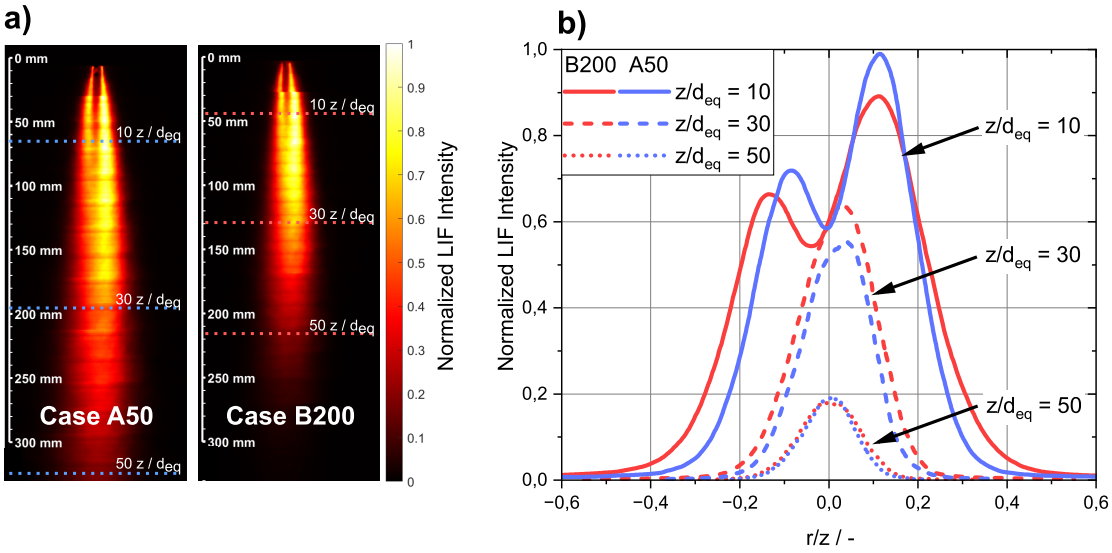


Figure 5.4: Normalized OH-LIF-signals for cases A50 (J_{gas}=0.20 N, $\text{ID}_{32,jet}$ = 88 µm, $\theta_{0.9}$ = 40 °) and B200 (J_{gas}=0.45 N, $\text{ID}_{32,jet}$ = 68 µm, $\theta_{0.9}$ = 39 °) from the GLYCEROL data set. Radial profiles of both quantities are shown at different normalized nozzle distances z/d_{eq}. Fuel: Glycerol.

λ_{abs}. The additional decrease of λ_{abs} by fuel evaporation is small, as the mass fraction of fuel vapor is $x_{\text{FV}} < 5\%$ in the simulation domain in all presented cases (not depicted in the graph). This shows that under the investigated conditions, syngas entrainment is the governing factor for λ_{abs}.

For all cases, the mixing of syngas into the jet first leads to an increase of temperature and the formation of OH through exothermic oxidation reactions. At the point where stoichiometric conditions ($\lambda_{\text{abs}} = 1$) are met, temperature shows a maximum. As stoichiometry further decreases, gas temperature and OH mole fraction are reduced. The low gas momentum case (d_{eq} = 9 mm) thus shows a longer zone of high temperatures and high OH concentrations than the case featuring a high gas momentum (d_{eq} = 3 mm).

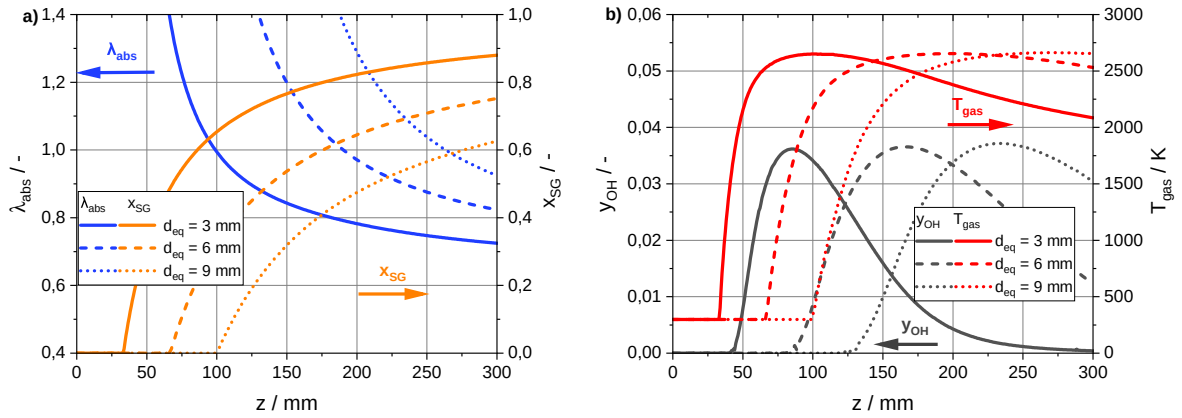


Figure 5.5: Calculated λ_{abs}, T_{gas}, x_{SG} and y_{OH} on jet axis for different d_{eq}, using input mass flows conditions analogous to the GLYCEROL data set. Constant parameters: $d_{32} = 100$ µm, $\theta_{0.9} = 40\,°$, evaporation model: d^2-law, Fuel: Glycerol.

5.1.3 Influence of Fuel Droplet Size on EFG Flame

This section numerically investigates the effect of droplet size, which influences fuel evaporation rate, on the EFG flame structure. A model study based on the **GLYCEROL**-dataset described in section 3.4.2 is conducted to study temperature field, local fuel evaporation and stochiometry as well as flame length and shape for varying droplet size. Additional experimental data for validation is given in Appendices C.2.2 and D.2.

In the model study, geometry parameters of Nozzle B were applied under input flows provided in section 3.4.2. Spray angle is kept constant at 25 °, while using droplet size distributions with Sauter mean diameter (d_{32}) values ranging from 50 µm to 400 µm.

In Fig. 5.6, calculated OH concentration fields and L_{OH} are shown for varying d_{32}. The general shape of the OH zone is unaffected by the droplet size. However, a clear increase in longitudinal extension with increasing droplet size is observed. This effect is more pronounced for smaller droplet diameters, as indicated by the strong increase of L_{OH} from 207 mm to 263 mm by increasing d_{32} from 50 µm to 100 µm. For larger droplet diameters, an asymptotic approach of L_{OH} to a maximum value is observed.

To explain this observation, droplet evaporation has to be regarded. Fig. 5.7 a) shows the calculated fuel vapor mass fraction in the jet mixture x_{FV} (eq. 4.8) on the jet centerline for the 50 µm, 100 µm and 400 µm cases. For smaller droplets, a considerable amount of fuel evaporates along the jet axis, while the evaporated fuel mass for $d_{32} = 400$ µm is negligible. In the 400 µm case, oxygen consumption and thus absolute stoichiometry λ_{abs} along the jet axis are therefore almost exclusively determined by entrainment of syngas. For smaller droplet diameters, fuel evaporation leads to an additional reduction of λ_{abs} as shown in Fig. 5.7 a). For the 50 µm case, stoichiometric conditions ($\lambda_{\text{abs}} = 1$) are met at an axial distance of 117 mm, while for the 400 µm case, $\lambda_{\text{abs}} = 1$ is found at $z = 144$ mm.

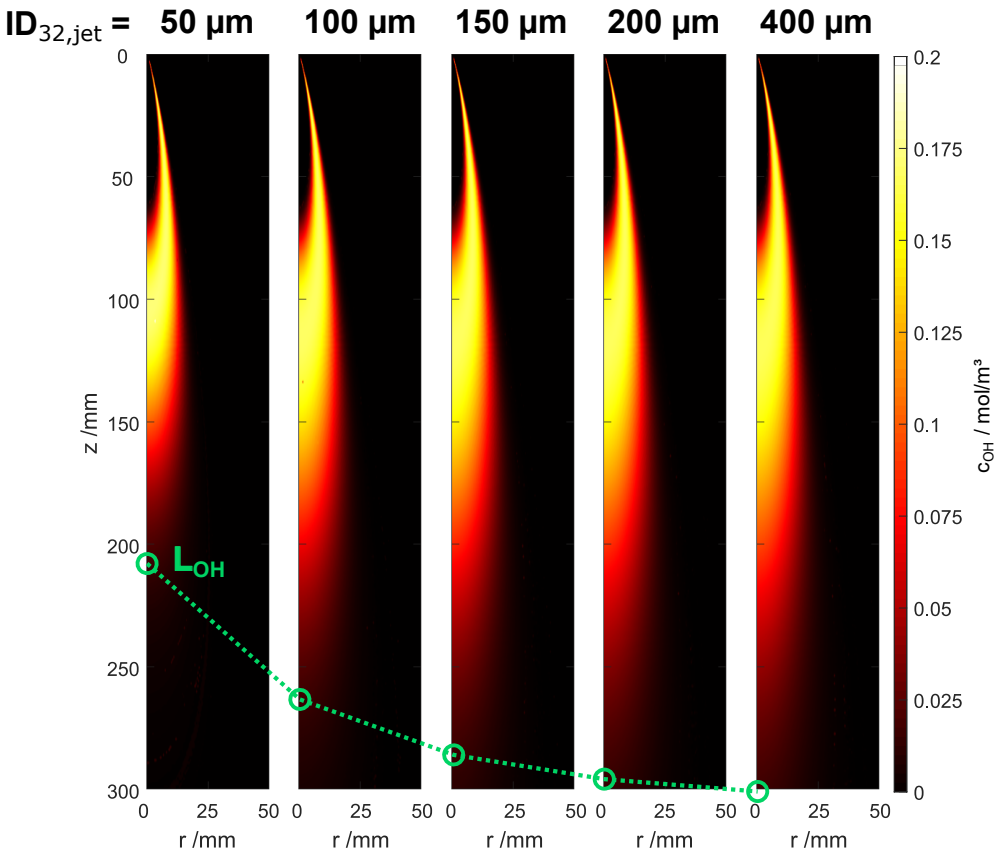


Figure 5.6: Calculated OH-concentration fields and L_{OH} derived from the OH-data for droplet sizes from d_{32} = 50 µm to d_{32} = 400 µm. Constant parameters: J_{gas}=0.45 N, $\theta_{0.9}$ = 25 °, evaporation model: d^2-law. Fuel: Glycerol, input mass flows analogous to the GLYCEROL-experiments.

As long as lean conditions are present, the higher fuel evaporation rate for the smaller d_{32} cases leads to slightly higher gas temperatures due to fuel combustion in addition to syngas combustion reactions, as shown in Fig. 5.7 b). After reaching $\lambda_{\mathrm{abs}} = 1$, further fuel evaporation causes a decrease in temperature due to evaporation cooling and endothermic gasification reactions in addition to entrainment of syngas. This leads to lower temperatures in the downstream flame region for the smaller d_{32} cases in comparison to the 400 µm case. As shown by Fig. 5.7 b), the lower stiochiometry λ_{abs} and the lower temperatures in the downstream flame region also lead to a faster decline of the OH molar fraction y_{OH} for smaller droplet diameters, which is in line with the experimental validation data (see Appendix D.2).

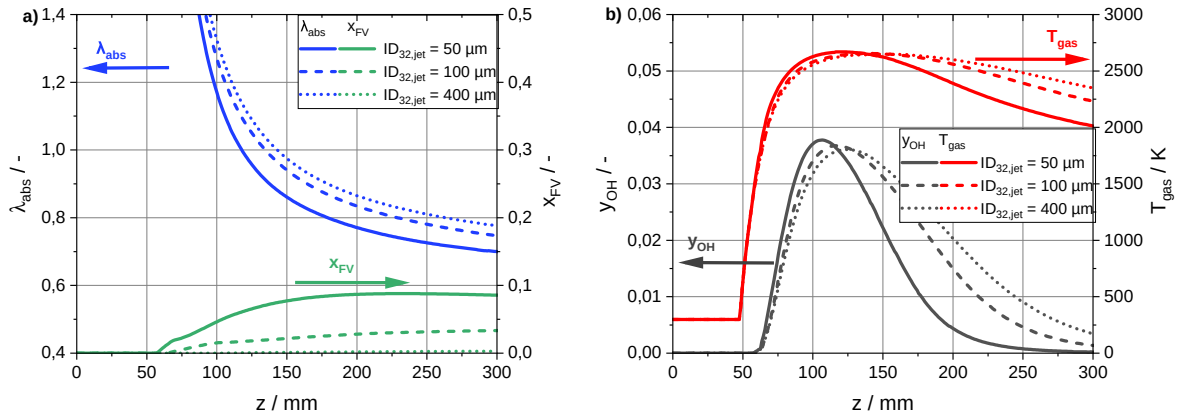


Figure 5.7: Impact of droplet size on axial profiles of λ_{abs}, T_{gas}, x_{FV}, y_{OH} calculated using the 2-Ph-FJM. Droplet size was varied from d_{32} = 50 µm to d_{32} = 400 µm. Constant parameters: J_{gas}=0.45 N, $\theta_{0.9}$ = 25 °, evaporation model: d^2-law. Fuel: Glycerol, input mass flows analogous to the experiment.

5.1.4 Influence of Spray Angle on EFG Flame

This section aims to numerically investigate the effect of liquid mass flux distribution on EFG flame length and shape using the spray angle $\theta_{0.9}$ as representative parameter (see section 3.3.5). A model study based on the **GLYCEROL**-dataset described in section 3.4.2 is conducted to study temperature field and OH distribution in the EFG flame under the influence of spray angle. Experimental validation data for the effect of spray angle is given in Appendices C.2.2, D.1 and D.2. The considerations made in this section are partly published in [15].

Fig. 5.8 shows OH concentration and L_{OH} in the burner near region for input conditions analogous to the **GLYCEROL**-experiments applying geometry parameters of nozzle B (d_{eq} = 4.3 mm). Spray angle is varied from $\theta_{0.9}$ = 15 ° to $\theta_{0.9}$ = 40 °. A droplet size of d_{32} = 50 µm is applied, as the effect of spray angle becomes more pronounced for smaller droplet sizes. It is observed that a decrease in spray angle from 40 ° to 25 ° leads to a shorter OH zone, which is reflected by the decrease in L_{OH}. Further narrowing the spray again decreases L_{OH}, but additionally, a shift of the closed flame shape to a hollow cone shape occurs. This hollow cone shape is especially pronounced for the smallest spray angle $\theta_{0.9}$ = 15 ° and resembles the flame observed under similar conditions for case MEG-B in section 5.1.1.

To explain this effect, radial profiles of absolute stoichiometry λ_{abs}, gas temperature T_{gas}, fuel vapour mass fraction in the jet mixture x_{FV} (eq. 4.8) and OH mole fraction y_{OH} at an axial distance z = 150 mm are presented in Fig. 5.9 for 3 selected model cases. A wider spray angle reduces liquid mass flux at the jet centerline, whereas at higher radial distances from the jet centerline, liquid mass flux is increased. The case featuring $\theta_{0.9}$ = 40 ° thus shows the highest λ_{abs} at the jet centerline in comparison to the other cases,

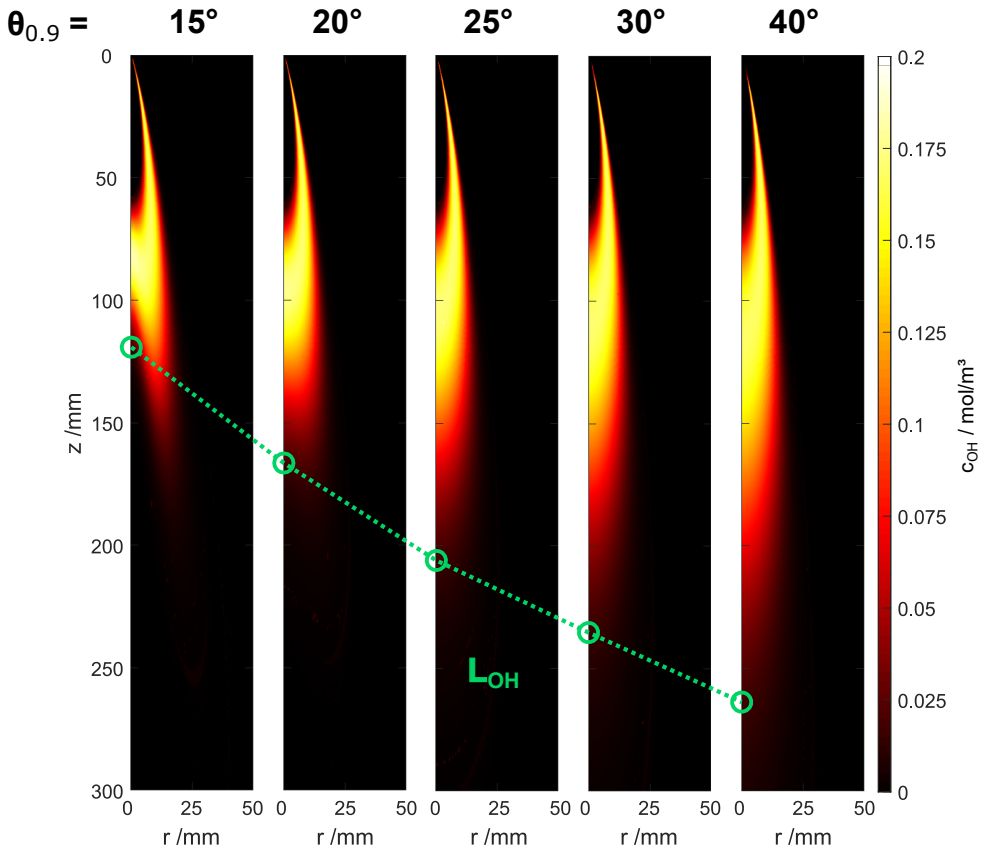


Figure 5.8: OH-concentration fields and L_{OH} for spray angles from $\theta_{0.9} = 15\,^{\circ}$ to $\theta_{0.9} = 40\,^{\circ}$ calculated using the 2-Ph-FJM. Constant parameters: J_{gas}=0.45 N, $d_{32} = 50$ µm, evaporation model: d^2-law. Fuel: Glycerol, input mass flows analogous to the GLYCEROL-experiments.

because the amount of fuel evaporation indicated by x_{FV} at the jet centerline is lowest as the smallest amount of liquid fuel is available for evaporation. This also causes the highest T_{gas} and y_{OH} at the jet axis. A narrower spray angle with $\theta_{0.9} = 25\,^{\circ}$ increases the amount of liquid fuel within the gas free jet angle, enhancing evaporation in the jet dominated region (see Fig. 5.9). This leads to lower gas phase stoichiometries, which reduces T_{gas} and y_{OH}.

A further decrease of spray angle to $\theta_{0.9} = 15\,^{\circ}$ strongly increases the amount of fuel evaporation at the jet centerline, which is reflected by the high values of x_{FV} in this case. In contrast to the other cases, local stoichiometry shows a local minimum at $r = 0$. The profiles of both T_{gas} and y_{OH} show a transition from a bell-shape to am M-shape, which is in agreement with the experimental results from section 5.1.1.

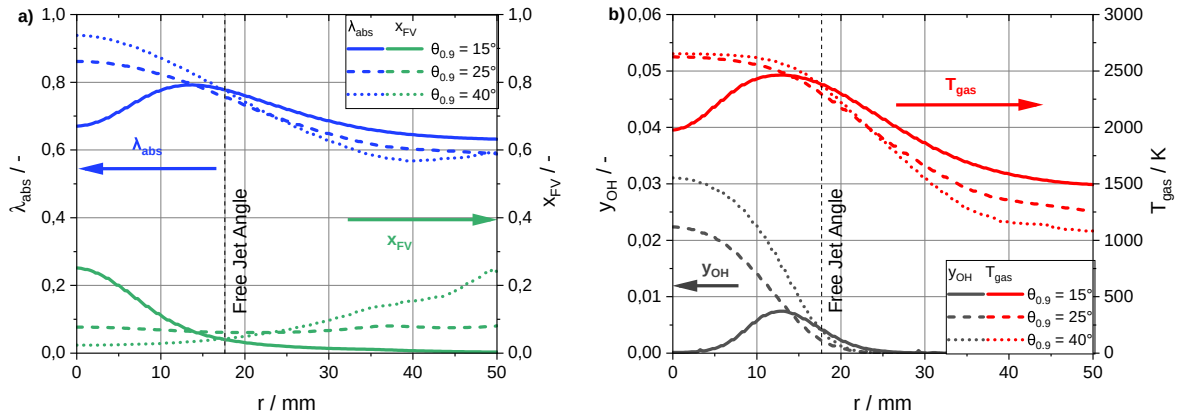


Figure 5.9: Radial profiles of λ_{abs}, T_{gas}, x_{FV}, y_{OH} at z = 150 mm for spray angles from $\theta_{0.9} = 15\,^{\circ}$ to $\theta_{0.9} = 40\,^{\circ}$. Constant parameters: J_{gas}=0.45 N, d_{32} = 50 µm, evaporation model: d^2-law. Fuel: Glycerol, input mass flows analogous to the GLYCEROL-experiments.

5.1.5 Comparison of Parameter Sensitivities

After the individual impacts of the burner related parameters gas momentum flow, droplet size and spray angle on the flame have been analyzed in the previous sections 5.1.2 - 5.1.4, their interaction is now assessed using the 2-Ph-FJM.

As fuel evaporation is influenced by both spray angle and droplet size, their impact is compared in Fig. 5.10 using the longitudinal extension of the OH zone L_{OH} as a characteristic parameter. Spray angle was varied from 15° to 50°, while droplet size distributions with Sauter mean diameter (d_{32}) values ranging from 25 µm to 400 µm were applied.

As analyzed before, both an increase in $\theta_{0.9}$ and d_{32} lead to a longer flame, indicated by increasing L_{OH}. For small spray angles $\theta_{0.9} < 25°$ and small droplet sizes $d_{32} < 150$ µm, the sensitivity of L_{OH} on these parameters is most pronounced, since these cases feature the highest amount of evaporation within the jet. For larger spray angles and droplet sizes, i.e. cases with lower fuel evaporation rate, L_{OH} approaches a maxmimum value of around $L_{\mathrm{OH}}/d_{\mathrm{eq}} = 70$. This value is determined by the entrainment of syngas into the gas jet and corresponds to the length of a pure gas inverse diffusion flame of oxidizer and syngas under the given conditions. There is no significant influence of spray angle on L_{OH} for $d_{32} = 400$ µm, as in this case, only a negligible amount of fuel evaporation takes place in the flame (see above).

For model validation, experimental values of L_{OH} for the cases B50, B100 an B200 are displayed in Fig. 5.10 together with a calculated curve for $d_{32} = 64.5$ µm, approximately corresponding to the experimental cases. The model overpredicts the values of L_{OH} for the experimental cases by at maximum 13 %. Since the main goal of applying the 2-Ph-FJM is to investigate the interaction of the sub-processes and to evaluate their impact on reaction zone structure and fuel conversion, deviations from the absolute experimental

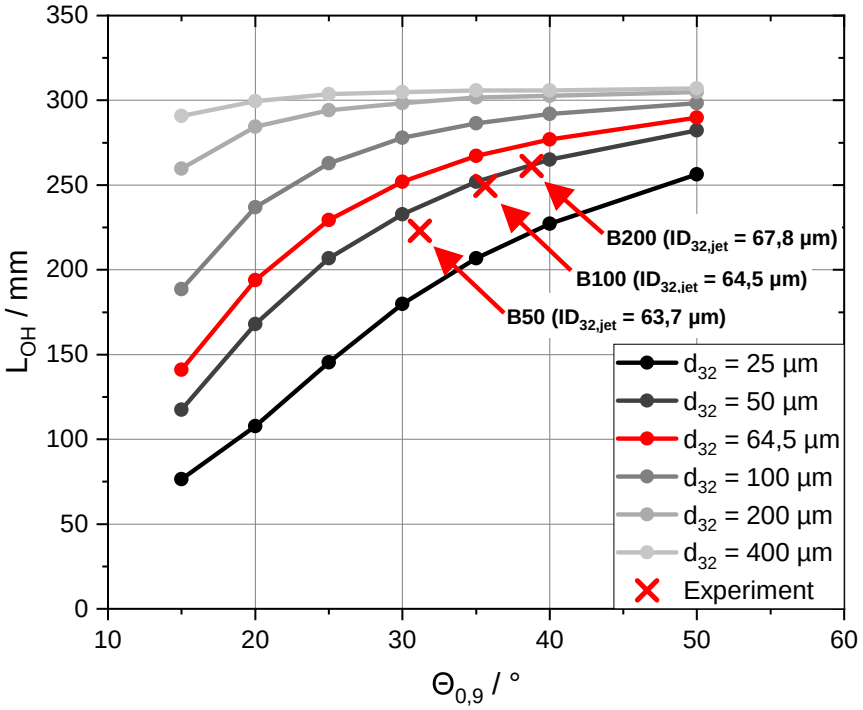


Figure 5.10: Calculated L_{OH} for spray angles from $\theta_{0.9} = 15\,^{\circ}$ to $\theta_{0.9} = 40\,^{\circ}$ and droplet sizes from $d_{32} = 25$ µm to $d_{32} = 400$ µm using the d^2-law as evaporation model. Measured values of L_{OH} from cases B50, B100 and B200 are displayed for reference. Constant parameters: J_{gas}=0.45 N, Fuel: Glycerol.

values are to be expected. Considering this aspect however, the calculated values match the experimentally determined longitudinal extensions of OH well.

As the longitudinal extension of the OH zone defined by L_{OH} only considers the jet centerline, it cannot describe the transition from the closed to the hollow cone flame shape discussed above. Thus, the OH aspect ratio AR_{OH} (see section 4.3.5) will now be considered as additional parameter. Fig. 5.11 shows a heatmap of AR_{OH} for the model cases described above. Fields of local stoichiometry and the respective OH contours are provided for two selected cases. It is evident that for high spray angles and droplet diameters, i.e. conditions that reduce fuel evaporation within the jet, the flames show a closed shape, which is expressed by $AR_{OH} = 1$. If the spray conditions promote fuel evaporation within the jet, the flame shape can deviate from this. For small spray angles of $\theta_{0.9} < 20\,^{\circ}$, fuel evaporation at the jet centerline can be high enough to induce a local minimum of absolute stoichiometry. Under these conditions, a hollow cone flame shape expressed by $AR_{OH} < 1$ can occur, which is amplified by smaller droplet sizes.

In the following, syngas entrainment determined by J_{gas} is additionally considered in order to identify the most relevant parameters for the EFG flame. Cases B50 and A200 were selected as reference for further numerical investigation, which both are validated against experimental results (see Appendix D.2). Case B50 was chosen as a case with

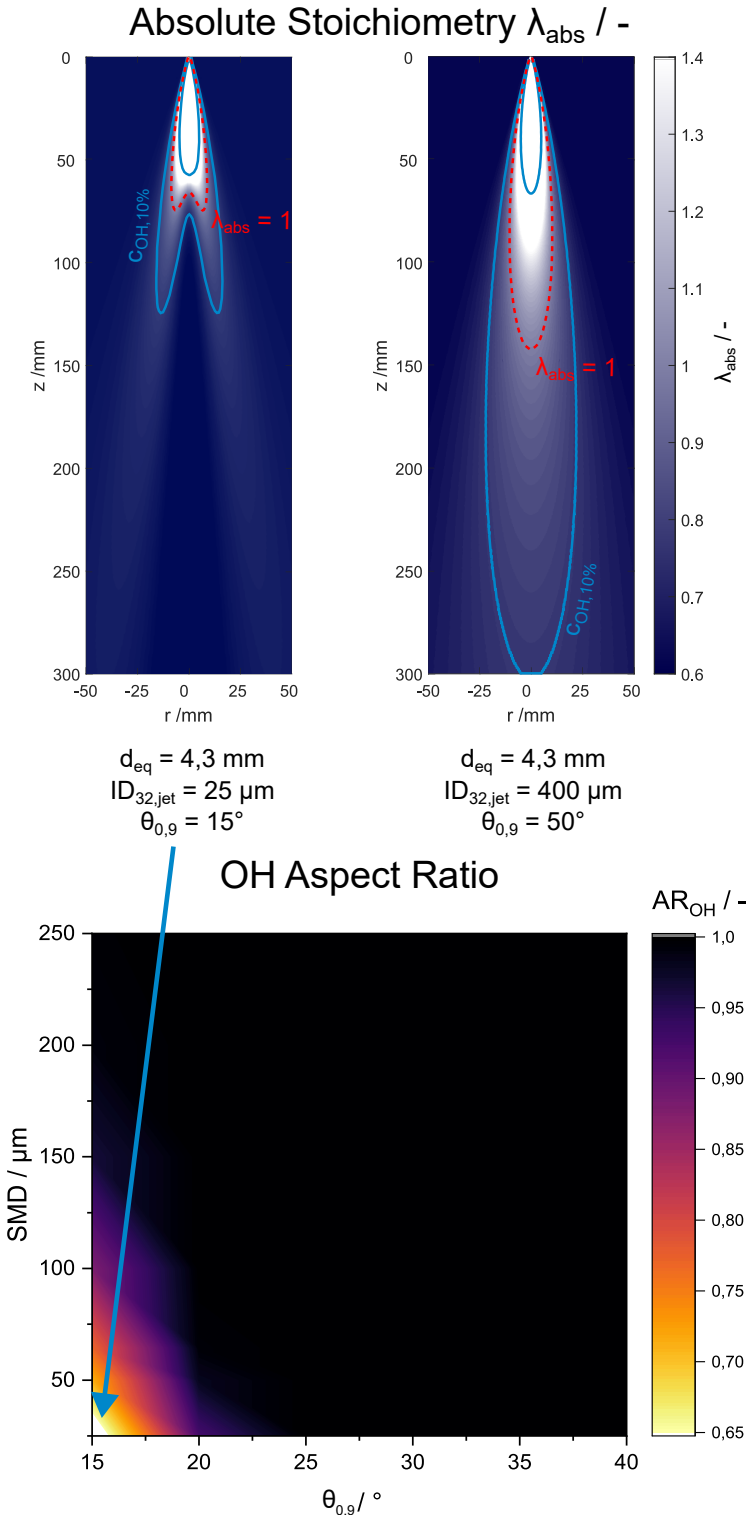


Figure 5.11: Calculated fields of λ_{abs} and $\mathrm{AR_{OH}}$ for spray angles from $\theta_{0.9} = 15\,^{\circ}$ to $\theta_{0.9} = 50\,^{\circ}$ and droplet sizes from $d_{32} = 25$ µm to $d_{32} = 400$ µm using the d^2-law as evaporation model. J_{gas}=0.45 N, Fuel: Glycerol, input mass flows analogous to the GLYCEROL-experiments.

small droplet diameter and narrow fuel spray where a high spray influence is expected, whereas case A200 is selected as a case with larger droplets and wider spray angle. The

parameters $\theta_{0.9}$, d_{32} and d_{eq} were varied in a range of ±30 % around the setpoints of the respective cases. Results for the calculated values of L_{OH} are displayed in Fig. 5.12.

Variation of d_{eq} results in the strongest effect on L_{OH} in both cases, showing the entrain-

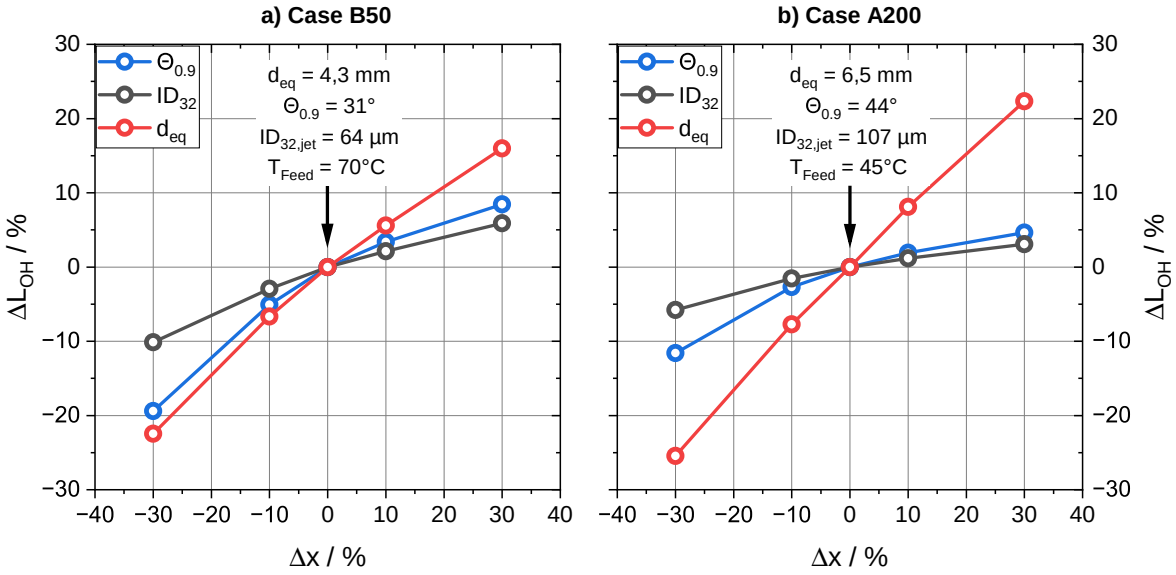


Figure 5.12: Sensitivity of L_{OH} towards changes in $\theta_{0.9}$, d_{32} and d_{eq} calculated using the 2-Ph-FJM. Fuel: Glycerol, evaporation model: d^2-law, input mass flows analogous to the GLYCEROL-experiments.

ment of syngas to be the dominant factor determining flame length under the investigated conditions. For case A200, an almost proportional dependence of L_{OH} on d_{eq} is observed. This proportional relationship would ideally be expected from free jet theory for a pure turbulent gas diffusion flame without a fuel spray superposition (see Fundamentals section 2.2.7). For case B50 featuring a higher fuel evaporation rate, the spray influence indicated by the curves of $\theta_{0.9}$ and d_{32} is stronger and the impact of d_{eq} is reduced compared to case A200. These results imply that for larger droplet diameters and spray angles as in case A200, the flame is almost exclusively governed by entrainment of ambient syngas, while for spray conditions promoting fuel evaporation in the jet, the fuel spray parameters become an additional secondary source of influence.

5.2 Fuel Evaporation

This section deals with the detailed analysis of the liquid evaporation processes in the EFG flame, focusing on **Objective 2** (Quantification of the influence of gas momentum flow, droplet size and spray angle on liquid fuel conversion within a liquid fuel EFG flame). After the response of the flame to changes in process parameters has been investigated in the last section, this section concentrates on the amount of liquid evaporation occurring within the flame boundaries, how it is influenced by the process parameters and the resulting implications for technical EFG burners. Results of this section have in part been published in [16]. All experimental data and modeling results are based on the **MEG** dataset (see section 3.4.1).
The section is structured as follows: Section 5.2.1 describes the processes during fuel evaporation in the EFG flame using experimental data of case MEG-A supported by model calculations. The observations gained in the first chapter again provide a starting point for model sensitivity studies. The impact of droplet residence time in the EFG flame and its relation to gas momentum flow is assessed in section 5.2.2 by numerical calculations supported by experimental data. As droplet size and spray angle significantly affect fuel evaporation but also alter flame length and shape, this coupling is numerically investigated in section 5.2.3. The relation between gas momentum flow and spray parameters is also considered in this section.
Further validation data regarding the prediction of spray parameters under ambient and reacting conditions by the 2-Ph-FJM is provided in Appendix C.2.4. An additional numerical study on the impact of the liquid evaporation model is presented in Appendix C.3.1.

5.2.1 Droplet Evaporation in the EFG Flame

In this section, fuel evaporation in the EFG flame is investigated using detailed spray data from case MEG-A (see 3.4.1) and supporting model calculations. The flame for this case has been analyzed in section 5.1.1.
Fig. 5.13 shows representative images of the near-nozzle region for case MEG-A recorded under ambient and reacting conditions, respectively. The image under ambient conditions (Fig. 5.13 left) shows a flapping primary instability caused by the low gas exit velocity of 69 m/s, which is consistent with prior work on atomization using external mixing twin-fluid nozzles (see section 2.2.1). It is evident that through the flapping primary instability, a significant portion of the liquid fuel is found outside the gas jet, indicated by the dotted red lines. These droplets are typically large and follow ballistic trajectories. The comparatively wide spray angle of $\theta_{0.9} = 40.4\,^\circ$, measured under ambient conditions by patternator experiments, is represented by the dashed blue lines (see Appendix D.1).

The spray images under reacting conditions (Fig. 5.13 right) indicate the same situation for the gasification experiment.

Fig. 5.14 shows radial profiles of mean droplet velocties u_{drop} and Sauter mean diameter

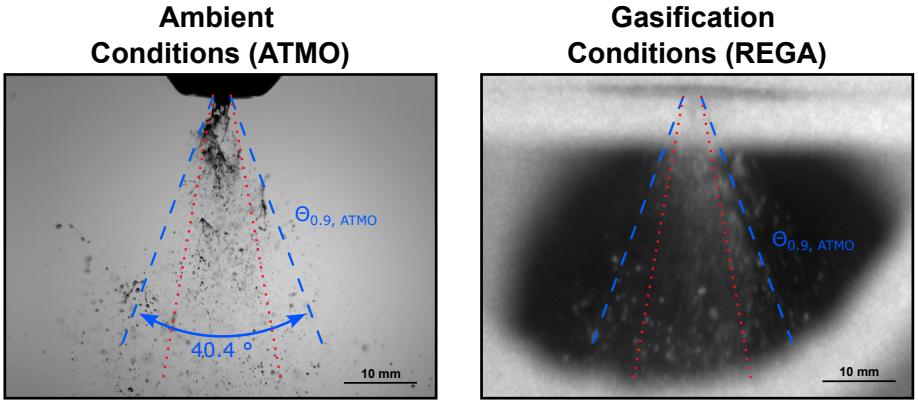


Figure 5.13: High-speed camera images of the nozzle near area for case MEG-A under ambient and reacting conditions. Spray angle (dashed blue lines) and gas free jet angle starting from the virtual jet origin (dotted red lines) are marked. Process conditions: J_{gas}=0.20 N, ID_{32} = 160 µm, $\theta_{0.9}$ = 40.4 °, T_{ad} = 1700 °C, Fuel: MEG. Data published in [15].

d_{32} for case MEG-A at different axial nozzle distances under reacting conditions. The graph shows bell-shaped droplet velocity profiles that become wider with increasing nozzle distance, which is expected for a 2-Phase Free Jet (see Fundamentals section 2.2.2).
Whereas under non-reacting conditions, the centerline velocity of the droplets would decrease along the jet axis, the centerline droplet velocity under reacting conditions shows no substantial decline and even increases from z = 50 mm to z = 100 mm. This is caused by the expansion of the gas phase through exothermic oxidation reactions and fuel evaporation [11] and is consistent with model calculations (see Appendix C.2.4).
At z = 50 mm, d_{32} shows a U-shaped profile with a minimum at the jet axis and an increase of droplet size further outwards. For increasing axial nozzle distances, the profiles flatten, expressed by an increase of d_{32} at the jet centerline and a decrease in the outer regions of the jet. While the decrease of droplet size far from the jet centerline is also present in the ambient spray data, the increase of droplet size at the jet centerline occurs exclusively under reacting conditions as it is caused by evaporation. The data generated by the 2-Ph-FJM shows the same qualitative trends, although quantitative discrepancies appear (see Appendix C.2.4 for further detail).

To explain the increasing d_{32}, measured droplet size distributions at the jet centerline at z = 50, 150 and 250 mm are shown in Fig. 5.15 (top). The data clearly shows a shift towards higher droplet sizes with increasing nozzle distance. Small droplets with $d < 50$ µm present at z = 50 mm have almost completely vanished at z = 250 mm. While droplets with $d < 100$ µm constitute roughly 50 wt-% of the spray at z = 50 mm, this fraction

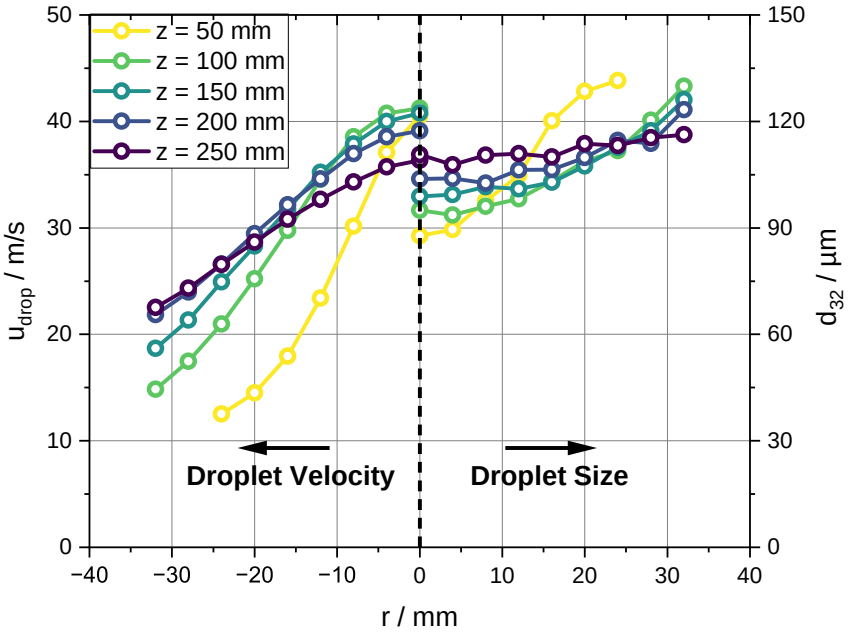


Figure 5.14: Radial half-profile of droplet velocity and radial half-profile of droplet size for case MEG-A measured by PDA under reactive conditions. Process conditions: J_{gas}=0.20 N, ID_{32} = 160 µm, $\theta_{0.9}$ = 40.4 °, Fuel: MEG. Data published in [16].

contributes only around 30 wt-% to the spray at z = 250 mm. The 2-Ph-FJM-calculation is in line with this observation. Fig. 5.15 (bottom) shows calculated diameters of selected droplet size classes from the droplet collective along the trajectory at the jet centerline together with the respective OH-concentration profile. Simulations show that heating of the droplets starts at an axial distance of about 71 mm at the end of the core zone. The initial increase in droplet diameter is caused by the reduction of liquid density with increasing droplet temperature. The droplet diameters then decrease according to the d^2-law. The 12.5 µm droplet class fully evaporates within a nozzle distance of 103 mm, whereas larger droplets take a longer distance to heat up and evaporate. The 59.8 µm droplet class (not shown) is the largest class to fully evaporate within the OH zone. Larger droplet classes take considerably longer to heat up and show only a small decrease in droplet size within the OH zone, which shows that only a small amount of fuel is released by these large droplets within the oxidation zone. These droplets release most of the fuel vapor in the gasification zone and may thus contribute to the formation of unwanted by-products during the technical process. These observations and the model based description within this work provide a starting point for further investigations on this matter.

To study the fuel evaporation progress within the entire flame volume, the OH concentration field of case MEG-A is displayed in Fig. 5.16 together with mass concentration of liquid fuel $\chi_{liq}(z,r)$ and local fuel conversion $X_{liq}(z,r)$ calculated using the 2-Ph-FJM. It

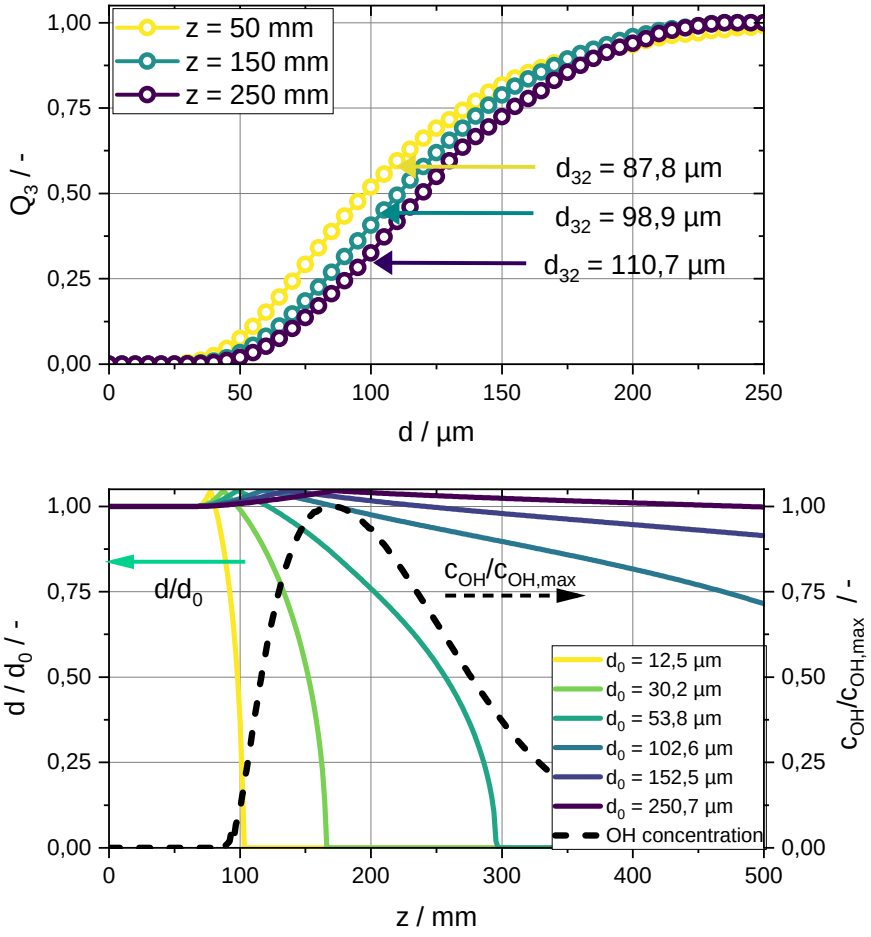


Figure 5.15: Droplet size distribution at the jet centerline for different nozzle distances, measured under reaction conditions using PDA (upper). Calculated diameter of different droplet size classes along the jet centerline using the d^2-law as evaporation model (lower) using the 2-Ph-FJM. Process conditions: MEG-A, J_{gas}=0.20 N, ID_{32} = 160 µm, $\theta_{0.9}$ = 40.4 °, Fuel: MEG. Data published in [16].

is evident that only low X_{liq} are reached in the flame zone. The total amount of liquid evaporation within the flame volume was calculated to be $X_{liq,OH}$ = 15 %, applying the d^2-law ($X_{liq,OH}$ = 23 % for the heat transfer controlled evaporation model, see section 2.2.3).

For case MEG-B on the other hand, an integral fuel conversion of $X_{liq,OH}$ = 22 % is calculated using the d^2-law ($X_{liq,OH}$ = 32 % for the heat transfer controlled evaporation model). This substantial difference to case A is caused by the changes in gas momentum flow, droplet size and spray angle induced by the different burner nozzles. The impact of these parameters on fuel evaporation in the EFG flame will be further investigated in the following sections. Spray data under ambient and reactive conditions as well as modeling results for case MEG-B are provided in Appendix sections C.2.4 and D.1.

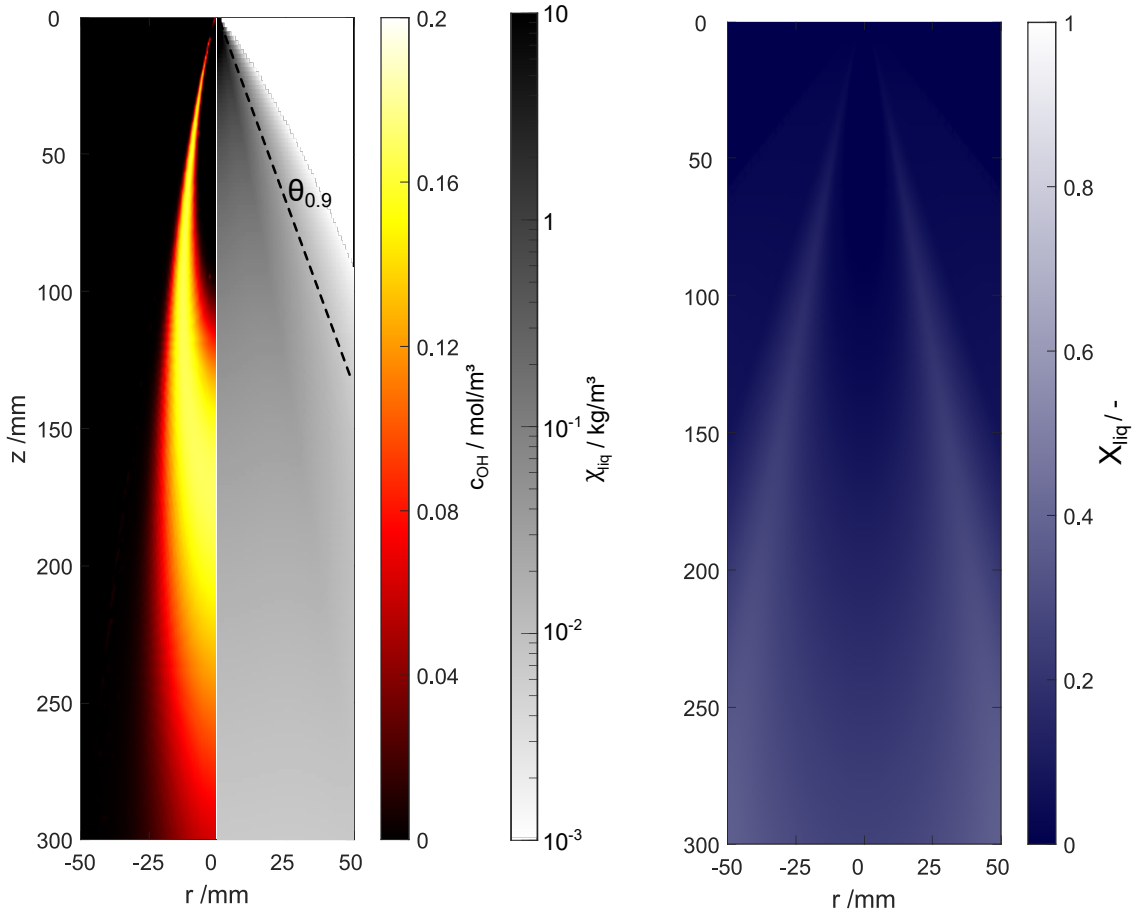


Figure 5.16: Calculated fields of OH concentration c_{OH}, liquid fuel concentration χ_{liq} and local liquid evaporation progress X_{liq} applying the d^2-law as evaporation model. Process conditions: MEG-A, J_{gas}=0.20 N, ID_{32} = 160 µm, $\theta_{0.9}$ = 40,4 °, Fuel: MEG. Data published in [16].

5.2.2 Influence of Droplet Residence Time on Evaporation Progress in Flame

This section discusses the impact of droplet residence time on fuel evaporation in the EFG-flame and its relation to gas momentum flow using experimental data and model calculations. Fig. 5.17 shows droplet residence times τ for cases MEG-A and MEG-B along the jet centerline derived from experimental PDA data (see section 3.3.3) and the longitudinal extensions of the OH zone L_{OH} calculated from the OH-LIF measurements. Additionally, droplet residence time calculated using the 2-Ph-FJM and the d^2-law are

added for comparison.

The lower gas momentum flow in case MEG-A in comparison to case MEG-B leads to lower droplet velocities, which results in a higher residence time over nozzle distance z. The calculated droplet residence times match the values derived from the experimental droplet velocities well for both cases. Additionally, as analyzed in section 5.1.2, the lower gas momentum flow also causes a higher L_{OH} for case MEG-A in comparison to case MEG-B due to the lower entrainment rate of ambient syngas into the jet. These two effects both contribute to the overall residence time of the droplets in the flame along the jet centerline, which is substantially higher for case MEG-A ($\tau_{OH,axis} \approx 10.1$ ms) as compared to case MEG-B ($\tau_{OH,axis} \approx 2.5$ ms).

In order to study the impact of this effect on fuel evaporation, model calculations using

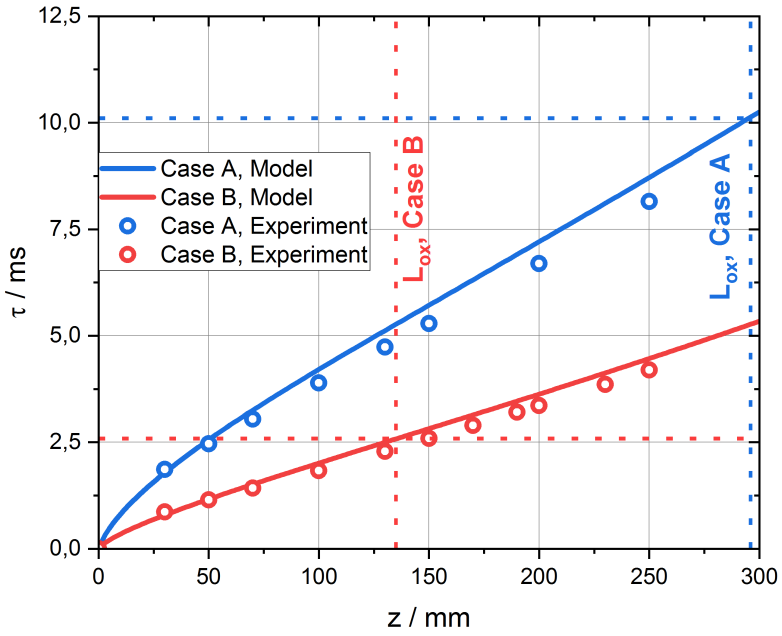


Figure 5.17: Calculated and experimentally determined droplet residence times along the jet axis for cases MEG-A (J_{gas}=0.20 N, ID_{32} = 160 µm, $\theta_{0.9}$ = 40,4 °) and MEG-B (J_{gas}=0.45 N, ID_{32} = 73 µm, $\theta_{0.9}$ = 23,5 °). Fuel: MEG. Data published in [16].

the input conditions of the **MEG**-cases were conducted for nozzles with d_{eq} ranging from 4 - 10 mm, leading to gas momentum flows J_{gas} from 0.08 - 0.48 N ($u_{0,gas}$ from 184 - 29 m/s). A spray angle of $\theta_{0.9} = 20\,°$ and a droplet size distribution featuring a Sauter mean diameter of d_{32} = 100 µm was used in all calculations. Calculated droplet residence times along the axis $\tau_{OH,axis}$ and fuel evaporation progress along the jet centerline $X_{liq,OH,axis}$ each within the OH zone are shown in Fig. 5.18. Because the longitudinal extension of the OH zone L_{OH} itself is affected by fuel evaporation, its values are also displayed in absolute and nondimensional form L_{OH}/d_{eq}. A similar investigation has been conducted by [13].

The graph shows that for decreasing J_{gas}, the residence time of the droplets in the OH zone significantly increases, which was also observed in the experiments above. As droplets have more time to evaporate, this causes higher degrees of fuel evaporation $X_{liq,OH,axis}$ within the OH zone for lower J_{gas}. This leads to an increased amount of fuel vapor reacting under oxidizing conditions, which shifts oxygen consumption from oxidation of entrained syngas towards oxidation of fuel vapor. The proportional relationship between d_{eq} and L_{OH}, which would be expected for an ideal IDF of syngas and gasification medium, thus shifts to a slower increase (further detail given in section 5.1.5). Normalized values of L_{OH} also reflect this by a decrease from $L_{OH}/d_{eq} \approx 57$ for conditions featuring the lowest fuel evaporation to $L_{OH}/d_{eq} \approx 34$ for the $d_{eq} = 10$ mm case.
In conclusion, as long as spray parameters are kept constant, a low gas momentum increases the amount of fuel evaporation within the EFG flame. However, spray parameters are strongly affected by gas momentum flow if external mixing twin fluid nozzles are applied. This interaction is explored in the next section.

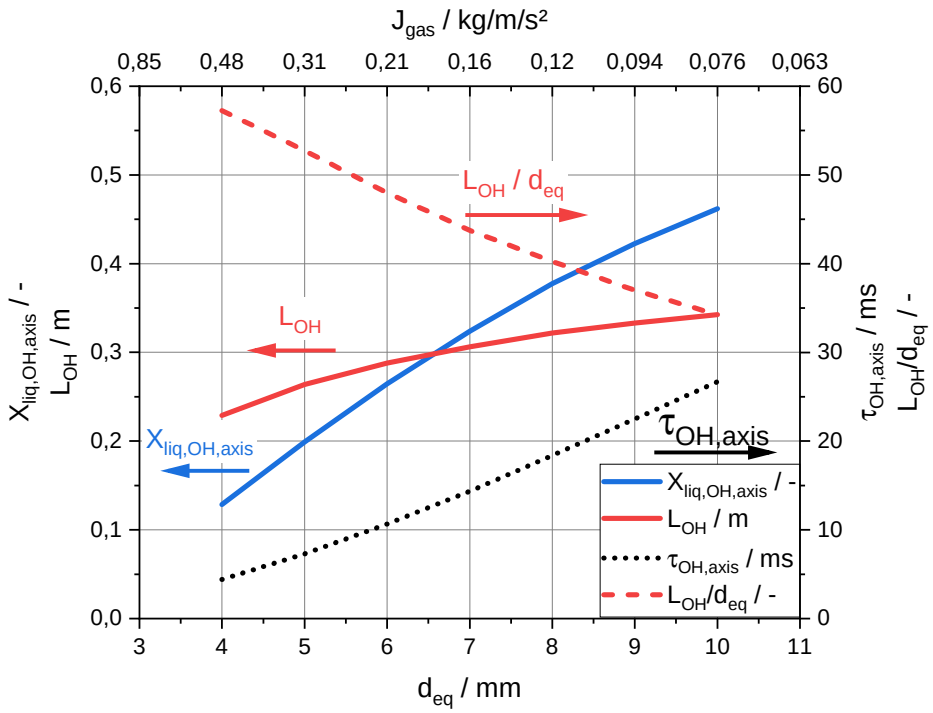


Figure 5.18: Influence of J_{gas} on droplet residence time $\tau_{OH,axis}$ and evaporation progress $X_{liq,OH,axis}$ within the OH zone along the jet centerline calculated using the 2-Ph-FJM. Constant parameters: $\theta_{0.9} = 20\,°$, $d_{32} = 100$ µm, evaporation model: d^2-law. Fuel: MEG, input mass flows analogous to the MEG-experiments.

5.2.3 Influence of Spray Parameters on Evaporation Progress in Flame

Isolated Variation of Spray Parameters

This section aims to quantify the effects of droplet size and spray angle on the total amount of liquid fuel evaporation within the EFG flame using the 2-Ph-FJM. In section 5.1, it was shown that both parameters affect the flame through their influence on local stoichiometry. Due to this coupling, no straight forward conclusions on the impact of spray parameters on total fuel evaporation within the flame can be drawn.

The integral degree of fuel evaporation within the OH zone $X_{\mathrm{liq,OH}}$ is considered in a modeling study for a range of spray angles ($\theta_{0.9} = 15 - 40\,^{\circ}$) and droplet size distributions ($d_{32} = 50 - 250$ µm) for a nozzle featuring $d_{\mathrm{eq}} = 6$ mm and input mass flows as in the **MEG**-experiments. The d^2-law was applied as evaporation model. The results in Fig. 5.19 indicate that over the entire investigated parameter range, finer sprays lead to higher $X_{\mathrm{liq,OH}}$, which is not surprising. For larger d_{32}, only very small amounts (< 10 %) of the fuel evaporate within the OH zone. Even under the most favorable investigated conditions, only around 40 % of the fuel is found to evaporate within the flame.

A wide spray angles causes a substantial amount of fuel droplets to move on trajectories outside the flame, decreasing $X_{\mathrm{liq,OH}}$. This situation occurs in case MEG-A, which has been analyzed above (see section 5.2.1). A narrower spray angle increases $X_{\mathrm{liq,OH}}$, because more liquid fuel is on trajectories within the gas jet. This leads to an optimum of $X_{\mathrm{liq,OH}}$ at around $\theta_{0.9} = 20\,^{\circ}$, as indicated by the isolines. For very narrow spray angles $\theta_{0.9} < 20\,^{\circ}$, a decrease of $X_{\mathrm{liq,OH}}$ is evident. This is caused by the development of a cold, fuel rich zone at the jet centerline that inhibits evaporation (hollow cone flame). This situation has been experimentally observed in case MEG-B and is described in section 5.1.4 and 5.1.5.

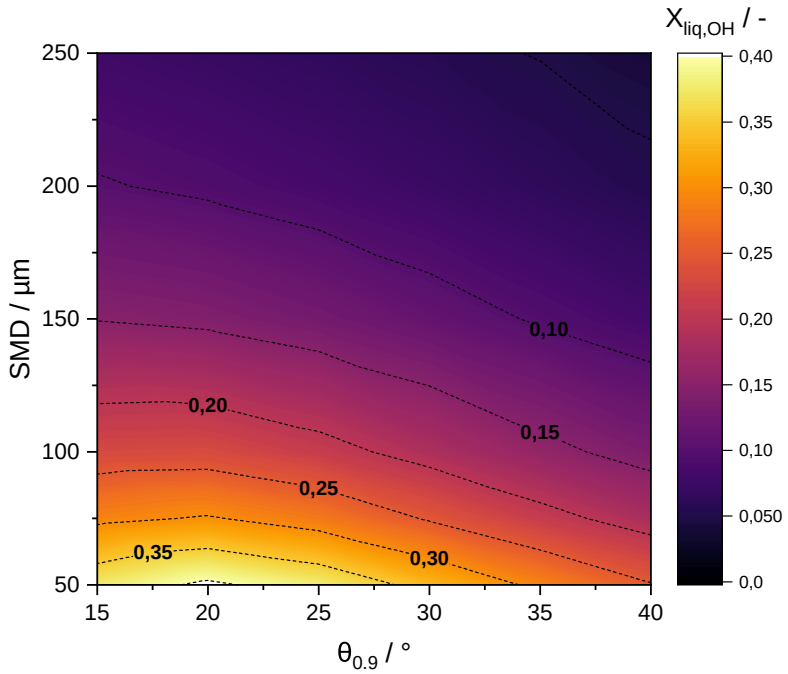


Figure 5.19: Calculated $X_{\mathrm{liq,OH}}$ for spray angles from $\theta_{0.9} = 15\,^{\circ}$ to $\theta_{0.9} = 40\,^{\circ}$ and droplet sizes from $d_{32} = 50$ µm to $d_{32} = 250$ µm using the d^2-law as evaporation model. J_{gas}=0.21 N, Fuel: MEG, input mass flows analogous to the MEG-experiments. Data published in [16].

Coupling of Spray Parameters and Gas Momentum Flow

The last section investigated the impact of gas momentum flow on droplet residence time, which was revealed to have a strong impact on the amount of fuel evaporation in the flame. For technical external mixing twin-fluid nozzles, gas momentum flow and spray parameters are linked (see section 2.2.1). Typically, a higher gas momentum flow leads to smaller droplets and narrower spray angles. Fig. 5.20 shows a series of model calculations for input conditions analogous to the **MEG**-dataset, where the gas momentum flow J_{gas} and the Sauter mean diameter d_{32} was varied. For simplification, a constant spray angle of $\theta_{0.9} = 20\,^{\circ}$ is assumed. The integral degree of fuel conversion within the OH zone $X_{\mathrm{liq,OH}}$ is calculated for all J_{gas} and d_{32}. To consider the relationship between gas momentum flow and droplet size for the applied external mixing twin-fluid nozzles, an empirical correlation for Sauter mean diameter in dependence of Weber number developed by [110] was additionally applied in the model calculations, indicated by the red line (see Appendix C.1 for further detail).

It is evident that $X_{\mathrm{liq,OH}}$ generally decreases with gas momentum flow J_{gas} (increases with d_{eq}) for a constant droplet diameter due to the reasons discussed above. The absolute value of $X_{\mathrm{liq,OH}}$ strongly depends on droplet size. Highest fuel conversion within the flame occurs when a small droplet size is produced at low gas momentum flow. For a technical burner, this is however a contradiction. The correlation by [110] was applied

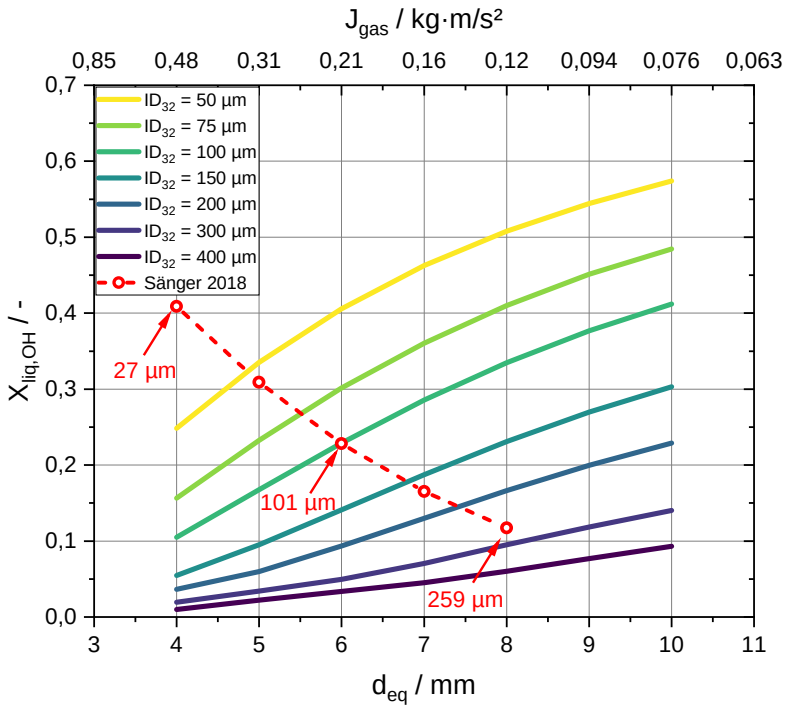


Figure 5.20: Fuel evaporation within the OH zone $X_{\mathrm{liq,OH}}$ calculated for different J_{gas} and droplet sizes from $d_{32} = 50$ µm to $d_{32} = 400$ µm. The red dots indicate values where d_{32} is calculated from J_{gas} using a correlation developed by Sänger [110]. Evaporation model: d^2-law, $\theta_{0.9} = 20\,°$, Fuel: MEG, input mass flows analogous to the MEG-experiments. Data partially published in [16].

in the model calculations in order to investigate which effect dominates for the applied type of burner nozzle (dotted red line). As the correlation does not provide information on spray angle, $\theta_{0.9} = 20\,°$ is again assumed. As indicated by the dotted red line, the highest $X_{\mathrm{liq,OH}}$ is achieved at high gas momentum flow, where the droplet size is the smallest. For decreasing J_{gas}, the effect of the increasing droplet size surpasses the beneficial impact of the increased droplet residence time, leading to decreasing $X_{\mathrm{liq,OH}}$. If a high fuel conversion within the flame boundaries is desired by an operator, a high gas momentum flow should be used, given this atomization characteristic. The model based description of these parameter sensitivities provides a starting point for further investigations on the impact of the burner on the formation of by-products like soot and cenospheres.

5.3 Suspension Fuels

This section investigates addresses **Objective 3** (Assessment of the conversion of suspension fuels in an EFG flame, including (i) the impact of suspension fuel parameters (solid content, solid particle size) on flame structure and (ii) the impact of different suspension droplet models on the predictions of the flame).
To describe the increased complexity of the burner near processes in comparison to liquid fuel gasification, the 2-Ph-FJM was extended with respect to solid phase reactions and suspension droplet conversion in the EFG flame (see sections 4.3.3 and 4.3.4). OH-LIF measurements for different reference suspension fuels consisting of MEG mixed with beech-wood char are used as experimental database for flame structure analysis and for model validation (**SLURRY**-dataset, see section 3.4.3). The complete dataset including char properties, rheological data of the suspensions and ambient spray parameters is given in Appendix B and D.3.
First, flames of a liquid and a suspension fuel are compared. Differences and similarites are discussed based on experimental data supported by model calculations (section 5.3.1). A detailed numerical assessment of suspension droplet conversion in the EFG flame is conducted in section 5.3.2, focussing on the conditions the droplets and solid particles experience during their conversion. Different model approaches are systematically compared in order to study the impact of the droplet conversion model on the flame in section 5.3.3. In the following, the influence of solid particle content and solid particle size in the reference suspension on the flame is assessed using a combined experimental and numerical approach (section 5.3.4).
Validation of the model against all experimental OH data is provided in Appendix D.3. Results of this section have in part been published in [17].

5.3.1 Comparison of Liquid and Suspension Fuel EFG Flame

In this section, the flames of a pure liquid and a suspension fuel are compared using experimental data and model calculations. The **SLURRY**-dataset is designed to compare the gasification of liquid and suspension fuels in the REGA gasifier under constant fuel mass flow, gas momentum flow, adiabatic temperature and residence time. Cases S0 and S30-A are selected for comparison, featuring pure MEG and a mixture of 70 wt-% MEG and 30 wt-% char BWC-A as fuel. Fig. 5.21 shows results of the OH-LIF measurement for both cases together with their respective calculated OH distribution using the Fragmenting Particle Model (see section 4.3.4). For comparison, both quantities are normalized to their maximum value. Ambient condition spray data are used as input for the model calculations (Appendix D.3). Details on the suitability of the Fragmenting Particle Model

approach for the used suspension fuel are given in section 5.3.4. In all calculations, a char conversion degree of $X_{sol,rec} = 100$ % in the recirculated gas was assumed (see Appendix C.3.3)

The structure of the MEG flame indicated by the OH-LIF measurements in Fig. 5.21 is

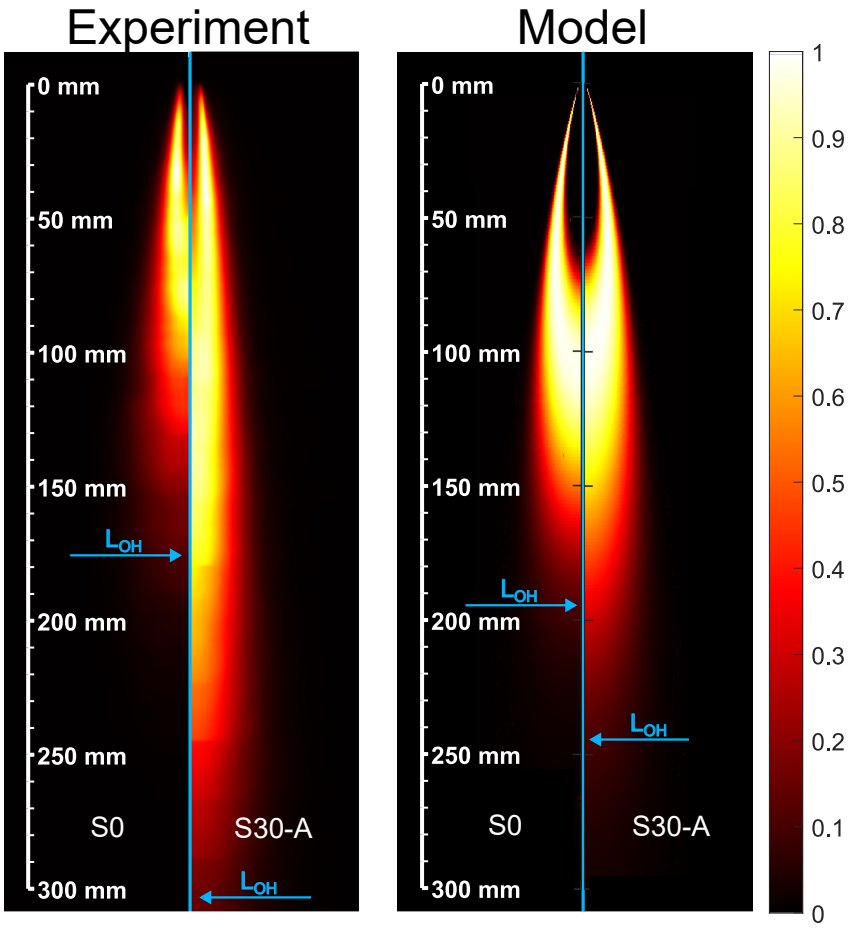


Figure 5.21: Normalized measured OH-LIF intensities and normalized calculated OH concentration fields for cases S0 (J_{gas}=0.34 N, ID_{32} = 114 µm, $\theta_{0.9} = 27\,°$, Fuel: MEG) and S30-A (J_{gas}=0.34 N, ID_{32} = 189 µm, $\theta_{0.9} = 29\,°$, $d_{\mathrm{p,sol}} = 9$ µm, Fuel: MEG with 30 wt-% BWC-A). Evaporation model: Fragmenting Particle model.

the result of the interaction of syngas entrainment and fuel evaporation in the jet and has been discussed in section 5.1.1. The comparison with the measured S30-A flame shows that the principal structure of the flame is not fundamentally altered when solid particles are added to the liquid fuel. However, the OH zone for case S30-A shows a larger extension ($L_{\mathrm{OH}} = 300$ mm) in comparison to the MEG case ($L_{\mathrm{OH}} = 174$ mm).

The 2-Ph-FJM also predicts similar flame structures in both cases. The extension of the core zone is overpredicted by the model in both cases, which is caused by the simplified

description of mixing in the nozzle near area (Appendix C.2.3). Further downstream, better agreement between model and experiment is found. The 2-Ph-FJM captures the trend of a longer OH zone for the suspension fuel. In comparison to the experiments, the longitudinal extension of the OH zone is estimated with reasonable accuracy for MEG ($\Delta L_{\mathrm{OH}} = 13\%$), whereas it is underpredicted for S30-A ($\Delta L_{\mathrm{OH}} = -19\%$).

In order to analyze the increased extension of the OH zone in the suspension fuel case in

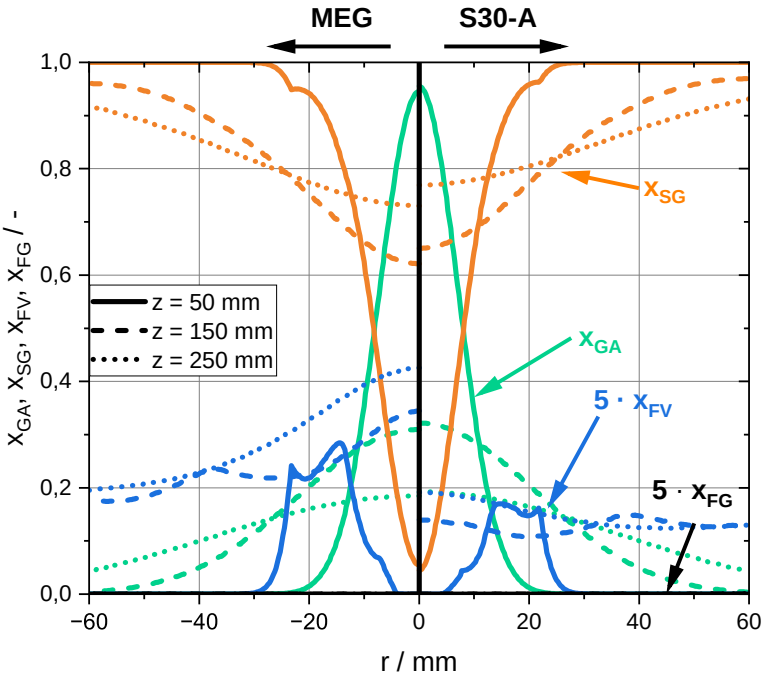


Figure 5.22: Radial profiles of calculated mixture fractions of gasification agent (GA), syngas (SG), fuel vapor (FV) and gasified solid fuel (FG) for cases S0 (J_{gas}=0.34 N, ID_{32} = 114 µm, $\theta_{0.9} = 27\,°$, Fuel: MEG) and S30-A (J_{gas}=0.34 N, ID_{32} = 189 µm, $\theta_{0.9} = 29\,°$, $d_{\mathrm{p,sol}}$ = 9 µm, Fuel: MEG with 30 wt-% BWC-A). Evaporation model: Fragmenting Particle model.

comparison to the pure liquid fuel, calculated radial profiles of mixture fractions x_i for gasification agent, syngas, fuel vapor and gasified solid fuel at three axial nozzle distances are shown in Fig. 5.22. Mass fractions of fuel vapor and gasified solid fuel are multiplied by 5 for better visibility. The jet entrainment rates in both cases are equal due to identical gas momentum flow. Hence, mixing of jet medium and syngas does not differ between both cases, as indicated by x_{GA} and x_{SG} (green and orange lines). It is however evident that more liquid fuel is found in the vapour phase for the gasification of pure MEG compared to the suspension fuel (x_{FV}, blue lines). The lower amount of liquid evaporation in the jet for S30-A leads to higher local stoichiometry λ_{abs} at a given nozzle distance, causing a longer flame zone. Gasified solid fuel mass is not present in significant amounts in the gas phase (x_{FG}, black lines), implying that solid reactions play a minor role for the processes in the flame zone under the investigated conditions. These aspects are analyzed in the

following sections in further detail.

5.3.2 Conversion of Suspension Droplets in EFG Flame

In a numerical study, the conversion of suspension droplets in the EFG flame is examined based on the sub-models described in section 4.3.4. Process conditions for case S30-A (section 3.4.3) are used as input conditions for the 2-Ph-FJM. Fig. 5.23 shows droplet trajectories originating from the nozzle exit in angles of 0°, 7° and 15° for an example droplet size class $d = 75$ µm present in the investigated sprays. Droplet conversion histories in the burner near region are compared for the Fragmenting Particle model and the Shell Formation model (section 4.3.4). The calculated normalized OH concentration field is shown as a reference for the flame.

The figure shows that both models exhibit similar flame lengths and shapes, but concerning droplet conversion, significant differences between the models occur. To reach complete liquid evaporation, the droplets require considerably less distance using the Fragmenting Particle model in comparison to the two-stage evaporation process in the Shell Formation model. The droplets at the outer trajectories generally require a shorter nozzle distance to reach complete liquid evaporation as compared to the droplets at the jet centerline, which is caused by their lower velocities and thus longer residence times in comparison to the inner trajectories. For the Fragmenting Particle model, the 75 µm droplets reach the char conversion stage within or shortly after leaving the OH zone, while for the Shell Formation model, the char conversion is reached further outside the flame. For none of the models, complete char conversion is reached at the end of the simulation domain at an axial nozzle distance of z = 500 mm. Gas temperatures, particle temperatures and species mole fractions surrounding the particles are provided for these trajectories in Appendix C.3.2.

A quantitative comparison of droplet diameter d, evaporated liquid mass fraction of the droplet $X_{\mathrm{liq,drop}}$, converted solid mass fraction $X_{\mathrm{sol,drop}}$ and normalized total droplet mass m/m_0 is shown in Fig. 5.24 for all three investigated droplet conversion models. A 75 µm droplet on the jet centerline trajectory is regarded as an example. As the Wet Particle model assumes single char particles surrounded by a liquid film, droplet and solid particle diameter are linked. Given a char particle size of $d_{\mathrm{p,sol}} = 9$ µm, a solid mass fraction of $x_{\mathrm{sol},0} = 30$ % and the respective densities, the diameter of all droplets for the Wet Particle Model is fixed to 15 µm.

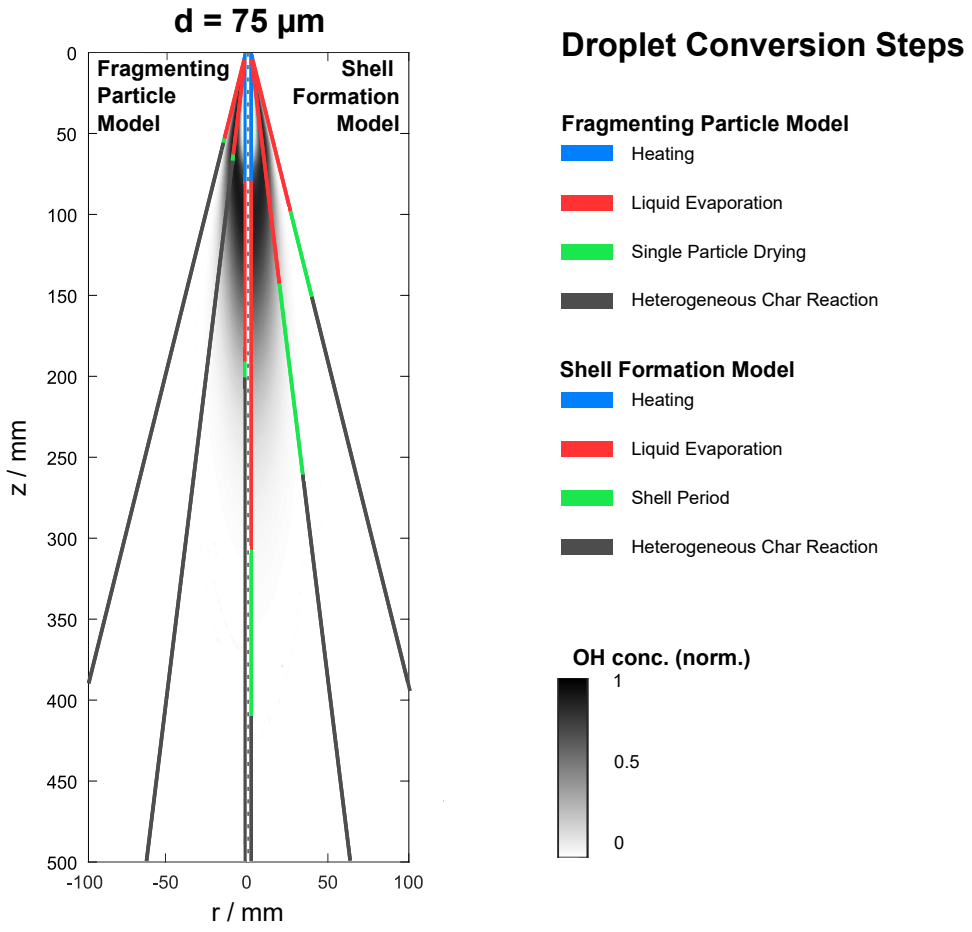


Figure 5.23: Calculated OH concentration fields and particle conversion steps of a 75 µm droplet along selected trajectories for two different suspension droplet conversion models. Input conditions of case S30-A were applied (J_{gas}=0.34 N, d_{32} = 189 µm, $\theta_{0.9}$ = 29 °, $d_{p,sol}$ = 9 µm, Fuel: MEG with 30 wt-% BWC-A). The trajectories displayed are in an angle of 0°, 7° and 15° to the jet centerline.

All models first show a droplet heat up period, in which droplet size initially increases due to the temperature induced decrease in liquid density. The distance required to heat the droplets to the boiling point is around z = 80 mm for the Fragmenting Particle and the Shell Formation Model and around z = 55 mm for the Wet Particle Model, which is caused by the smaller initial droplet size. Due to the quick droplet heat up, the amount of liquid evaporation during the heating phase is shown to be negligible.

The heat up step is followed by a liquid evaporation step in all models. As the Wet Particle model assumes single char particles that are surrounded by a liquid film, the low initial droplet diameter of 15 µm leads to an extremely short liquid evaporation distance of around z = 62 mm. In the Fragmenting Particle model, the 75 µm droplet shrinks during evaporation until the critical porosity of the char particles is reached at

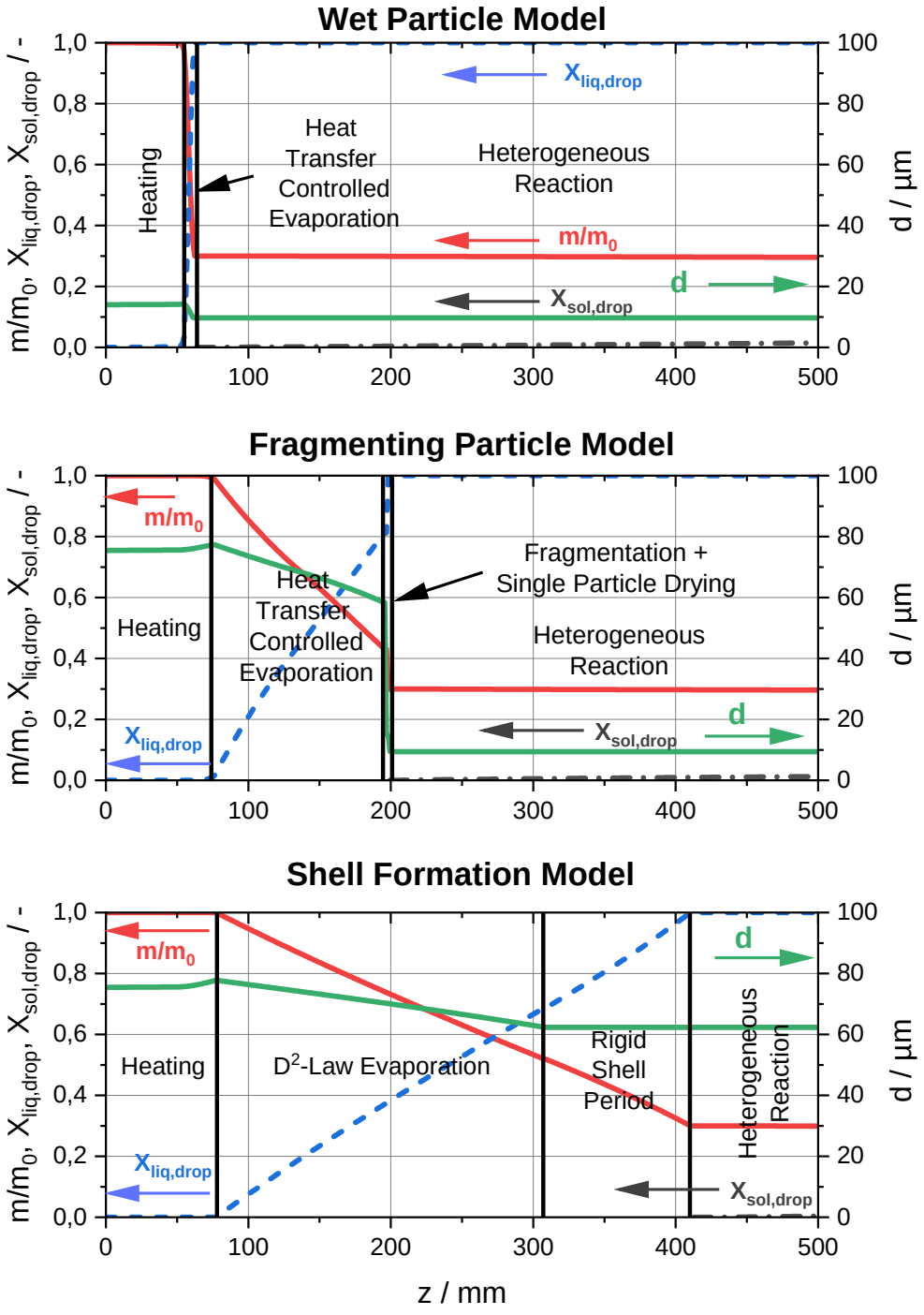


Figure 5.24: Calculated evaporation progress variables of a 75 µm droplet along the jet centerline for the suspension droplet conversion models investigated in this work. Input conditions of case S30-A were applied (J_{gas}=0.34 N, d_{32} = 189 µm, $\theta_{0.9}$ = 29 °, $d_{p,sol}$ = 9 µm, Fuel: MEG with 30 wt-% BWC-A).

z = 195 mm. At this point, the droplet fragments into the single char particles that are each surrounded by the remaining liquid as a film, in analogy to the Wet Particle model. Since the fragmentation into the sub particles generates a higher surface area as compared

to the initial slurry droplet, the evaporation rate increases rapidly, leading to complete liquid evaporation at $z = 214$ mm.
The Shell Formation model leads to a significantly slower evaporation rate in comparison to the two models discussed above. A first receding diameter period up to the formation of a rigid porous shell is followed by a constant diameter period until the liquid has completely evaporated at $z = 419$ mm, leaving a spherical hollow agglomerate with a diameter of $d = 63$ µm.
Solid conversion reactions start for all models when the liquid phase has completely evaporated. The devolatilization and heterogeneous gasification reactions are slow in comparison to the liquid evaporation processes. In none of the model calculations, a significant reduction of mass takes place during this step. Since the solid phase leaves the flame zone in different conditions (single particle or agglomerate, as indicated by the droplet diameter), the conversion of the solid phase downstream the flame is presumably strongly affected by these in-flame processes. Especially for technical fuels, such agglomerate formation processes gain relevance (see section 2.2.4), making the application of experimentally supported suspension droplet conversion models necessary for an accurate description of the EFG process.

5.3.3 Influence of Suspension Droplet Model on Flame

The results of the prior section showed major differences in liquid evaporation rate between the droplet models, suggesting a substantial influence of the droplet model on the prediction of flame and fuel conversion. This is further investigated in this section using model calculations. Fig. 5.25 shows the total evaporated mass fraction of liquid fuel $X_{\mathrm{liq,OH}}$, total mass fractions of dried char available for reaction with the gas phase $X_{\mathrm{sol,dry,OH}}$ and total mass fraction of converted char $X_{\mathrm{sol,OH}}$ (see section 4.3.5) integrated over all droplet size classes and the entire flame volume for input conditions of case S30-A.
The Shell Formation model shows the lowest amount of liquid evaporation within the flame ($X_{\mathrm{liq,OH}} \approx 9$ %), while the Fragmenting Particle model predicts a higher amount of evaporation ($X_{\mathrm{liq,OH}} \approx 17$ %). While these values are relatively low, they are of comparable magnitude to the results of the fuel evaporation analysis for MEG in sections 5.2.2 and 5.2.3 considering the droplet sauter mean diameter of $d_{32} = 189$ µm. The increased liquid evaporation for the Fragmenting Particle model reduces the longitudinal extension of the OH zone L_{OH} in comparison to the Shell Formation model. Both models produce L_{OH} values that are reasonable in comparison to the experimental value of $L_{\mathrm{OH}} = 300$ mm.
The Wet Particle model on the other hand produces high evaporation rates due to the small initial droplet diameter, leading to around 86 % fuel evaporation within the flame. The resulting longitudinal extension of the OH zone $L_{\mathrm{OH}} = 82$ mm does not fit the experimental

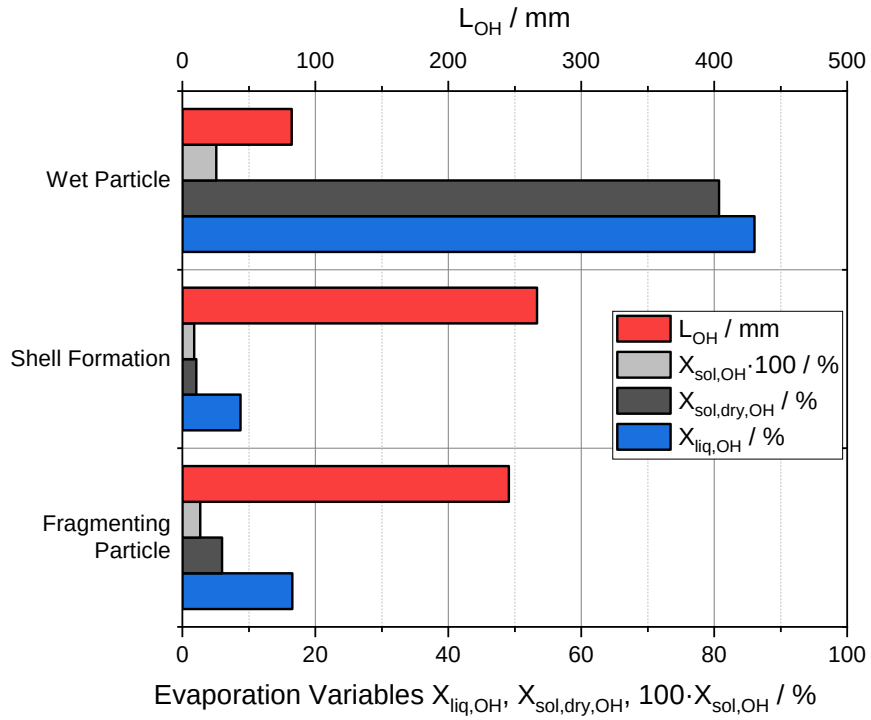


Figure 5.25: Calculated integral conversion variables of the flame zone for the suspension droplet conversion models investigated in this work. Input conditions of case S30-A were applied (J_{gas}=0.34 N, d_{32} = 189 µm, $\theta_{0.9}$ = 29 °, $d_{\mathrm{p,sol}}$ = 9 µm, Fuel: MEG with 30 wt-% BWC-A).

data. Due to the coupling of solid particle diameter and droplet diameter, this model is not suitable for simulations of suspension fuel EFG.

Only minor amounts of char completely dry up within the flame zone for the Shell Formation ($X_{\mathrm{sol,dry,OH}} \approx 2$ %) and Fragmenting Particle model ($X_{\mathrm{sol,dry,OH}} \approx 6$ %). Due to the slow char gasification reactions, the total amount of char converted within the flame volume $X_{\mathrm{sol,OH}}$ is below 1 % for all cases.

In order to assess the situation in case of a more reactive char, a calculation applying the measured solid kinetics from literature (see section 4.3.4) is compared to a calculation featuring inert solid particles and a calculation applying devolatilization and heterogeneous solid reaction rates increased by a factor of 10 in Fig. 5.26. The comparison shows no significant impact of the solid conversion rate on L_{OH}. Given the prior insights, this result is expected as only a minor amount of solid particles are released from droplets within the flame zone. The possible influence of solid reactions is on local stoichiometry within the flame is therefore inherently small. Even for the char kinetics enhanced by a factor of 10, its contribution is orders of magnitude smaller than that of evaporation (see section 5.3.2). As a consequence, the impact of the solid particles on the flame can be considered as limited and the flame length is mostly determined by fuel evaporation under the investigated conditions. This emphasizes the choice of an appropriate suspension droplet evaporation

model when accurate flame predictions for suspension fuels are desired.

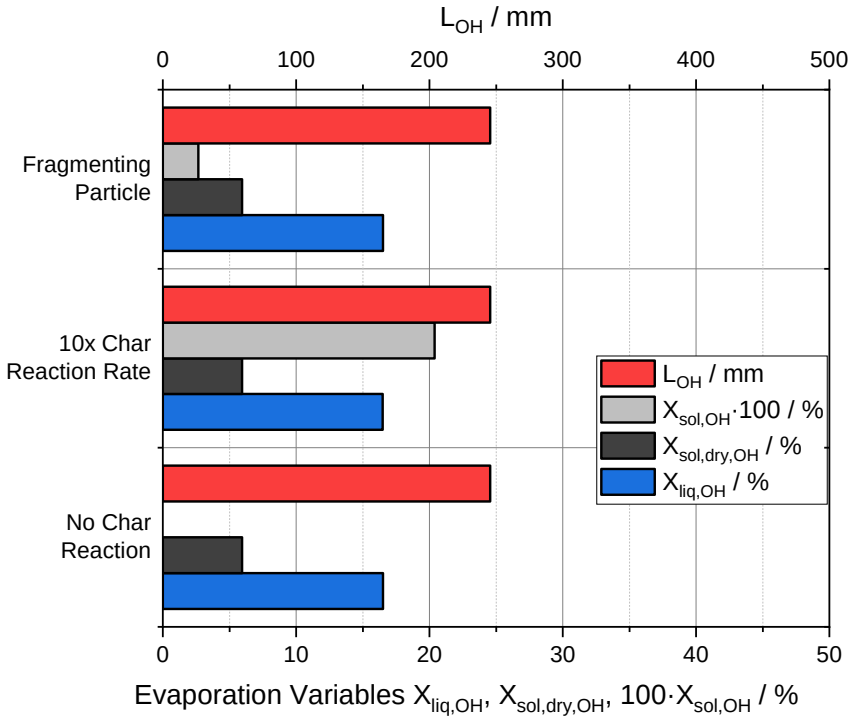


Figure 5.26: Calculated integral conversion variables of the flame zone for the Fragmenting Particle model applying different evaporation and char conversion conditions. Input conditions of case S30-A were applied (J_{gas}=0.34 N, d_{32} = 189 µm, $\theta_{0.9}$ = 29 °, $d_{\mathrm{p,sol}}$ = 9 µm, Fuel: MEG with 30 wt-% BWC-A).

5.3.4 Impact of Suspension Fuel Specifications on Flame

The previously observed elongation of the flame zone when switching from liquid to suspension fuel (section 5.3.1) is now investigated applying the insights gained in the above sections. The impact of solid mass fraction $x_{\mathrm{sol,0}}$ and solid particle size $d_{\mathrm{p,sol}}$ is investigated using experimental data supported by 2-Ph-FJM calculations for interpretation of the experimental results. Model calculations were conducted using the Fragmenting Particle Model (see 4.3.4). Applying this model to the given suspension fuels is justified for the following reasons. MEG is a monocomponent fuel with a defined boiling point that does not produce a solid residue during evaporation. Additionally, in the experiments for determination of reaction kinetics caking of the beech wood char particles was not observed. These conditions typically prohibit shell or agglomerate formation during suspension droplet conversion [158]. In particle extraction experiments for the experimental case S30-A, no particle agglomerates were found, further supporting the use of the Fragmenting Particle

Model (see Appendix D.3). Thus, for further model calculations, the Fragmenting Particle model was chosen as it best reflects the gasification behavior of the applied suspension fuels.

Effect of Solid Mass Fraction $x_{\mathbf{sol,0}}$

First, the impact of the solid mass fraction in the suspension fuel on the flame length is analyzed using data of cases S0, S10-A, S20-A, S30-A. All cases feature constant gas momentum flow J_{gas}, fuel mass flow $\dot{m}_{\mathrm{fuel}}$, adiabatic temperature T_{ad}, residence time τ and particle size distribution (see Table 3.3 and Appendix D.3).

Fig. 5.27 shows measured and calculated values for the longitudinal extension of the OH zone L_{OH} as well as calculated values for the absolute evaporated liquid mass within the flame volume $\dot{m}_{\mathrm{liq,vap,OH}}$ for interpretation of the results. This absolute quantity is chosen because the initial liquid mass fractions in the suspensions varies, so the relative expression $X_{\mathrm{liq,OH}}$ would not provide meaningful results. The full dataset on the OH distributions is provided in Appendix D.3.

The experimental data shows a monotonous increase of L_{OH} with increasing solid content. However, several parameters impacting the flame are changed simultaneously with increasing solid content in the experiment. These are i) feed viscosity, which affects atomization, ii) elemental composition of the applied feedstocks leading to different composition of recirculated syngas and iii) oxygen content in the gasification agent $y_{\mathrm{O2,GA}}$, which was adapted in order to keep a constant adiabatic equilibrium temperature of 1700 °C (see section 3.4.3). In order to decouple these effects and to assess their individual impact on the flame, a model sensitivity study is conducted.

The isolated influence of solid mass fraction $x_{\mathrm{sol,0}}$ on flame length without superposition by the effects i)-iii) was investigated in a series of model calculations applying spray conditions, $y_{\mathrm{O2,GA}}$ and composition of recirculated gas set equal to the MEG case while only varying $x_{\mathrm{sol,0}}$. As expected from the previous results, the total amount of fuel evaporation within the flame $\dot{m}_{\mathrm{liq,vap,OH}}$ is not significantly changed by the increase of $x_{\mathrm{sol,0}}$. Particle reactions itself were shown to exhibit no significant influence on the flame under the present conditions. Local stoichiometry and temperature remain therefore unaffected and $x_{\mathrm{sol,0}}$ does not show a significant influence on L_{OH} (see dotted lines).

The influence of effects ii) and iii), i.e. the changes in $y_{\mathrm{O2,GA}}$ and the composition of recirculated gas due to the different feedstock elemental composition is investigated by a separate series of model calculations (dashed line). These parameters influence local stoichiometry and thus may have an impact on the flame. For the investigated cases though, only a minor difference to the isolated variation of $x_{\mathrm{sol,0}}$ occurs when taking these additional effects into account.

If additionally, the impact of spray parameters (effect i)) is considered, a considerable change in $\dot{m}_{\mathrm{liq,vap,OH}}$ and thus L_{OH} occurs (solid line). The addition of particles increases viscosity (see Appendix B.2) and thus impacts atomization. Only when spray influence is

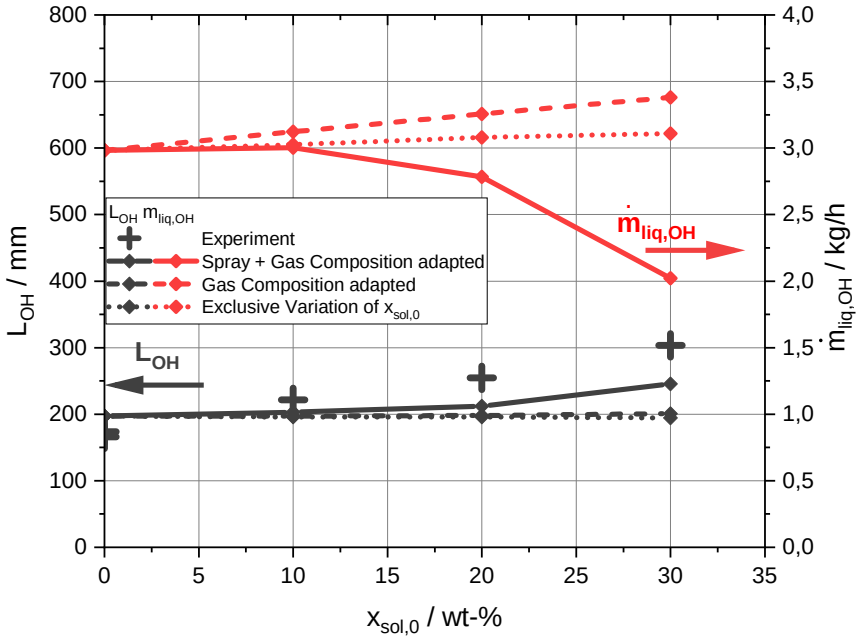


Figure 5.27: Experimental and calculated L_{OH} for different initial suspension solid content under input conditions of case S0 - S30-A. Calculated values for the liquid mass flow evaporated within the OH zone are added for comparison. Evaporation model: Fragmenting Particle.

taken into account, the experimentally observed trend of L_{OH} is reproduced by the model. The observation is also consistent with results of section 5.1, where the impact of liquid evaporation rate on local stoichiometry is investigated. Due to uncertainties in measuring the droplet size and spray angles at higher $x_{\mathrm{sol},0}$ (see Appendix D.3), a better agreement between experiment and model may be expected for more accurate input data.

Effect of Solid Particle Size $d_{\mathrm{p,sol}}$

The influence of solid particle size on the flame was investigated for suspensions containing $x_{\mathrm{sol},0} = 30$ wt-% of char with $\mathrm{d}_{32,\mathrm{sol}}$ ranging from 4 - 19 µm under constant process conditions (see cases S30-A, S30-B and S30-C in section 3.4.3). From the previous investigations, no significant influence of the char particle size should be expected. This is verified by the experimental data shown in Fig. 5.28, and also reflected in the model calculations where only negligible differences between the calculated values of L_{OH} and $\dot{m}_{\mathrm{liq,vap,OH}}$ occur.

The exclusive variation of char particle size does not affect liquid evaporation rate in the Fragmenting Particle Model. Because $y_{\mathrm{O2,GA}}$ is the same for all three cases and the composition of recirculated gas exhibits only negligible changes, the additional consideration of these parameters neither significantly contributes to $\dot{m}_{\mathrm{liq,vap,OH}}$ and L_{OH}. As the differences in spray parameters between the investigated cases are also small, no considerable spray effects occur.

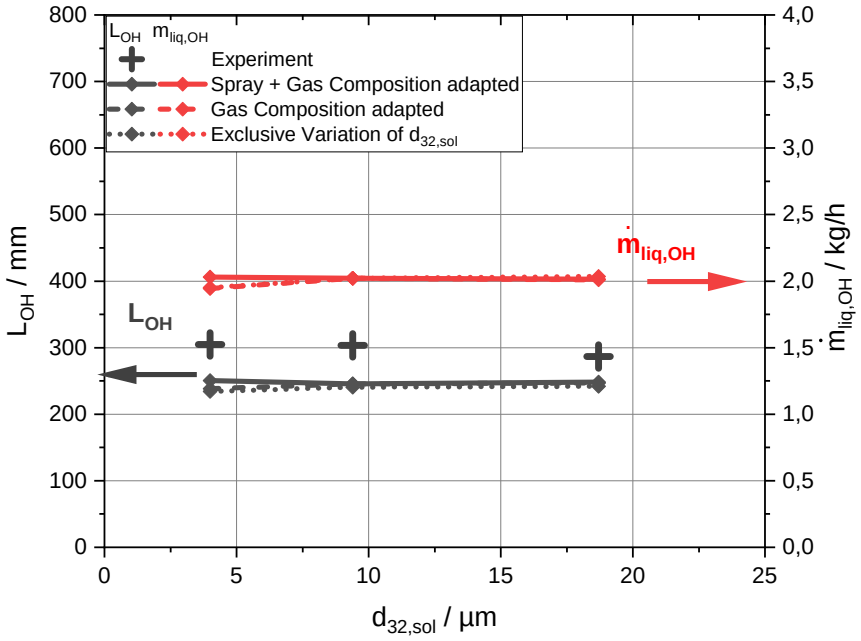


Figure 5.28: Experimental and calculated L_{OH} for different initial particle size in the suspensions at $x_{\mathrm{sol},0} = 30$ % under input conditions of case S30-A - S30-C. Calculated values for the liquid mass flow evaporated within the OH zone are added for comparison. Evaporation model: Fragmenting Particle.

6 Conclusions

The goal of this thesis was a comprehensive assessment and quantitative description of the interaction of sub-processes in the EFG flame zone for liquid and suspension fuels based on detailed experimental data and validated model calculations. The flame zone provides thermal energy for the gasification process, defines the temperature field in the reactor and establishes the boundary conditions for conversion of fuel droplets. A literature study revealed significant deficits in process understanding of the EFG flame zone due to limited experimental data and the lack of validated models. Especially the impact of spray parameters on the flame and the conversion of suspension droplets within the flame have not received sufficient attention (see section 2.1.2).
In this work, a burner concept applying a central fuel jet surrounded by an annular stream of gasification agent is selected as a reference burner configuration. Experiments were carried out at an optically accessible, atmospheric pressure EFG plant (REGA) using surrogate fuels. An OH-LIF system and other optical and invasive diagnostics were implemented at the REGA plant and applied to study the flame and the reacting spray. An existing 2-Phase Free-Jet model was expanded to describe suspension fuels, allow for a variable spray angle and to describe the experimentally accessible OH radical distribution. The model was validated using the experimental data and applied to conduct numerical studies on different sub-processes in the flame zone. Special focus is put on assessing the impact of burner related parameters (gas momentum flow, droplet size, spray angle) and fuel specifications (liquid /suspension, solid particle content, solid particle size) on flame shape and fuel conversion within the flame.

Main Findings
The thesis is structured into three detail objectives (see section 1.2). In the following, these are presented here together with the respective main findings.

Objective 1: *Quantitative description of the impact of the burner related parameters gas momentum flow, droplet size and spray angle on the reaction zone structure of a liquid fuel EFG flame.*

This objective is addressed in section 5.1. A detailed experimental dataset of two EFG flames including OH radical and fuel spray distribution, spray high-speed images, radial

profiles of droplet size, droplet velocity and gas temperature was generated. Based on the experimental data and model calculations, a core zone, an oxidation zone and a gasification zone were identified. Results show that as a first approximation, the EFG flame can be regarded as a turbulent inverse diffusion flame of an oxidizer jet reacting with syngas from the surrounding atmosphere, featuring a structure defined by jet entrainment. This flame is superimposed by a fuel spray. Transfer of fuel to the gas phase by evaporation of fuel droplets locally reduces absolute stoichiometry in the flame zone, which produces a shorter flame and can alter flame shape. Both principle flame structures found in CFD literature (closed and hollow cone, see section 2.1.2) were experimentally verified and explained using model calculations. Validated model sensitivity studies show the effect of burner related parameters on the sub-processes in the flame, influencing flame length and shape:

- Gas momentum flow, which determines entrainment of ambient syngas into the jet of gasification agent, is the primary parameter influencing temperature field and flame length. Higher gas momentum flow leads to an enhanced entrainment rate of surrounding syngas, causing a shorter flame (see sections 5.1.1 and 5.1.2).
- Droplet size impacts the rate of fuel evaporation in the flame, which poses a secondary influence on the flame through decreasing absolute stoichiometry within the flame. Smaller droplets feature an higher evaporation rate and lead to a shorter flame (see section 5.1.3).
- Spray angle impacts local stoichiometry by determining the amount of liquid fuel available in the jet. A more narrow spray angle causes a shorter flame due to higher amount of fuel vapor within the flame contour. A transition from a compact to a hollow cone flame structure occurs for very narrow spray angles when the evaporation rate at the jet axis is especially high (see sections 5.1.4 and 5.1.5).

Objective 2: *Quantification of the influence of gas momentum flow, droplet size and spray angle on liquid fuel conversion within a liquid fuel EFG flame.*

This objective is addressed in section 5.2. As flame geometry is itself dependent on fuel evaporation, the findings of Objective 1 have to be considered. By model calculations, a significant mass fraction of liquid fuel (35 % up to 98 % for the investigated conditions) was found to evaporate outside the boundaries of the oxidation zone, depending on burner related parameters. This fuel is converted in the gasification zone under the absence of oxygen and under lower temperatures than in the flame. As this may contribute to the formation of undesired by-products like soot and cenospheres in a technical process, the results of this objective provide a basis for further research on this topic. Model

calculations supported by experiments provide the following conclusions on the impact of the burner related parameters on liquid fuel conversion in the flame:

- Gas momentum flow: A lower gas momentum flow leads to reduced droplet velocity combined with a longer flame (see above). Both effects increase droplet residence time and thus increase liquid fuel conversion within the flame (see section 5.2.2).
- Droplet size: smaller droplets unsurprisingly enhance liquid fuel conversion in the flame zone. Using twin-fluid atomizer nozzles, however, a fine spray requires high shear forces between gas and liquid phase that are provided by a high gas momentum flow. Regarding the application to technical EFG burners, these two parameter influences are opposing each other (see sections 5.2.1 and 5.2.3).
- Spray angle: For a given droplet size and gas momentum flow, liquid fuel conversion within the flame zone is highest at spray angles close to the gas free jet angle. A wider spray angle causes more droplets to evaporate in the gasification zone outside the flame. A too narrow spray angle causes a cold and fuel rich zone on the jet centerline, inhibiting fuel evaporation (see section 5.2.3).

Objective 3: *Assessment of the conversion of suspension fuels in an EFG flame, including (i) the impact of suspension fuel parameters (solid content, solid particle size) on flame structure and (ii) the impact of different suspension droplet models on the predictions of the flame.*

This objective is addressed in section 5.3. A combined experimental and numerical approach leads to the findings listed below.

- The structure of the flame is not fundamentally changed when solid particles are added to the liquid fuel, as it is still governed by syngas entrainment and local mass transfer of fuel to the gas phase within the flame (see section 5.3.1).
- For increasing solid content in the suspension fuel, model calculations supported by experimental data show that under the investigated conditions, the primary impact on flame length and shape does not stem from solid particle reactions, but from the change in spray parameters induced by increased fuel viscosity. Furthermore, no significant impact of solid particle size on the flame was observed for the investigated process conditions (see section 5.3.4).

- Calculations show that only the smallest droplets in the fuel spray evaporate quick enough for solid reactions to take place within the flame (see section 5.3.3). The impact of solid particle reactions on the flame was thus found to be considerably weaker than that of liquid fuel evaporation.
- The droplet conversion sub-model has significant impact on the prediction of the flame. For the three droplet models investigated, the different mass transfer rates of fuel to the gas phase influence local stoichiometry and thus impact temperature and gas phase reactions in the simulation. For an accurate description of the EFG flame, the selection of a sub-model correctly describing the fuel specific droplet conversion processes is thus important (see section 5.3.2 and 5.3.3). The widely applied Wet Particle model shows severe limitations, while the Fragmenting Particle model is identified as suitable to describe the reference suspension fuel applied in this work.

Remarks on the 2-Ph-FJM

Based on the model investigations conducted in this work, the following conclusions on the 2-Ph-FJM approach used to describe the EFG flame can be drawn:

- The 2-Ph-FJM proves to be a useful tool to gain understanding of the dependencies of sub-processes in the EFG flame. Using appropriate sub-process models, it shows the capability to reproduce the experimentally observed trends for liquid and suspension fuels in a broad range of operating conditions and input parameters. The model provides a basis to interpret experimental results and to identify relevant process parameters, improving process understanding of the EFG flame zone.
- As the 2-Ph-FJM is able to independently predict the impact of process parameters on reaction zone structure and fuel conversion in the EFG flame zone with low computational time with reasonable accuracy, it is well suited to conduct parameter sensitivity studies. The 2-Ph-FJM can thus be applied as a tool to support development and optimization of EFG burners.
- The 2-Ph-FJM provides a framework to evaluate sub-process models and to analyze their impact on the prediction of the EFG flame. This makes the model suitable to assist the further development of more complex CFD models that focus on modeling the integral system.

Outlook

The present work provides a basis for future research. An area of major interest is understanding the impact of the processes in the EFG flame on global fuel conversion and

the formation of unwanted by-products like soot, hydrocarbons and cenospheres in the gasification process. This requires further experimental work that can be complemented by 2-Ph-FJM calculations. The results obtained under Objectives 2 and 3 provide a starting point for this. The development of improved droplet evaporation models for technical fuels like pyrolysis oils is necessary. A detailed analysis of droplet conversion in the burner near zone in a combined 2-Ph-FJM/LES approach can provide further insight.
The 2-Ph-FJM can be further improved to describe the effect of pressure on the EFG flame. This requires experiments on the exchange of mass, energy and momentum in pressurized two phase jets. A further improvement lies in the transfer of the present results to other burner concepts. For this, the applicability of the 2-Ph-FJM to other configurations of the input flows needs to be assessed.
The influence of additional energy sources like plasma on the processes in the burner near field is another focus of research that may soon gain relevance in the context of process electrification [254].

References

[1] M. Bachmann, C. Zibunas, J. Hartmann, V. Tulus, S. Suh, G. Guillén-Gosálbez, and A. Bardow. "Towards circular plastics within planetary boundaries". In: *Nature Sustainability* 6.5 (2023), pp. 599–610. doi: 10.1038/s41893-022-01054-9.

[2] V. Dieterich, A. Hanel, S. Bastek, H. Spliethoff, and S. Fendt. "Entrained flow gasification-based biomass-to-X processes: A techno-economic assessment". In: *Energy Conversion and Management* 301 (2024), p. 118061. doi: 10.1016/j.enconman.2024.118061.

[3] P. Rößger, L. G. Seidl, F. Compart, J. Hußler, M. Gräbner, and A. Richter. "Integrating biomass and waste into high-pressure partial oxidation processes: Thermochemical and economic multi-objective optimization". In: *Journal of Cleaner Production* 358 (2022), p. 132053. doi: 10.1016/j.jclepro.2022.132053.

[4] F. Li, Y. Li, J. Cao, L. Carvalho, J. Lundgren, K. Engvall, X. Zhang, Y. Liu, and X. Ji. "Combination of CO2 electrochemical reduction and biomass gasification for producing methanol: A techno-economic assessment". In: *Energy Conversion and Management* 307 (2024), p. 118380. doi: 10.1016/j.enconman.2024.118380.

[5] I. Janajreh, I. Adeyemi, S. S. Raza, and C. Ghenai. "A review of recent developments and future prospects in gasification systems and their modeling". In: *Renewable and Sustainable Energy Reviews* 138 (2021), p. 110505. doi: 10.1016/j.rser.2020.110505.

[6] M. Hennig, T. M. Dreising, A. Reeves, T. Oehlcke, S. Tavakkol, R. Volk, F. Schultmann, and D. Stapf. "Entrained-Flow Gasification for the Utilization of Pyrolysis Oil from Mixed Plastic Waste". In: *ACS Sustainable Chemistry & Engineering* 13.48 (2025), pp. 20638–20648. issn: 2168-0485. doi: 10.1021/acssuschemeng.5c03932.

[7] H. Hiller, R. Reimert, and H.-M. Stönner, eds. *Ullmann's Encyclopedia of Industrial Chemistry: Gas Production, 2. Processes*. Wiley, 2000. doi: 10.1002/14356007.

[8] S. Fleck, U. Santo, C. Hotz, T. Jakobs, G. Eckel, M. Mancini, R. Weber, and T. Kolb. "Entrained flow gasification. Part 1: gasification of glycol in an atmospheric-pressure experimental rig". In: *Fuel* 217 (2018-04), pp. 306–319. issn: 0016-2361. doi: 10.1016/j.fuel.2017.12.077. url: https://doi.org/10.1016/j.fuel.2017.12.077.

[9] M. Dammann. "Numerical modelling and simulation of atmospheric entrained flow gasification of surrogate fuels". PhD-Thesis. Karlsruher Institut für Technologie (KIT), 2024. doi: 10.5445/IR/1000172116.

[10] G. Eckel, P. Le Clercq, T. Kathrotia, A. Saenger, S. Fleck, M. Mancini, T. Kolb, and M. Aigner. “Entrained flow gasification. Part 3: Insight into the injector near-field by Large Eddy Simulation with detailed chemistry”. In: *Fuel* 223 (2018), pp. 164–178. issn: 00162361. doi: 10.1016/j.fuel.2018.02.176.

[11] C. Hotz, M. Haas, S. Wachter, S. Fleck, and T. Kolb. “Two-phase free jet model of an atmospheric entrained flow gasifier”. In: *Fuel* 304.21–23 (2021), p. 121392. issn: 00162361. doi: 10.1016/j.fuel.2021.121392.

[12] C. Hotz, M. Haas, S. Wachter, S. Fleck, and T. Kolb. “Experimental investigation on entrainment in two-phase free jets”. In: *Fuel* 335.21–23 (2023), p. 126912. issn: 00162361. doi: 10.1016/j.fuel.2022.126912.

[13] C. Hotz. “Zweiphasen-Freistrahlmodell eines atmosphärischen Flugstromvergasers”. PhD-Thesis. Karlsruhe: Karlsruhe Institute of Technology, 2024.

[14] M. Eberhard, U. Santo, B. Michelfelder, A. Günther, P. Weigand, J. Matthes, P. Waibel, V. Hagenmeyer, and T. Kolb. “The bioliq® Entrained-Flow Gasifier–A Model for the German Energiewende”. In: *ChemBioEng Reviews* 7.4 (2020), pp. 106–118. doi: 10.1002/cite.201700086.

[15] M. Haas, M. Dammann, S. Fleck, and T. Kolb. “Entrained flow gasification: Impact of fuel spray distribution on reaction zone structure”. In: *Fuel* 334.4 (2023), p. 126572. issn: 00162361. doi: 10.1016/j.fuel.2022.126572.

[16] M. Haas, S. Fleck, T. Jakobs, and T. Kolb. “Liquid fuel evaporation under entrained flow gasification conditions–Insights for burner development”. In: *Thermal Science and Engineering Progress* (2025), p. 103342. doi: 10.1016/j.tsep.2025.103342.

[17] M. Haas, S. Fleck, F. Scheiff, and T. Kolb. “Conversion of suspension fuel droplets in the flame zone of an entrained flow gasifier”. In: *Fuel* 416 (2026), p. 138473. issn: 00162361. doi: 10.1016/j.fuel.2026.138473.

[18] C. Higman and M. van der Burgt. *Gasification*. Elsevier, 2003.

[19] Y. Jafri, E. Furusjö, K. Kirtania, R. Gebart, and F. Granberg. “A study of black liquor and pyrolysis oil co-gasification in pilot scale”. In: *Biomass Conversion and Biorefinery* 8.1 (2018), pp. 113–124. issn: 2190-6815. doi: 10.1007/s13399-016-0235-5.

[20] M. Kremling, L. Briesemeister, M. Gaderer, S. Fendt, and H. Spliethoff. “Oxygen-Blown Entrained Flow Gasification of Biomass: Impact of Fuel Parameters and Oxygen Stoichiometric Ratio”. In: *Energy & Fuels* 31.4 (2017), pp. 3949–3959. issn: 0887-0624. doi: 10.1021/acs.energyfuels.6b02949.

[21] P. Mondal, G. S. Dang, and M. O. Garg. “Syngas production through gasification and cleanup for downstream applications — Recent developments”. In: *Fuel Processing Technology* 92.8 (2011), pp. 1395–1410. issn: 03783820. doi: 10.1016/j.fuproc.2011.03.021.

[22] E. J. Leijenhorst, D. Assink, L. van de Beld, F. Weiland, H. Wiinikka, P. Carlsson, and O. Öhrman. "Entrained flow gasification of straw- and wood-derived pyrolysis oil in a pressurized oxygen blown gasifier". In: *Biomass and Bioenergy* 79 (2015), pp. 166–176. issn: 09619534. doi: 10.1016/j.biombioe.2014.11.020.

[23] F. Weiland, M. S. Qureshi, J. Wennebro, C. Lindfors, T. Ohra-Aho, H. Shafaghat, and A.-C. Johansson. "Entrained Flow Gasification of Polypropylene Pyrolysis Oil". In: *Molecules (Basel, Switzerland)* 26.23 (2021). doi: 10.3390/molecules26237317.

[24] RWE AG. *FUREC - Producing Hydrogen from Household Waste*. 2026. url: https://www.rwe.com/en/research-and-development/hydrogen-projects/furec/ (visited on 2026-01-23).

[25] thyssenkrupp Uhde GmbH. *thyssenkrupp Uhde selected for Elyse Energy Biomass-to-SAF project in France*. 2026. url: https://www.thyssenkrupp-uhde.com/en/media/press-releases/press-detail/thyssenkrupp-uhde-selected-for-elyse-energy's-biomass-to-saf-project-in-france-296266 (visited on 2026-01-23).

[26] National Energy Technology Laboratory. *Commercial Gasifiers*. 2026. url: https://www.netl.doe.gov/research/Coal/energy-systems/gasification/gasifipedia/types-gasifiers (visited on 2026-01-23).

[27] M. Dammann, U. Santo, D. Böning, H. Knoch, M. Eberhard, and T. Kolb. "Entrained flow gasification: Pilot-scale experimental, balancing and equilibrium data for model validation". In: *Fuel* 382 (2025), p. 132809. issn: 00162361. doi: 10.1016/j.fuel.2024.132809.

[28] N. Fang, Y. Lu, Z. Li, Y. Lu, and Z. Chen. "Improving mixing and gasification characteristics in an industrial-scale entrained flow gasifier with a novel burner". In: *Journal of Cleaner Production* 362 (2022), p. 132157. issn: 09596526. doi: 10.1016/j.jclepro.2022.132157.

[29] W. A. Sowa, P. O. Hedman, L. D. Smoot, and D. O. Richards. "The sensitivity of entrained-flow coal gasification diffusion burners to changes in geometry". In: *Fuel* 71.5 (1992), pp. 593–604. issn: 0016-2361. doi: 10.1016/0016-2361(92)90159-L. url: https://doi.org/10.1016/0016-2361(92)90159-L.

[30] F. Weiland, P. T. Nilsson, H. Wiinikka, R. Gebart, A. Gudmundsson, and M. Sanati. "Online Characterization of Syngas Particulates Using Aerosol Mass Spectrometry in Entrained-Flow Biomass Gasification". In: *Aerosol Science and Technology* 48.11 (2014), pp. 1145–1155. issn: 0278-6826. doi: 10.1080/02786826.2014.965772.

[31] N. Samani, R. Khalil, M. Seljeskog, J. Bakken, R. K. Thapa, and M. S. Eikeland. "Experimental and simulation studies of oxygen-blown, steam-injected, entrained flow gasification of lignin". In: *Fuel* 362 (2024), p. 130713. issn: 00162361. doi: 10.1016/j.fuel.2023.130713.

[32] H. F. Fasih, H. Ghassemi, and H. K. MazraeShahi. "Experimental investigation of heavy fuel oil gasification in an entrained flow gasifier". In: *Fuel* 351.12 (2023), p. 128955. issn: 00162361. doi: 10.1016/j.fuel.2023.128955.

[33] J. Yang, Y. Gong, Q. Guo, L. Ding, F. Wang, and G. Yu. “Experimental study on the spectral characteristics of impinging flames in an opposed multi-burner entrained-flow gasifier”. In: *Journal of the Energy Institute* 101 (2022), pp. 168–177. issn: 17439671. doi: 10.1016/j.joei.2022.01.012.

[34] F. Lüdtke. “Vorrichtung zur Vergasung von homogenen Brenn-, Rest- und Abfallstoffen”. Patent DE 200 01 421 U1. 2000.

[35] X. Wu, Q. Guo, Y. Gong, J. Liu, X. Luo, T. Wu, and G. Yu. “Influence of burner geometry on atomization of coal water slurry in an entrained-flow gasifier”. In: *Chemical Engineering Science* 247.3-4 (2022), p. 117088. issn: 00092509. doi: 10.1016/j.ces.2021.117088.

[36] Y. C. Choi, X. Y. Li, T. J. Park, J. H. Kim, and J. G. Lee. “Numerical study on the coal gasification characteristics in an entrained flow coal gasifier”. In: *Fuel* 80.15 (2001), pp. 2193–2201. issn: 00162361. doi: 10.1016/S0016-2361(01)00101-6.

[37] H. Lu, Y. Gong, Q. Guo, Y. Wang, X. Song, and G. Yu. “In-situ study on flow and rotation behaviors of coal particles near the burner plane in an impinging entrained-flow gasifier”. In: *Applied Energy* 359 (2024), p. 122694. issn: 03062619. doi: 10.1016/j.apenergy.2024.122694.

[38] N. Fang, L. Zeng, B. Zhang, Z. Li, H. Wang, and X. Liu. “Numerical simulation of flow and gasification characteristics with different swirl vane angles in a 2000 t/d GSP gasifier”. In: *Applied Thermal Engineering* 153 (2019), pp. 791–799. issn: 13594311. doi: 10.1016/j.applthermaleng.2019.03.006.

[39] M. Hartwich and A. Richter. “Development of novel concepts for entrained-flow gasifiers”. In: *Fuel* 403 (2026), p. 135968. issn: 00162361. doi: 10.1016/j.fuel.2025.135968.

[40] Z. Cao, Q. Wu, H. Zhou, P. Chen, and F. You. “Dynamic modeling, systematic analysis, and operation optimization for shell entrained-flow heavy residue gasifier”. In: *Energy* 197 (2020), p. 117220. issn: 03605442. doi: 10.1016/j.energy.2020.117220.

[41] H. J. A. Hasenack. “Verfahren zur Erzeugung von Synthesegas aus einem Kohlenwasserstoffbrennstoff”. Patent DE 3444590 A1. 1984.

[42] X. Lan, H. Zhong, and J. Gao. “CFD simulation on the gasification of asphalt water slurry in an entrained flow gasifier”. In: *Petroleum Science* 11.2 (2014), pp. 308–317. issn: 1672-5107. doi: 10.1007/s12182-014-0345-2.

[43] Y. Gong, Q. Guo, H. Zhu, and G. Yu. “Refractory failure in entrained-flow gasifier: Investigation of partitioned erosion characteristics in an industrial opposed multi-burner gasifier”. In: *Chemical Engineering Science* 210.5 (2019), p. 115227. issn: 00092509. doi: 10.1016/j.ces.2019.115227.

[44] C. Hu, Y. Gong, Q. Guo, X. Song, and G. Yu. “An experimental study on the spectroscopic characteristics in coal-water slurry diffusion flames based on hot-oxygen burner technology”. In: *Fuel Processing Technology* 154 (2016), pp. 168–177. issn: 03783820. doi: 10.1016/j.fuproc.2016.08.029.

[45] W. Materne. “Verfahren und Vorrichtung zur Herstellung von Synthesegas durch partielle Oxidation von Kohle-Wasser-Suspensionen”. Patent DE 32 19316 A1. 1983.

[46] U. Zwiefelhofer. “Brenner für die partielle Oxidation von flüssigen, kohlenstoffhaltigen Brennstoffen”. Patent EP 1016 705 A1. 2000.

[47] R. J. Stellacio. “Burner and partial oxidation process for slurries of solid fuel”. Patent EP 0 127 273 A2. 1984.

[48] R. J. Stellacio. “Process for the gasification of heavy oil”. Patent US 6,773,630 B2. 2004.

[49] N. Fang, L. Zeng, Z. Li, Y. Lu, and Z. Chen. “Numerical analysis of an 80,000 Nm3/h fly ash entrained-flow gasifier at various burner inclination angles”. In: *Environmental science and pollution research international* 29.18 (2022), pp. 26726–26737. doi: 10.1007/s11356-021-17770-2.

[50] Y. Lu, Z. Li, C. Huang, Y. Wang, and Z. Chen. “Applicability analysis of burners arrangement for an improved entrained-flow fine slag gasifier”. In: *Applied Thermal Engineering* 248 (2024), p. 123268. issn: 13594311. doi: 10.1016/j.applthermaleng.2024.123268.

[51] Y. Lu, Z. Li, X. Zhang, C. Huang, Y. Wang, and Z. Chen. “A novel burners arrangement of an entrained-flow gasifier studied by experimental and simulation methods”. In: *Energy* 330 (2025), p. 136906. issn: 03605442. doi: 10.1016/j.energy.2025.136906.

[52] J. Nam, M. Kim, G. Sohn, C. Ryu, B. Kim, and J. Lee. “Evaluation of abnormal burner operation in an entrained flow coal gasifier using numerical modeling”. In: *Applied Thermal Engineering* 191 (2021), p. 116859. issn: 13594311. doi: 10.1016/j.applthermaleng.2021.116859.

[53] T. Förster, Y. Voloshchuk, A. Richter, and B. Meyer. “3D numerical study of the performance of different burner concepts for the high-pressure non-catalytic natural gas reforming based on the Freiberg semi-industrial test facility HP POX”. In: *Fuel* 203.5 (2017), pp. 954–963. issn: 00162361. doi: 10.1016/j.fuel.2017.03.089.

[54] J. Xu, Q. Liang, Z. Dai, and H. Liu. “The influence of swirling flows on pulverized coal gasifiers using the comprehensive gasification model”. In: *Fuel Processing Technology* 172 (2018), pp. 142–154. issn: 03783820. doi: 10.1016/j.fuproc.2017.12.012.

[55] R. Li, M. Xie, H. Jin, L. Guo, and F. Liu. “Effect of Swirl on Gasification Characteristics in an Entrained-flow Coal Gasifier”. In: *International Journal of Chemical Reactor Engineering* 18.3 (2020). doi: 10.1515/ijcre-2019-0203.

[56] C. Chen, M. Horio, and T. Kojima. “Numerical simulation of entrained flow coal gasifiers. Part I: modeling of coal gasification in an entrained flow gasifier”. In: *Chemical Engineering Science* 55.18 (2000), pp. 3861–3874. issn: 00092509. doi: 10.1016/S0009-2509(00)00030-0.

[57] C. Chen, M. Horio, and T. Kojima. “Numerical simulation of entrained flow coal gasifiers. Part II: effects of operating conditions on gasifier performance”. In: *Chemical Engineering Science* 55.18 (2000), pp. 3875–3883. issn: 00092509. doi: 10.1016/S0009-2509(00)00031-2.

[58] J.-W. Lee, Y. Yun, S.-W. Chung, S.-H. Kang, J.-H. Ryu, G.-T. Kim, and Y.-J. Kim. “Application of multiple swirl burners in pilot-scale entrained bed gasifier for short residence time”. In: *Fuel* 117 (2014), pp. 1052–1060. issn: 00162361. doi: 10.1016/j.fuel.2013.10.013.

[59] Y. Ögren, M. Gullberg, J. Wennebro, A. Sepman, P. Tóth, and H. Wiinikka. “Influence of oxidizer injection angle on the entrained flow gasification of torrefied wood powder”. In: *Fuel Processing Technology* 181.2 (2018), pp. 8–17. issn: 03783820. doi: 10.1016/j.fuproc.2018.09.005.

[60] J. Lee, S. Park, H. Seo, M. Kim, S. Kim, J. Chi, and K. Kim. “Effects of burner type on a bench-scale entrained flow gasifier and conceptual modeling of the system with Aspen Plus”. In: *Korean Journal of Chemical Engineering* 29.5 (2012), pp. 574–582. issn: 0256-1115. doi: 10.1007/s11814-011-0217-z.

[61] B. Göktepe, K. Umeki, and R. Gebart. “Does distance among biomass particles affect soot formation in an entrained flow gasification process?” In: *Fuel Processing Technology* 141 (2016), pp. 99–105. issn: 03783820. doi: 10.1016/j.fuproc.2015.06.038.

[62] Y. Lu, Z. Li, G. Jiang, C. Huang, and Z. Chen. “Study on mixing performance of atmospheric entrained flow gasification burner using fine ash as feedstock”. In: *Energy* 292 (2024), p. 130443. doi: 10.1016/j.energy.2024.130443.

[63] Z. Zhao, H. Qin, T. Li, B. Hua, Y. Hou, T. Chen, and H. Ström. “CFD simulation of soot generation during biomass gasification in a cyclone gasifier”. In: *Fuel* 364 (2024), p. 131103. doi: 10.1016/j.fuel.2024.131103.

[64] Z. Xue, Q. Guo, Y. Gong, X. Wu, F. Wang, and G. Yu. “Detailed deposition characteristics around burner plane in an impinging entrained-flow coal gasifier”. In: *Chemical Engineering Science* 198 (2019), pp. 85–97. issn: 00092509. doi: 10.1016/j.ces.2019.01.016.

[65] A. Bader, M. Hartwich, A. Richter, and B. Meyer. “Numerical and experimental study of heavy oil gasification in an entrained-flow reactor and the impact of the burner concept”. In: *Fuel Processing Technology* 169 (2018), pp. 58–70. issn: 03783820. doi: 10.1016/j.fuproc.2017.09.003.

[66] J. Simonsson, H. Bladh, M. Gullberg, E. Pettersson, A. Sepman, Y. Ögren, H. Wiinikka, and P.-E. Bengtsson. “Soot Concentrations in an Atmospheric Entrained Flow Gasifier with Variations in Fuel and Burner Configuration Studied Using Diode-Laser Extinction Measurements”. In: *Energy & Fuels* 30.3 (2016), pp. 2174–2186. issn: 0887-0624. doi: 10.1021/acs.energyfuels.5b02561.

[67] X. Li, Z. Dai, Q. Guo, Q. Liang, and F. Wang. “Experimental and numerical study of MILD combustion in a bench-scale natural gas partial oxidation gasifier”. In: *Fuel* 193 (2017), pp. 197–205. issn: 00162361. doi: 10.1016/j.fuel.2016.12.056.

[68] D. Ulber. “Modellierung der Flugstromvergasung von Öl-Rückstanden”. PhD-Thesis. Aachen: RWTH Aachen, 2003.

[69] Q. Fradet, M. Braun-Unkhoff, and U. Riedel. “A Sectional Approach for the Entrained-Flow Gasification of Slurry Fuels”. In: *Energy & Fuels* 32.12 (2018), pp. 12532–12544. issn: 0887-0624. doi: 10.1021/acs.energyfuels.8b02785.

[70] C. Hu, Y. Gong, Q. Guo, L. He, and G. Yu. “Investigations of CH∗ chemiluminescence and blackbody radiation in opposed impinging coal-water slurry flames based on an entrained-flow gasifier”. In: *Fuel* 211 (2018), pp. 688–696. issn: 00162361. doi: 10.1016/j.fuel.2017.09.094.

[71] Q. Zhang, Y. Gong, Q. Guo, X. Song, and G. Yu. “Experimental study on CH* chemiluminescence characteristics of impinging flames in an opposed multi–burner gasifier”. In: *AIChE Journal* 63.6 (2017), pp. 2007–2018. issn: 0001-1541. doi: 10.1002/aic.15555.

[72] Y. Gong, Q. Guo, Q. Liang, Z. Zhou, and G. Yu. “Three-Dimensional Temperature Distribution of Impinging Flames in an Opposed Multiburner Gasifier”. In: *Industrial & Engineering Chemistry Research* 51.22 (2011), pp. 7828–7837. issn: 0888-5885. doi: 10.1021/ie2028602.

[73] K. Kidoguchi, S. Hara, M. Ashizawa, and J. Inumaru. “Study on extra heavy oil gasification reaction process”. In: *JSME International Journal Series B Fluids and Thermal Engineering* 45.3 (2002), pp. 523–529. doi: 10.1299/jsmeb.45.523.

[74] T. Parameswaran, M. A. Duchesne, S. Champagne, and R. W. Hughes. “Petroleum Coke Gasification Temperatures and Flame Spectra in the Visible Region at High Pressure”. In: *Energy & Fuels* 30.11 (2016), pp. 9867–9875. issn: 0887-0624. doi: 10.1021/acs.energyfuels.6b01751.

[75] X. Song, Q. Guo, C. Hu, Y. Gong, and G. Yu. “Optical experimental study on the characteristics of impinging coal-water slurry flame in an opposed multi-burner gasifier”. In: *Fuel* 188 (2017), pp. 132–139. issn: 00162361. doi: 10.1016/j.fuel.2016.10.028.

[76] S. Azuhata, P. O. Hedman, L. Smoot, and W. A. Sowa. “Effects of flame type and pressure on entrained coal gasification”. In: *Fuel* 65.11 (1986), pp. 1511–1515. issn: 00162361. doi: 10.1016/0016-2361(86)90326-1.

[77] M. Ashizawa, S. Hara, K. Kidoguchi, and J. Inumaru. “Gasification characteristics of extra-heavy oil in a research-scale gasifier”. In: *Energy* 30.11-12 (2005), pp. 2194–2205. issn: 03605442. doi: 10.1016/j.energy.2004.08.023.

[78] K. Sun, R. Sur, X. Chao, J. B. Jeffries, R. K. Hanson, R. J. Pummill, and K. J. Whitty. “TDL absorption sensors for gas temperature and concentrations in a high-pressure entrained-flow coal gasifier”. In: *Proceedings of the Combustion Institute* 34.2 (2013), pp. 3593–3601. doi: 10.1016/j.proci.2012.05.018.

[79] A. Sepman, Y. Ögren, Z. Qu, H. Wiinikka, and F. M. Schmidt. “Real-time in situ multi-parameter TDLAS sensing in the reactor core of an entrained-flow biomass gasifier”. In: *Proceedings of the Combustion Institute* 36.3 (2017), pp. 4541–4548. issn: 15407489. doi: 10.1016/j.proci.2016.07.011.

[80] P. J. Schroeder, A. S. Makowiecki, M. A. Kelley, R. K. Cole, N. A. Malarich, R. J. Wright, J. M. Porter, and G. B. Rieker. "Temperature and concentration measurements in a high-pressure gasifier enabled by cepstral analysis of dual frequency comb spectroscopy". In: *Proceedings of the Combustion Institute* 38.1 (2021), pp. 1561–1569. issn: 15407489. doi: 10.1016/j.proci.2020.06.011.

[81] P. Nau, P. Kutne, G. Eckel, W. Meier, C. Hotz, and S. Fleck. "Infrared absorption spectrometer for the determination of temperature and species profiles in an entrained flow gasifier". In: *Applied optics* 56.11 (2017), pp. 2982–2990. doi: 10.1364/AO.56.002982.

[82] K. Qin, P. A. Jensen, W. Lin, and A. D. Jensen. "Biomass Gasification Behavior in an Entrained Flow Reactor: Gas Product Distribution and Soot Formation". In: *Energy & Fuels* 26.9 (2012), pp. 5992–6002. issn: 0887-0624. doi: 10.1021/ef300960x.

[83] X. Song, Q. Guo, C. Hu, Y. Gong, and G. Yu. "OH* Chemiluminescence Characteristics and Structures of the Impinging Reaction Region in Opposed Impinging Diffusion Flames". In: *Energy & Fuels* (2016). issn: 0887-0624. doi: 10.1021/acs.energyfuels.5b02721.

[84] M. Mancini, M. Alberti, M. Dammann, U. Santo, G. Eckel, T. Kolb, and R. Weber. "Entrained flow gasification. Part 2: Mathematical modeling of the gasifier using RANS method". In: *Fuel* 225 (2018), pp. 596–611. issn: 00162361. doi: 10.1016/j.fuel.2018.03.100.

[85] N. Abani and A. F. Ghoniem. "Large eddy simulations of coal gasification in an entrained flow gasifier". In: *Fuel* 104 (2013), pp. 664–680. issn: 00162361. doi: 10.1016/j.fuel.2012.06.006.

[86] M. Kumar and A. F. Ghoniem. "Multiphysics Simulations of Entrained Flow Gasification. Part I: Validating the Nonreacting Flow Solver and the Particle Turbulent Dispersion Model". In: *Energy & Fuels* 26.1 (2012), pp. 451–463. issn: 0887-0624. doi: 10.1021/ef200884j.

[87] B. Göktepe, K. Umeki, A. Hazim, T. S. Lundström, and R. Gebart. "Soot reduction in an entrained flow gasifier of biomass by active dispersion of fuel particles". In: *Fuel* 201 (2017), pp. 111–117. issn: 00162361. doi: 10.1016/j.fuel.2016.09.039.

[88] X. Wu, Q. Guo, Y. Gong, C. Cheng, L. Ding, F. Wang, and G. Yu. "Visualization study on particle flow behaviors during atomization in an impinging entrained-flow gasifier". In: *Chemical Engineering Science* 225.3 (2020), p. 115834. issn: 00092509. doi: 10.1016/j.ces.2020.115834.

[89] J. A. Bossard and R. E. Peck. "Droplet size distribution effects in spray combustion". In: *Symposium (International) on Combustion* 26.1 (1996), pp. 1671–1677. issn: 00820784. doi: 10.1016/S0082-0784(96)80391-2.

[90] J. Hayashi, H. Watanabe, R. Kurose, and F. Akamatsu. "Effects of fuel droplet size on soot formation in spray flames formed in a laminar counterflow". In: *Combustion and Flame* 158.12 (2011), pp. 2559–2568. doi: 10.1016/j.combustflame.2011.05.015.

[91] P. Jenny, D. Roekaerts, and N. Beishuizen. “Modeling of turbulent dilute spray combustion”. In: *Progress in Energy and Combustion Science* 38.6 (2012), pp. 846–887. issn: 03601285. doi: 10.1016/j.pecs.2012.07.001.

[92] K. K.-y. Kuo and R. Acharya. *Fundamentals of Turbulent and Multi-Phase Combustion*. 1st Edition. s.l.: Wiley, 2012. isbn: 9780470226223. doi: 10.1002/9781118107683.

[93] G. M. Faeth. “Current status of droplet and liquid combustion”. In: *Progress in Energy and Combustion Science* 3.4 (1977), pp. 191–224. issn: 03601285. doi: 10.1016/0360-1285(77)90012-0.

[94] S. K. Chen, A. H. Lefebvre, and J. Rollbuhler. “Factors Influencing the Effective Spray Cone Angle of Pressure-Swirl Atomizers”. In: *Journal of Engineering for Gas Turbines and Power* 114.1 (1992), pp. 97–103. doi: 10.1115/1.2906313.

[95] A. Datta and S. K. Som. “Effects of spray characteristics on combustion performance of a liquid fuel spray in a gas turbine combustor”. In: *International Journal of Energy Research* 23.3 (1999), pp. 217–228.

[96] V. G. McDonell and G. S. Samuelsen. “Measurement of fuel mixing and transport processes in gas turbine combustion”. In: *Measurement Science and Technology* 11.7 (2000), pp. 870–886. issn: 0957-0233. doi: 10.1088/0957-0233/11/7/304.

[97] A. N. Karpetis and A. GOMEZ. “Self-similarity, momentum scaling and Reynolds stress in non-premixed turbulent spray flames”. In: *Journal of Fluid Mechanics* 397 (1999), pp. 231–258. issn: 0022-1120. doi: 10.1017/S0022112099006102.

[98] M. W. Thring and M. P. Newby. “Combustion length of enclosed turbulent jet flames”. In: *Symposium (International) on Combustion* 4.1 (1953), pp. 789–796. issn: 00820784. doi: 10.1016/S0082-0784(53)80103-7.

[99] D. Stepowski, P. Goix, and A. Cessou. “Simple description of the combustion structures in the stabilization stage of a spray jet flame”. In: *Atomization and Sprays* 9.1 (1999), pp. 1–27. issn: 1046-5111. doi: 10.1615/AtomizSpr.v9.i1.10.

[100] R. J. Sornek, R. Dobashi, and T. Hirano. “Effect of turbulence on vaporization, mixing, and combustion of liquid-fuel sprays”. In: *Combustion and Flame* 120.4 (2000), pp. 479–491. doi: 10.1016/S0010-2180(99)00105-4.

[101] A. Labbafan and H. Ghassemi. “Numerical modeling of an E-Gas entrained flow gasifier to characterize a high-ash coal gasification”. In: *Energy Conversion and Management* 112 (2016), pp. 337–349. issn: 01968904. doi: 10.1016/j.enconman.2016.01.040.

[102] Y.-T. Luan, Y.-P. Chyou, and T. Wang. “Numerical analysis of gasification performance via finite-rate model in a cross-type two-stage gasifier”. In: *International Journal of Heat and Mass Transfer* 57.2 (2013), pp. 558–566. issn: 00179310. doi: 10.1016/j.ijheatmasstransfer.2012.10.026.

[103] H.-T. Kim, J.-H. Lee, J.-W. Lee, B.-H. Lee, and C.-H. Jeon. “Effect of Operating Conditions on the Gasification of Pet-Coke Water Slurry in an Entrained-Flow Gasifier Simulation”. In: *ACS omega* 8.48 (2023), pp. 45933–45941. doi: 10.1021/acsomega.3c06688.

[104] Q. Fradet. “Novel modeling approaches for the entrained-flow gasification of bio-slurries”. PhD-Thesis. Universität Stuttgart, 2020.

[105] M. Dammann, F. Hüsing, U. Santo, D. Böning, M. Mancini, and T. Kolb. “Characterisation of beech wood pyrolysis oil: Chemical and physical properties and decomposition kinetics”. In: *Fuel* 404 (2026), p. 134897. issn: 00162361. doi: 10.1016/j.fuel.2025.134897.

[106] M. W. Jarvis, T. J. Haas, B. S. Donohoe, J. W. Daily, K. R. Gaston, W. J. Frederick, and M. R. Nimlos. “Elucidation of Biomass Pyrolysis Products Using a Laminar Entrained Flow Reactor and Char Particle Imaging”. In: *Energy & Fuels* 25.1 (2011), pp. 324–336. issn: 0887-0624. doi: 10.1021/ef100832d.

[107] P. Stoesser, J. Ruf, R. Gupta, N. Djordjevic, and T. Kolb. “Contribution to the Understanding of Secondary Pyrolysis of Biomass-Based Slurry under Entrained-Flow Gasification Conditions”. In: *Energy & Fuels* 30.8 (2016), pp. 6448–6457. issn: 0887-0624. doi: 10.1021/acs.energyfuels.6b00935.

[108] A. H. Lefebvre. *Atomization and Sprays: Combustion: An International Series*. London: Hemisphere Publishing Corporation, 1989.

[109] N. A. Chigier and C. G. McCreath. “Combustion of droplets in sprays”. In: *Acta Astronautica* 1.5-6 (1974), pp. 687–710. issn: 00945765. doi: 10.1016/0094-5765(74)90028-9.

[110] A. Sänger. “Zerstäubung hochviskoser Fluide bei variierendem Systemdruck”. PhD-Thesis. Karlsruhe: Karlsruhe Institute of Technology, 2018. doi: 10.5445/IR/1000087397.

[111] P. Marmottant and E. Villermaux. “On spray formation”. In: *Journal of Fluid Mechanics* 498 (2004), pp. 73–111. issn: 0022-1120. doi: 10.1017/S0022112003006529.

[112] H. Schlichting and K. Gersten. *Boundary Layer Theory: Ninth Edition*. Berlin Heidelberg: Springer Nature, 2017. isbn: 978-3-662-52917-1.

[113] S. R. Turns. *An Introduction to Combustion: Concepts and Applications*. 3. New Delhi, India: McGraw-Hill, 2012. isbn: 1-25-902594-2.

[114] A. N. Kolmogorov. “The local structure of turbulence in incompressible viscous fluid for very large Reynolds numbers”. In: *Numbers. In Dokl. Akad. Nauk SSSR* 30 (1941), p. 301. doi: 10.1098/rspa.1991.0075.

[115] R. Weber, V. N. Tanga, M. Mancini, A. Lindmüller, and M. Alberti. “Entrainment rate predictions of axis-symmetric non-swirling jets using free-jet-theory, Reynolds-averaged Navier-Stokes modelling and large-eddy-simulations resolved up to Kolmogorov scale”. In: *Journal of the Energy Institute* 117 (2024), p. 101806. issn: 17439671. doi: 10.1016/j.joei.2024.101806.

[116] V. N. Tanga, R. Weber, M. Mancini, A. Lindmüller, and M. Olbricht. “Entrainment rate predictions of axis-symmetric non-swirling free jets for engineering applications: Hydrogen, helium, propane and carbon dioxide jets entraining air”. In: *Journal of the Energy Institute* 119 (2025), p. 101959. issn: 17439671. doi: 10.1016/j.joei.2024.101959.

[117] J.M. Beér and N.A. Chigier. *Combustion Aerodynamics*. London: Applied Science Publishers Limited, 1972. isbn: 0 85334 513 9.

[118] R. Günther. *Verbrennung und Feuerungen*. Berlin Heidelberg: Springer, 1984. isbn: 3-540-13256-2.

[119] A. Capone, A. Soldati, and G. P. Romano. "Mixing and entrainment in the near field of turbulent round jets". In: *Experiments in Fluids* 54.1 (2013), p. 2149. issn: 0723-4864. doi: 10.1007/s00348-012-1434-x.

[120] C. G. Ball, H. Fellouah, and A. Pollard. "The flow field in turbulent round free jets". In: *Progress in Aerospace Sciences* 50 (2012), pp. 1–26. issn: 03760421. doi: 10.1016/j.paerosci.2011.10.002.

[121] G. N. Abramovich. *The Theory of Turbulent Jets*. 1. Cambrige, MA: MIT Press, 1963.

[122] F. P. Ricou and D. Spalding. "Measurements of entrainment by axisymmetrical turbulent jets". In: *Journal of fluid mechanics* 11.1 (1961), pp. 21–32.

[123] R. Curtet. "Confined jets and recirculation phenomena with cold air". In: *Combustion and Flame* 2.4 (1958), pp. 383–411.

[124] H. J. Sheen, B. H. Jou, and Y. T. Lee. "Effect of particle size on a two-phase turbulent jet". In: *Experimental Thermal and Fluid Science* 8.4 (1994), pp. 315–327. issn: 08941777. doi: 10.1016/0894-1777(94)90061-2.

[125] T. C. W. Lau and G. J. Nathan. "The effect of Stokes number on particle velocity and concentration distributions in a well-characterised, turbulent, co-flowing two-phase jet". In: *Journal of Fluid Mechanics* 809 (2016), pp. 72–110. issn: 0022-1120. doi: 10.1017/jfm.2016.666.

[126] M. B. Stakič and D. Z. Milojevič. "The effect of particles on the gas velocity in a free turbulent flow". In: *Journal of Engineering Physics and Thermophysics* 68.3 (1995), pp. 302–306. issn: 1062-0125. doi: 10.1007/BF00859039.

[127] J. Schelling and L. Reh. "Influence of atomiser design and coaxial gas velocity on gas entrainment into sprays". In: *Chemical Engineering and Processing: Process Intensification* 38.4-6 (1999), pp. 383–393. issn: 02552701. doi: 10.1016/S0255-2701(99)00036-7.

[128] W. K. Melville and K. Bray. "The two-phase turbulent jet". In: *International Journal of Heat and Mass Transfer* 22.2 (1979), pp. 279–287. issn: 00179310. doi: 10.1016/0017-9310(79)90151-0.

[129] V. Subramanian and R. Ganesh. "Influence of free stream velocity on the entrainment by single– and two–phase axisymmetric jets". In: *AIChE Journal* 30.6 (1984), pp. 1010–1013. issn: 0001-1541. doi: 10.1002/aic.690300626.

[130] G. Hetsroni. "Particles-turbulence interaction". In: *International Journal of Multiphase Flow* 15.5 (1989), pp. 735–746. issn: 03019322. doi: 10.1016/0301-9322(89)90037-2.

[131] F. Fröde, O. Desjardins, M. Bieber, M. Reddemann, R. Kneer, and H. Pitsch. "Multiscale simulation of spray and mixture formation for a coaxial atomizer". In: *International Journal of Multiphase Flow* 182 (2025), p. 104971. issn: 03019322. doi: 10.1016/j.ijmultiphaseflow.2024.104971.

[132] F. Zhang, T. Zirwes, S. Wachter, T. Jakobs, P. Habisreuther, N. Zarzalis, D. Trimis, T. Kolb, H. Bockhorn, and D. Stapf. “Numerical simulations of air-assisted primary atomization at different air-to-liquid injection angles”. In: *International Journal of Multiphase Flow* 158.2 (2023), p. 104304. issn: 03019322. doi: 10.1016/j.ijmultiphaseflow.2022.104304.

[133] F. Zhang, T. Zirwes, T. Müller, S. Wachter, T. Jakobs, P. Habisreuther, N. Zarzalis, D. Trimis, and T. Kolb. “Effect of elevated pressure on air-assisted primary atomization of coaxial liquid jets: Basic research for entrained flow gasification”. In: *Renewable and Sustainable Energy Reviews* 134.3 (2020), p. 110411. issn: 13640321. doi: 10.1016/j.rser.2020.110411.

[134] J. C. Lasheras and E. Hopfinger. “Liquid jet instability and atomization in a coaxial gas stream”. In: *Annual review of fluid mechanics* 32.1 (2000), pp. 275–308. doi: 10.1146/annurev.fluid.32.1.275.

[135] R. van Hout, S. Murugan, A. Mitra, and B. Cukurel. “Coaxial Circular Jets—A Review”. In: *Fluids* 6.4 (2021), p. 147. issn: 2311-5521. doi: 10.3390/fluids6040147.

[136] L. Aisa, J. A. Garcia, L. M. Cerecedo, I. Garcia Palacin, and E. Calvo. “Particle concentration and local mass flux measurements in two-phase flows with PDA. Application to a study on the dispersion of spherical particles in a turbulent air jet”. In: *International Journal of Multiphase Flow* 28.2 (2002), pp. 301–324. issn: 03019322. doi: 10.1016/S0301-9322(01)00071-4.

[137] M. K. Laats. “Experimental study of the dynamics of an air-dust jet”. In: *Inzhenerno-Fiztcheskii Zhurnal,* 10 (1966), pp. 11–15.

[138] S. Sazhin. *Droplets and Sprays*. London: Springer London, 2014. doi: 10.1007/978-1-4471-6386-2.

[139] W. A. Sirignano. “Fuel droplet vaporization and spray combustion theory”. In: *Progress in Energy and Combustion Science* 9.4 (1983), pp. 291–322. issn: 03601285. doi: 10.1016/0360-1285(83)90011-4.

[140] C. S. Handscomb and M. Kraft. “Simulating the structural evolution of droplets following shell formation”. In: *Chemical Engineering Science* 65.2 (2010), pp. 713–725. issn: 00092509. doi: 10.1016/j.ces.2009.09.025.

[141] A. Lee and C. K. Law. “Gasification and shell characteristics in slurry droplet burning”. In: *Combustion and Flame* 85.1-2 (1991), pp. 77–93. doi: 10.1016/0010-2180(91)90178-E.

[142] T. Elperin and B. Krasovitov. “Evaporation of liquid droplets containing small solid particles”. In: *International Journal of Heat and Mass Transfer* 38.12 (1995), pp. 2259–2267. issn: 00179310. doi: 10.1016/0017-9310(94)00337-U.

[143] M. J. Z. Ganji and H. Ghassemi. “Theoretical shell formation model for single droplet of heavy fuel oil”. In: *Journal of Analytical and Applied Pyrolysis* 169.5 (2023), p. 105760. issn: 01652370. doi: 10.1016/j.jaap.2022.105760.

[144] P. L. Murdoch, M. Pourkashanian, and A. Williams. “The mechanism of combustion of coal-water slurries”. In: *Symposium (International) on Combustion* 20.1 (1985), pp. 1409–1418. issn: 00820784. doi: 10.1016/S0082-0784(85)80633-0.

[145] P. Roy Choudhury. “Slurry fuels”. In: *Progress in Energy and Combustion Science* 18.5 (1992), pp. 409–427. issn: 03601285. doi: 10.1016/0360-1285(92)90008-D.

[146] K. Y. Ahn, S. W. Baek, and C. E. Choi. “Investigation of a Coal-Water Slurry Droplet Exposed to Hot Gas Stream”. In: *Combustion Science and Technology* 97.4-6 (1994), pp. 429–447. issn: 0010-2202. doi: 10.1080/00102209408935389.

[147] K. Y. Vershinina, D. O. Glushkov, G. V. Kuznetsov, and P. A. Strizhak. “Differences in the ignition characteristics of coal–water slurries and composite liquid fuel”. In: *Solid Fuel Chemistry* 50.2 (2016), pp. 88–101. issn: 0361-5219. doi: 10.3103/S0361521916020117.

[148] M. Broumand, S. Albert-Green, S. Yun, Z. Hong, and M. J. Thomson. “Spray combustion of fast pyrolysis bio-oils: Applications, challenges, and potential solutions”. In: *Progress in Energy and Combustion Science* 79 (2020), p. 100834. issn: 03601285. doi: 10.1016/j.pecs.2020.100834.

[149] R. Calabria, F. Chiariello, and P. Massoli. “Combustion fundamentals of pyrolysis oil based fuels”. In: *Experimental Thermal and Fluid Science* 31.5 (2007), pp. 413–420. issn: 08941777. doi: 10.1016/j.expthermflusci.2006.04.010.

[150] M. Garcia-Perez, P. Lappas, P. Hughes, L. Dell, A. Chaala, D. Kretschmer, and C. Roy. “Combustion Properties of Vacuum Pyrolysis Wood Industry residues Oils”. In: *IFRF Combustion Journal* 20.1 (2006), pp. 364–375. issn: 1562-479X.

[151] S. C. Sital. “Pyrolysis oil evaporation including liquid phase polymerization reaction”. PhD-Thesis. Technical University Delft, 2018.

[152] G. van Rossum, B. M. Güell, R. P. B. Ramachandran, K. Seshan, L. Lefferts, W. P. M. van Swaaij, and S. R. A. Kersten. “Evaporation of pyrolysis oil: Product distribution and residue char analysis”. In: *AIChE Journal* 56.8 (2010), pp. 2200–2210. issn: 0001-1541. doi: 10.1002/aic.12126.

[153] N. Bomo, J. Lahaye, G. Prado, and G. Claus. “Formation of cenospheres during pyrolysis of residual fuel oils”. In: *Symposium (International) on Combustion* 20.1 (1985), pp. 903–911. issn: 00820784. doi: 10.1016/S0082-0784(85)80579-8.

[154] L. Jiang, A. M. Elbaz, P. Guida, S. M. Al-Noman, I. A. AlGhamdi, S. Saxena, and W. L. Roberts. “Cenosphere Formation during Single-Droplet Combustion of Heavy Fuel Oil”. In: *Energy & Fuels* 33.2 (2019), pp. 1570–1581. issn: 0887-0624. doi: 10.1021/acs.energyfuels.8b03632.

[155] N. J. Marrone, I. M. Kennedy, and F. L. Dryer. “Coke Formation in the Combustion of Isolated Heavy Oil Droplets”. In: *Combustion Science and Technology* 36.3-4 (1984), pp. 149–170. issn: 0010-2202. doi: 10.1080/00102208408923731.

[156] P. Moszkowicz, L. Witzel, and G. Claus. “Modelling of very fast pyrolysis of heavy fuel oil droplets”. In: *Chemical Engineering Science* 51.17 (1996), pp. 4075–4086. issn: 00092509. doi: 10.1016/0009-2509(96)00253-9.

[157] H. Y. Setyawan and M. Zhu. “Cenosphere Formation and Combustion Characteristics of Single Droplets of Vacuum Residual Oils”. In: *Combustion Science and Technology* 197.1 (2025), pp. 59–76. issn: 0010-2202. doi: 10.1080/00102202.2023.2170750.

[158] S.-C. Yao and L. Liu. “Behavior of suspended coal-water slurry droplets in a combustion environment”. In: *Combustion and Flame* 51 (1983), pp. 335–345. doi: 10.1016/0010-2180(83)90111-6.

[159] M. Sitarski. “On the Feasibility of Secondary Atomization of Small Slurry Droplets Exposed to Intense Thermal Radiation”. In: *Combustion Science and Technology* 54.1-6 (1987), pp. 177–201. issn: 0010-2202. doi: 10.1080/00102208708947052.

[160] D. J. Maloney and J. F. Spann. “Evaporation, Agglomeration, and explosive boiling characteristics of coal-water fuels under intense heating conditions”. In: *Symposium (International) on Combustion* 22.1 (1989), pp. 1999–2008. issn: 00820784. doi: 10.1016/S0082-0784(89)80215-2.

[161] W. Hallett and N. A. Clark. “A model for the evaporation of biomass pyrolysis oil droplets”. In: *Fuel* 85.4 (2006), pp. 532–544. issn: 00162361. doi: 10.1016/j.fuel.2005.08.006.

[162] A. Silaen and T. Wang. “Effect of turbulence and devolatilization models on coal gasification simulation in an entrained-flow gasifier”. In: *International Journal of Heat and Mass Transfer* 53.9-10 (2010), pp. 2074–2091. issn: 00179310. doi: 10.1016/j.ijheatmasstransfer.2009.12.047.

[163] M.-H. Chen, Y.-P. Chyou, and T. Wang. “Simulation of Coal Gasification in a Low-Temperature, High-Pressure Entrained-Bed Reactor with a Volatiles Condensation and Re-Evaporation Model”. In: *Applied Sciences* 9.3 (2019), p. 510. issn: 2076-3417. doi: 10.3390/app9030510.

[164] Z. Sun, Z. Dai, Z. Zhou, Q. Guo, and G. Yu. “Numerical Simulation of Industrial Opposed Multiburner Coal–Water Slurry Entrained Flow Gasifier”. In: *Industrial & Engineering Chemistry Research* 51.6 (2012), pp. 2560–2569. issn: 0888-5885. doi: 10.1021/ie201542q.

[165] P. J. Benyon. “Computational modeling of entrained flow slagging gasifiers”. PhD-Thesis. Sydney: University of Sydney, 2002.

[166] J. Xu, Z. Dai, H. Liu, L. Guo, and F. Sun. “Modeling of multiphase reaction and slag flow in single-burner coal water slurry gasifier”. In: *Chemical Engineering Science* 162.1 (2017), pp. 41–52. issn: 00092509. doi: 10.1016/j.ces.2016.12.029.

[167] T. Jakobs, N. Djordjevic, S. Fleck, M. Mancini, R. Weber, and T. Kolb. “Gasification of high viscous slurry R&D on atomization and numerical simulation”. In: *Applied Energy* 93 (2012), pp. 449–456. issn: 03062619. doi: 10.1016/j.apenergy.2011.12.026.

[168] S. Hafner. “Modellentwicklung zur numerischen Simulation eines Flugstromvergasers für Biomasse”. PhD-Thesis. Heidelberg: Ruprechts-Karls-Universität, 2010.

[169] C. Hasse, P. Debiagi, X. Wen, K. Hildebrandt, M. Vascellari, and T. Faravelli. "Advanced modeling approaches for CFD simulations of coal combustion and gasification". In: *Progress in Energy and Combustion Science* 86 (2021), p. 100938. doi: 0.1016/j.pecs.2021.100938.

[170] J. Mularski, H. Pawlak-Kruczek, and N. Modlinski. "A review of recent studies of the CFD modelling of coal gasification in entrained flow gasifiers, covering devolatilization, gas-phase reactions, surface reactions, models and kinetics". In: *Fuel* 271 (2020), p. 117620. issn: 00162361. doi: 10.1016/j.fuel.2020.117620.

[171] A. Trubetskaya, P. A. Jensen, A. D. Jensen, M. Steibel, H. Spliethoff, and P. Glarborg. "Influence of fast pyrolysis conditions on yield and structural transformation of biomass chars". In: *Fuel Processing Technology* 140 (2015), pp. 205–214. issn: 03783820. doi: 10.1016/j.fuproc.2015.08.034.

[172] A. Tremel and H. Spliethoff. "Gasification kinetics during entrained flow gasification – Part II: Intrinsic char reaction rate and surface area development". In: *Fuel* 107 (2013), pp. 653–661. issn: 00162361. doi: 10.1016/j.fuel.2012.10.053.

[173] C. Schneider. "Reaction Kinetics of Biogenic Solid Fuels under Process Conditions of Technical Entrained-Flow Gasifiers". PhD-Thesis. Karlsruhe: Karlsruhe Institute of Technology, 2021.

[174] H. Bockhorn. *Soot Formation in Combustion: Mechanisms and Models*. Springer Berlin Heidelberg, 1994. isbn: 3-540-58398-X.

[175] T. Kathrotia, C. Naumann, P. Oßwald, M. Köhler, and U. Riedel. "Kinetics of Ethylene Glycol: The first validated reaction scheme and first measurements of ignition delay times and speciation data". In: *Combustion and Flame* 179 (2017), pp. 172–184. doi: 10.1016/j.combustflame.2017.01.018.

[176] S. Hafner, A. Rashidi, G. Baldea, and U. Riedel. "A detailed chemical kinetic model of high-temperature ethylene glycol gasification". In: *Combustion Theory and Modelling* 15.4 (2011), pp. 517–535. issn: 1364-7830. doi: 10.1080/13647830.2010.547602.

[177] F. Hunger, B. Stelzner, D. Trimis, and C. Hasse. "Flamelet-Modeling of Inverse Rich Diffusion Flames". In: *Flow, Turbulence and Combustion* 90.4 (2013), pp. 833–857. issn: 1386-6184. doi: 10.1007/s10494-012-9422-z.

[178] F. Hunger, M. F. Zulkifli, B. A. O. Williams, F. Beyrau, and C. Hasse. "Comparative flame structure investigation of normal and inverse turbulent non-premixed oxy-fuel flames using experimentally recorded and numerically predicted Rayleigh and OH-PLIF signals". In: *Proceedings of the Combustion Institute* 36.2 (2017), pp. 1713–1720. issn: 15407489. doi: 10.1016/j.proci.2016.06.183.

[179] J. Warnatz, U. Maas, and R. W. Dibble. *Combustion*. New York: Springer-Verlag Berlin Heidelberg, 2006. isbn: 3-540-25992-9.

[180] R. Weber. *Combustion fundamentals with elements of chemical thermodynamics*. 4. ed. Vol. 11. International studies in science and engineering. Clausthal-Zellerfeld: Papierflieger-Verl., 2013. isbn: 9783897209213.

[181] T. Kathrotia, M. Fikri, M. Bozkurt, M. Hartmann, U. Riedel, and C. Schulz. “Study of the H+O+M reaction forming OH∗: Kinetics of OH∗ chemiluminescence in hydrogen combustion systems”. In: *Combustion and Flame* 157.7 (2010), pp. 1261–1273. doi: 10.1016/j.combustflame.2010.04.003.

[182] A. B. Sahu, S. Krishna, and R. V. Ravikrishna. “Quantitative OH measurements and numerical investigation of H2/CO kinetics in syngas-air counterflow diffusion flames”. In: *Fuel* 193 (2017), pp. 119–133. issn: 00162361. doi: 10.1016/j.fuel.2016.12.023.

[183] J. Heinze, U. Meier, T. Behrendt, C. Willert, K.-P. Geigle, O. Lammel, and R. Lückerath. “PLIF Thermometry Based on Measurements of Absolute Concentrations of the OH Radical”. In: *Zeitschrift für Physikalische Chemie* 225.11-12 (2011), pp. 1315–1341. issn: 0942-9352. doi: 10.1524/zpch.2011.0168.

[184] M. J. Dyer and D. R. Crosley. “Two-dimensional imaging of OH laser-induced fluorescence in a flame”. In: *Optics letters* 7.8 (1982), pp. 382–384. doi: 10.1364/OL.7.000382.

[185] K. Kohse-Höinghaus. “Laser techniques for the quantitative detection of reactive intermediates in combustion systems”. In: *Progress in Energy and Combustion Science* 20.3 (1994), pp. 203–279. issn: 03601285. doi: 10.1016/0360-1285(94)90015-9.

[186] A. C. Eckbreth. *Laser Diagnostics for Combustion Temperature and Species*. 2. London: CRC Press, 1996. doi: 10.1201/9781003077251.

[187] E. P. Hassel and S. Linow. “Laser diagnostics for studies of turbulent combustion”. In: *Measurement Science and Technology* 11.2 (2000), R37–R57. issn: 0957-0233. doi: 10.1088/0957-0233/11/2/201.

[188] N. T. Clemens and P. H. Paul. “Effects of heat release on the near field flow structure of hydrogen jet diffusion flames”. In: *Combustion and Flame* 102.3 (1995), pp. 271–284. doi: 10.1016/0010-2180(94)00277-Y.

[189] J. M. Donbar, J. F. Driscoll, and C. D. Carter. “Reaction zone structure in turbulent nonpremixed jet flames—from CH-OH PLIF images”. In: *Combustion and Flame* 122.1-2 (2000), pp. 1–19. doi: 10.1016/S0010-2180(00)00098-5.

[190] V. Sick and N. Wermuth. “Single-shot imaging of OH radicals and simultaneous OH radical/acetone imaging with a tunable Nd: YAG laser”. In: *Applied Physics B* 79.2 (2004), pp. 139–143. issn: 0946-2171. doi: 10.1007/s00340-004-1545-z.

[191] A. Cessou and D. Stepowski. “Planar Laser Induced Fluorescence Measurement of OH in the Stabilization Stage of a Spray Jet Flame”. In: *Combustion Science and Technology* 118.4-6 (1996), pp. 361–381. issn: 0010-2202. doi: 10.1080/00102209608951986.

[192] A. Cessou, U. Meier, and D. Stepowski. “Applications of planar laser induced fluorescence in turbulent reacting flows”. In: *Measurement Science and Technology* 11.7 (2000), pp. 887–901. issn: 0957-0233. doi: 10.1088/0957-0233/11/7/305.

[193] H. N. Najm, P. H. Paul, C. J. Mueller, and P. S. Wyckoff. “On the adequacy of certain experimental observables as measurements of flame burning rate”. In: *Combustion and Flame* 113.3 (1998), pp. 312–332.

[194] P. H. Paul and H. N. Najm. "Planar laser-induced fluorescence imaging of flame heat release rate". In: *Symposium (International) on Combustion* 27.1 (1998), pp. 43–50. issn: 00820784. doi: 10.1016/S0082-0784(98)80388-3.

[195] B. Stelzner, F. Hunger, S. Voss, J. Keller, C. Hasse, and D. Trimis. "Experimental and numerical study of rich inverse diffusion flame structure". In: *Proceedings of the Combustion Institute* 34.1 (2013), pp. 1045–1055. issn: 1540-7489. doi: 10.1016/j.proci.2012.06.153. url: https://doi.org/10.1016/j.proci.2012.06.153.

[196] S. Choi, T. Y. Kim, H. K. Kim, J. Koo, J. S. Kim, and O. C. Kwon. "Properties of inverse nonpremixed pure O2/CH4 coflow flames in a model combustor". In: *Energy* 93 (2015), pp. 1105–1115. doi: https://doi.org/10.1016/j.energy.2015.09.110.

[197] T. Zhang, Q. Guo, X. Song, Z. Zhou, and G. Yu. "The chemiluminescence and structure properties of normal/inverse diffusion flames". In: *Journal of Spectroscopy* 2013 (2013). issn: 2314-4939. doi: 10.1155/2013/304717. url: https://doi.org/10.1155/2013/304717.

[198] I. Glassman, R. A. Yetter, and N. G. Glumac. *Combustion*. Academic press, 2014.

[199] V. Hariharan, M. S, and D. P. Mishra. "The inverse jet diffusion flames: A systematic review". In: *Progress in Energy and Combustion Science* 109 (2025), p. 101218. issn: 03601285. doi: 10.1016/j.pecs.2025.101218.

[200] H. S. Zhen, Z. L. Wei, X. Y. Liu, Z. H. Liu, X. C. Wang, Z. H. Huang, and C. W. Leung. "A state-of-the-art review of lab-scale inverse diffusion burners & flames: From laminar to turbulent". In: *Fuel Processing Technology* 222.1 (2021), p. 106940. issn: 03783820. doi: 10.1016/j.fuproc.2021.106940.

[201] C. Chu, P. Liu, I. Alsheikh, F. Aydin, R. A. Serrano-Bayona, and W. L. Roberts. "The flame length measurements of oxygen-enriched carbon dioxide-diluted methane inverse diffusion flames". In: *Combustion and Flame* 262 (2024), p. 113282. doi: 10.1016/j.combustflame.2023.113282.

[202] Y. Jung, K. C. Oh, C. Bae, and H. D. Shin. "The effect of oxygen enrichment on incipient soot particles in inverse diffusion flames". In: *Fuel* 102 (2012), pp. 199–207. issn: 00162361. doi: 10.1016/j.fuel.2012.05.047.

[203] P. Liu, C. Chu, I. Alsheikh, S. R. Gubba, S. Saxena, O. Chatakonda, J. W. Kloosterman, F. Liu, and W. L. Roberts. "Soot production in high pressure inverse diffusion flames with enriched oxygen in the oxidizer stream". In: *Combustion and Flame* 245 (2022), p. 112378. doi: 10.1016/j.combustflame.2022.112378.

[204] X. Li, Z. Dai, Y. Xu, C. Li, Z. Zhou, and F. Wang. "Inverse diffusion flame of CH 4 –O 2 in hot syngas coflow". In: *International Journal of Hydrogen Energy* 40.46 (2015), pp. 16104–16114. issn: 03603199. doi: 10.1016/j.ijhydene.2015.09.073.

[205] B. M. Kumfer, S. A. Skeen, and R. L. Axelbaum. "Soot inception limits in laminar diffusion flames with application to oxy–fuel combustion". In: *Combustion and Flame* 154.3 (2008), pp. 546–556. doi: 10.1016/j.combustflame.2008.03.008.

[206] D. R. Richardson, N. Jiang, D. L. Blunck, J. R. Gord, and S. Roy. "Characterization of inverse diffusion flames in vitiated cross flows via two-photon planar laser-induced fluorescence of CO and 2-D thermometry". In: *Combustion and Flame* 168 (2016), pp. 270–285. doi: 10.1016/j.combustflame.2016.03.005.

[207] B. Stelzner, F. Hunger, A. Laugwitz, M. Gräbner, S. Voss, K. Uebel, M. Schurz, R. Schimpke, S. Weise, S. Krzack, D. Trimis, C. Hasse, and B. Meyer. "Development of an inverse diffusion partial oxidation flame and model burner contributing to the development of 3rd generation coal gasifiers". In: *Fuel Processing Technology* 110 (2013), pp. 33–45. issn: 03783820. doi: 10.1016/j.fuproc.2013.01.005.

[208] B. A. Rabee. "The effect of inverse diffusion flame burner-diameter on flame characteristics and emissions". In: *Energy* 160.1 (2018), pp. 1201–1207. issn: 03605442. doi: 10.1016/j.energy.2018.07.061.

[209] H. Chiu. "Advances and challenges in droplet and spray combustion. I. Toward a unified theory of droplet aerothermochemistry". In: *Progress in Energy and Combustion Science* 26.4-6 (2000), pp. 381–416. issn: 03601285. doi: 10.1016/S0360-1285(00)00016-2.

[210] A. V. Brito Lopes, N. Emekwuru, and K. Joshi. "Are the available data from laboratory spray burners suitable for CFD modelling validations? A review". In: *Energy Conversion and Management: X* 16.9 (2022), p. 100289. issn: 25901745. doi: 10.1016/j.ecmx.2022.100289.

[211] J. W. Daily. "Laser induced fluorescence spectroscopy in flames". In: *Progress in Energy and Combustion Science* 23.2 (1997), pp. 133–199. issn: 03601285. doi: 10.1016/S0360-1285(97)00008-7.

[212] K. Kohse-Höinghaus, R. S. Barlow, M. Aldén, and J. Wolfrum. "Combustion at the focus: Laser diagnostics and control". In: *Proceedings of the Combustion Institute* 30.1 (2005), pp. 89–123. issn: 15407489. doi: 10.1016/j.proci.2004.08.274.

[213] K. Kohse-Hinghaus. "Quantitative laser-induced fluorescence: Some recent developments in combustion diagnostics". In: *Applied Physics B* 50.6 (1990), pp. 455–461. issn: 0946-2171. doi: 10.1007/BF00408771.

[214] M. Tamura, P. A. Berg, J. E. Harrington, J. Luque, J. B. Jeffries, G. P. Smith, and D. R. Crosley. "Collisional quenching of CH (A), OH (A), and NO (A) in low pressure hydrocarbon flames". In: *Combustion and Flame* 114.3-4 (1998), pp. 502–514.

[215] M. J. Dunn and A. R. Masri. "A comprehensive model for the quantification of linear and nonlinear regime laser-induced fluorescence of OH under a2S+-x2P(1,0)) excitation". In: *Applied Physics B* 101.1-2 (2010), pp. 445–463. issn: 0946-2171. doi: 10.1007/s00340-010-4129-0.

[216] M. J. Dunn, A. Macfarlane, R. S. Barlow, D. Geyer, K. Dieter, and A. R. Masri. "Spontaneous Raman–LIF–CO–OH measurements of species concentration in turbulent spray flames". In: *Proceedings of the Combustion Institute* 38.1 (2021), pp. 1779–1786. issn: 15407489. doi: 10.1016/j.proci.2020.07.037.

[217] R. S. Barlow, R. W. Dibble, and R. P. Lucht. “Simultaneous measurement of Raman scattering and laser-induced OH fluorescence in nonpremixed turbulent jet flames”. In: *Optics letters* 14.5 (1989), pp. 263–265. doi: 10.1364/OL.14.000263.

[218] L. Angelilli, P. P. Ciottoli, T. F. Guiberti, R. M. Galassi, F. E. Hernández Pérez, W. R. Boyette, G. Magnotti, W. L. Roberts, M. Valorani, and H. G. Im. “A method to convert stand-alone OH fluorescence images into OH mole fraction”. In: *Proceedings of the Combustion Institute* 38.1 (2021), pp. 1771–1778. issn: 15407489. doi: 10.1016/j.proci.2020.06.256.

[219] C. Schulz and V. Sick. “Tracer-LIF diagnostics: Quantitative measurement of fuel concentration, temperature and fuel/air ratio in practical combustion systems”. In: *Progress in Energy and Combustion Science* 31.1 (2005), pp. 75–121. issn: 03601285. doi: 10.1016/j.pecs.2004.08.002.

[220] T. D. Fansler and S. E. Parrish. “Spray measurement technology: A review”. In: *Measurement Science and Technology* 26.1 (2015), p. 012002. issn: 0957-0233. doi: 10.1088/0957-0233/26/1/012002.

[221] P. G. Felton, F. V. Bracco, and M. E. A. Bardsley. “On the Quantitative Application of Exciplex Fluorescence to Engine Sprays”. In: *Journal of Engines* (1993), pp. 1254–1262.

[222] B. Williams, P. Ewart, X. Wang, R. Stone, H. Ma, H. Walmsley, R. Cracknell, R. Stevens, D. Richardson, H. Fu, and S. Wallace. “Quantitative planar laser-induced fluorescence imaging of multi-component fuel/air mixing in a firing gasoline-direct-injection engine: Effects of residual exhaust gas on quantitative PLIF”. In: *Combustion and Flame* 157.10 (2010), pp. 1866–1878. doi: 10.1016/j.combustflame.2010.06.004.

[223] T. D. Fansler, M. C. Drake, B. Gajdeczko, I. Düwel, W. Koban, F. P. Zimmermann, and C. Schulz. “Quantitative liquid and vapor distribution measurements in evaporating fuel sprays using laser-induced exciplex fluorescence”. In: *Measurement Science and Technology* 20.12 (2009), p. 125401. issn: 0957-0233. doi: 10.1088/0957-0233/20/12/125401.

[224] K. Jung, H. Koh, and Y. Yoon. “Assessment of planar liquid-laser-induced fluorescence measurements for spray mass distributions of like-doublet injectors”. In: *Measurement Science and Technology* 14.8 (2003), pp. 1387–1395. issn: 0957-0233. doi: 10.1088/0957-0233/14/8/326.

[225] J. Pastor, J. López, J. Juliá, and J. Benajes. “Planar Laser-Induced Fluorescence fuel concentration measurements in isothermal Diesel sprays”. In: *Optics express* 10.7 (2002), pp. 309–323. doi: 10.1364/OE.10.000309.

[226] A. A. Rotunno, M. Winter, G. M. Dobbs, and L. A. Melton. “Direct Calibration Procedures for Exciplex-Based Vapor/ Liquid Visualization of Fuel Sprays”. In: *Combustion Science and Technology* 71.4-6 (1990), pp. 247–261. issn: 0010-2202. doi: 10.1080/00102209008951635.

[227] J. M. Desantes, J. V. Pastor, J. M. Pastor, and J. E. Juliá. “Limitations on the use of the planar laser induced exciplex fluorescence technique in diesel sprays”. In: *Fuel* 84.18 (2005), pp. 2301–2315. issn: 00162361. doi: 10.1016/j.fuel.2005.05.009.

[228] Y. N. Mishra, E. Kristensson, S. G. Pettersson, and E. Berrocal. “Planar droplets sizing of a hollow-cone spray using SLIPI-LIF/MIE”. In: *ILASS – Europe 2013, 25th European Conference on Liquid Atomization and Spray Systems* (2013).

[229] A. Labergue, A. Delconte, G. Castanet, and F. Lemoine. “Study of the droplet size effect coupled with the laser light scattering in sprays for two-color LIF thermometry measurements”. In: *Experiments in Fluids* 52.5 (2012), pp. 1121–1132. issn: 0723-4864. doi: 10.1007/s00348-011-1242-8.

[230] G. Chen, M. Mohiuddin Mazumder, R. K. Chang, J. Christian Swindal, and W. P. Acker. “Laser diagnostics for droplet characterization: Application of morphology dependent resonances”. In: *Progress in Energy and Combustion Science* 22.2 (1996), pp. 163–188. issn: 03601285. doi: 10.1016/0360-1285(96)00003-2.

[231] R. Domann and Y. Hardalupas. “A Study of Parameters that Influence the Accuracy of the Planar Droplet Sizing (PDS) Technique”. In: *Particle & Particle Systems Characterization* 18.1 (2001), pp. 3–11. issn: 0934-0866.

[232] W. Chaze, O. Caballina, G. Castanet, and F. Lemoine. “The saturation of the fluorescence and its consequences for laser-induced fluorescence thermometry in liquid flows”. In: *Experiments in Fluids* 57.4 (2016), p. 422. issn: 0723-4864. doi: 10.1007/s00348-016-2142-8.

[233] V. Deprédurand, P. Miron, A. Labergue, M. Wolff, G. Castanet, and F. Lemoine. “A temperature-sensitive tracer suitable for two-colour laser-induced fluorescence thermometry applied to evaporating fuel droplets”. In: *Measurement Science and Technology* 19.10 (2008), p. 105403. issn: 0957-0233. doi: 10.1088/0957-0233/19/10/105403.

[234] F. Lemoine and G. Castanet. “Temperature and chemical composition of droplets by optical measurement techniques: A state-of-the-art review”. In: *Experiments in Fluids* 54.7 (2013), p. 1089. issn: 0723-4864. doi: 10.1007/s00348-013-1572-9.

[235] G. de Sercey, G. Awcock, and M. Heikal. “Use of LIF image acquisition and analysis in developing a calibrated technique for in-cylinder investigation of the spatial distribution of air-to-fuel mixing in direct injection gasoline engines”. In: *Computers in Industry* 56.8-9 (2005), pp. 1005–1015. issn: 01663615. doi: 10.1016/j.compind.2005.05.026.

[236] M. Andersson, J. Warnberg, S. Hemdal, P. Dahlander, and I. Denbratt. “Evaporation of Gasoline-Like and Ethanol-Based Fuels in Hollow-Cone Sprays Investigated by Planar Laser-Induced Fluorescence and Mie Scattering”. In: *SAE International Powertrains, Fuels and Lubricants Meeting* (2011). doi: 10.4271/2011-01-1889.

[237] L. Zigan, I. Schmitz, A. Flügel, M. Wensing, and A. Leipertz. “Structure of evaporating single- and multicomponent fuel sprays for 2nd generation gasoline direct injection”. In: *Fuel* 90.1 (2011), pp. 348–363. issn: 00162361. doi: 10.1016/j.fuel.2010.08.001.

[238] I. Düwel, J. Schorr, J. Wolfrum, and C. Schulz. “Laser-induced fluorescence of tracers dissolved in evaporating droplets”. In: *Applied Physics B: Lasers and Optics* 78.2 (2004), pp. 127–131. issn: 0946-2171. doi: 10.1007/s00340-003-1378-1.

[239] P. Bojarski, A. Matczuk, C. Bojarski, A. Kawski, B. Kukliński, G. Zurkowska, and H. Diehl. “Fluorescent dimers of rhodamine 6G in concentrated ethylene glycol solution”. In: *Chemical Physics* 210.3 (1996), pp. 485–499. issn: 03010104. doi: 10.1016/0301-0104(96)00141-3.

[240] S. Qiu, H. Chu, Y. Zou, C. Xiang, H. Zhang, L. Sun, and F. Xu. “Thermochemical studies of Rhodamine B and Rhodamine 6G by modulated differential scanning calorimetry and thermogravimetric analysis”. In: *Journal of Thermal Analysis and Calorimetry* 123.2 (2016), pp. 1611–1618. doi: doi.org/10.1007/s10973-015-5055-5.

[241] J. Zhu, C. Shan, K. Nishida, W. Long, and D. Dong. “Simultaneous PIV/LIF-PIV measurements and numerical simulation of liquid flow and ambient gas flow for transient diesel spray”. In: *Fuel* 309.1-2 (2022), p. 122211. issn: 00162361. doi: 10.1016/j.fuel.2021.122211.

[242] S. Wachter, T. Jakobs, and T. Kolb. “Experimental investigation on the influence of system pressure on resulting spray quality and jet breakup applying pressure adapted twin-fluid nozzles”. In: *International Journal of Multiphase Flow* 125 (2020), p. 103189. issn: 03019322. doi: 10.1016/j.ijmultiphaseflow.2019.103189.

[243] H.-E. Albrecht, M. Borys, N. Damaschke, and C. Tropea. *Laser Doppler Systems*. Springer, 2003, pp. 337–408.

[244] S. Fischer. “Zur Messung hoher Temperaturen in strömenden Gasen mit Thermoelementen”. In: *Die Technik* 23.1. (1968), pp. 29–33.

[245] J. Zhuang and W. Leuckel. “A Modified Two-sensor-method for the Measurement of High Gas Temperature Facing Surroundings with Different Surface Temperatures”. In: *Combustion Science and Technology* 139.1 (1998), pp. 229–247. issn: 0010-2202. doi: 10.1080/00102209808952089.

[246] B. J. McBride. *NASA Glenn coefficients for calculating thermodynamic properties of individual species*. National Aeronautics and Space Administration, John H. Glenn Research Center, 2002.

[247] J. Schmitz. “Modellierung der Gasphasenreaktionen in einem Flugstromvergaser mit einem 2-Phasen-Freistrahlansatz”. Bachelor Thesis. Karlsruhe Institute of Technology, 2023.

[248] D. G. Goodwin, H. K. Moffat, I. Schoegl, R. L. Speth, and B. W. Weber. *Cantera: An Object-oriented Software Toolkit for Chemical Kinetics, Thermodynamics, and Transport Processes*. https://www.cantera.org. Version 3.0.0. 2023. doi: 10.5281/zenodo.8137090.

[249] H. D. Baehr and K. Stephan. “Wärme- und Stoffübertragung”. In: (2019). doi: 10.1007/978-3-662-58441-5.

[250] P. A. Nikrityuk and B. Meyer. *Gasification processes: Modeling and simulation*. John Wiley & Sons, 2014.

[251] M. Dammann, S. C. Walker, M. Mancini, and T. Kolb. “Devolatilisation of beech wood char: Kinetics from thermogravimetric analyses and drop-tube reactor experiments”. In: *Fuel* 375 (2024), p. 131967. doi: 10.1016/j.fuel.2024.131967.

[252] C. Schneider, M. Zeller, D. Böhm, and T. Kolb. “Influence of pressure on the gasification kinetics of two high-temperature beech wood chars with CO2, H2O and its mixture”. In: *Fuel* 299 (2021), p. 120523. doi: 10.1016/j.fuel.2021.120523.

[253] T. Kreitzberg, A. Phounglamcheik, N. E. L. Haugen, R. Kneer, and K. Umeki. “A Shortcut Method to Predict Particle Size Changes during Char Combustion and Gasification under regime II Conditions”. In: *Combustion Science and Technology* 194.2 (2022), pp. 272–291. issn: 0010-2202. doi: 10.1080/00102202.2019.1678919.

[254] M. Dossow, D. Klüh, K. Umeki, M. Gaderer, H. Spliethoff, and S. Fendt. “Electrification of gasification-based biomass-to-X processes – a critical review and in-depth assessment”. In: *Energy & Environmental Science* 17.3 (2024), pp. 925–973. issn: 1754-5692. doi: 10.1039/D3EE02876C.

[255] sico-tec. *Transmission of synthetic quartz glass (SQ) and Silux*. 2020. url: https://www.sico-tec.com/competences/quartz (visited on 2020-01-24).

[256] X. Hui, Z. Tuo, and Y. Rui-Peng. “Study on the Absorption and Fluorescence Spectra of Ethylene Glycol and Glycerol”. In: *Spectroscopy and Spectral Analysis* 27 (2007), pp. 1381–1384.

[257] J. B. Segur and H. E. Oberstar. “Viscosity of glycerol and its aqueous solutions”. In: *Industrial & Engineering Chemistry* 43.9 (1951), pp. 2117–2120.

[258] P. Stoesser. “Investigation of solid-phase processes during the conversion of biogenic slurry in entrained-flow gasifiers”. PhD thesis. Karlsruhe: Karlsruher Instituts für Technologie, 2019.

A Appendix - Methods

A.1 Experimental Facilities

Flow sheets of the REGA and ATMO plants are provided in Figs. A.1 and A.2. A transmission diagram of the quartz glass windows applied at REGA is shown in A.3. Fig. A.4 depicts detailed sketches of the applied burner nozzles.

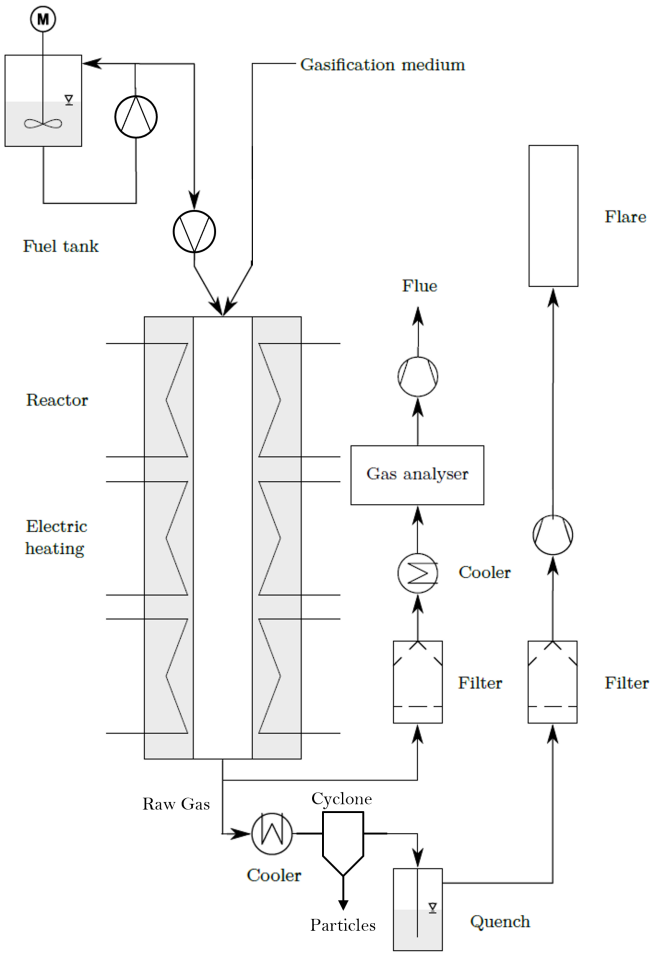


Figure A.1: Flow sheet of REGA plant, adapted from [8, 9].

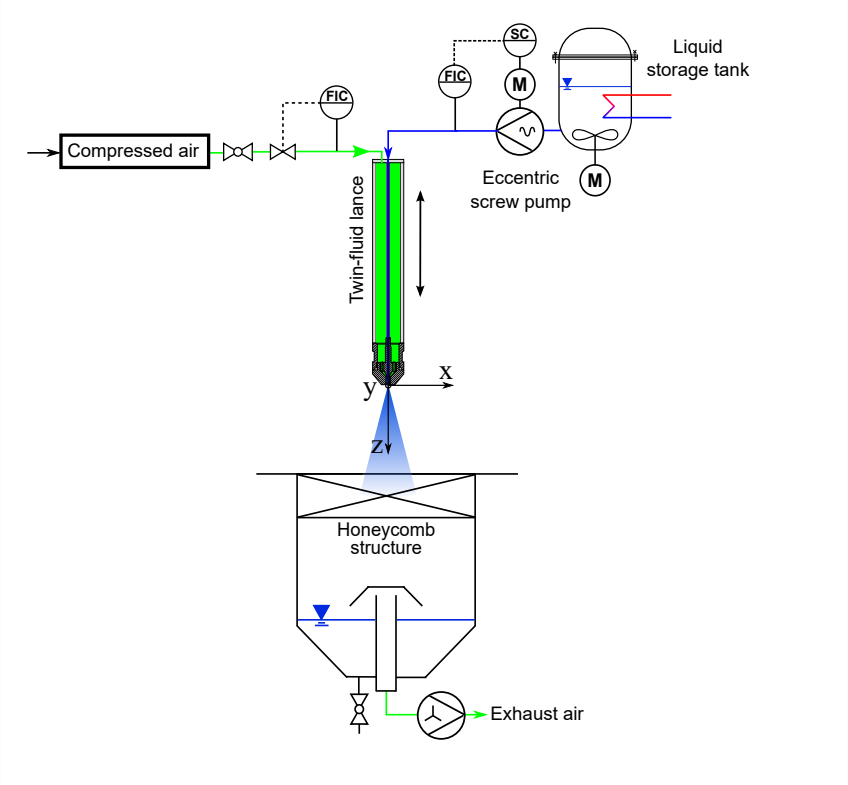


Figure A.2: Flow sheet of ATMO plant, adapted from [242].

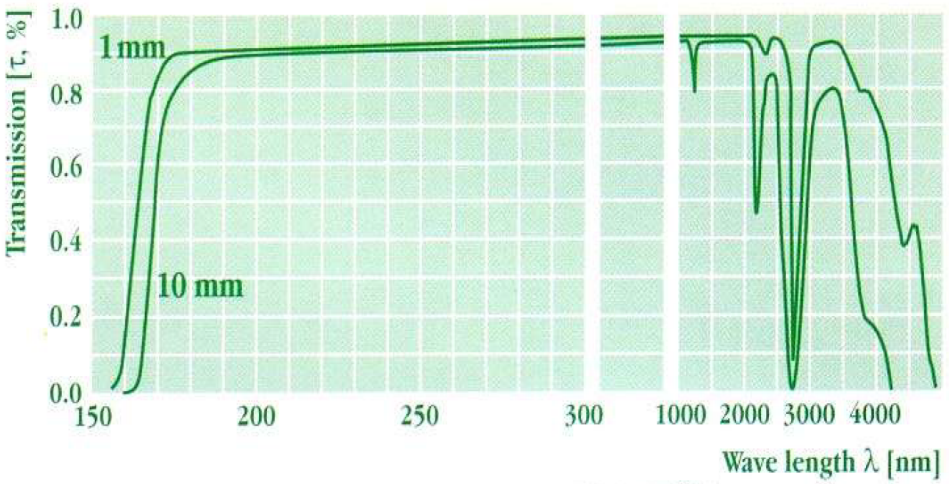


Figure A.3: Wavelength dependent transmission of the quartz glass windows applied at REGA [255].

A.2 Burner Nozzles

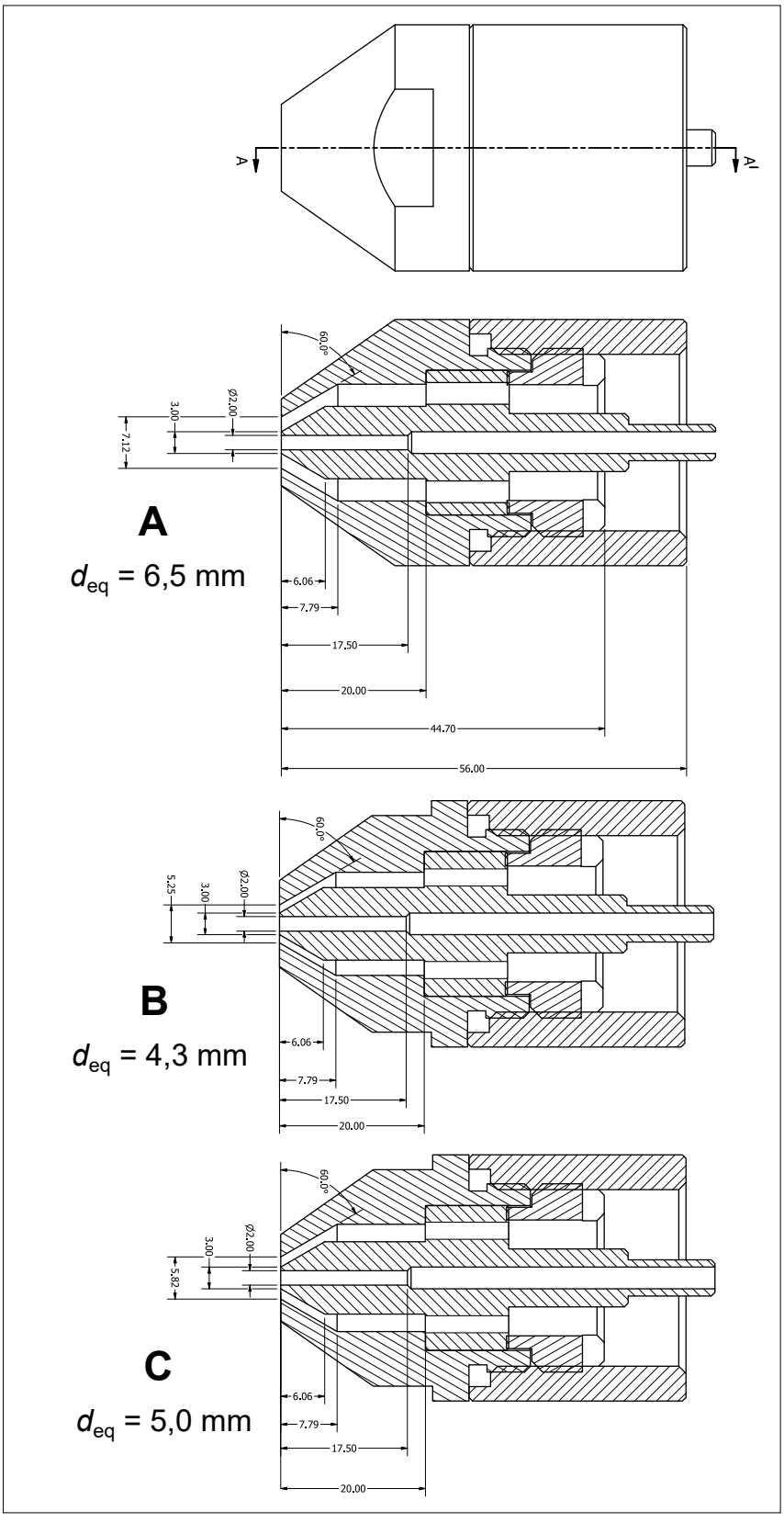


Figure A.4: Detailed sketches of the applied burner nozzles.

A.3 Diagnostics

LIF Measurements

This section provides additional information on the LIF measurements described in sections 3.3.1 and 3.3.2. Absorption spectra of OH and Rhodamine 6G are shown together with their respective fluorescence spectra upon excitation at 283.55 nm in Fig. A.3. Spectral data for OH was calculated using LIFBASE, spectral data for Rhodamine 6G are taken from [239]. Transmission windows of the applied bandpass filters are shown for reference. Fluorescence of MEG and glycerol is negligible at the excitation wavelength [256].

The process of collisional quenching, explained in section 3.3.1, is further discussed in

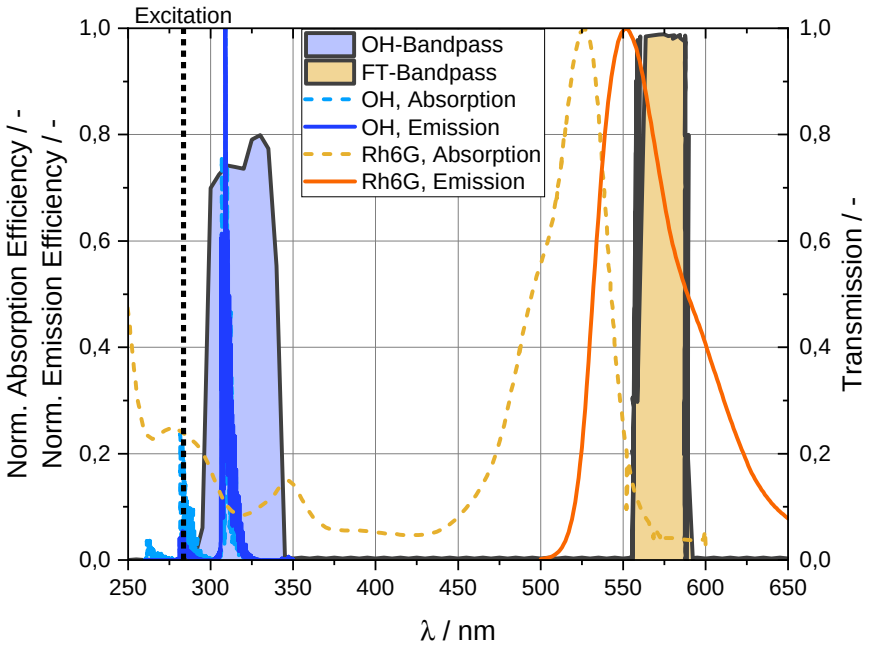


Figure A.5: Normalized absorption and emission of OH and Rhodamine 6G.

this section. It is assessed if collisional quenching impacts the qualitative interpretation of the measured signals. The collisional quenching rate Q_{21} depends on local species concentrations and temperature and impacts flourescence quantum yield of the OH radical. Therefore, the measured OH-LIF signal distribution can deviate from the actual distribution of OH concentration. To assess the relevance of this effect on the interpretation of the measured OH-LIF signals, 2-Ph-FJM results are used to calculate quench rates for typical conditions.

The physical background on collisional quenching is detailed by [186, 211, 213, 214]. The description of the quenching processes and the parameters given by Tamura et al. [214] are used to calculate Q_{21}. According to eq. 3.1, the measured LIF signal I_{LIF} is proportional to the population density of the ground state N_1^0 and the fluorescence quantum yield

depending on Q_{21}:

$$I_{\mathrm{LIF}} \propto c_i \cdot \frac{A_{21}}{A_{21} + Q_{21}} \tag{A.1}$$

Using the 2-Ph-FJM, normalized OH-LIF signals are calculated by applying eq. A.1. Results are compared in Fig. A.6 for the example of case S30-A, where the highest differences occured. The comparison shows that in a region up to the axial maximum of OH concentration, the calculated normalized OH-LIF intensities show higher values than the normalized concentrations without quenching correction. For larger nozzle distances, the effect is inverted. Axial profiles of both quantities however show no substantial quantitative differences. The longitudinal extension of the OH zone L_{OH} deviates by 2.7 % between both calculations. These results imply that collisional quenching is not a relevant source of error for the interpretation of measured OH-LIF signals and for the comparison of experimental and calculated values under the conditions in this work.

PDA Measurements

System parameters and instrument settings of the PDA system used in this work are given in Table A.1.

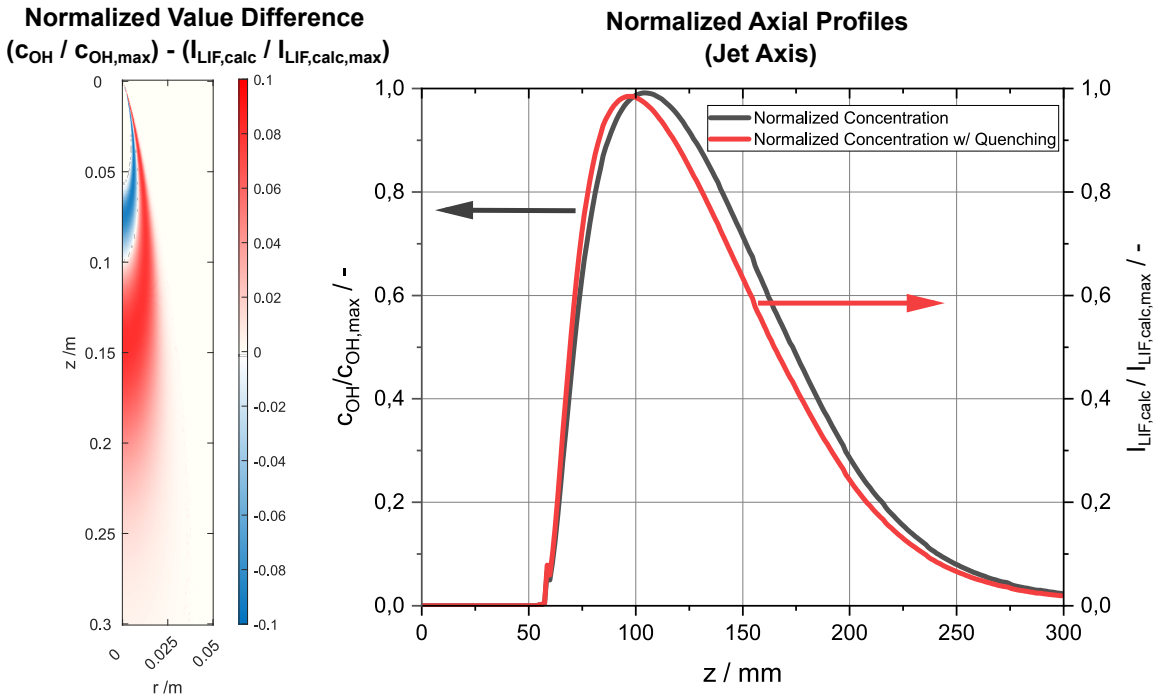


Figure A.6: Normalized calculated LIF signals considering quenching compared to normalized calculated OH concentration for case S30-A.

Table A.1: System parameters and instrument settings of the PDA system.

Paremeter	**Unit**	**Value**
Transmitter focal length	mm	1000
Receiver focal length	mm	1000
Beam expander ratio	-	1.00
Receiver slit width	µm	200
Laser wavelength	µm	561
Laser power	mW	140
Off axis angle	°	70
Frequency shift	MHz	80.00
Beam diameter	mm	2.20
Beam spacing	mm	40
Detector sensitivity	V	1000
Gain	dB	8
Anode current limit	µA	3000
Signal to noise ratio	dB	2

Shadowgraphy Measurements

Shadowgraphy measurements were conducted to measure droplet size distributions for the suspension fuels, where PDA was not applicable due to the opacity of the droplets. The shadowgraphy system was calibrated using a size calibration plate and verified using a monodisperse droplet generator. For case S0 using pure MEG (see section 3.4.3), both methods were applied. A comparison of droplet size distributions using both methods is shown in Fig. A.7. With the used shadowgraphy setup, the image evaluation software is only able to reliably detect droplets with $d \geq 30$ µm and is therefore underestimating the amount of small droplets. This results in a higher $d_{\mathrm{v},10}$ than for the PDA measurement (72 µm in comparison to 44 µm). $d_{\mathrm{v},90}$ is also increased (216 µm in comparison to 188 µm). For Sauter mean diameter d_{32}, better agreement between both methods is found (117 µm in comparison to 102 µm). As the shadowgraphy data is primarily used as input for the model sensitivity study, this deviation is considered acceptable.

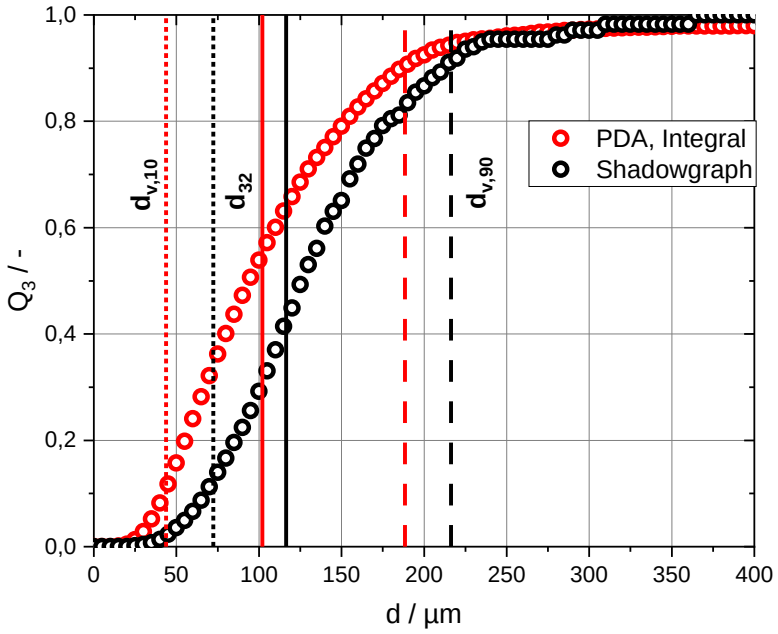


Figure A.7: Integral droplet size distributions for case S0 measured at z = 100 mm using PDA and Shadowgraphy.

A.4 Evaluation of Flame Parameters

This section provides additional information on the calculation of the longitudinal extension of the OH zone L_{OH} and the volume of the OH zone V_{OH}, originally described in section 4.3.5. For measured OH-LIF intensities and calculated OH concentrations, L_{OH} and V_{OH} were calculated using a threshold of 10 % of the global maximum value. Especially for evaluation of L_{OH}, the question can be asked if a normalization to the axial maximum instead of the global maximum is more reasonable. Both maxima may differ in value, leading to different absolute threshold values. A comparison of both normalization methods is shown in Fig. A.8 for all experimental data points in this work. The evaluation of V_{OH} shows to be more sensitive towards changes in the threshold, as indicated by the stronger scattering in comparison to L_{OH}. For certain single points, deviations up to 16 % occur for V_{OH}.

V_{OH} is calculated by integration of the volume within the 10 % OH contour assuming rotational symmetry of the flame. Therefore, uncertainties in determination of the radial extension of the OH zone contribute to the value of V_{OH} (see eq. 4.42). This makes the evalutaion of V_{OH} more prone to error in contrast to L_{OH}, which contains only the uncertainty in axial direction. For L_{OH}, a better agreement with the highest deviation of 6 % is found. It can thus be concluded that the choice of the maximum does not significantly affect the calculation of L_{OH} and that L_{OH} is the more robust quantity for assessment of the flames in this work. It should be noted that the agreement between both

methods is also good for the hollow-cone flame shape of case MEG-B (L_{OH} = 135 mm in comparison to L_{OH} = 133 mm).
For the datasets calculated using the 2-Ph-FJM, differences between axial and global maximum of the OH concentration fields were typically negligible, resulting in even smaller differences.

For different fuels and operating conditions, maximum OH concentrations in the flame

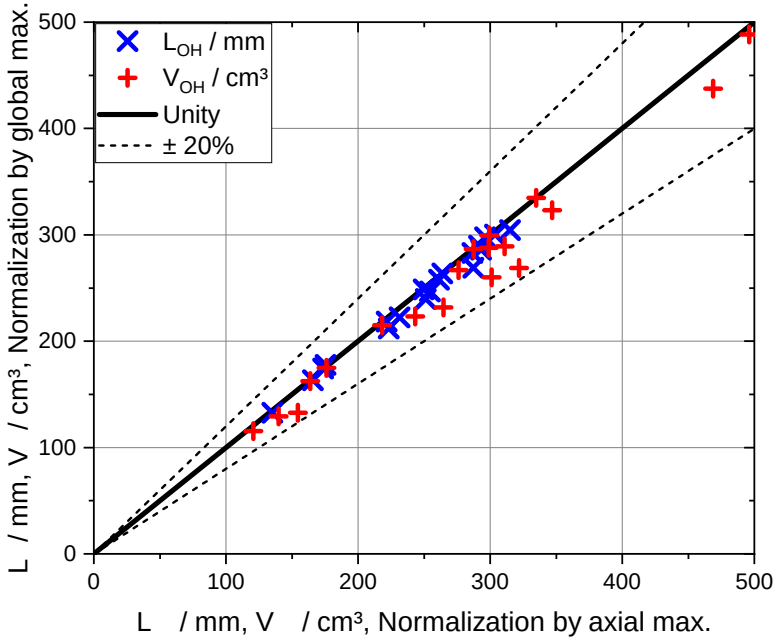


Figure A.8: Values of L_{OH} and V_{OH} determined using 2 different normalization methods for all experimental datapoints in this work.

may change. This is for example the case in dataset **SLURRY**. A definition of L_{OH} using an absolute OH concentration would be more stringent in these cases. As absolute OH concentrations cannot be measured using the current experimental setup (see section 3.3.1), this approach is not applicable in this work. Using absolute values of measured OH-LIF intensity would be an alternative option. These are however affected by laser and fluorescence absorption by particles in the gas phase as well as contamination of the optical windows. For these reasons, the normalization of the OH-LIF intensity fields to the global maximum was chosen to evaluate the flame parameters. To assess the influence of different maximum OH concentration on the determination of L_{OH}, calculated axial profiles of OH concentration for cases S0 and S30-A are compared in Fig. A.9. Using the standard method applied in this work, L_{OH} is calculated as 198 mm for case S0 and 246 mm for case S30-A (left). If the absolute OH-concentration at L_{OH} = 198 mm for case S0 is used as reference, the new L_{OH} for S30-A is calculated as 259 mm (right), which is a deviation of 5 %. The method used in this work is thus considered as an acceptable approximation.

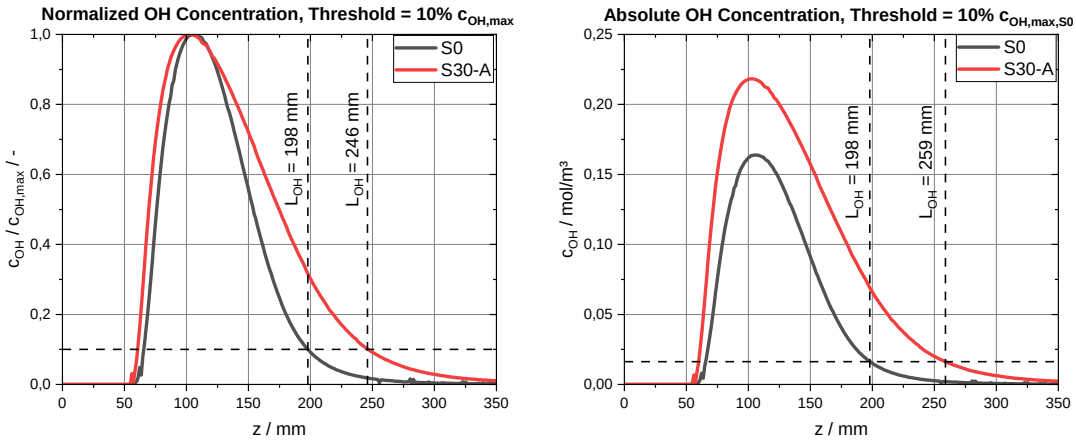


Figure A.9: Axial profiles of normalized (left) and absolute (right) OH concentrations for cases S0 and S30-A calculated using the 2-Ph-FJM. Different calculation methods for L_{OH} are visualized.

B Appendix - Fuel Data

B.1 Liquid Fuels

Table B.1 shows relevant fuel data for MEG and glycerol. Fig. B.1 depicts the temperature dependence of viscosity for glycerol. Literature values were taken from [257] and verified by viscosity measurements using a cylinder-cylinder rheometer system *(Anton Paar MCR 302e)* For interpolation of the values, a bi-exponential fit function was used.

Table B.1: Fuel data of MEG and glycerol.

Parameter	**Unit**	**MEG**	**Glycerol**
Viscosity (20°)	mPas	21	1412
Boiling point (1 bar)	°C	196	290
Lower heating value	MJ/kg	17.0	16.1
Elemental composition	-	$C_2H_6O_2$	$C_3H_8O_3$

B.2 Solid and Suspension Fuels

Fuel properties of the chars applied in this work are summarized in B.2. Kinetic data for BWC-A was determined for devolatilization in a drop tube reactor by [251], imitating the high temperatures and heating rates present under EFG conditions. For determination of gasification kinetics, the raw char was pyrolyzed in a drop tube reactor at $T = 1600°C$, followed by measurement of gasification kinetics with CO_2 and H_2O using a pressurized single particle reactor by [252]. Kinetic parameters for BWC-A are summarized in Table B.3. The porosity of the fast-pyrolyzed BWC-A was determined to be 55.3 % by Hg-intrusion porosimetry [107], giving a mean pore diameter of 0.22 µm by [258]. The skeletal solid density was determined to be 2203 kg/m^3 by He-pycnometry [107]. For the all chars, a packing density corresponding to a cubical packing of spheres was assumed.

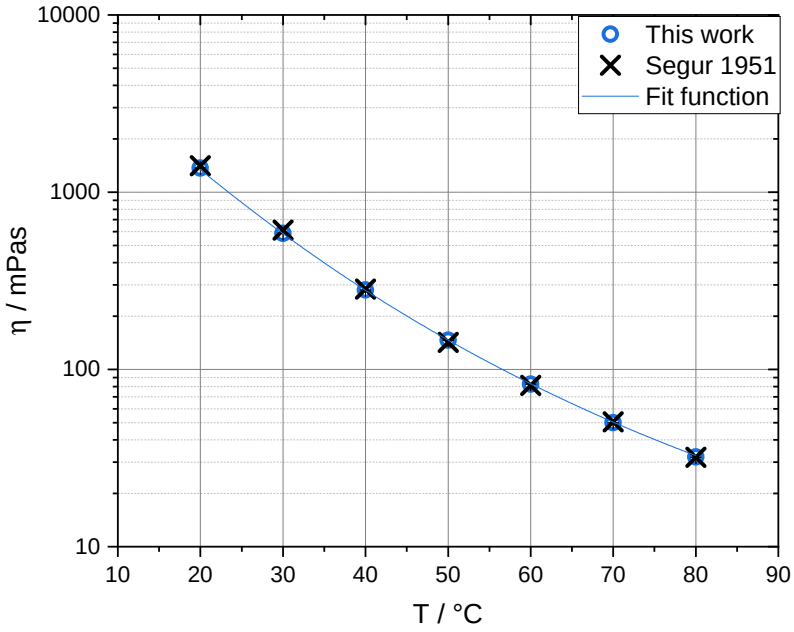


Figure B.1: Viscosity of glycerol at different temperatures. Values measured in this work were fitted by a bi-exponential fit function and compared with literature values [257].

The char fractions BWC-B and BWC-C applied in this work were obtained by grinding and sieving char BWC-A. Because of their origin from BWC-A and because their composition does not substantially differ from the main fraction, kinetic parameters for BWC-A were applied for description of BWC-B and BWC-C. Particle size distribution of the char fractions were measured applying laser diffraction *(Malvern Spraytec)* and are shown in Fig. B.2. REM images of the different char fractions applied in this work are shown in B.3.

The chars were mixed with MEG to produce the suspension for experiment cases S10-A - S30-C (see section 3.4.3). Viscosities of the suspensions were measured using a cylinder-cylinder rheometer system *(Anton Paar MCR 302e)* at shear rates of $\gamma = 10 - 2000 \cdot 1/\mathrm{s}$. Three flow curves of fresh samples were recorded and averaged for each suspension. Pure MEG and the suspensions featuring solid mass fractions up to $x_{\mathrm{sol},0} = 20$ % exhibited Newtonian behaviour, whereas suspensions featuring the highest solid load of $x_{\mathrm{sol},0} = 30$ % behaved non-Newtonian. Viscosity values of all suspensions are shown for a shear rate of $\gamma = 1000 \cdot 1/\mathrm{s}$ at a temperature of 20°C in Fig. B.4. Flow curves of the non-Newtonian suspensions are provided in Fig. B.5. Atomization data for cases S0 - S30-C will be discussed in section D.3.

Table B.2: Fuel data of the chars applied in this work. Measured by *Eurofins Umwelt Ost GmbH*, DIN EN ISO/IEC 17025:2018.

Parameter	**Unit**	**BWC-A**	**BWC-B**	**BWC-C**
Lower heating value (ar)	MJ/kg	28.8	29.9	30.5
Fixed carbon (ar)	wt-%	76.00	78.8	79.7
Volatiles (ar)	wt-%	11.8	11.9	12.2
Humidity (ar)	wt-%	7.3	6.3	4.5
Ash (815°C, ar)	wt-%	4.8	3.1	3.5
C (d)	wt-%	84.8	86.6	86.6
H (d)	wt-%	2.5	2.5	2.5
N (d)	wt-%	0.3	0.4	0.4
O (d, difference)	wt-%	7.1	7.2	6.6
Cl (d)	wt-%	0.0	0.0	0.0
S (d)	wt-%	0.1	0.1	0.1

Table B.3: Kinetic data for BWC-A.

Parameter	**Unit**	**Value**	**Source**
$k_{0,\mathrm{vol}}$	1/s	266	[251]
$E_{\mathrm{A,vol}}$	kJ/mol	48.2	[251]
$k_{0,\mathrm{CO2}}$	mol/(g s bar^n)	$5.76 \cdot 10^9$	[252]
$E_{\mathrm{A,CO2}}$	kJ/mol	301	[252]
n_{CO2}	-	0.186	[252]
$k_{0,\mathrm{H2O}}$	mol/(g s bar^n)	$5.76 \cdot 10^6$	[252]
$E_{\mathrm{A,H2O}}$	kJ/mol	235	[252]
n_{H2O}	-	0.445	[252]

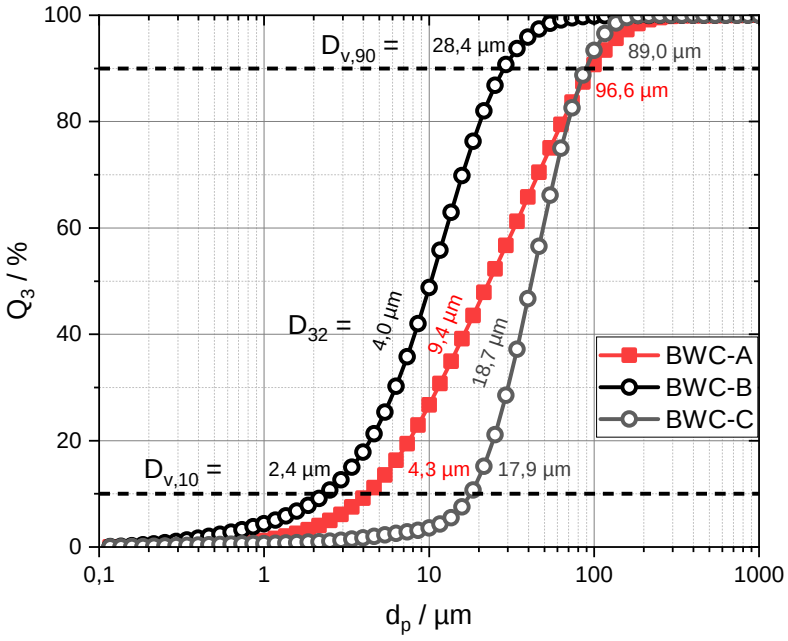


Figure B.2: Particle size distribution of the chars applied in this work, measured by laser diffraction.

B.3 Adaptation of Process Parameters for Changing Fuels

The experiments in dataset **SLURRY** were designed to exchange fuels while keeping input gas momentum flow J_{gas}, adiabatic equilibrium temperature T_{ad}, reactor residence time τ_{R} and fuel mass flow $\dot{m}_{\mathrm{fuel}}$ constant.

The base case is given by case S0, featuring pure MEG as fuel. In this case, the same liquid and gas input mass flows as in dataset **MEG** are applied using nozzle C. This leads to a gas momentum flow $J_{\mathrm{gas}} = 0.34$ N at $T_{\mathrm{ad}} = 1700$°C, $\tau_{\mathrm{R}} = 3.2$ s and $\dot{m}_{\mathrm{fuel}} = 12.4$ kg/h.

The fuels in dataset **SLURRY** feature varying lower heating values and elemental compositions, which would lead to a change in equilibrium temperature and reactor residence time if fuels were substituted applying equal input mass flows. For compensation of adiabatic equilibrium temperature, oxygen content in the gasification agent $y_{\mathrm{O2,GA}}$ was adjusted at constant gas volume flow. The effect on reactor residence time by the change in amount of product gas was compensated by a minor adjustment of fuel mass flow $\dot{m}_{\mathrm{fuel}}$.

The adjustment of $y_{\mathrm{O2,GA}}$ affects gas density, causing a deviation of gas momentum flow J_{gas} by a maximum of 1.0 % between the setpoints in the dataset. The fuel mass flows $\dot{m}_{\mathrm{fuel}}$ deviate by a maximum of 2.4 %.

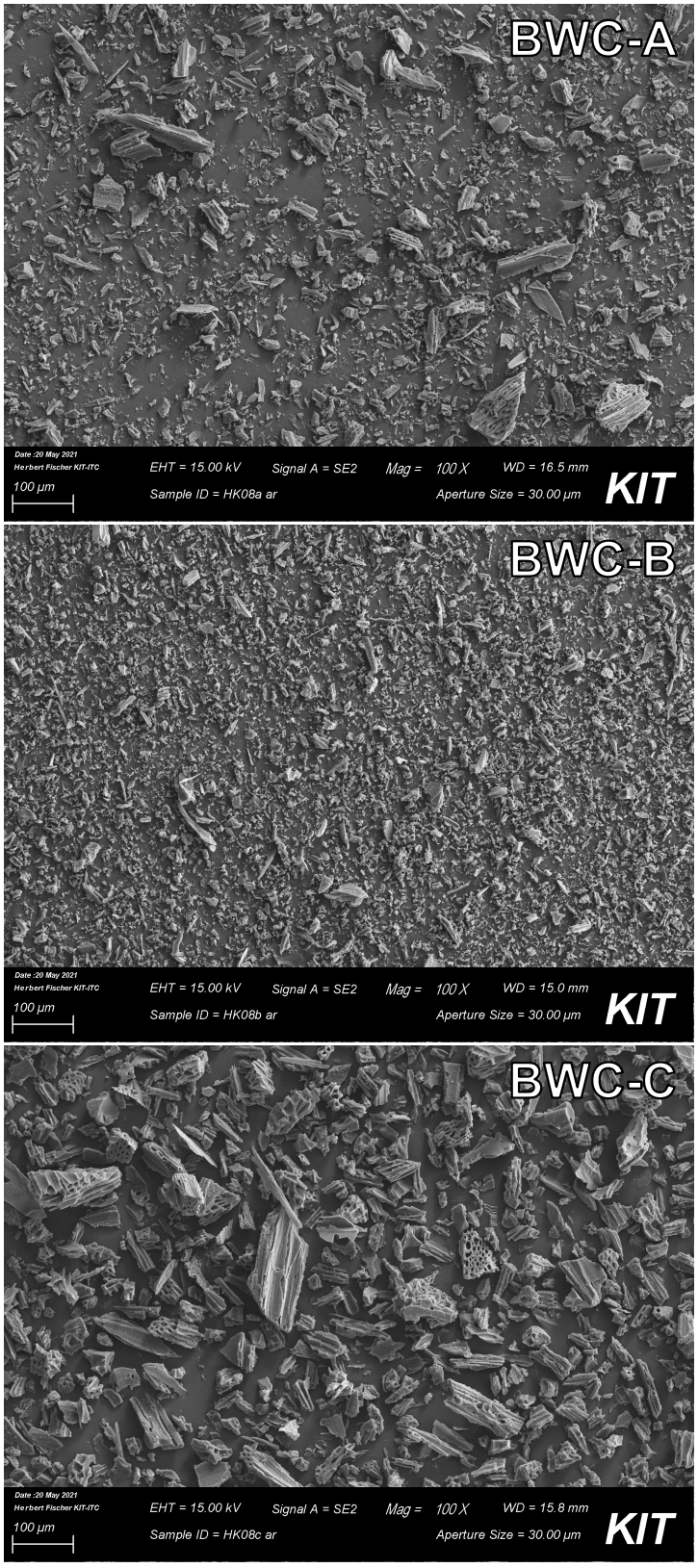


Figure B.3: REM images of the applied char fractions.

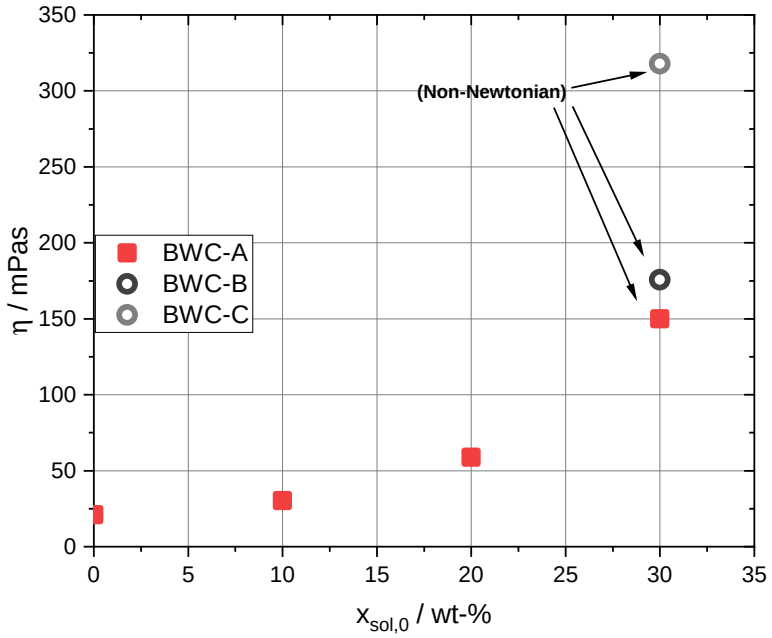


Figure B.4: Viscosities of all applied suspension fuels at $\gamma = 1000 \cdot 1/\mathrm{s}$ and $T_{\mathrm{liq}} = 20°\mathrm{C}$.

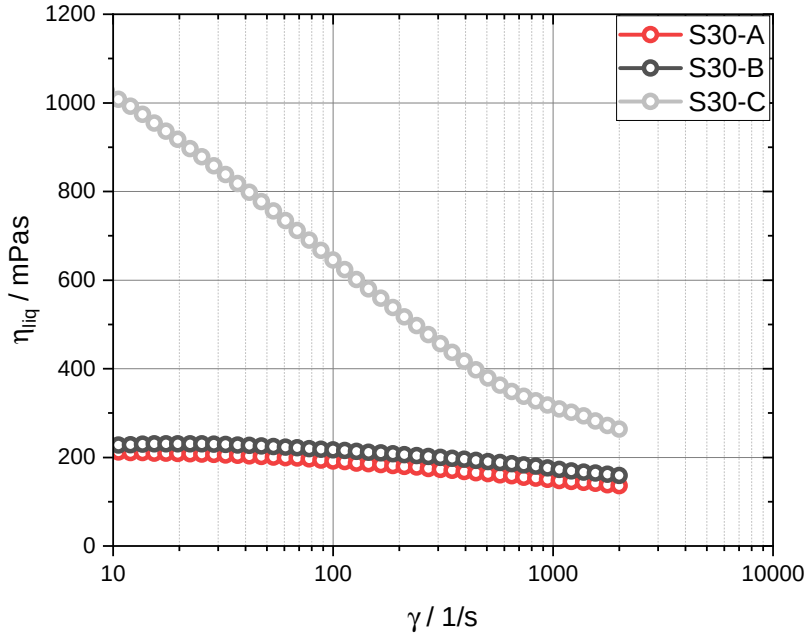


Figure B.5: Flow curves of the non-Newtonian suspensions at $x_{\mathrm{sol},0} = 30\ \%$ and $T_{\mathrm{liq}} = 20°\mathrm{C}$.

C Appendix - Model

C.1 Model Details

This section provides additional information on the 2-Ph-FJM. Section C.1.1 describes the implementation of droplet size distributions in the model. Section C.1.2 elaborates on a correlation applied in a sensitivity study on droplet evaporation. Section C.1.3 gives additional information on the gas phase reaction model.

C.1.1 Implementation of Droplet Size Distributions

Section 4.3.1 described the definition of input conditions for the 2-Ph-FJM regarding droplet size, which is further detailed here. For modeling the experimental cases, measured radial profiles of d_{32} at z = 100 mm were fitted using 4-th degree polynomials. The polynomials were used to define a d_{32} for each trajectory in the model. For the sensitivity studies using the 2-Ph-FJM, uniform profiles of d_{32} were used for simplicity.
In each trajectory, the assigned d_{32}-value was used to define a droplet size distribution featuring 50 size classes applying a Weibull-distribution with a scale parameter σ and a shape parameter of 2. The equations are given in section 4.3.1 and are repeated here for convenience.

$$Q_3(d) = 1 - \exp\left(-\left(\sigma \cdot d\right)^2\right). \tag{C.1}$$

$$Q_3(d) = 1 - \exp\left(-\left(\frac{d}{\sqrt{\pi} \cdot d_{32}}\right)^2\right) \tag{C.2}$$

Eq. C.2 can be derived from eq. C.1 by applying the definition of d_{32}. The applicability of Weibull-distributions to describe the measured droplet size distributions was verified. Fig. C.1 shows droplet size distributions measured by PDA for case MEG-B under ambient conditions at z = 100 mm for different radial distances r. It can be seen that the Weibull-distributions describe the measured droplet size distributions well, justifying their application in the 2-Ph-FJM.

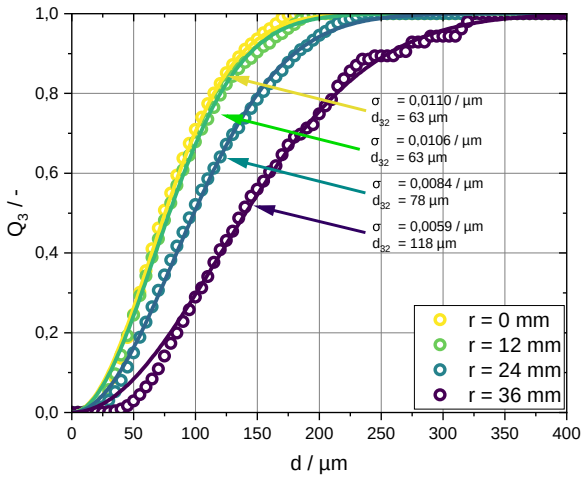


Figure C.1: Measured droplet size distributions under ambient conditions for case MEG-A at z = 100 mm and different radial positions. Measured data was fit using Weibull-distributions.

C.1.2 Correlation for Droplet Diameter

In the modeling study in section 5.2.3, a correlation is used to calculate the Sauter mean diameter d_{32} from nozzle input conditions, i.e. fuel mass flow $\dot{m}_{\mathrm{fuel}}$ and gas momentum flow J_{gas}. The correlation was developed by Sänger [110] for coaxial jet nozzles featuring a central fuel jet and an annular gas stream, using a similar geometry as the nozzles applied in this work ($d_{\mathrm{liq}} = 2.0$ mm, $s = 0.1$ mm, $d_{\mathrm{gas}} = 1.6$ mm, compare 3.4). In contrast to this work ($\alpha_{\mathrm{gas}} = 30°$), the nozzle investigated by Sänger featured a gas angle of $\alpha_{\mathrm{gas}} = 0°$. For glycerol-water mixtures at $\dot{m}_{\mathrm{fuel}} = 10$ kg/h featuring liquid viscosities η_{liq} from 1 - 400 mPas, Sänger varied gas mass flow from $\dot{m}_{\mathrm{gas}}$ from 4 to 15 kg/h, influencing gas-to-liquid ratio GLR, aerodynamic Weber number We_{aero} and Ohnesorge number Oh. Droplet size was measured using a laser diffraction system *(Malvern Spraytec)*. The measured values were fitted by the function

$$d_{32} = C_{\mathrm{LP}} \cdot Oh^{C_1} \cdot (\mathrm{GLR} \cdot We_{\mathrm{aero}})^{C_2} \tag{C.3}$$

yielding the constants $C_{\mathrm{LP}} = 5.5$, $C_1 = 0.13$ and $C_2 = -0.81$. The Ohnesorge number Oh is given by

$$Oh = \frac{\eta_{\mathrm{liq}}}{\sqrt{\sigma \cdot \rho_{\mathrm{liq}} \cdot L_{\mathrm{c}}}} \tag{C.4}$$

featuring the liquid surface tension σ and the characteristic length L_{c}. The definition of the aerodynamic Weber number We_{aero} is given in eq. 2.6.
The change of gas momentum flow that was investigated in section 5.2.3 modulates We_{aero},

which was varied by Sänger in a range of 80 - 1200. For the conditions investigated in this work, this leads to a validity range from $d_{\mathrm{eq}} = 4$ mm ($J_{\mathrm{gas}} = 0.48$ N) to $d_{\mathrm{eq}} = 8$ mm ($J_{\mathrm{gas}} = 0.12$ N). It should be noted that in the work of Sänger, We_{aero} was changed through $\dot{m}_{\mathrm{gas}}$. A correlation featuring an explicit variation of We_{aero} by changing d_{gas} is not known for the operating conditions in this work.

C.1.3 Reaction Model

This section deals with the verification of the Gibbs-minimization approach implemented in the 2-Ph-FJM, which is described in section 4.3.2. The main species O_2, N_2, CO_2, CO, H_2O and H_2 as well as the radicals OH, O, H and NO were considered in the 2-Ph-FJM. The radicals were chosen based on an analysis applying GRI 3.0, in which equilibrium concentrations of 53 species were calculated for exemplary mixtures of gasification agent and syngas based on case MEG-A (see table C.1). Molar mixture fraction y_{SG} of syngas in a hypothetical binary gas mixture was varied between 0 and 1:

$$y_{\mathrm{SG}} = \frac{n_{\mathrm{SG}}}{n_{\mathrm{SG}} + n_{\mathrm{GA}}} \tag{C.5}$$

The maximum molar fraction of each species over the molar mixture fraction range is shown in Fig. C.2. All species featuring a maximum molar fraction of $y_{\mathrm{i,max}} > 10^{-3}$ were considered as relevant and were implemented in the 2-Ph-FJM.

Table C.1: Example gas compositions for the verification of the implemented Gibbs-minimization approach.

Gas	$\frac{y_{\mathrm{O2}}}{-}$	$\frac{y_{\mathrm{N2}}}{-}$	$\frac{y_{\mathrm{CO}}}{-}$	$\frac{y_{\mathrm{CO2}}}{-}$	$\frac{y_{\mathrm{H2}}}{-}$	$\frac{y_{\mathrm{H2O}}}{-}$	$\frac{T}{\mathrm{K}}$
GA	0.693	0.307	0	0	0	0	298
SG	0	0.104	0.219	0.131	0.188	0.340	1473

For typical mixture fractions of gasification agent, syngas and MEG present in the flame zone, predictions of the implemented model were compared to equilibrium calculations applying GRI 3.0 (gasification agent - syngas) and AspenPlus (gasification agent - fuel). The calculations were also compared with the reaction model from the original 2-Ph-FJM by Hotz. Calculated results are compared in Figs. C.3 and C.4 for mixtures of gasification agent and syngas (see table C.1). Temperatures show no notable differences between the models for mixture fractions $y_{\mathrm{SG}} < 0.45$ and $y_{\mathrm{SG}} > 0.85$. For conditions

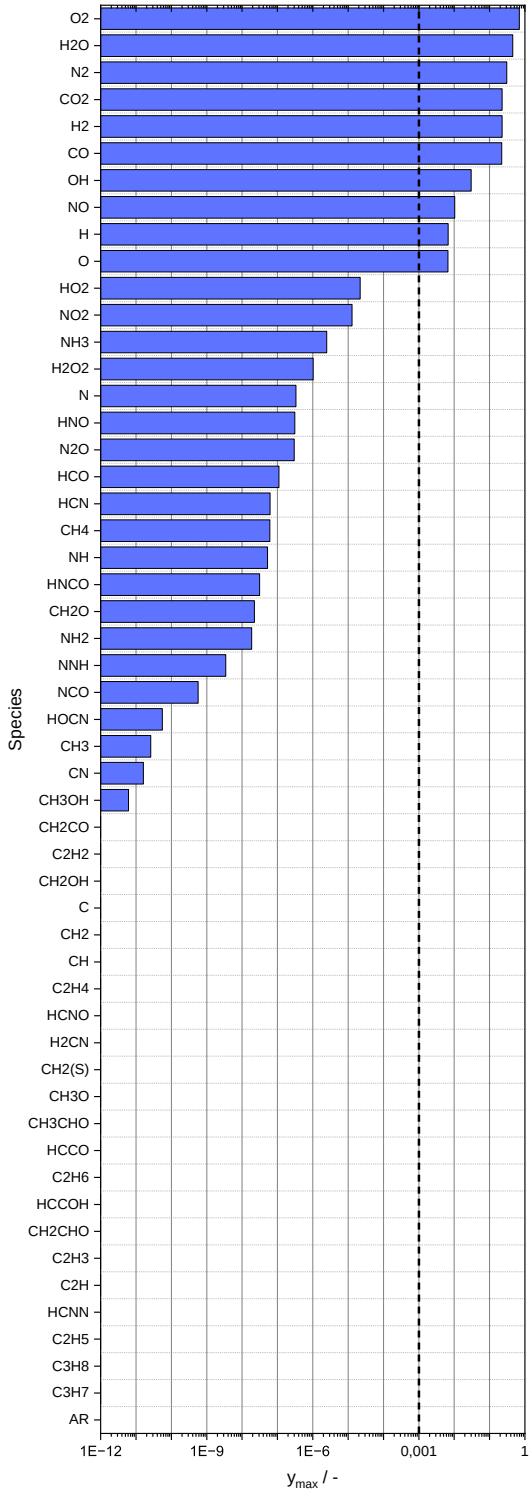


Figure C.2: Calculated maximum molar fractions $y_{\mathrm{i,max}}$ of the 53 species contained in GRI 3.0 for mixtures of example syngas and gasification agent.

near stoichiometry however ($y_{\mathrm{SG,stoic}} \approx 0.76$), deviations between the models occur. The temperature calculated by the original reaction model is significantly higher than predicted by GRI 3.0 and the model implemented in the present work. The latter two models agree well over the entire range of mixture fraction. The deviations are mainly caused by the neglect of radical formation by the original model, which becomes relevant at the high temperatures $T > 2000$ K present around stoichiometric conditions. Main species and radical concentrations in Fig. C.4 show good agreement between GRI 3.0 equilibrium calculations and the present reaction model for all mixture fractions. Further data is provided in [247]. The results verify the correct implementation of the Gibbs-minimization approach and show that the consideration of the radical species OH, O, H and NO is sufficient to enable reasonably accurate species and temperature predictions in the flame.

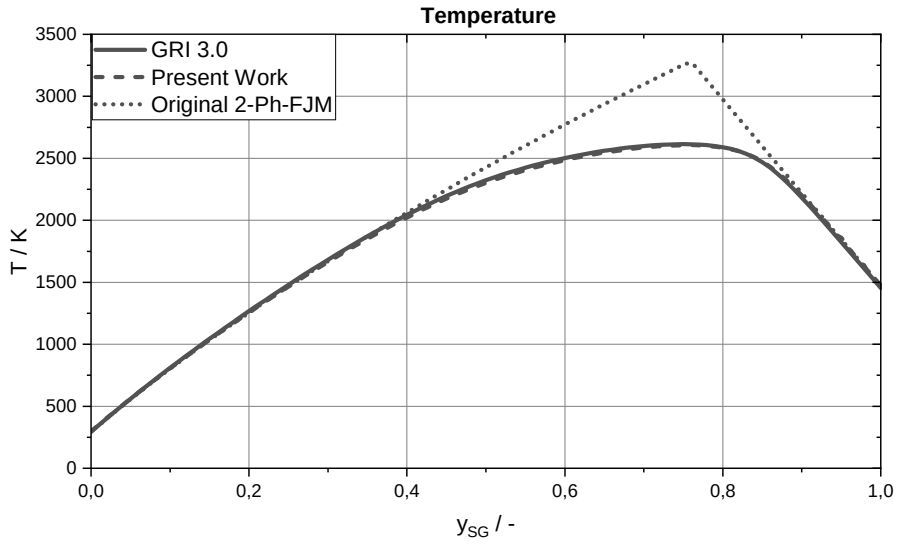


Figure C.3: Calculated gas temperature T for mixtures of example syngas and gasification agent compared for different model approaches.

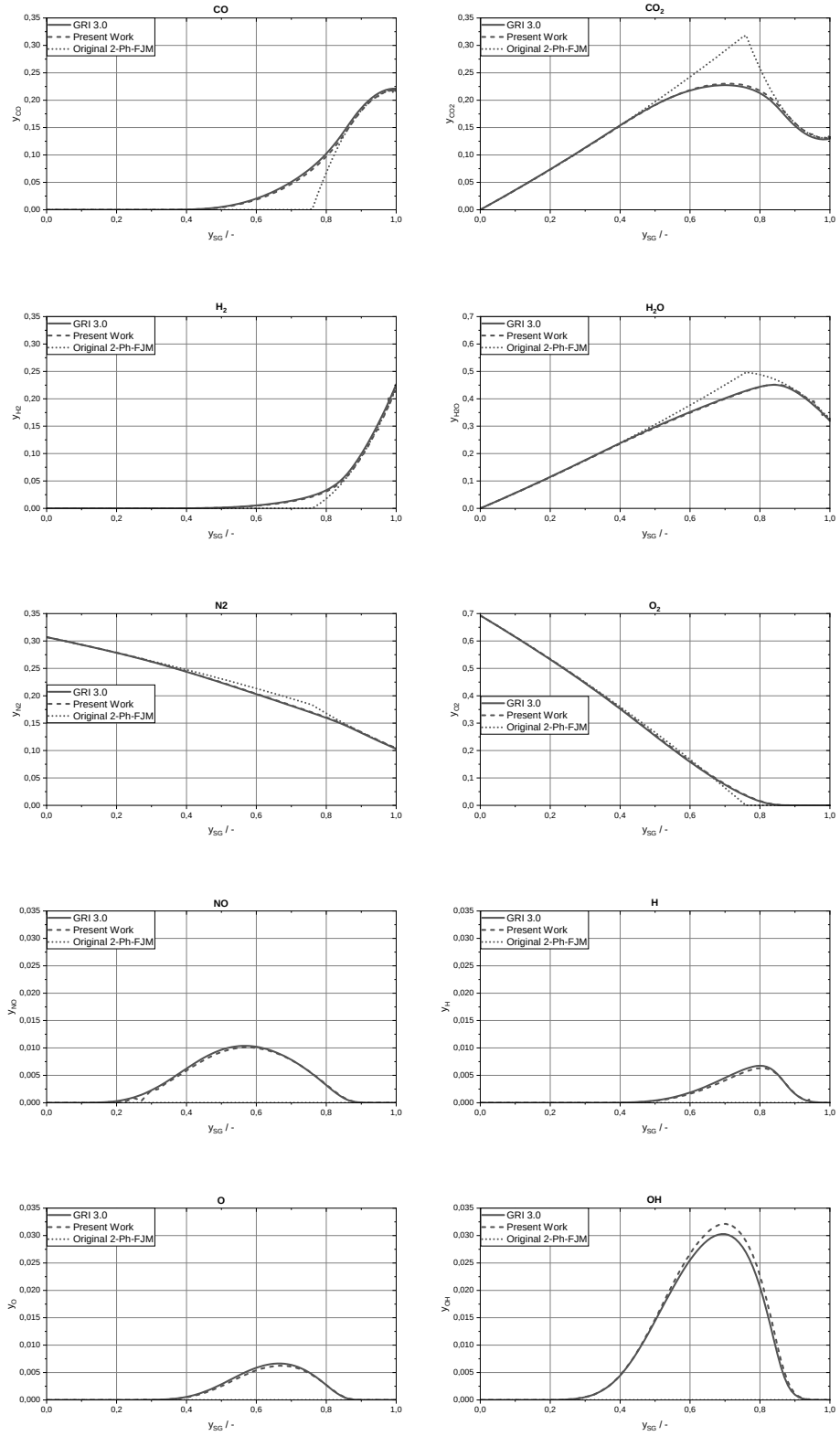


Figure C.4: Calculated molar fractions y_i of main species and radicals for example mixtures of syngas and gasification agent compared for different model approaches.

C.2 Model Validation

The 2-Ph-FJM was applied in chapter 5 to analyze the interaction of sub-processes within the EFG flame, conduct sensitivity studies of process parameters and sub-models and to interpret experimental observations. The model was validated at selected examples throughout chapter 5. Detailed validation of the 2-Ph-FJM is provided in this section. Section C.2.1 first assesses the prediction of the characteristic flame parameters by the 2-Ph-FJM. In section C.2.2, the trend predictions made by the 2-Ph-FJM regarding the imapct of gas momentum flow, droplet size and spray angle on the liquid fuel EFG flame are experimentally validated. The deviations between measured and calculated OH data in the nozzle-near region are discussed in section C.2.3. A detailed validation of the prediction of spray data is conducted in section C.2.4. Measured and calculated gas temperature is compared in section C.2.5. Section C.2.6 discusses the effect of turbulent droplet dispersion and compares it to the model description.

C.2.1 Prediction of Characteristic Flame Parameters

One focus of the present work lies in the model based analysis of the characteristic flame parameters L_{OH} and V_{OH} by the 2-Ph-FJM. This aspect is validated in this section. A comparison of measured and calculated values of these quantities is provided in Fig. C.5 for all experimental cases. The datapoints for dataset **SLURRY** were calculated using the Fragmenting Particle model, which uses an evaporation rate determined by convective heat transfer (eqs. 2.32 - 2.34). Datapoints for the dataset **GLYCEROL** were calculated using the standard d^2-law (eq. 2.30). For dataset **MEG**, both approaches are displayed for comparison.

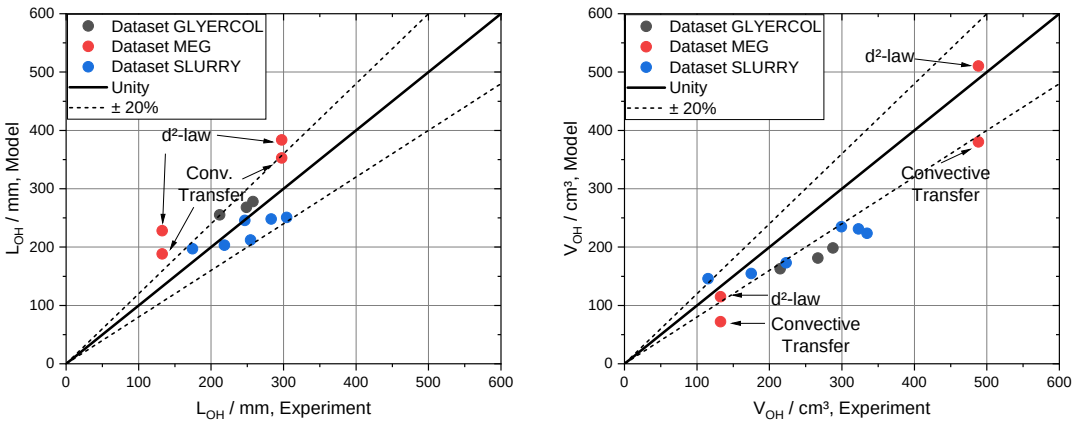


Figure C.5: Comparison of measured and calculated L_{OH} and V_{OH} for all experimental cases.

Concerning L_{OH}, most datapoints lie within a maximum deviation of 20 %. The largest deviations are found for dataset **MEG** when the d^2-law is applied as evaporation model (ΔL_{OH} = 71 % and 29 %). The reason for the large deviation in case MEG-B is that the transition from a closed flame shape to a hollow cone flame shape in the model requires slightly smaller spray angles than provided by the experimental input data [15]. For the evaporation rate determined by convective heat transfer, the model matches the experimental values better (ΔL_{OH} = 41 % and 19 %). For the **SLURRY**-dataset using the same evaporation approach, the agreement is better, with the highest deviation ΔL_{OH} = -20 % at case S30-B. Dataset **GLYCEROL** also shows good agreement in terms of L_{OH} with a maximum deviation of ΔL_{OH} = 20 %.
Concerning V_{OH}, the model mostly underestimates the measured values with a maximum deviation of ΔV_{OH} = -46 %. Generally, larger deviations between experiment and model are found for V_{OH} in comparison to L_{OH}. One reason for this may lie in the higher uncertainties in predicting V_{OH} (see section A.4).
It can be concluded that the 2-Ph-FJM is able to provide reasonable quantitative agreement regarding L_{OH} if the appropriate sub-models are used.

C.2.2 Impact of Gas Momentum Flow, Spray Angle and Droplet Size

The impact of gas momentum flow, droplet size and spray angle is analyzed in this section based on the experimental data to validate the trends identified by the model sensitivity studies in sections 5.1.2 - 5.1.5. Axial profiles of normalized OH-LIF intensity and calculated normalized OH concentration are shown in Fig. C.6 for cases A50, A200,

B50 and B200 of the **GLYCEROL**-dataset.
Based on the spray characterization results in section D.2, cases B50 and B200 were selected to investigate the influence of spray angle on the flame. Since both cases use the same nozzle, d_{eq} and gas momentum flows are identical. From case B50 to B200, the spray angle $\theta_{0.9}$ increases by 24 % while the Sauter Mean Diameter in the jet region increases only by 4 µm (7 %), enabling a statement on the variation of spray angle. Comparison of the axial OH profiles shows a longer OH zone for the wider spray angle (case B200), which is in accordance with the trend predicted by the model. The calculated values match the experimental data in the region downstream the axial OH maximum well.
In order to experimentally assess the influence of droplet size on the processes in the nozzle-near region, the cases A50 and A200 were chosen. Increasing liquid viscosity from 50 to 200 mPas leads to a moderate increase of $\theta_{0.9}$ by 10 % and a more pronounced increase of droplet diameter in the jet region by 21 % while keeping d_{eq} and therefore gas momentum flow unchanged. The axial OH-LIF profiles in Fig. C.6 indicate that case A200, featuring larger droplets, exhibits a longer OH zone. This result is in line with the model prediction. Again, reasonable agreement between measured and calculated OH data in the downstream flame region is found.
If the axial coordinate is normalized to d_{eq} (Fig. C.6 right), the axial profiles of the cases featuring different gas momentum flow show strong similarity. This experimental observation has also been discussed in section 5.1.2 and is in accordance with the 2-Ph-FJM predictions.
It can be concluded that the 2-Ph-FJM is able to correctly describe the impact of gas momentum flow, spray angle and droplet size on the flame within the parameter range of this work. The shape of the OH profiles and the qualitative trends are predicted well and the quantitative agreement between experiment and model is good in the region downstream the axial OH maximum. However, discrepancies between model and experiment in the nozzle-near region occur, which will be investigated in the following section.

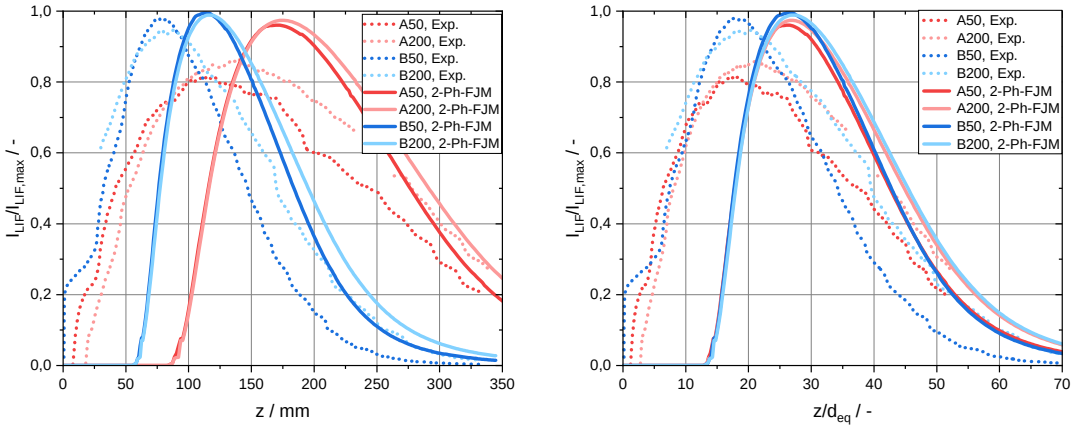


Figure C.6: Axial profiles of normalized OH-LIF intensity and normalized calculated OH concentrations for cases A50, A200, B50 and B200. Profiles are shown for absolute (left) and normalized (right) axial coordinates.

C.2.3 Deviations between Measured and Calculated OH-Data in the Nozzle-Near Region

The measured and calculated OH fields in section D show that the 2-Ph-FJM, which is designed to describe the mixing in the similarity region of the jet, achieves reasonable agreement with the experiment in the downstream flame region. In the nozzle-near region however, the present description leads to strong deviations.

As elaborated in section 2.2.2, a comprehensive mathematical theory to describe mixing in 2-phase free jets in the nozzle-near region does not exist. For 2-phase jets, the interaction of gas and liquid phase during the atomization process influences mixing between jet medium and ambient medium in the nozzle-near region. Enhanced mixing can lead to higher temperatures and the presence of OH early in the jet (see Fig. C.7).

In general, the 2-Ph-FJM calculates fields of mixture fraction using eq. 2.21. For all control volumes where $x_{\mathrm{GA}} > 1$, the value is set equal to 1. This simplifying approximation leads to radial profiles of x_{GA} as shown in Fig. C.8 (left) for the example of case MEG-A. At $z/d_{\mathrm{eq}} = 3$ to $z/d_{\mathrm{eq}} = 9$ this approach generates profiles featuring a flat top with a value of 1 at the jet axis, imitating a potential core. For larger nozzle distances, Gaussian profiles are calculated.

The axial profile of x_{GA} displayed in Fig. C.8 shows the abrupt transition to the self-similar region at $z/d_{\mathrm{eq}} \approx 10$. An hypothetical approach similar to the dotted red line could account for the transition region present in free jets and consider the additional disturbances to the flow field caused by the atomization process (see Fig. C.7), which might provide more realistic results.

Several additional limitations of model and experiment contribute to the observed differences:

- Mixing of jet medium ($T = 25\,°C$) and surrounding syngas ($T = 1200\,°C$) leads to a temperature increase and onset of oxidation reactions in the jet. At the relatively low temperatures in the region close to the nozzle exit, OH is not present in equilibrium and occurs only as a kinetic intermediate of the oxidation reactions, which is neglected by the equilibrium reaction approach used in the model. This causes the model to predict a later onset of OH than found in the experiment.
- The model does not account for the enhancement of droplet residence time through turbulent dispersion of droplets. This effect can increase local evaporation rate and therefore induce additional oxidation reactions (see section 2.2.7). However, this effect is presumably more relevant in the downstream flame region.
- Scattering effects of laser and fluorescence light in the highly dense spray region at the nozzle exit should be considered as an experimental source of error. Droplets may scatter laser light perpendicular to the laser sheet, exciting OH radicals that are not within the measurement plane. Scattering of fluorescence emitted by OH may also be a contributing factor for fluorescence detected in the core region of the jet. This may lead to an over-estimation of OH within the first few nozzle diameters on the jet axis. Estimations on these processes would require complex computations using Mie-theory and have not been performed in this work [220].

The main purpose of applying the 2-Ph-FJM is to predict the sensitivites of sub-processes on process parameters and sub-process models in the similarity region of the jet. Thus, the model should not be applied to derive insight into the situation in the nozzle-near region.

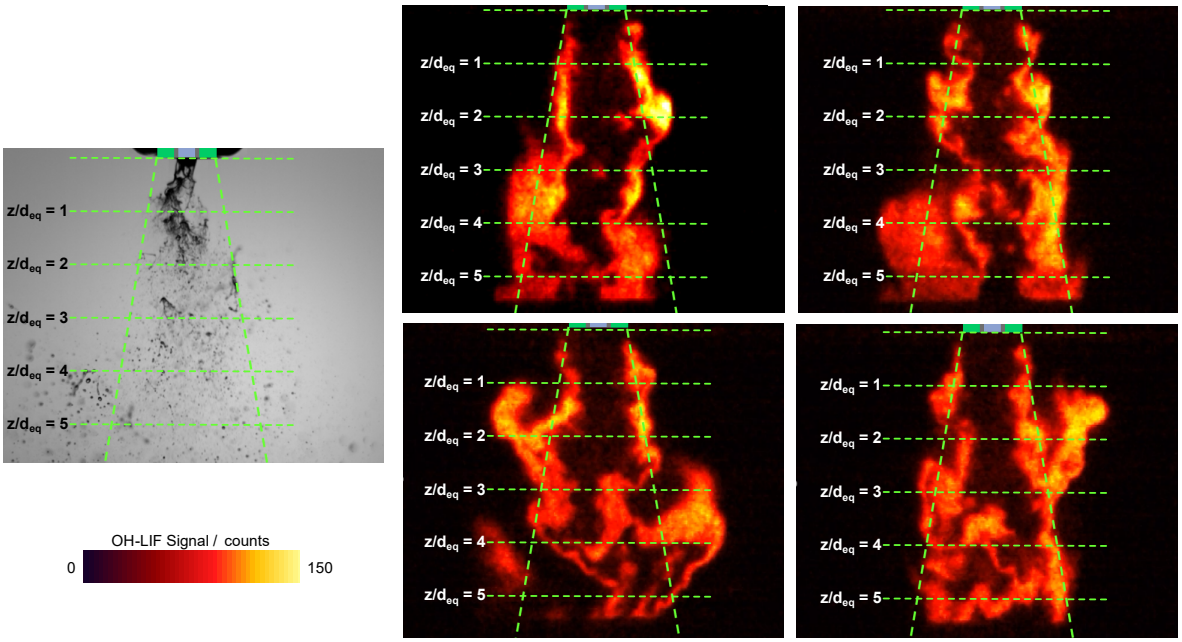


Figure C.7: Spray image under ambient conditions and single OH-LIF raw images in the vicinity of the nozzle exit (Case MEG-A).

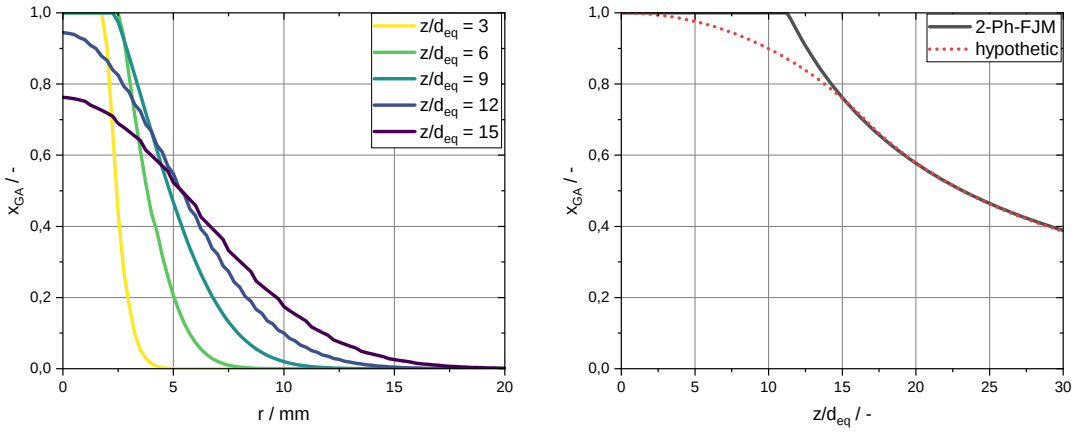


Figure C.8: Mixture fraction of gasification agent for case MEG-A calculated using the 2-Ph-FJM. Radial profiles are shown at different nozzle distances (left). An axial profile featuring a hypothetical improvement is also displayed (right)

C.2.4 Prediction of Spray Behavior

This section validates the 2-Ph-FJM against the detailed spray data of cases MEG-A and MEG-B presented in section D.1 for ambient and reacting conditions. MEG-A features a lower gas momentum flow, wider spray angle and larger droplet size in comparison to MEG-B.

Ambient Conditions

Fig. C.9 shows radial profiles of mass averaged axial droplet velocities $u_{\mathrm{drop,m}}$ for both cases under ambient conditions. The measured profiles show the highest centerline velocity at z = 50 mm, which decreases for higher nozzle distances. Additionally, the profiles widen with increasing nozzle distances. The shape of the profiles and both effects are captured by the 2-Ph-FJM. In the model, droplet velocities are limited to 5 m/s in order to avoid stagnating droplets in the quiescent environment. The 2-Ph-FJM tendentially overestimates droplet velocites at the jet centerline and underestimates droplet velocity in the outer jet region. At the jet centerline, measured and calculated values deviate between 0 and 39 %.

In the outer regions, relative deviations are larger for the profiles closer to the nozzle. Droplet velocities in a spray are determined by the atomization process and the downstream exchange of momentum between droplets and gas phase. While the latter is calculated within the 2-Ph-FJM, the atomization process is not resolved, which is presumably the main source of error (see section 4.2).

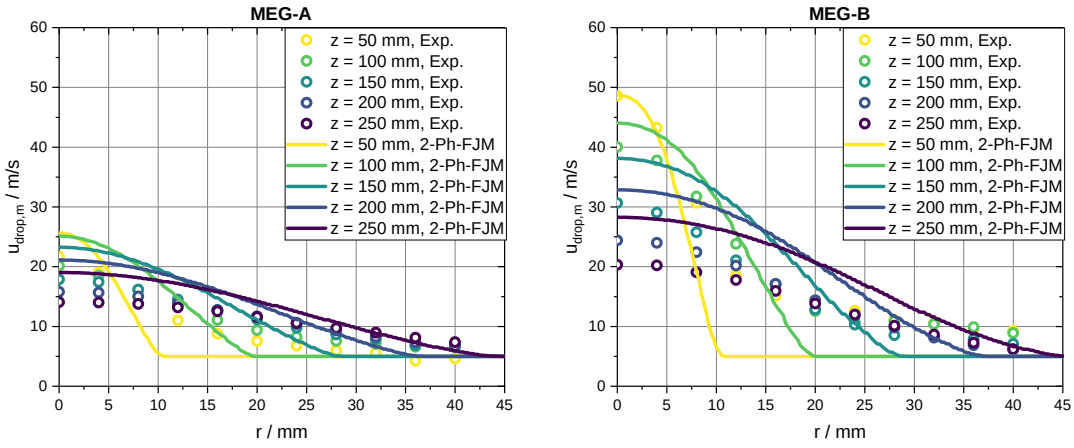


Figure C.9: Comparison of measured and calculated mass averaged droplet velocities (PDA, ambient conditions) for cases MEG-A and MEG-B.

Mean gas velocities u_{gas} were estimated from the PDA measurements by averaging the velocity of droplets $d < 10$ µm, which follow the gas flow in good approximation [110]. Results are displayed in Fig. C.10. The profiles show the typical Gaussian shape which is expected for the 2-Phase jets investigated in this work (see section 2.2.2). The shape and trend of the profiles is correctly predicted by the model. For z = 50 mm, the deviations between experiment and model are most pronounced, especially for case MEG-A ($\Delta u_{gas} = 41$ % at the jet centerline). At larger nozzle distances, the quantitative agreement improves (Δu_{gas} =1 % at the jet centerline, z = 250 mm). For case MEG-B, the maximum relative deviation at the jet centerline for all nozzle distances is Δu_{gas} = -14 %.

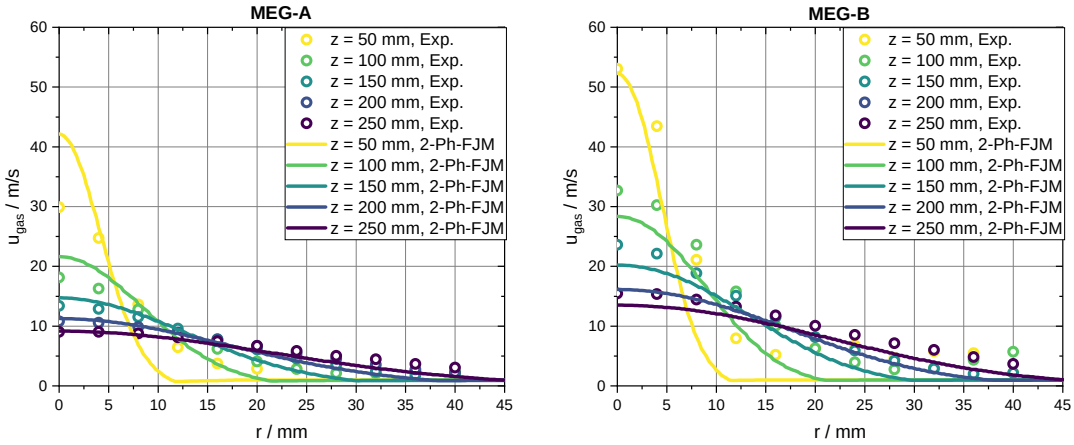


Figure C.10: Comparison of measured and calculated gas velocities (PDA, ambient conditions) for cases MEG-A and MEG-B.

Radial profiles of liquid mass flux ϕ_{liq} are compared in Fig. C.11. Case MEG-B shows a more narrow spray in comparison to case MEG-A, which is caused by the higher gas momentum flow. The profiles flatten and widen for increasing nozzle distances, which is again expected for 2-phase jets (see section 2.2.2). This is also predicted by the 2-Ph-FJM. Measured radial profiles at z = 100 mm were used as input for these calculations. The overprediction of ϕ_{liq} by the model at this measurement position by at most $\Delta\phi_{liq} = 17$ % stems from the fact that the input data for the 2-Ph-FJM are corrected for the mass balance error from the patternator measurement (see section 4.3.1).

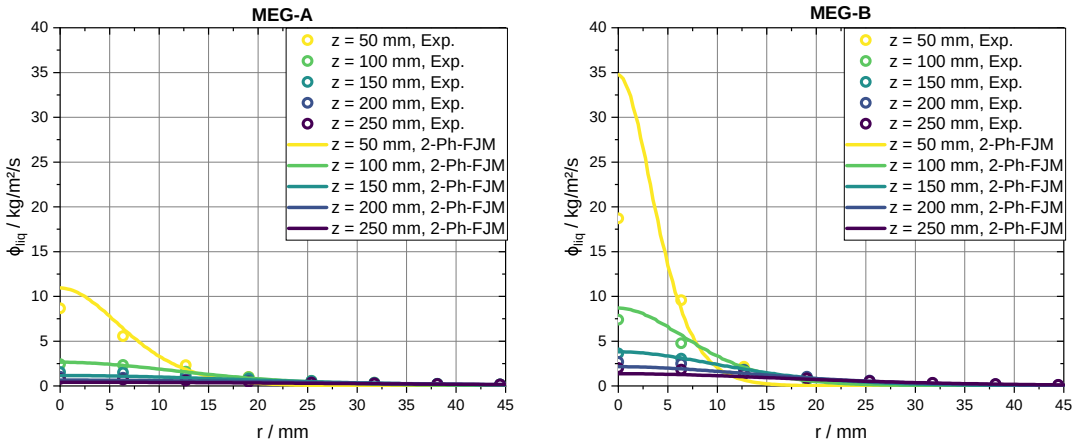


Figure C.11: Comparison of measured and calculated liquid mass flux (Patternator, ambient conditions) for cases MEG-A and MEG-B.

Measurements of Sauter mean diameter d_{32} under ambient conditions are shown in Fig. C.12. Case MEG-B generally shows smaller droplet sizes in comparison to case MEG-A due to the higher gas momentum flow at the nozzle exit. Again, notable deviations between 2-Ph-FJM predictions and experimental values at z = 50 mm occur. The profiles at z = 100 mm, which were fitted by 4-th degree polynoms and used as input conditions, are reproduced by the model. The widening of the profiles for further nozzle distances is correctly predicted by the 2-Ph-FJM. The quantitative accuracy for larger nozzle distances is acceptable, based on a maximum deviation of $\Delta d_{32} = 17\%$ in the dataset at z = 250 mm. This result shows that the description of droplets propagating on straight-line trajectories originating at the nozzle is a reasonable approximation.

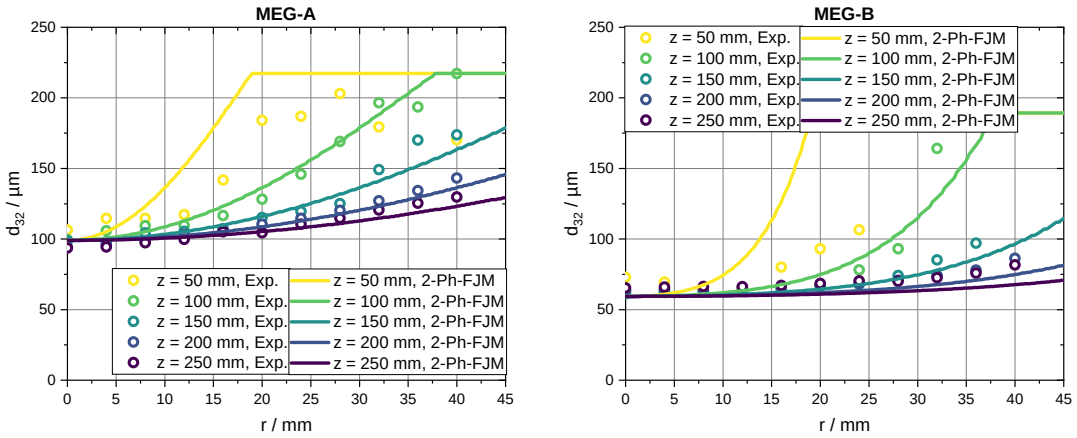


Figure C.12: Comparison of measured and calculated Sauter mean diameter (PDA, ambient conditions) for cases MEG-A and MEG-B.

Reacting Conditions

Mass averaged droplet velocities $u_{\mathrm{drop,m}}$ measured by PDA under reacting conditions are compared with 2-Ph-FJM calculations in Fig. C.13. In contrast to ambient conditions, the profiles are wider. The centerline droplet velocity does not change significantly for increasing nozzle distances in both cases. This effect is caused by the volume expansion through temperature increase and evaporation and has been discussed in [11]. The 2-Ph-FJM predicts this behavior. The jet centerline velocities are predicted with a maximum deviation of $\Delta u_{\mathrm{drop,m}}$ = -22 %. As already observed for ambient conditions, the droplet velocities in the outer jet region are underestimated, which is especially the case for low nozzle distances, as the transfer of momentum from the gas phase to the droplets during the atomization process is not accounted for by the model (see section 4.2).

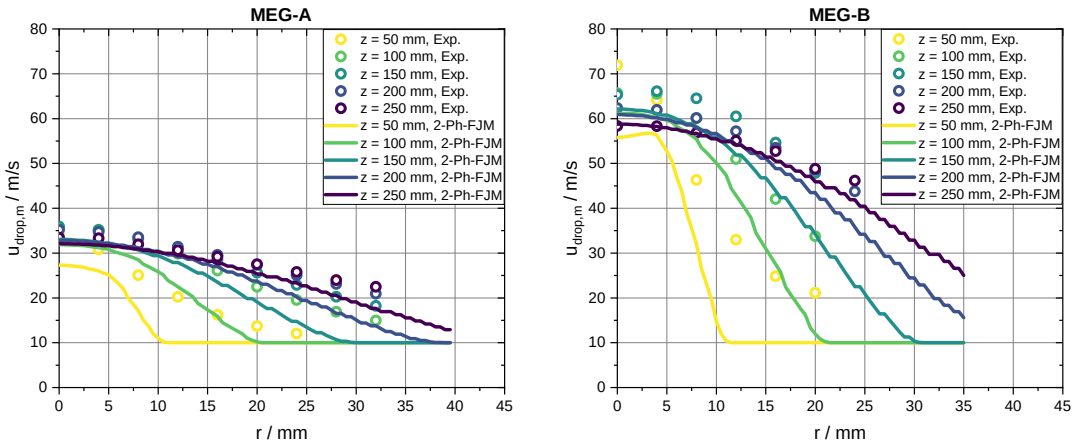


Figure C.13: Comparison of measured and calculated mass averaged droplet velocities (PDA, reacting conditions) for cases MEG-A and MEG-B.

Fig. C.14 depicts radial profiles of d_{32} under reacting conditions for both cases. It can be seen that especially for MEG-A, the droplet size at the jet centerline increases due to evaporation of small droplets. For case MEG-B, this is less pronounced. The 2-Ph-FJM predicts the general trend of the d_{32} profiles, but strong quantitative differences appear especially in the outer jet regions. This is presumably caused by the underestimation of droplet velocities in this region, as shown in Fig. C.13, leading to longer residence times and therefore higher evaporation rates.

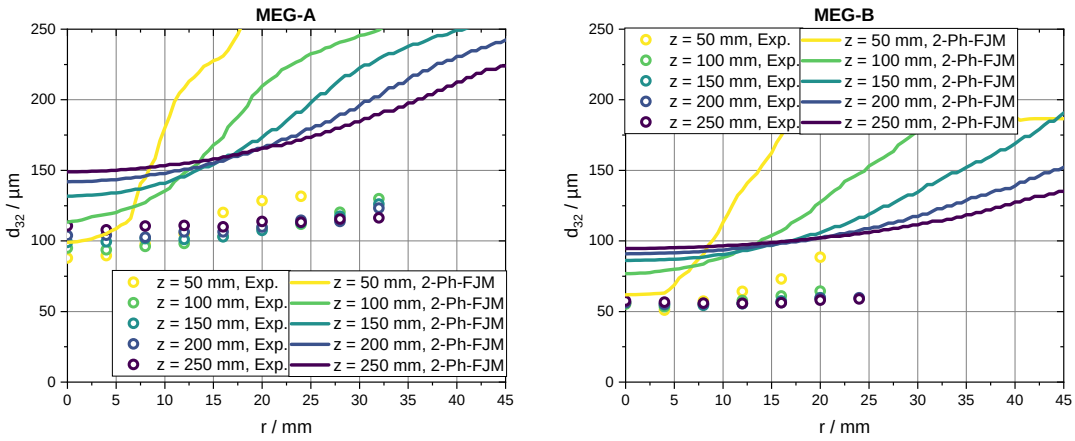


Figure C.14: Comparison of measured and calculated Sauter mean diameter (PDA, reacting conditions) for cases MEG-A and MEG-B.

The validation results show that the 2-Ph-FJM is able to qualitatively capture the relevant physical effects in the non-reacting and reacting spray in the investigated cases, which is the main goal of the applied model concept. Especially close to the jet centerline, reasonable quantitative predictions of the spray variables are also achieved. In the outer jet regions and close to the nozzle exit, the model limitations cause more pronounced quantitative discrepancies.

C.2.5 Prediction of Gas Temperature

A comparison of measured and calculated temperature profiles is displayed in Fig. C.15. While case MEG-A shows a temperature maximum at the jet centerline, MEG-B features a local temperature minimum at $r = 0$ in the experiment. This is a consequence of the narrow spray angle in case MEG-B and has been investigated in section 5.1.4. The shape of the profile is correctly predicted for case MEG-A. For case MEG-B, a flat profile at the jet centerline is predicted by the model. For narrower spray angles under otherwise equal input conditions, a local minimum has been calculated for case MEG-B, as reported in [15]. Regarding quantitative comparison, deviations between experiment and model occur. Especially at the jet centerline, temperature predictions by the 2-Ph-FJM exceed the measured values. This may be caused by the neglect of gas radiation by the 2-Ph-FJM, which would reduce calculated flame temperature. The fact that turbulent dispersion of droplets is not modeled in the 2-Ph-FJM may also contribute to the overestimation of temperatures, as this effect would increase mass transfer of fuel to the gas phase and therefore reduce temperature (also see [15]).

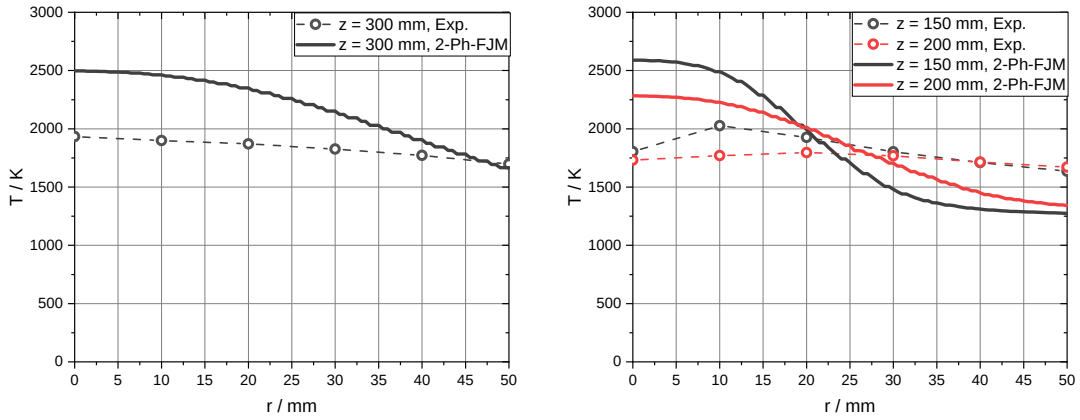


Figure C.15: Comparison of measured and calculated gas temperatures (double-bead thermocouple) for cases MEG-A and MEG-B. Profiles are diesplayed for z = 300 mm (MEG-A) and z = 150 mm and z = 200 mm (MEG-B).

C.2.6 Turbulent Droplet Dispersion

The effect of turbulent droplet dispersion has been mentioned above, but is not modeled in the 2-Ph-FJM. PDA raw data of case MEG-A at z = 150 mm at the jet axis under ambient conditions are shown in Fig. C.16. It can be seen that the droplets in the spray feature a 2-dimensional distribution of droplet velocity and size. The 2-Ph-FJM

calculates mean velocities for each droplet class. The effects of turbulent droplet dispersion on droplet residence time and evaporation are thus not accounted for in the 2-Ph-FJM.

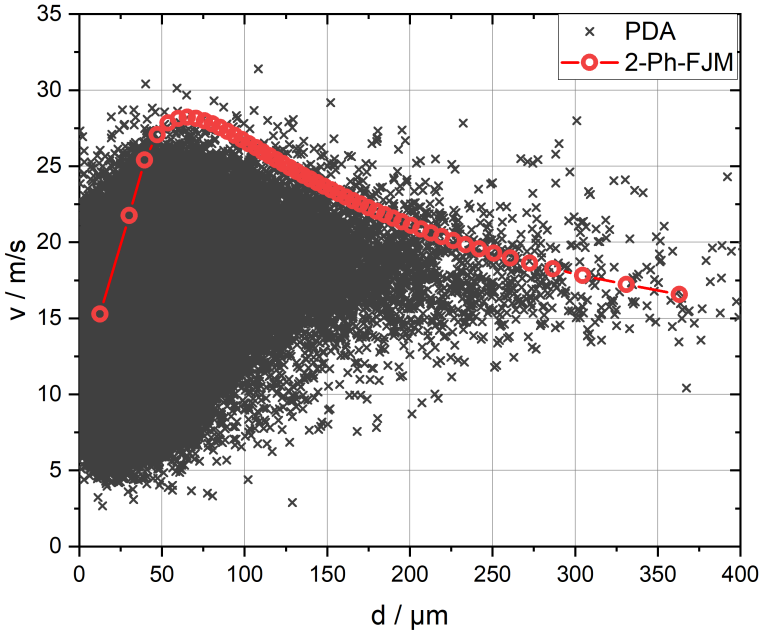


Figure C.16: Measured raw data of droplet velocity and droplet size, together with calculated droplet velocities and size in the 2-Ph-FJM (Case MEG-A, ambient conditions, z = 150 mm, r = 0 mm).

C.3 Additional Modeling Studies

C.3.1 Comparison of Liquid Evaporation Models

This section compares the 2 liquid evaporation models applied in this work, which was not shown in section 5.2.3 in order to improve readability. The results were published and discussed in [16].

A model sensitivity study was conducted for spray angles $\theta_{0.9} = 15\,^\circ$ to $\theta_{0.9} = 40\,^\circ$ and droplet sizes from $d_{32} = 50$ µm to $d_{32} = 250$ µm based on input mass flows of the **MEG**-dataset. A gas momentum flow of J_{gas}=0.21 N is applied. The d^2-law (left) and the evaporation rate controlled by convective heat transfer (right) are compared in Fig. C.17 regarding the total amount of liquid fuel evaporation within the flame $X_{\text{liq,OH}}$.

Comparison of both models shows that for the investigated parameter space, the evaporation rate controlled by convective heat transfer yields higher values for $X_{\text{liq,OH}}$ than the d^2-law, which only takes into account heat conduction. This is an expected result. The

absolute values of $X_{\mathrm{liq,OH}}$ differ by as much as 0.1. For low evaporation rates (e.g. at high droplet size and spray angle), this leads to high relative differences of up to 75 %. At the point of highest evaporation rate, the models differ by 21 %. Despite the quantitative differences, the trends predicted by both models is the same, showing that the simple d^2-law can give an reasonable approximation for parameter studies.

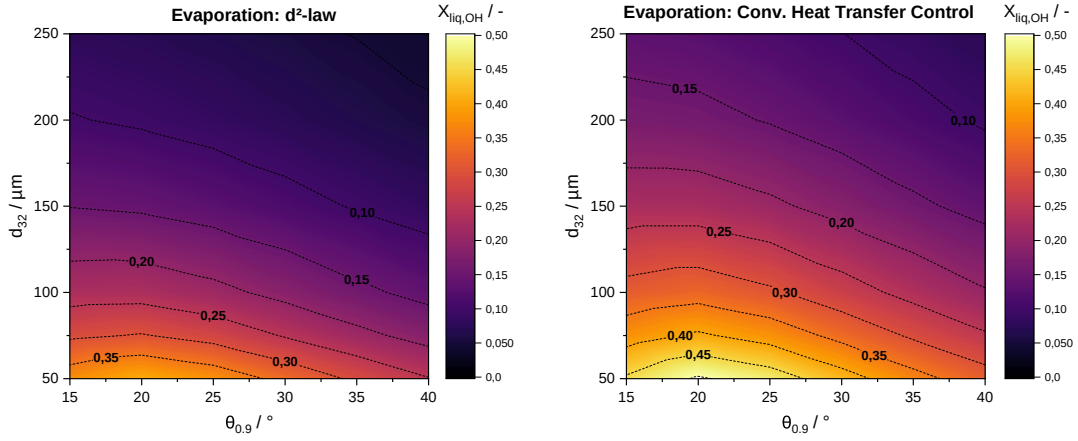


Figure C.17: Calculated $X_{\mathrm{liq,OH}}$ for spray angles from $\theta_{0.9} = 15\,^\circ$ to $\theta_{0.9} = 40\,^\circ$ and droplet sizes from $d_{32} = 50$ µm to $d_{32} = 250$ µm. The d^2-law (left) and the evaporation rate controlled by convective heat transfer (right) are compared. (J_{gas}=0.21 N, Fuel: MEG, input mass flows analogous to the MEG-experiments.) Adapted from [16].

C.3.2 Conversion of Suspension Droplets

In section 5.3.2, the conversion of suspension droplets along different trajectories was investigated. An example for the conditions the suspension droplets experience during conversion is provided in Fig. C.18. Calculated gas temperature T_{gas}, particle temperature T_{p} and mole fractions y_i of O_2, OH, CO_2 of case S30-A are shown for different droplet sizes and trajectories using the Fragmenting Particle model. The profiles are plotted as function of particle / droplet residence time τ.

Suspension droplets are first heated to the liquid boiling point, which occurs on a time scale of $\tau \approx 2$ ms for the 75 µm-droplets and $\tau \approx 3.4$ ms for the 150 µm droplet. At $\tau \approx 4$ ms, the liquid phase has completely evaporated for the 75 µm-droplets. This is indicated by the steep increase of particle temperature, which marks the point where the solid particles are fully dried and the temperature is no longer limited by liquid evaporation. The 150 µm-droplet takes significantly longer to fully evaporate ($\tau \approx 11.7$ ms). There is no substantial difference in evaporation time for the 75 µm-droplets between the jet

centerline and the 7°-trajectory.
It is clearly shown that the solid particles emerging from the droplets are predominantly released in the gasification zone where O_2 and OH are no longer present in significant amounts. Only for the smaller initial droplet size, char particles experience the high flame temperatures up to 2500 K. Solid particles are heated up quickly and adopt temperatures close to the gas temperature. The small particle size of 9 µm causes particle heating rates predicted by the model to reach up to 10^7 K/s. For larger particles, this value is reduced due to the higher particle mass. The influence of devolatilization gases emerging from solid particles on convective heat transfer is also not accounted for by the 2-Ph-FJM. In reality, this would reduce particle heating rates.

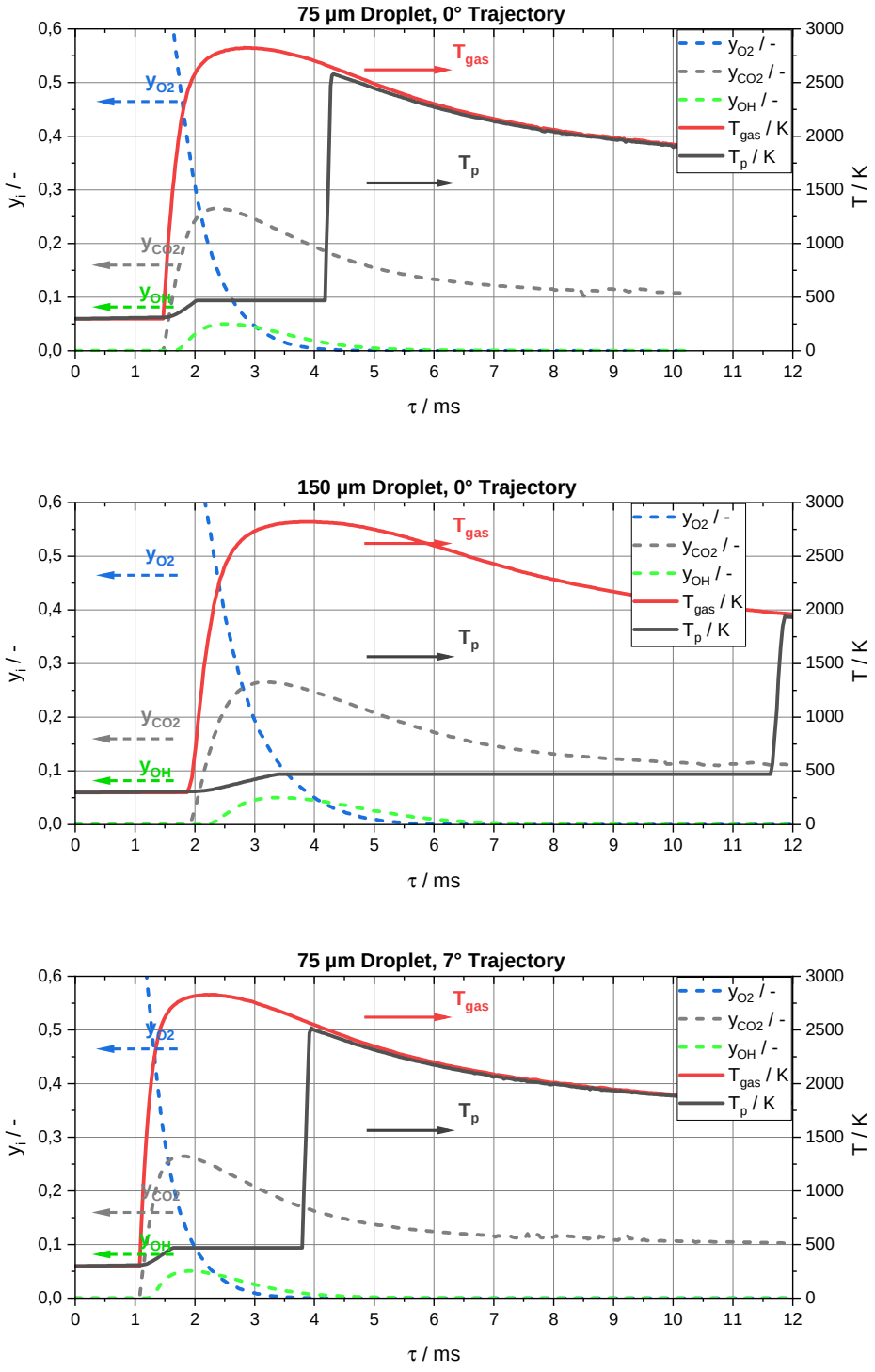


Figure C.18: Calculated gas temperature T_{gas}, particle temperature T_{p} and mole fractions y_i of O_2, OH, CO_2 of case S30-A are shown for different droplet sizes and trajectories using the Fragmenting Particle model. The profiles are plotted as function of particle / droplet residence time τ.

C.3.3 Influence of Recirculation Gas on Flame

The neglection of solid particle recirculation in the 2-Ph-FJM is a significant simplification. This has been discussed in the supplementary material of [17] and is repeated here for clarification. In order to estimate the effect of recirculated particles, a model calculation was performed. The development of a char particle ($d_{\mathrm{p,sol}} = 9$ µm) seeded into the gas jet at the nozzle exit is tracked for conditions of case S30-A. The calculation shows that the solid particle leaves the flame at a conversion of $X_{\mathrm{sol}} = 5.0$ %. The particle residence time in the flame zone is calculated as $\tau = 6$ ms. »This shows that particle residence times in the EFG flame are under the present conditions too short to induce a significant conversion of the investigated solid particles. The impact of recirculated char particles on gas composition in the flame is therefore likewise low, justifying their neglection for the present conditions. If other, more reactive solid fuels are applied, this needs to be checked in the individual case.«[17]

While the reactions of recirculated solid particles presumably exhibit a minor influence on the flame, the composition of the recirculated gas shows a higher influence on flame length. A sensitivity study for this aspect was conducted using input conditions of case S30-A (see Fig. C.19). »For the case when char particles are not completely converted in the recirculation zone, equlibrium compositions of recirculated gas were calculated from the input mass flows assuming full liquid phase conversion and a set degree of char conversion X_{rec}. Results show that for decreasing X_{rec}, the amount of non-fully oxidized species (H_2 and CO) present in the gas phase decreases. This effect leads to an increase of L_{OH}, as more syngas needs to be entrained into the oxidizer jet to achieve stoichiometric conditions. If the experimentally determined char conversion of $X_{\mathrm{sol}} \approx 0.90$ (see section D.3) at the reactor outlet is used as approximation for X_{rec}, the longitudinal extension of OH L_{OH} would decrease from 246 mm to 251 mm.«[17]

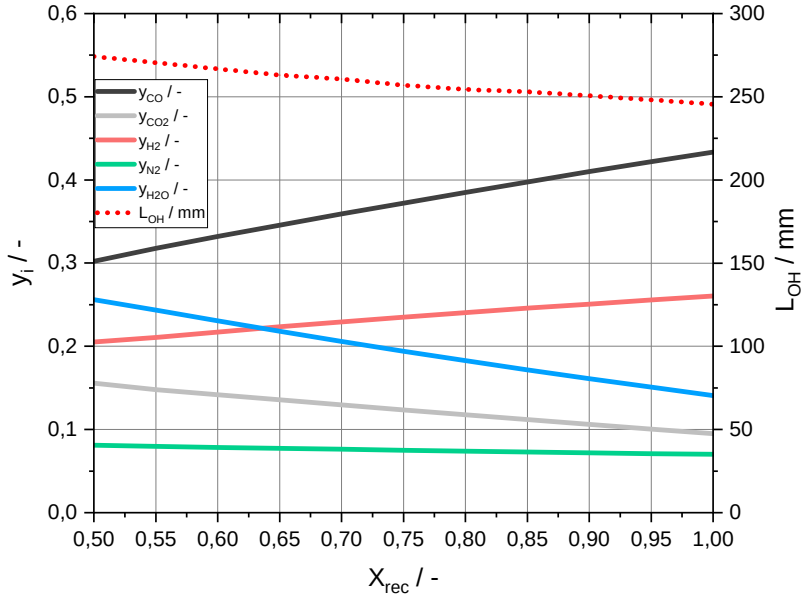


Figure C.19: Composition of recirculated syngas for different degrees of char conversion in the recirculation zone and its impact on longitudinal extension of the OH zone. Input conditions for case S30-A were applied. Adapted from [17]

D Appendix - Experimental Datasets

This section provides the complete experimental datasets obtained in this work. Calculated OH-data for the experimental cases is additionally provided for comparison. The complete validation of the 2-Ph-FJM using spray data, temperature fields and flame parameters including error analysis is provided in section C.2.

D.1 Dataset MEG

The relevant spray and flame data for cases MEG-A and MEG-B is summarized in Table D.1. Spray images under ambient and reacting conditions are shown in Fig. D.1. Case MEG-A features a fiber type primary breakup with a flapping sub-mode (see section 2.2.1). Case MEG-B on the other hand features a super-pulsating primary breakup caused by the higher gas momentum flow, which leads to a smaller droplet size and more narrow spray angle in comparison to case MEG-A. The spray images under gasification images indicate that the same qualitative spray characteristics are also present under reacting conditions [15].

Radial profiles of droplet size and droplet velocity measured under ambient and reactive conditions by PDA are provided in Fig. D.2. The data of liquid mass flux measured under ambient conditions by Patternator is provided in Fig. D.3. The radial profiles at z = 100 mm were used as input conditions for the model calculations according to the procedure described in section 4.3.1. Additional discussion of the effects in the spray and comparison to model results is given in section C.2.4.

Fields of measured OH-LIF intensity and calculated OH concentrations normalized to their maximum value are displayed in Fig. D.4. Respective axial and radial profiles are given in Fig. D.5.

Table D.1: Integral Sauter mean diameter ID_{32}, spray angle $\theta_{0.9}$ and Patternator mass balance error Δm_{liq} at z = 100 mm for the **MEG**-dataset. Longitudinal extensions of the OH zone from experiment $L_{OH,exp}$ and model $L_{OH,mod}$ are also provided. Model results were obtained for both evaporation models

Case	ID_{32} / μm	$\theta_{0.9}$ / °	Δm_{liq} / %	$L_{OH,exp}$ / mm	$L_{OH,mod,d2}$ / mm	$L_{OH,mod,conv}$ / mm
MEG-A	160.3 ±1.9	40.4	-8.5	298	384	353
MEG-B	72.8 ±0.3	23.5	-11.5	133	228	188

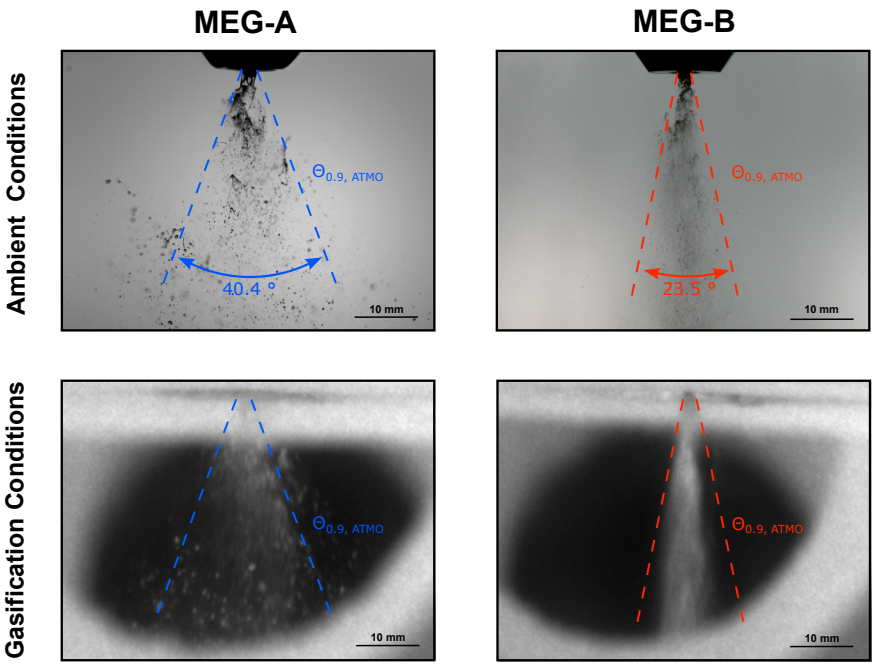


Figure D.1: Spray images for case MEG-A and MEG-B under ambient and reacting conditions (adapted from [15]).

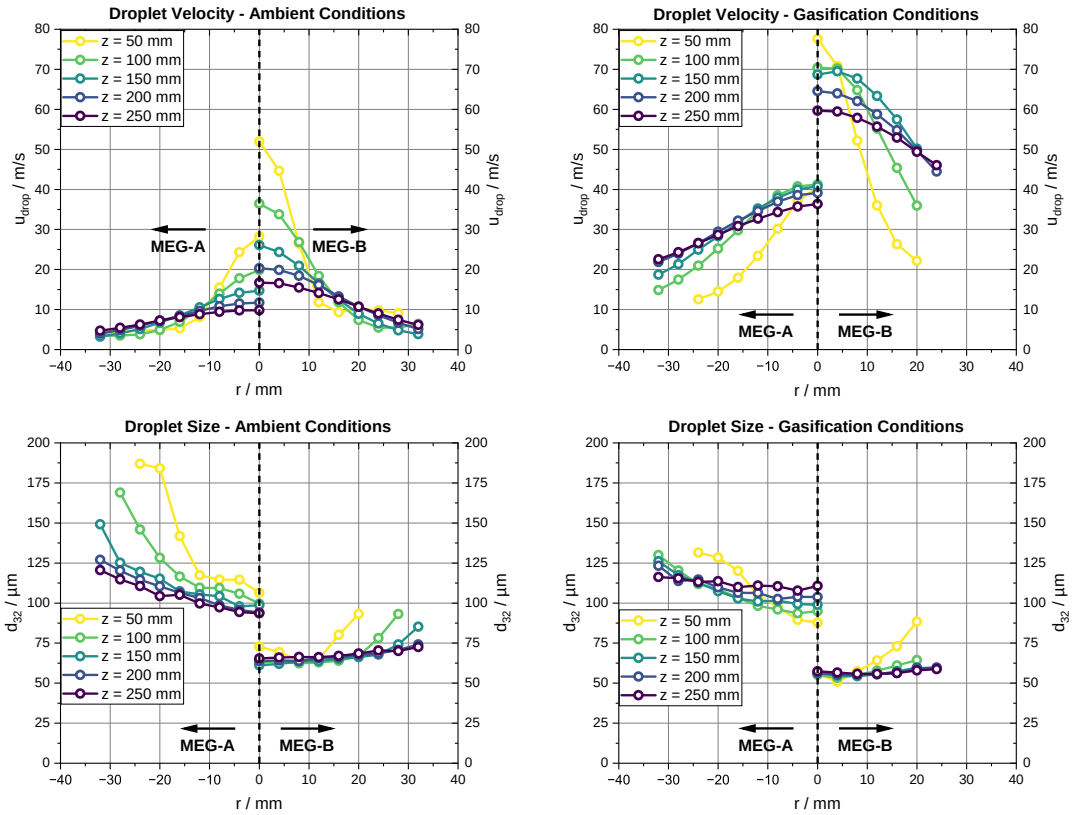


Figure D.2: Radial profiles of droplet size and droplet velocity measured under ambient and reactive conditions by PDA for cases MEG-A and MEG-B.

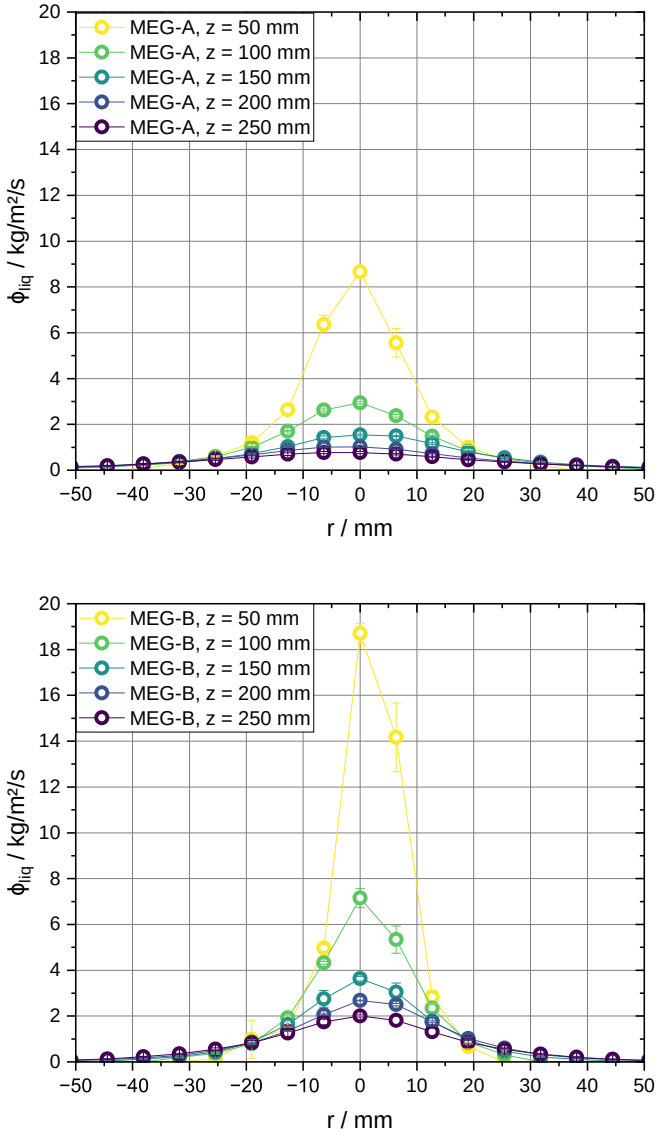


Figure D.3: Radial profiles of liquid mass flux measured under ambient and reactive conditions by Patternator for cases MEG-A and MEG-B.

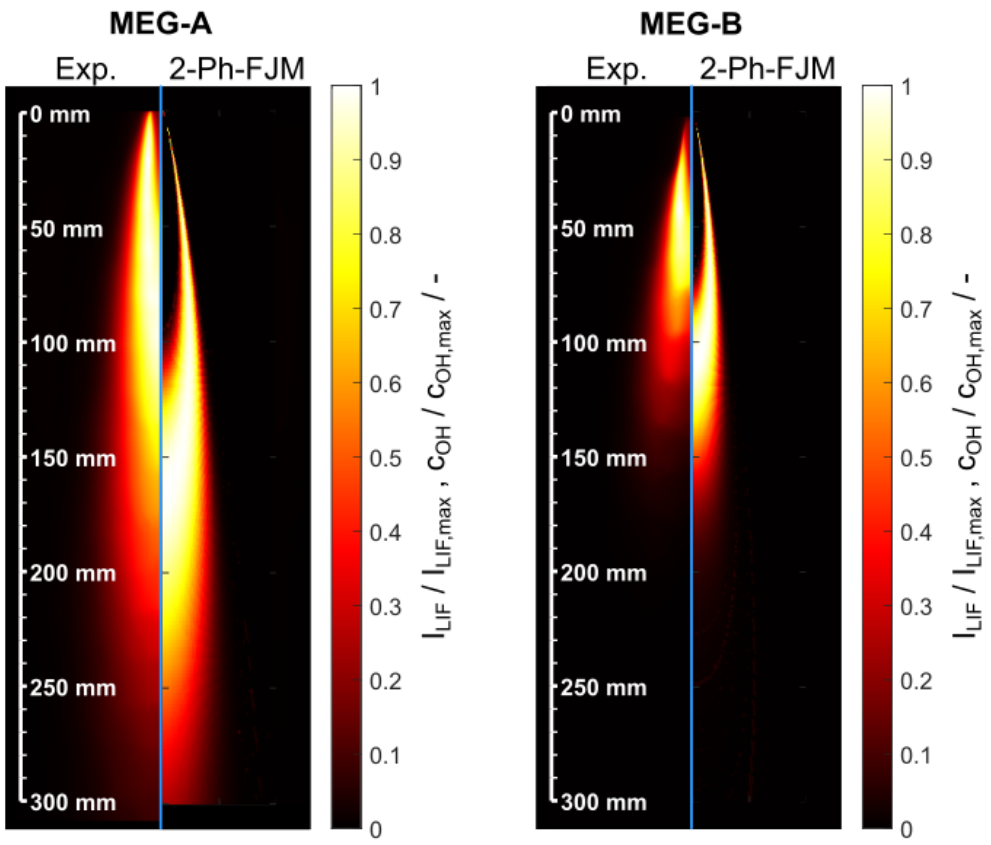


Figure D.4: Fields of normalized measured OH-LIF intensity and normalized caclulated OH concentration for cases MEG-A and MEG-B. Model results displayed were obtained using the evaporation rate determined by convective heat transfer.

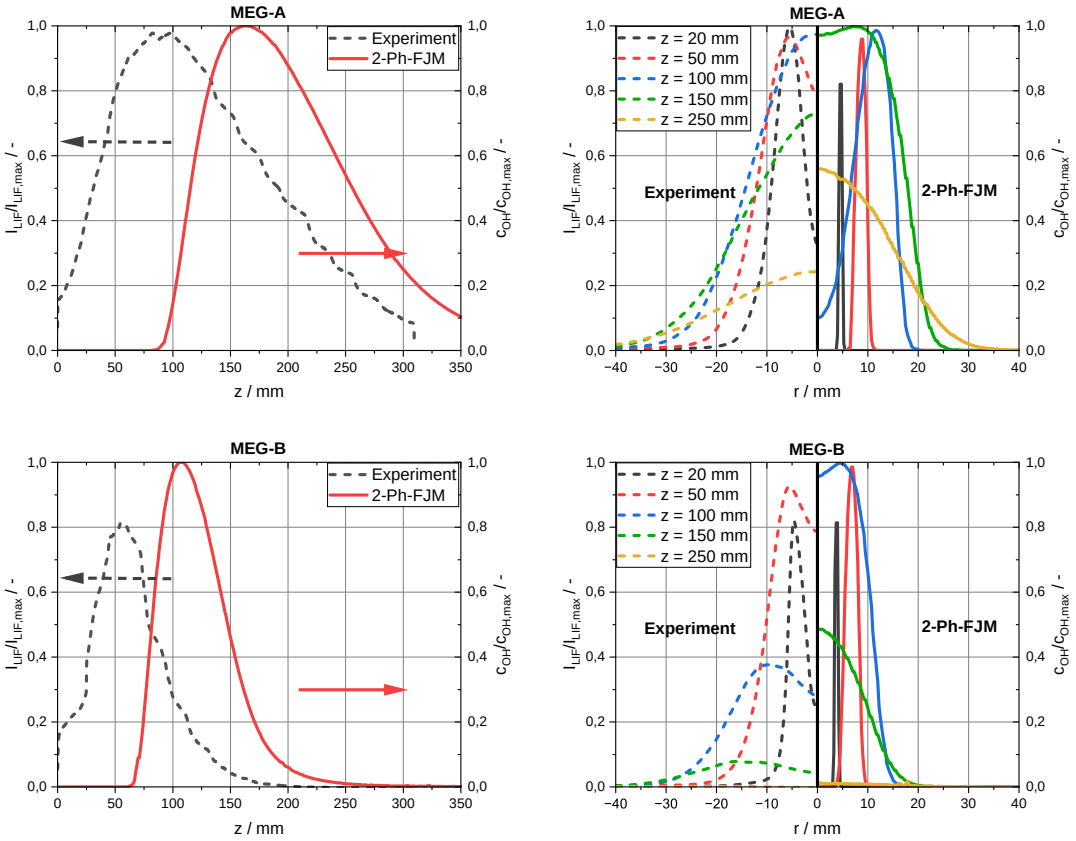


Figure D.5: Axial and radial profiles of normalized measured OH-LIF intensity and normalized caclulated OH concentration for cases MEG-A and MEG-B. Model results displayed were obtained using the evaporation rate determined by convective heat transfer.

D.2 Dataset GLYCEROL

This section provides the complete experimental spray data for dataset **GLYCEROL** as well as measured and calculated OH data. Spray images taken under ambient conditions recorded by the high speed camera are shown in Fig. D.6. Cases A50, A100 and A200 exhibit a predominantly membrane-type primary breakup mode with a flapping instability for increasing viscosities. Cases B50, B100 and B200 on the other hand are characterized by a higher gas momentum and show a fiber-type primary breakup mode coupled with a pulsating primary instability.
The relevant spray data at z = 100 mm is summarized in Table D.2. As OH-LIF data could only be measured up to an axial distance of $z \approx 340$ mm, L_{OH} could not be determined for cases A50, A100 and A200. Radial profiles of droplet size measured under ambient conditions by PDA at z = 100 mm are provided in Fig. D.2. The data of liquid mass flux measured under ambient conditions by Patternator at z = 100 mm is provided in Fig. D.8. The data were used as input conditions for the model calculations according to the procedure described in section 4.3.1. Measured OH-LIF intensity and calculated OH concentrations normalized to their maximum value are displayed for all cases in Figs. D.9 and D.10, along their respective axial and radial profiles (Figs. D.11 and D.12).

Table D.2: Integral Sauter mean diameter ID_{32}, Sauter mean diameter integrated within the gas jet boundaries $\mathrm{ID}_{32,\mathrm{jet}}$, spray angle $\theta_{0.9}$ and Patternator mass balance error Δm_{liq} at z = 100 mm for the **GLYCEROL**-dataset. Longitudinal extensions of the OH zone from experiment $L_{\mathrm{OH,exp}}$ and model $L_{\mathrm{OH,mod}}$ are also provided. Model results were obtained using the d^2-law.

Case	$\frac{\mathrm{ID}_{32}}{\mu\mathrm{m}}$	$\frac{ID_{32,\mathrm{jet}}}{\mu\mathrm{m}}$	$\frac{\theta_{0.9}}{^\circ}$	$\frac{\Delta m_{\mathrm{liq}}}{\%}$	$\frac{L_{\mathrm{OH,exp}}}{\mathrm{mm}}$	$\frac{L_{\mathrm{OH,mod}}}{\mathrm{mm}}$
A50	249.7 ±54.1	88.3 ±1.3	39.7	-19.4	-	392
A100	273.7 ±65.8	99.8 ±1.6	43.0	-14.9	-	412
A200	443.5 ±28.5	106.7 ±14.2	43.6	-14.3	-	418
B50	195.1 ±84.8	63.7 ±1.0	31.2	-11.8	212	255
B100	373.9 ±33.0	64.5 ±0.3	35.6	-12.9	249	268
B200	470.4 ±26.6	67.9 ±0.8	38.8	-15.7	258	278

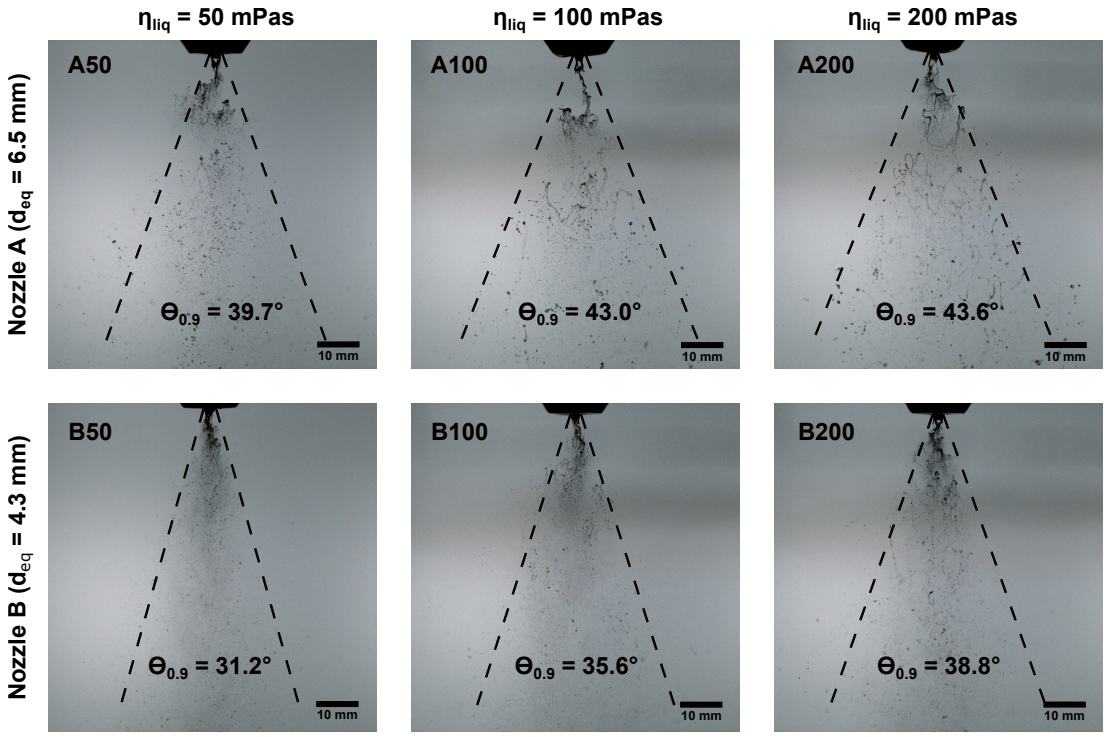


Figure D.6: Spray images for the **GLYCEROL**-dataset under ambient conditions.

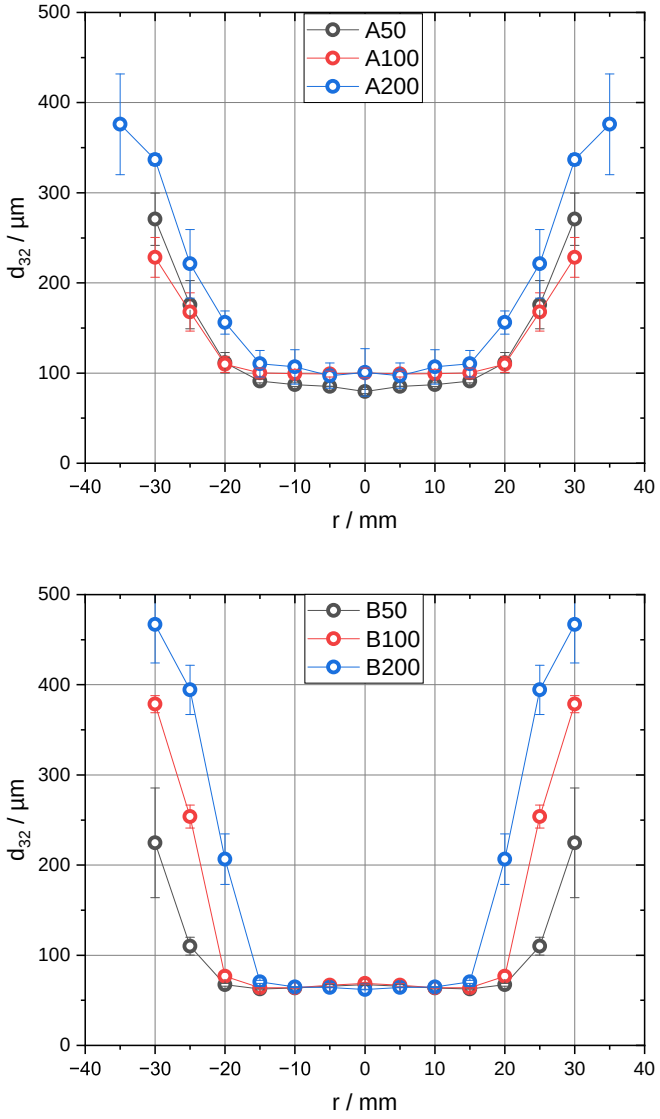


Figure D.7: Radial profiles of droplet size for the **GLYCEROL**-dataset at z = 100 mm measured by PDA under ambient conditions.

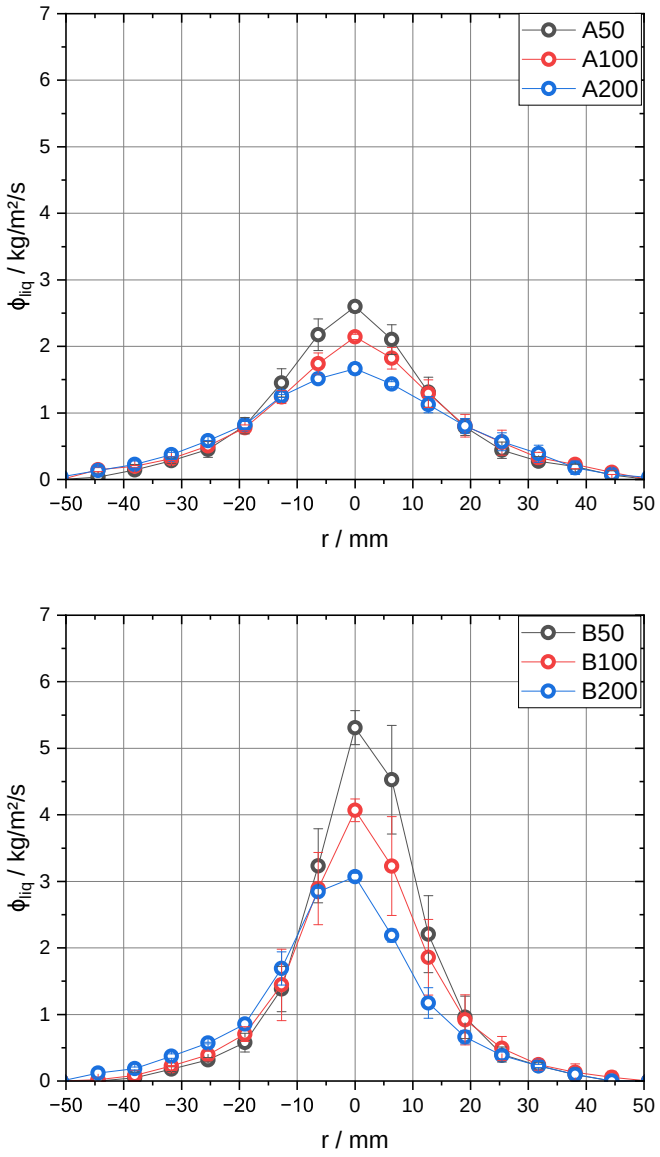


Figure D.8: Radial profiles of liquid mass flux for the **GLYCEROL**-dataset at z = 100 mm measured by Patternator under ambient conditions.

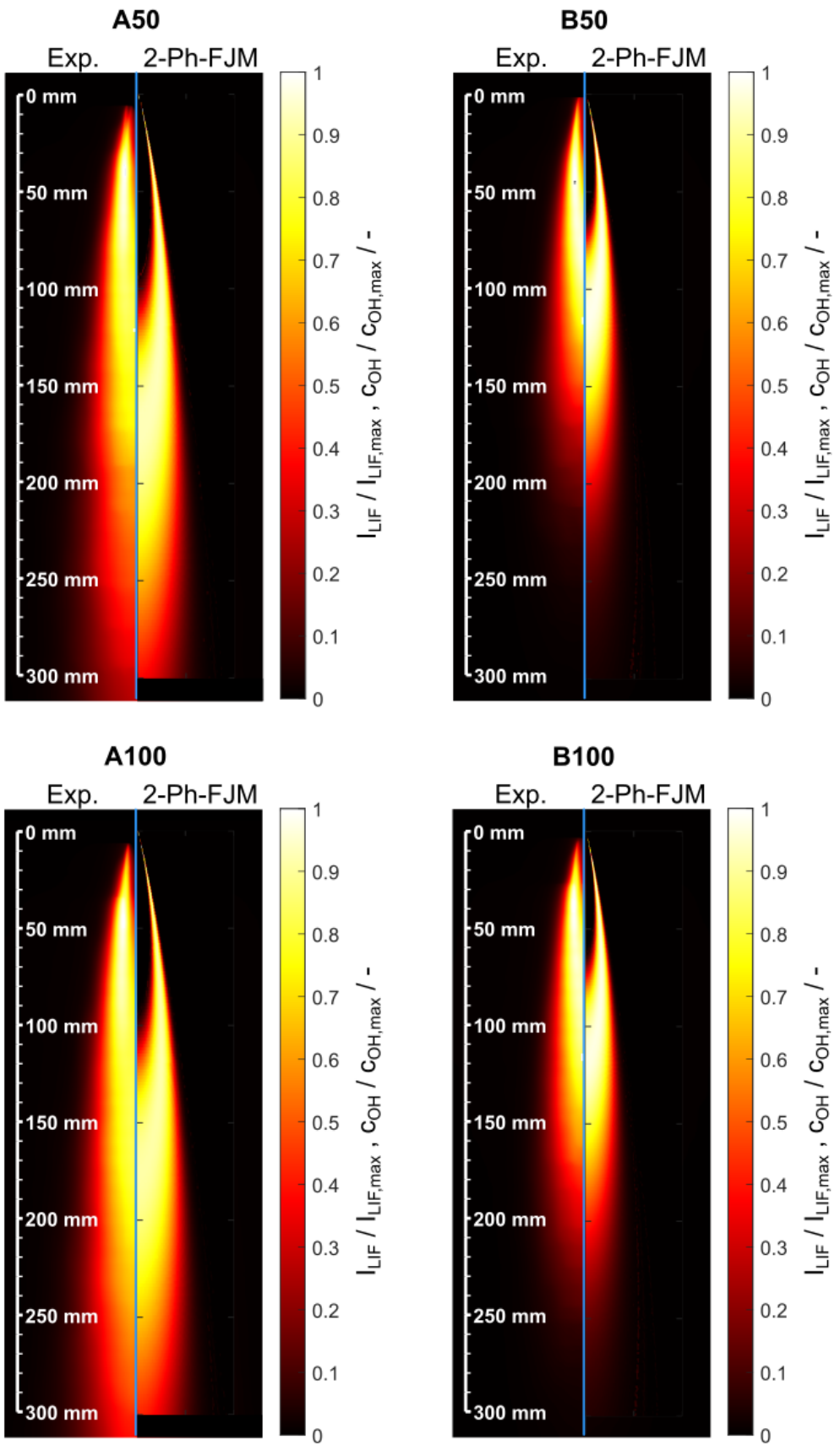


Figure D.9: Fields of normalized measured OH-LIF intensity and normalized caclulated OH concentration for the **GLYCEROL**-dataset. Model results were obtained using the d^2-law.

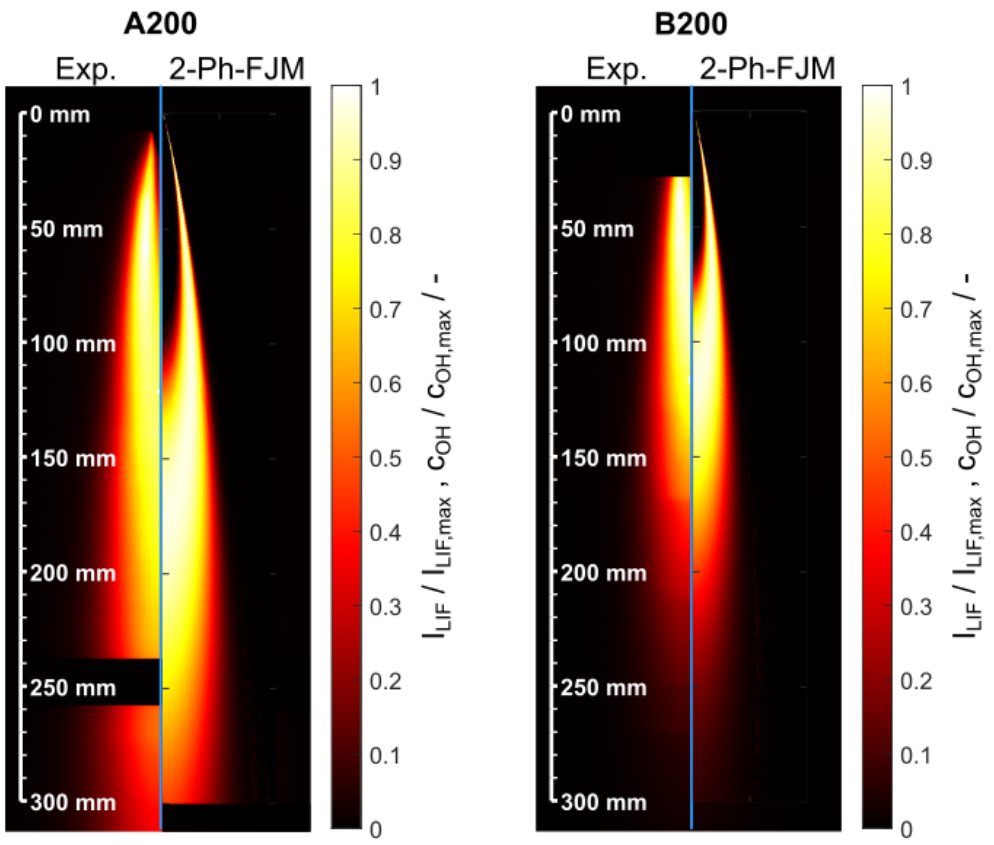


Figure D.10: Fields of normalized measured OH-LIF intensity and normalized caclulated OH concentration for the **GLYCEROL**-dataset (continued). Experimental data around z = 250 mm (Case A200) and z = 20 mm (Case B200) are not available. Model results were obtained using the d^2-law.

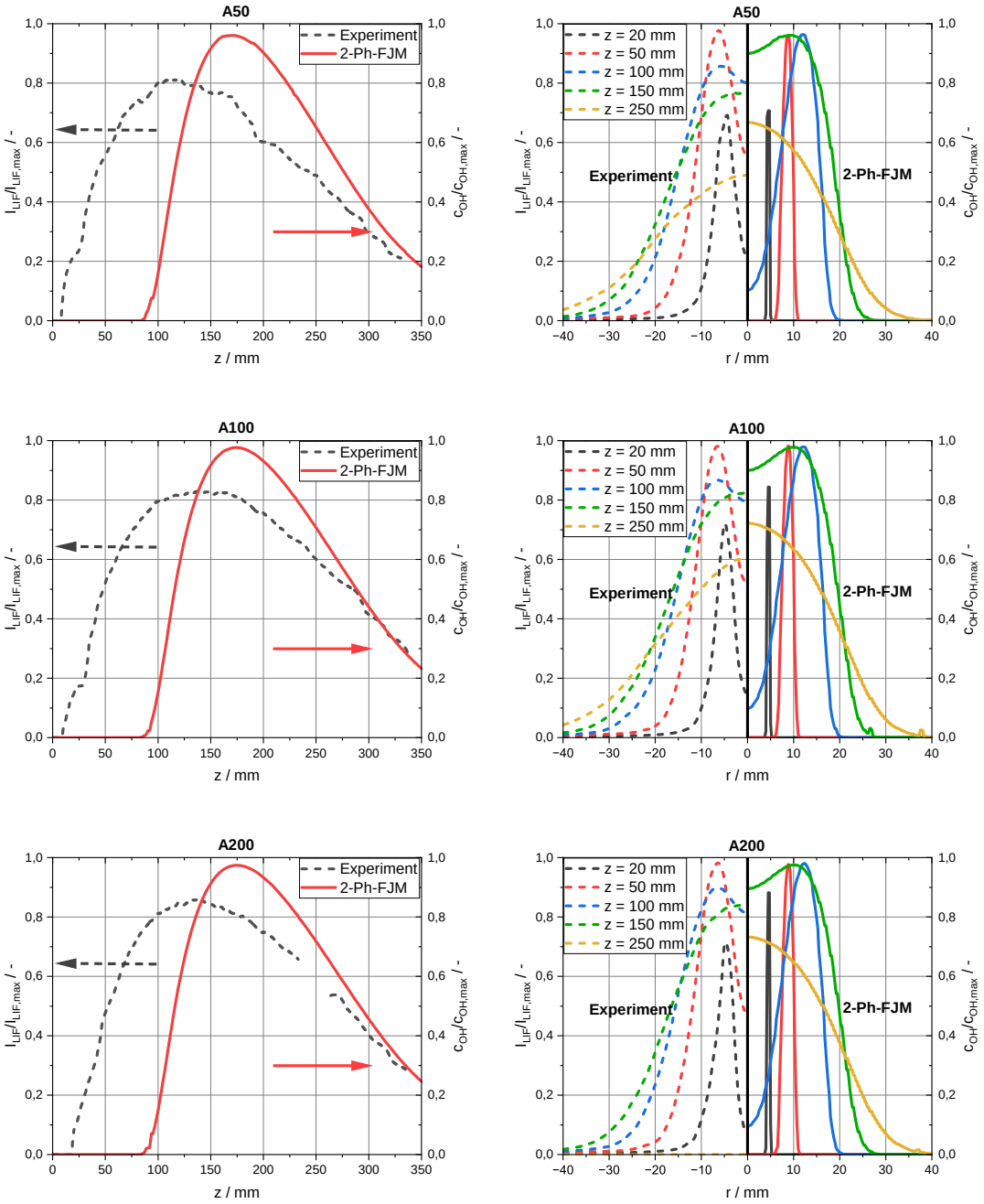


Figure D.11: Radial and axial profiles of normalized measured OH-LIF intensity and normalized caclulated OH concentration for the **GLYCEROL**-dataset. Experimental data around z = 250 mm (Case A200) are missing. Model results were obtained using the d^2-law.

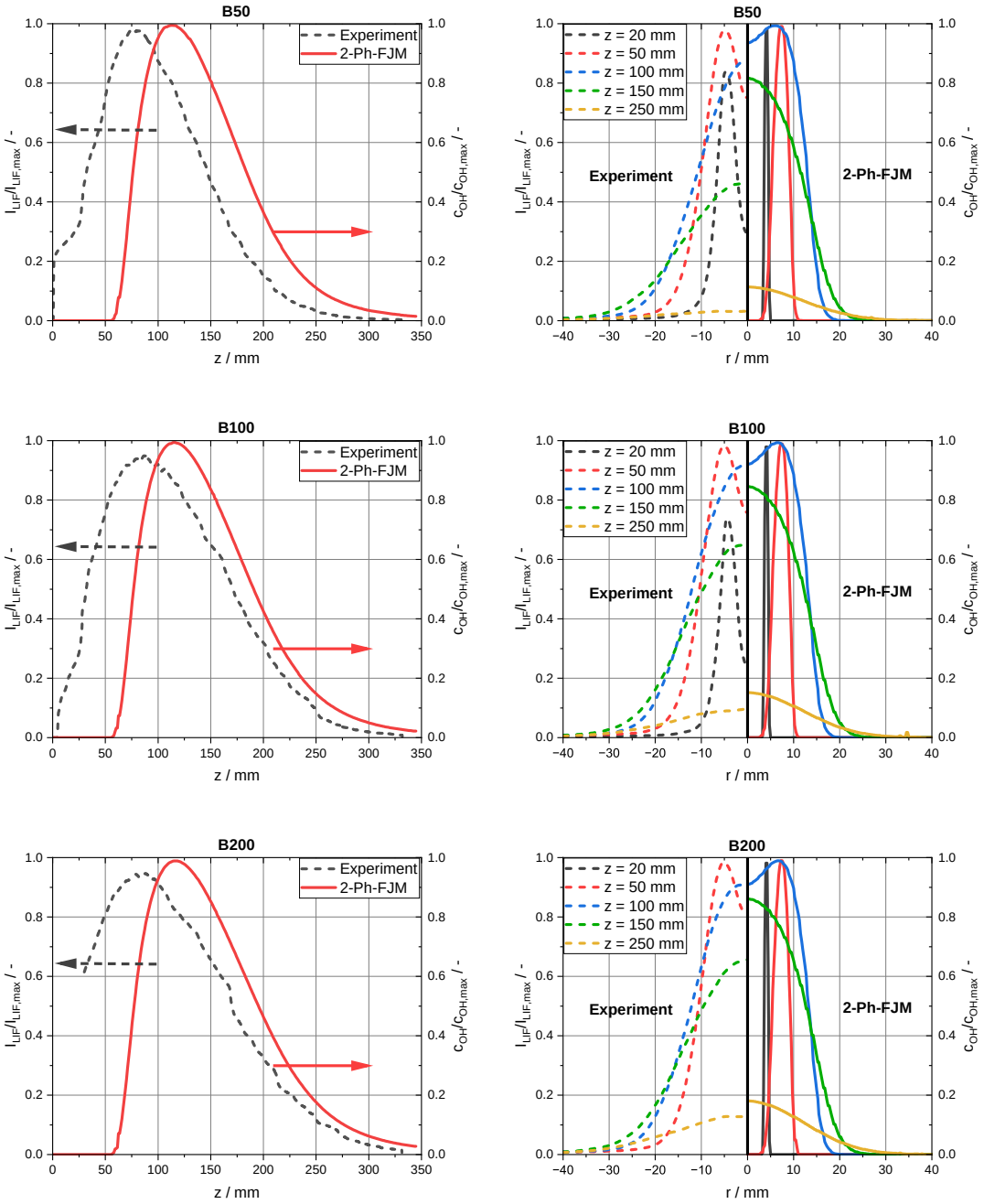


Figure D.12: Radial and axial profiles of normalized measured OH-LIF intensity and normalized caclulated OH concentration for the **GLYCEROL**-dataset (continued). Experimental data around z = 20 mm (Case B200) are missing. Model results were obtained using the d^2-law.

D.3 Dataset SLURRY

This section provides the complete experimental spray data for dataset **SLURRY** along measured and calculated OH data. The relevant spray data at z = 100 mm is summarized in Table D.3. As the shadowgraphy system can only measure integral droplet size distributions along a line of sight, radial profiles of droplet size are not available. Values of integral Sauter mean diameter ID_{32} measured under ambient conditions at z = 100 mm are provided in Fig. D.13. The data of liquid mass flux measured under ambient conditions by Patternator at z = 100 mm is provided in Fig. D.14. The data were used as input conditions for the model calculations according to the procedure described in section 4.3.1, assuming flat radial profiles. This leads to a possible source of error for the model calculations, as the values for droplet size in the jet region can differ from ID_{32}.
Measured OH-LIF intensity and calculated OH concentrations normalized to their maximum value are displayed for all cases in Figs. D.15 and D.16, along their respective axial and radial profiles (Figs. D.17 and D.18).
In addition to the discussion in section 5.3.3, a comparison of calculated OH fields for case S30-A using the three different suspension droplet conversion models applied in this work is provided in Fig. D.19.

Table D.3: Spray data at z = 100 mm for the **SLURRY**-dataset with longitudinal extensions of the OH zone from experiment $L_{OH,exp}$ and model $L_{OH,mod}$. Model results were obtained using the Fragmenting Particle Model.

Case	$\frac{ID_{32}}{\mu m}$	$\frac{\theta_{0.9}}{°}$	$\frac{\Delta m_{liq}}{\%}$	$\frac{L_{OH,exp}}{mm}$	$\frac{L_{OH,mod}}{mm}$
S0	114.0 ±3.5	26.8	-13.2	174	197
S10-A	119.7 ±2.0	27.1	-9.0	219	203
S20-A	134.1 ±2.6	26.9	-17.5	247	212
S30-A	188.8 ±7.0	29.0	-21.4	300	246
S30-B	184.6 ±1.6	33.2	-21.2	304	251
S30-C	195.0 ±0.7	27.8	-43.8	283	248

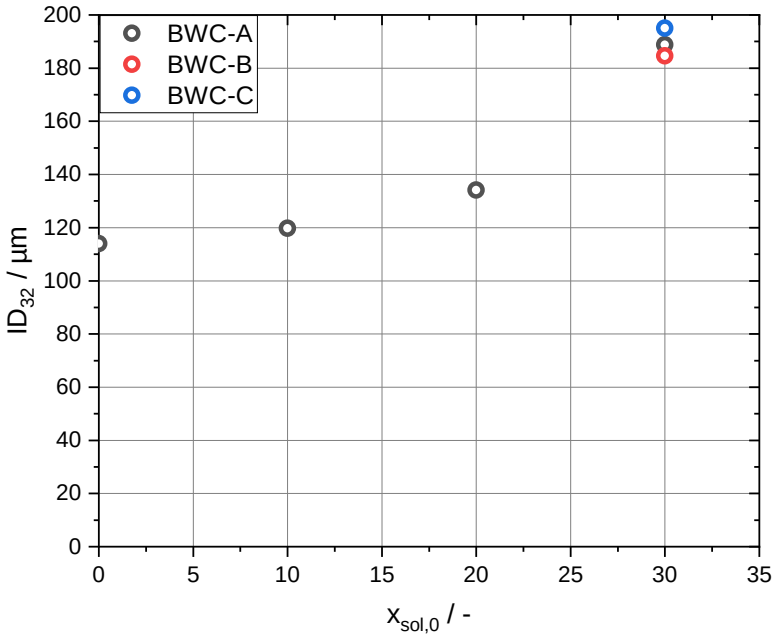


Figure D.13: Integral Sauter Diameter for the **SLURRY**-dataset measured at z = 100 mm under ambient conditions using shadowgraphy.

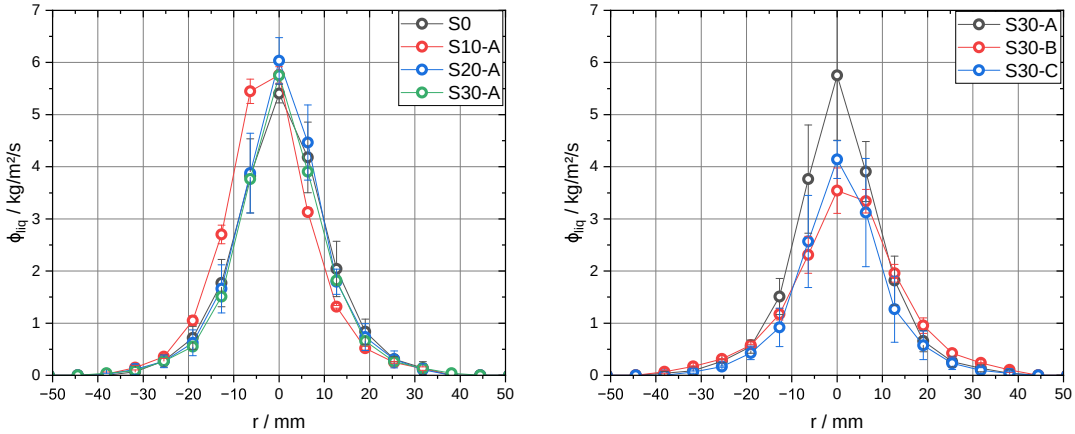


Figure D.14: Liquid mass flux for the **SLURRY**-dataset measured at z = 100 mm under ambient conditions using shadowgraphy.

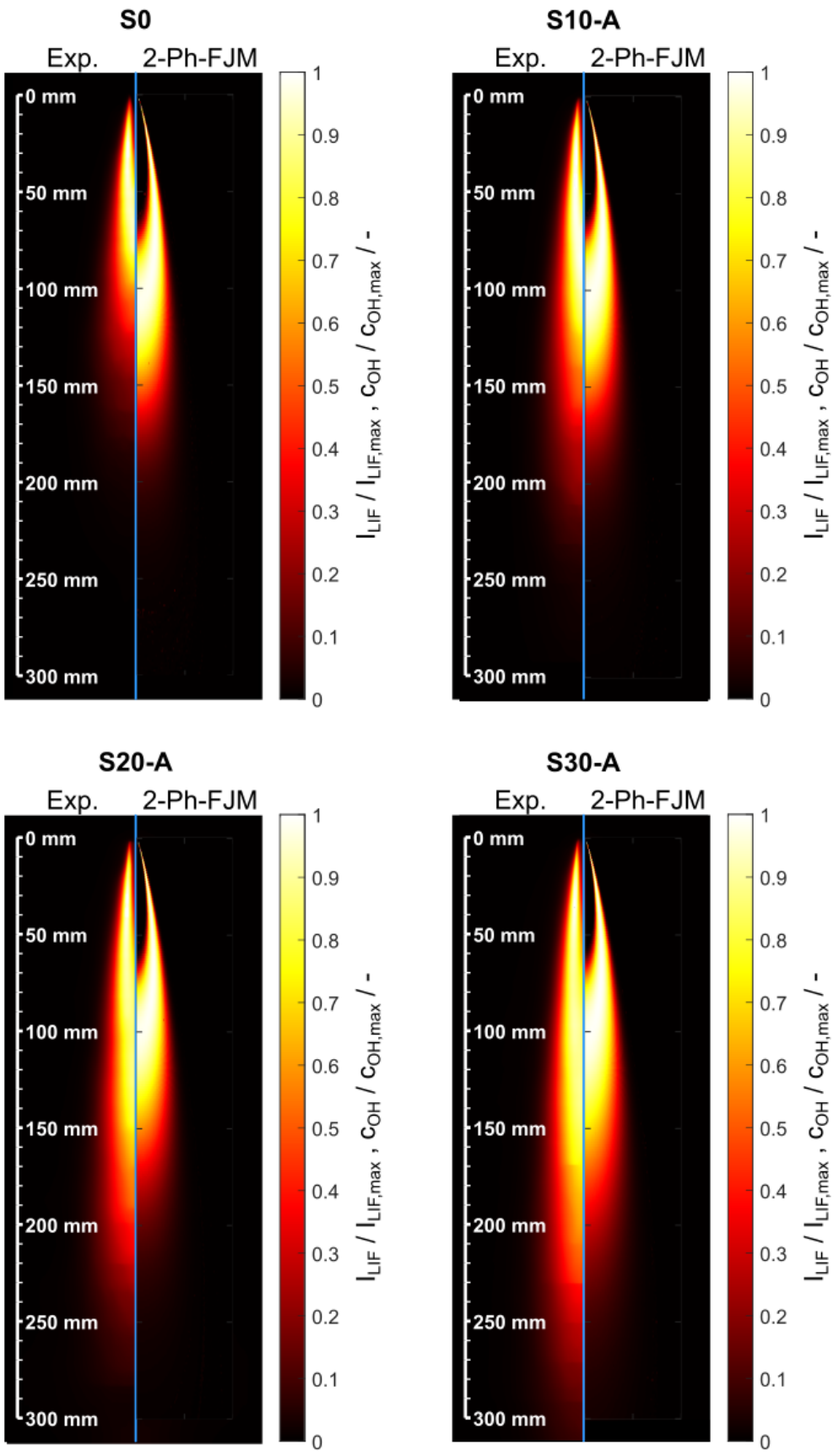


Figure D.15: Fields of normalized measured OH-LIF intensity and normalized caclulated OH concentration for the **SLURRY**-dataset. Model results were obtained using the Fragmenting Particle Model.

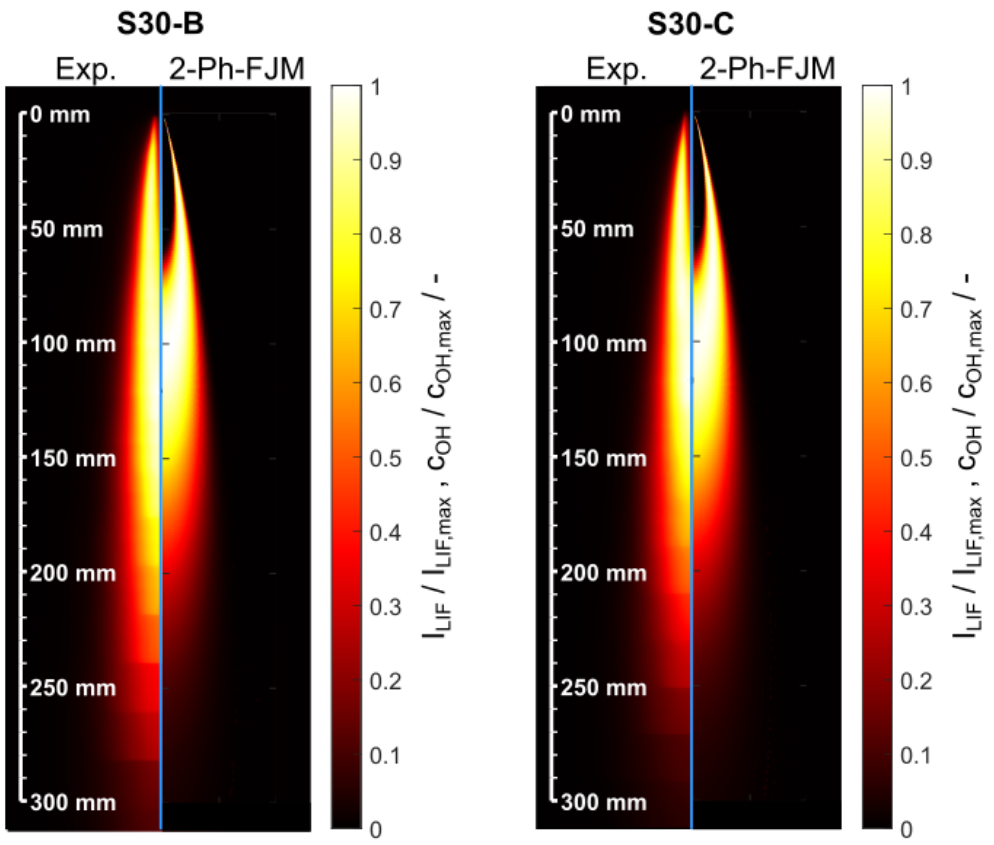


Figure D.16: Fields of normalized measured OH-LIF intensity and normalized caclulated OH concentration for the **SLURRY**-dataset (continued). Model results were obtained using the Fragmenting Particle Model.

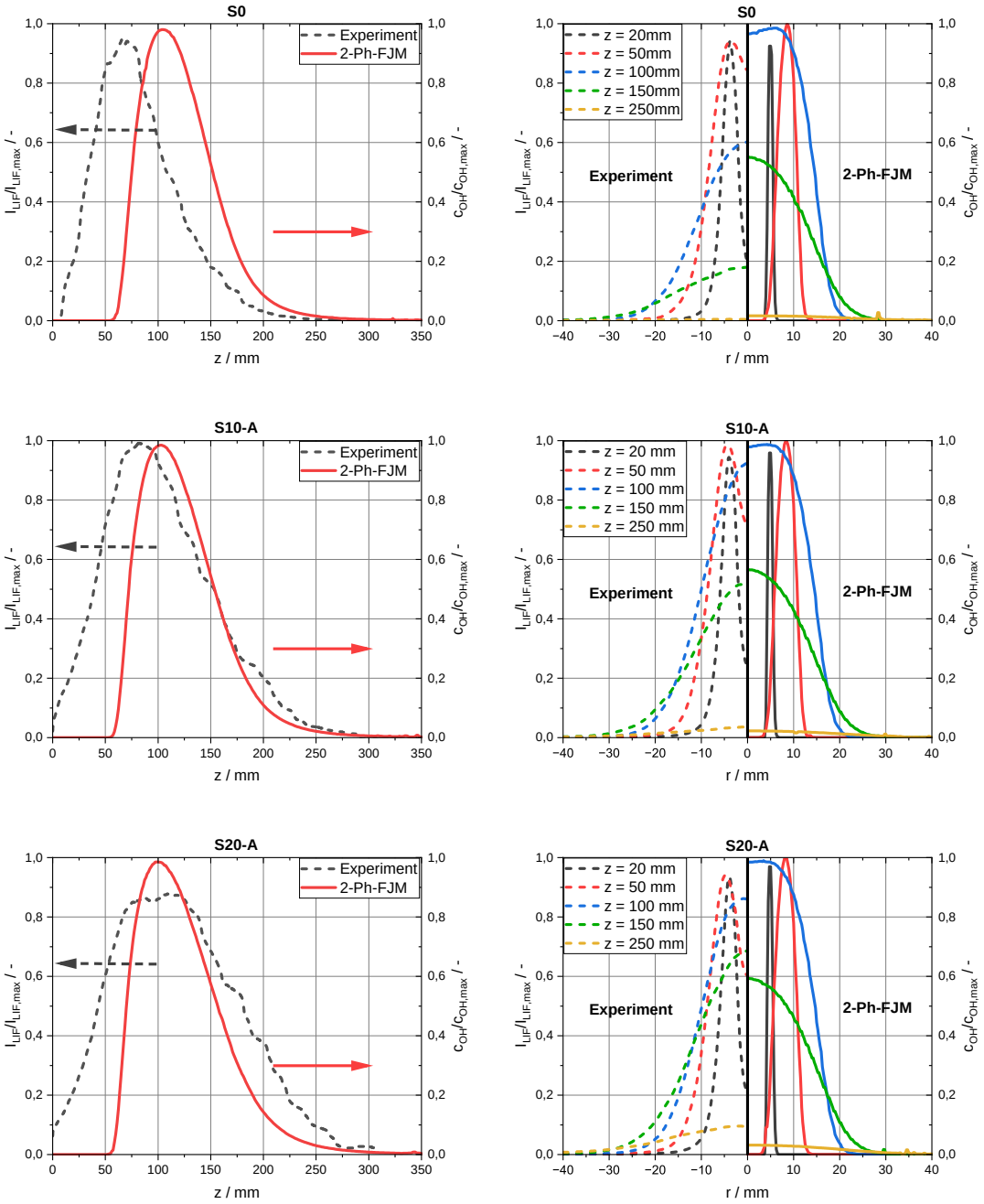


Figure D.17: Radial and axial profiles of normalized measured OH-LIF intensity and normalized caclulated OH concentration for the **SLURRY**-dataset. Model results were obtained using the Fragmenting Particle Model.

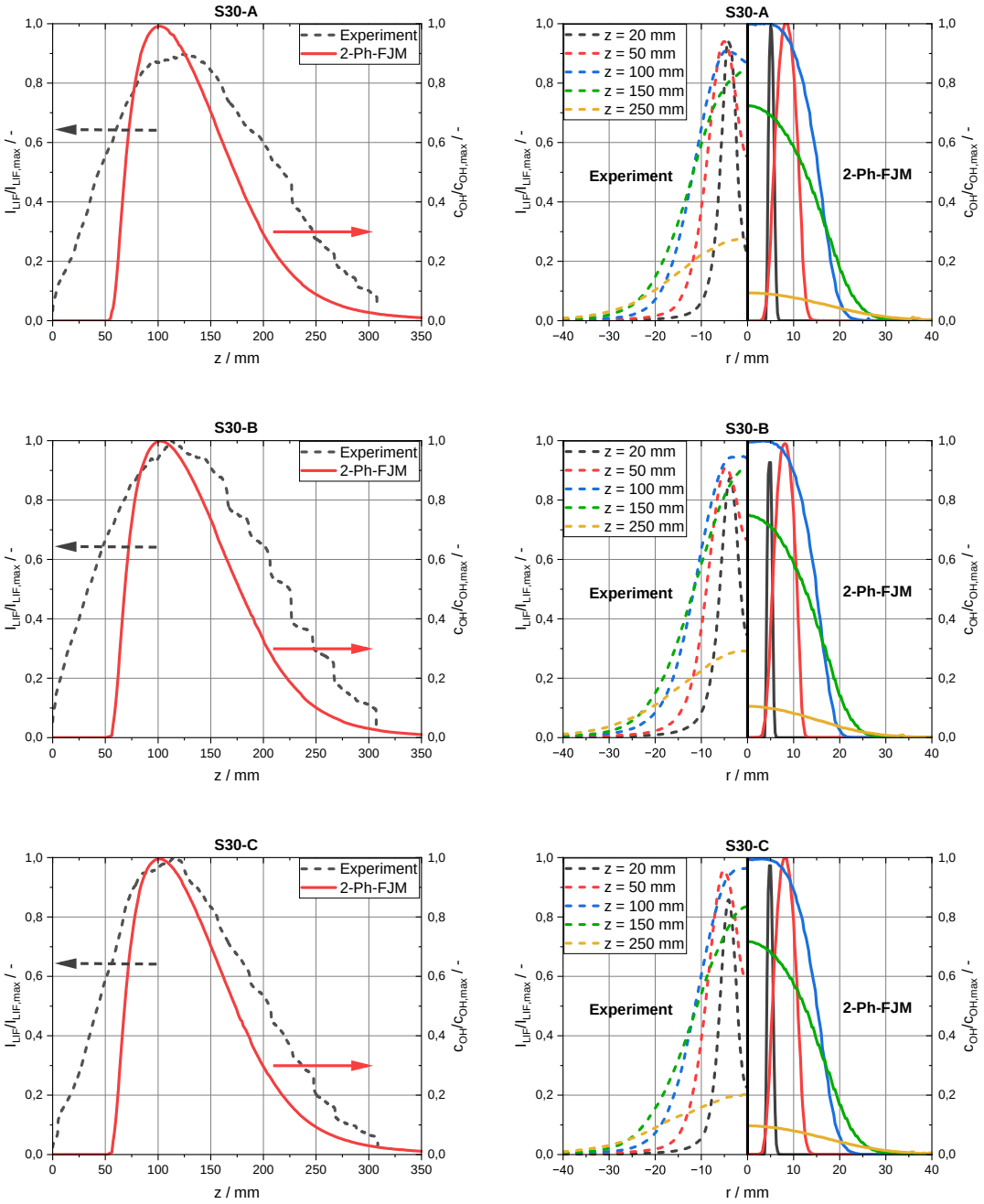


Figure D.18: Radial and axial profiles of normalized measured OH-LIF intensity and normalized caclulated OH concentration for the **SLURRY**-dataset (continued). Model results were obtained using the Fragmenting Particle Model.

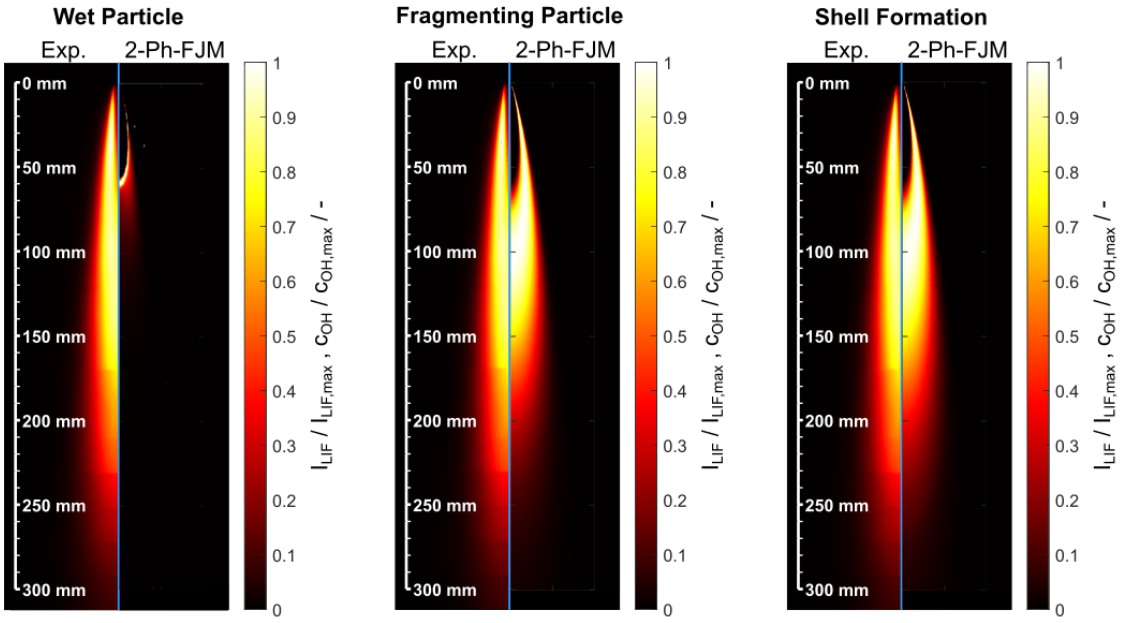


Figure D.19: Normalized calculated OH concentration fields for different suspension droplet conversion models compared against the normalized measured OH-LIF intensity for case S30-A.

Experimental Determination of Char Conversion

The conversion of the solid particles in the suspension fuel experiment was determined by gas phase balancing. Global carbon conversion CC, defined in eq. 2.4, is determined from measured gas concentrations in the REGA experiments by

$$\mathrm{CC} = \frac{\dot{n}_{\mathrm{SG}} \cdot (y_{\mathrm{CO}} + y_{\mathrm{CO2}} + y_{\mathrm{CH4}})}{\dot{n}_{\mathrm{C,fuel}}} \tag{D.1}$$

using the molar flow of syngas $\dot{n}_{\mathrm{SG}}$ and the molar flow of carbon in the fuel $\dot{n}_{\mathrm{C,fuel}}$. Based on these results, solid phase conversion in the suspension experiments was determined. For each suspension experiment, a liquid phase conversion equal to the CC of the pure MEG experiment S0 is assumed:

$$\mathrm{CC}_{\mathrm{solid}} = \frac{\mathrm{CC} \cdot (\dot{n}_{\mathrm{C,MEG}} + \dot{n}_{\mathrm{C,char}}) - \dot{n}_{\mathrm{C,MEG}} \cdot \mathrm{CC}_{\mathrm{S0}}}{\dot{n}_{\mathrm{C,char}}} \tag{D.2}$$

The values of total and solid carbon conversion at the reactor outlet are given in Table D.4.

Particle Extraction Experiments

Particle extraction experiments were conducted in order to determine the morphology of the remaining unconverted char. The procedure and results have been published in the supplementary material of [17] and are repeated here. »The experimental setup is shown schematically in Fig. D.20. Gas is extracted through a ceramic probe through a heated filter by a vacuum pump. The filter is flushed with nitrogen before and after a measurement to avoid the particles coming in contact with oxygen. A particle sample was extraced at the end of the reactor applying a gas volume flow of $\dot{V}_{\mathrm{probe}} = 2\mathrm{m}^3/\mathrm{h}$ (STP) over a time of 30 min.«[17]

»A representative REM image of an extracted particle sample is shown in D.21. Especially in comparison to the raw particles in section B.2, the sample clearly shows that no particle

Table D.4: Total and solid phase carbon conversion for the experiments in dataset **SLURRY** determined by gas phase balancing.

Case	S0	S10-A	S20-A	S30-A	S30-B	S30-C
CC	93.1	91.9	91.1	91.2	92.5	90.2
$\mathrm{CC}_{\mathrm{solid}}$	-	87.4	87.8	89.3	91.9	87.3

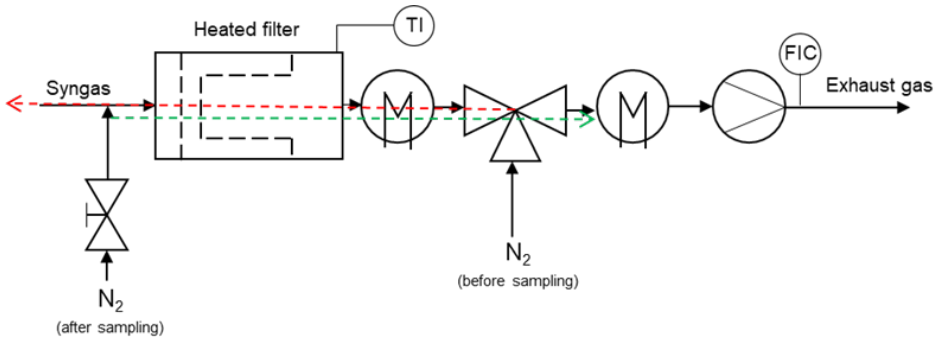


Figure D.20: Setup for particle extraction experiments [17]

agglomerates were found in the product gas. The char particles itself do not show any caking behavior, which was observed in TGA experiments. MEG as liquid phase has a clearly defined boiling point and does not undergo significant pyrolysis reactions before evaporation. Under these conditions, the use of a Fragmenting Particle model approach is justified [158].«[17]

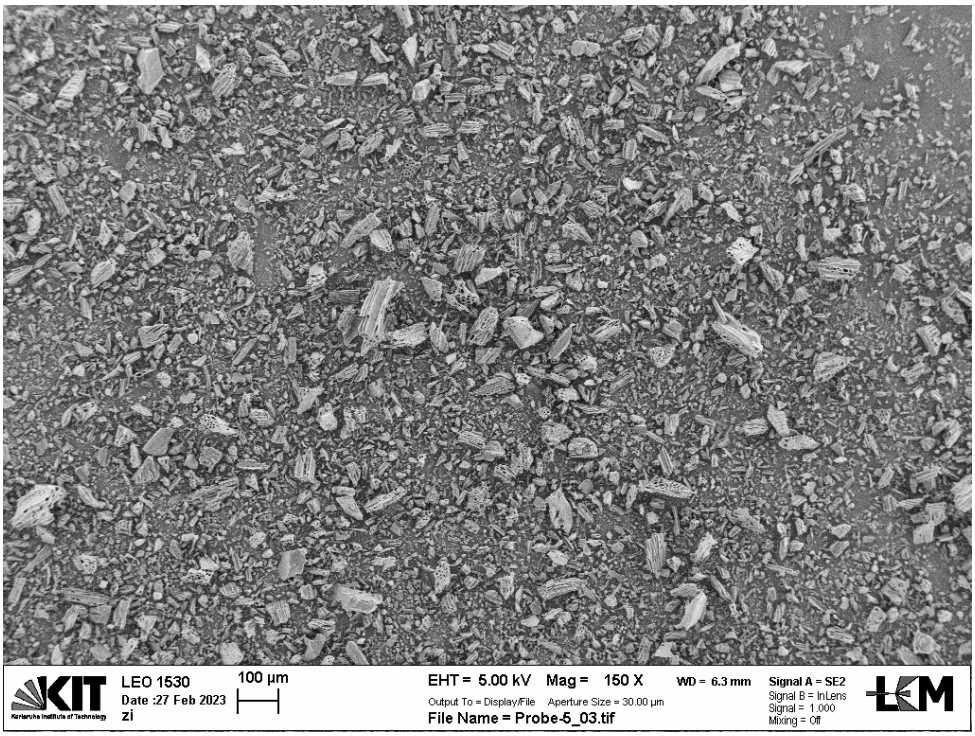


Figure D.21: Particle sample for case S30-A extracted at the end of the reactor. [17]

List of Publications

Journal Publications

- *Conversion of suspension fuel droplets in the flame zone of an entrained flow gasifier.*
  Haas, M.; Fleck, S.; Scheiff, F.; Kolb, T.; 2026, Fuel, 416, Art.-Nr.: 138473, doi:10.1016/j.fuel.2026.138473

- *Optical Measurement Method for Monitoring High-Mass-Concentration Slurry Sprays: An Experimental Study.*
  Schaefer, W.; Fleck, S.; **Haas, M.**; Jakobs, T.; 2025, Photonics 2025, 12(7), 673, doi:10.3390/photonics12070673

- *Liquid Fuel Evaporation under Entrained Flow Gasification Conditions – Insights for Burner Development.*
  Haas, M.; Fleck, S.; Jakobs, T.; Kolb, T.; 2025, Thermal Science and Engineering Progress, 59, Art.-Nr.: 103342, doi:10.1016/j.tsep.2025.10334

- *Entrained flow gasification: Impact of fuel spray distribution on reaction zone structure.*
  Haas, M.; Dammann, M.; Fleck, S.; Kolb, T.; 2023. Fuel, 334 (2), Art.-Nr.: 126572. doi:10.1016/j.fuel.2022.126572

- *Experimental investigation on entrainment in two-phase free jets.*
  Hotz, C.; **Haas, M.**; Wachter, S.; Fleck, S.; Kolb, T.; 2023. Fuel, 335, Article no: 126912. doi:10.1016/j.fuel.2022.126912

- *Two-phase free jet model of an atmospheric entrained flow gasifier.*
  Hotz, C.; **Haas, M.**; Wachter, S.; Fleck, S.; Kolb, T.; 2021. Fuel, 304, Art.-Nr.: 121392. doi:doi:10.1016/j.fuel.2021.121392

- *Insights into the catalytic CO_2 methanation of a boiling water cooled fixed-bed reactor: Simulation-based analysis.*
  Gruber, M.; Wiedmann, D.; **Haas, M.**; Harth, S.; Loukou, A.; Trimis, D.; 2021. The chemical engineering journal, 406, Article no: 126788. doi:doi:10.1016/j.cej.2020.126788

- *Polymer crystallinity and crystallization kinetics via benchtop 1-H-NMR relaxometry: Revisited method, data analysis, and experiments on common polymers.*
  Räntzsch, V.; **Haas, M.**; Özen, M. B.; Ratzsch, K.-F.; Riazi, K.; Kauffmann-Weiss, S.; Palacios, J. K.; Müller, A. J.; Vittorias, I.; Gisela Guthausen; Wilhelm, M.; 2018. Polymer, 145, 162–173. doi:10.1016/j.polymer.2018.04.066

Conference Presentations

- *Sheet burner nozzle: Influence of liquid mass flow and viscosity on droplet size.* Deutscher Flammentag (2025), 2025, Paderborn, Germany.
  Richter, J.; **Haas, M.;** Jakobs, T.; Fleck, S.; Scheiff, F.; Kolb, T.

- *Conversion of suspension fuels under entrained flow gasification conditions.* Deutscher Flammentag (2025), 2025, Paderborn, Germany.
  Haas, M.; Fleck, S.; Santo, U.; Jakobs, T.; Scheiff, F.; Kolb, T.

- *The role of hydrogen and syngas for coupling energy transformation and circular economy.* DGMK "Hydrogen and Syngas" (2025), Essen, Germany.
  Scheiff, F.; Kolb, T.; Bajohr, S.; Graf, F.; Fleck, S.; Santo, U.; Jakobs, T.; **Haas, M.;** Heneka, M.; Köppel, W.

- *Conversion of Suspension Fuel Droplets under Entrained Flow Gasification Conditions Investigated Using a Simplified Modeling Approach.* 5th International Workshop on Oxyfuel Combustion 2025, Aachen, Germany.
  Haas, M.; Fleck, S.; T.; Kolb, T., Scheiff, F.

- *Chemisches Recycling von Kunststoffabfällen: Untersuchungen zur Umsetzung kunststoffbasierter Pyrolyseöle im Flugstromvergaser.* Jahrestreffen der DECHEMA-Fachgruppen Abfallbehandlung und Wertstoffrückgewinnung (AuW), Hochtemperaturtechnik (HTT) und Rohstoffe (ROH), 2025, Dresden, Germany.
  Fleck, S.; **Haas, M.**; Santo, U.; Tavakkol, S.; Stapf, D.; Kolb, T.; Scheiff, F.

- *Measurement Method for Monitoring Slurry Sprays.* Jahrestreffen der DECHEMA/VDI-Fachgruppe Fluidverfahrenstechnik, 2025, Bochum, Germany.
  Schäfer, W.; **Haas, M.**; Fleck, S.; Jakobs, T.

- *Entrained Flow Gasification of Suspension Fuels – A New Modeling Approach to Investigate Processes in Burner Near Field.* TC Biomass 2024, Chicago, USA.
  Haas, M.; Fleck, S.; T.; Kolb, T.

- *Bewertung der Vergasungseigenschaften verschiedener Pyrolyseöle unter Flugstrombedingungen.* Jahrestreffen der ProcessNet Fachgruppe Hochtemperaturtechnik, 2024, Lindlar, Germany. Fleck, S.; **Haas, M.**; Santo, U.; Jakobs, T.; Kolb, T.

- *Liquid Fuel Evaporation under Entrained Flow Gasification Conditions – Insights for Burner Development.* 14th European Conference on Industrial Furnaces and Boilers, 2024, Albufeira, Portugal.
  Haas, M.; Fleck, S.; Jakobs, T.; Kolb, T.

- *High Pressure Entrained Flow Gasification - a Key Enabling Technology in Circular Economy.* Helmholtz Energy Conference 2023, Koblenz, Germany.
  Fleck, S.; **Haas, M.**; Santo, U.; Jakobs, T.; Kolb, T.

- *Burner Development for High Pressure Entrained Flow Gasification.* International Freiberg Conference 2023, Rotterdam, Netherlands.
  Jakobs, T.; Wachter, S.; **Haas, M.**; Fleck, S.; Kolb, T. doi:10.1002/cite.202255022

- *Einfluss der Brennergeometrie auf Flammenstruktur und Brennstoffumsatz bei der Flugstromvergasung von Pyrolyseöl.* Jahrestreffen der DECHEMA Fachgruppe Hochtemperaturtechnik 2023, Karlsruhe, Germany.
  Haas, M.; Fleck, S.; Kolb, T.

- *Burner Development for High Pressure Entrained Flow Gasification.* (Bio)Process Engineering - a Key to Sustainable Development, 2022, Aachen, Germany.
  Jakobs, T.; Wachter, S.; **Haas, M.**; Fleck, S.; Kolb, T. doi:10.1002/cite.202255022

- *Entrained flow gasification of pyrolysis oil – influence of flame structure on fuel conversion.* (Bio)Process Engineering - a Key to Sustainable Development, 2022, Aachen, Germany.
  Haas, M.; Fleck, S.; Böning, D.; Santo, U.; Kolb, T.

- *Detailed Experimental Analysis of Flow Field and Flame Structure in an Entrained Flow Gasifier – Insights into Reaction Zones in Liquid Fuel Gasification.* 30. Deutscher Flammentag 2021, held online.
  Haas, M.; Fleck, S.; Kolb, T.

- *Investigation of Burner Near Processes in Entrained Flow Gasification.* 4th Doctoral Colloquium BIOENERGY, 2021, Karlsruhe, Germany.
  Haas, M.; Fleck, S.; Kolb, T.

Conference Posters

- *Entrained flow gasification of biogenic fuels – application of characteristic parameters to describe syngas quality and yield.* 29. Deutscher Flammentag 2019, Bochum, Germany.
  Fleck, S.; Santo, U.; Eberhard, M.; **Haas, M.**; Kolb, T.

- *Charakterisierung von Reaktionszonen in unterstöchiometrischen Sprayflammen am Beispiel der Flugstromvergasung.* Jahrestreffen der DECHEMA Fachgruppe Hochtemperaturtechnik 2019, Karlsruhe, Germany.
  Haas, M.; Fleck, S.; Hotz, C.; Kolb, T.